

Spin Phenomena in the Fractional Quantum Hall Effect: NMR and Magnetotransport Studies

**Von der Fakultät Mathematik und Physik der Universität Stuttgart zur
Erlangung der Würde eines Doktors der Naturwissenschaften
(Dr. rer. nat.) genehmigte Abhandlung**

vorgelegt von

OMAR I. STERN

aus Monterrey, Mexico

Hauptberichter:	Prof. Dr. K. v. KLITZING
Mitberichter:	Prof. Dr. G. DENNINGER
Tag der Einreichung:	22.12.2004
Tag der mündlichen Prüfung:	23.02.2005

**MAX-PLANCK-INSTITUT FÜR FESTKÖRPERFORSCHUNG
STUTTGART, 2005**

Contents

Symbols and Abbreviations	7
1 Introduction	13
2 The Quantum Hall Effect	19
2.1 The Classical Hall Effect	19
2.1.1 The Two-Dimensional Electron System	19
2.1.2 Classical Magnetotransport	21
2.2 The Integer Quantum Hall Effect	22
2.2.1 Landau Quantization	22
2.2.2 Quantum Mechanical Magnetotransport	24
2.3 The Fractional Quantum Hall Effect	28
2.3.1 Laughlin's Trial Wavefunction	30
2.3.2 Composite Fermion (CF) Picture	32
2.4 The Spin Degree of Freedom in the Lowest Landau Level	34
2.4.1 Spin Phase Transitions	35
2.4.2 Spin in the CF Picture	38
2.4.3 Polarization at $\nu = 1/2$	40
2.4.4 Skyrmions and Quasiparticle Excitations	42
2.4.5 Interactions between Electrons and Nuclei	45
2.4.6 Measuring Techniques	47
3 Samples and Experimental Setup	51
3.1 The Samples	51
3.2 Experimental Setup	53
3.2.1 Quasi-DC Transport	54
3.2.2 NMR	54
4 Transport Studies of the $\nu = 2/3$ Spin Phase Transition	59
4.1 The Low and High Current Regimes	61

4.2	Phase Diagram of the $\nu = 2/3$ Ground State	62
4.2.1	Tilted B -field Experiments	63
4.2.2	Density Sweep	65
4.2.3	Phase Diagram	67
4.3	Hysteresis and Time Dependence of the Transition	69
4.4	Hall Resistance	72
4.5	Model of the Transition	73
4.6	Time, Frequency and Current Dependence at the Transition	76
4.6.1	AC measurements: Time and Current Dependence	76
4.6.2	DC and Differential Resistance Measurements	78
4.6.3	Conclusions	80
4.7	Activation Measurements	81
4.7.1	Temperature Dependence	82
4.7.2	Activation Gap	83
4.7.3	B_N Determination	88
5	NMR Studies of the Lowest Landau Level	91
5.1	NMR Basics	92
5.2	Measurements of the Electron Spin Polarization	96
5.2.1	The RDNMR/NMR Technique	97
5.2.2	Calibration Curve at $\nu = 1/2$	99
5.2.3	Study of the Electron Spin Polarization at the $\nu = 2/3$ Transition . . .	101
5.2.4	Study of the Transitions at $\nu = 3/5$ and $4/7$	104
5.2.5	Conclusions	107
5.3	The Low Current vs the High Current Regime at $\nu = 2/3$	108
5.3.1	The High Current Regime	108
5.3.2	The Low Current Regime	111
5.3.3	Temperature and Time Dependence of the SLR and HLR Transitions .	112
5.3.4	Conclusions	116
5.4	Samples under Strain: Quadrupole Splitting	116
5.5	Anomalous NMR Line Shape around $\nu = 1, 1/3$ and $2/3$	122
5.6	Outlook	126
6	Conclusions and Summary	129
7	Zusammenfassung	137
A	Surface Acoustic Waves: High Frequency Regime	147

B Structuring Procedure for Sample B (020502)	151
bibliography	153
Acknowledgments	163
Lebenslauf	165

Symbols and Abbreviations

Abbreviations

2DES	two-dimensional electron system
AC	alternating current
CIDNP	current-induced dynamical nuclear polarization
CF	composite fermion
CW	continuous wave
DC	direct current
DNP	dynamical nuclear polarization
DOS	density of states
EFG	electric field gradient
FID	free induction decay
FQH	fractional quantum Hall
FQHE	fractional quantum Hall effect
FT	Fourier transformation
GHMFL	Grenoble High Magnetic Field Laboratory
HLR	huge longitudinal resistance
IQHE	integer quantum Hall effect
LL	Landau level
LLL	lowest Landau level
MBE	molecular beam epitaxy
MQW	multiple quantum well
NMR	nuclear magnetic resonance
ODNMR	optically detected nuclear magnetic resonance
OPNMR	optically pumped nuclear magnetic resonance
QH	quantum Hall
QHE	quantum Hall effect
QHF	quantum Hall ferromagnet
QW	quantum well

RDNMR	resistance detected nuclear magnetic resonance
RF, rf	radio frequency
SAW	surface acoustic waves
SdH	Shubnikov-de Haas
SET	single electron transistor
SLR	small longitudinal resistance

Symbols

A	vector potential
A	area
A_{HF}	hyperfine coupling constant
A_{eff}	effective hyperfine coupling constant
a_i	abundance of the nuclear isotope i
arb. units	arbitrary units
α	fine structure constant
B	magnetic field
B_c	critical magnetic field
B_e	electronic magnetic field
B_{eff}, B^*	effective magnetic field
B_{ext}, B_0	external magnetic field
B_N	nuclear hyperfine magnetic field
$B_{\perp}, B_{\text{perp}}$	perpendicular magnetic field
B_{tot}	total magnetic field
B_z	magnetic field in z -direction
$B_1(t)$	alternating magnetic field \perp to B_z
C	capacitance
$D(\varepsilon)$	density of states
Δ	activation gap
Δ_{CF}	CF cyclotron energy
Δ_N	nuclear Zeeman energy splitting
ΔE_Q	quadrupole energy splitting
$\Delta \mathbf{E}$	electric field gradient
E	energy
E	electric field
E_{subband}	subband energy
E_C	Coulomb energy

E_{exch}	exchange energy
E_{F}	Fermi energy
E_{Z}	Zeeman energy
e	electron charge
e^*	fractional electron charge
ε_{N}	energy eigenvalue of the Nth LL
ϵ	dielectric constant of GaAs
ϵ_0	dielectric constant in vacuum
f	frequency
f_0	reference frequency
Φ_0, ϕ_0	magnetic flux quantum
Φ	magnetic flux
ϕ	tipping angle
g, g^*	effective Landé g -factor (≈ -0.44 in 2DES GaAs)
g_0	g -factor for a 15 nmQW (≈ -0.40)
g_{CF}^*	composite fermion g -factor
g_e	free electron g -factor
g_{N}	nuclear g -factor
g_s	spin degeneracy
γ_{N}	nuclear gyromagnetic ratio
H	Hamiltonian
H_{N}	Hyperfine Hamiltonian
H_{Q}	Quadrupole Hamiltonian
\mathbf{H}_{N}	Hermite polynomials
h	Planck's constant
\hbar	$h/2\pi$
η	Zeeman to Coulomb ratio
η_{c}	critical η
I	current
\mathbf{I}	nuclear spin operator
\mathbf{I}_+	raising nuclear spin operator
\mathbf{I}_-	lowering nuclear spin operator
\mathbf{j}, \mathbf{j}	current density
K_{eff}	effective electromechanical coupling coefficient
K_{S}	Knight shift
$K_{\text{S,max}}$	maximum Knight shift
k_{B}	Boltzmann constant

k	wavevector
k_x, k_y	wavevector components in the plane of the 2DES
$k_{F,CF}$	wavevector of the CF Fermi surface
k_S	wavevector of the SAW
L	length of the Hall bar
L_i	inductance
ℓ_B	magnetic length
ℓ_B^{eff}	effective magnetic length
λ	FWHM of the wavefunction
λ_S	wavelength of the SAW
M_0	total magnetization
M_x	x -magnetization
M_y	y -magnetization
M_z	z -magnetization
m	odd integer number
m_{CF}^*	composite fermion effective mass
m_{CF}^a	composite fermion activation mass
m_{CF}^p	composite fermion polarization mass
m_e	free electron mass
m^*	effective electron mass in 2DES GaAs
μ, μ_e	mobility
μ_0	permeability constant
μ_B	Bohr magneton
μ_I	magnetic moment of a nucleus
μ_N	nuclear magneton
N	Landau level index
N_+	spin-up LL
N_-	spin-down LL
N_e	total number of electrons
N	nuclear level index
n, n_e	electron density
n_{CF}	CF density
n_L	degree of degeneracy in each LL
ν, ν_e	electron filling factor
ν_{CF}	CF filling factor
ν_Q	quadrupole frequency
ν_{reset}	reset filling factor

\mathcal{P}	polarization
\mathbf{p}	momentum
p, b	integer number
Q_N	nuclear quadrupole moment
θ	tilt-angle
R_K	von Klitzing's constant
R_{xx}	longitudinal resistance
R_{xy}, R_H	transverse or Hall resistance
$\hat{\rho}$	resistivity tensor
ρ_s	spin stiffness
ρ_{xx}	longitudinal resistivity
\mathbf{S}	electron spin operator
\mathbf{S}_+	raising electron spin operator
\mathbf{S}_-	lowering electron spin operator
$\hat{\sigma}$	conductivity tensor
σ_{xx}	longitudinal conductivity
T	temperature
T_1	spin-lattice relaxation time
T_1^{-1}	spin-lattice relaxation rate
T_2, T_2^*	spin-spin relaxation time
τ	scattering time
τ_p	pulse duration
V_{xx}	longitudinal voltage
V_{xy}	Hall voltage
\mathbf{v}_D	drift velocity
v_0	sound velocity in GaAs
W	width of the Hall bar
w	QW thickness
ω_c	cyclotron frequency
$\omega_c^*, \omega_{c,CF}$	CF cyclotron frequency
ω_L	Larmor frequency
ω_R	resonance frequency of an LC-circuit
x, y, z	space coordinates
z_i	position of electron i denoted as a complex number

Chapter 1

Introduction

In 1922, Stern and Gerlach [1, 2] conducted an experiment which revealed the importance of quantum mechanics more than any other previous experiment. They discovered that silver atoms possess an intrinsic angular momentum or spin [3] which could not be explained from classical physics. Presently, it is well established that particles exhibit a spin which is restricted to integer or half-integer values of $h/2\pi$, where h is the Planck's fundamental natural constant. These particles will obey different statistics depending on whether they have half-integer (Fermi-Dirac statistics) or integer spins (Bose-Einstein statistics). The spin degree of freedom was essential in understanding many properties of matter by including spin-orbit and spin-spin interactions. This knowledge has led to an ample number of applications involving spin. For example, the progress achieved in studies of ferromagnetism and in nuclear magnetic resonance (NMR) has been essential to advances made in electronics and medicine. In semiconductor physics, understanding spin phenomena is of particular importance when researching fundamental issues in physics. Furthermore, the prospect of processing quantum information has recently led to an increased interest in investigating spin in semiconductor devices.

In this work, we investigate fundamental spin phenomena which occur in high quality GaAs semiconductor structures when the electrons are confined to two dimensions. In particular, we perform electrical transport and nuclear magnetic resonance experiments on such 2-dimensional electron systems (2DES) under conditions where the quantum Hall effect exists; that is at high magnetic fields and low temperatures.

In the integer quantum Hall effect (IQHE), electrons occupy an integral number of highly degenerate energy levels which are separated by the cyclotron energy, referred to as Landau levels (LLs). Each of these levels splits into two levels, separated by the Zeeman energy, due to spin. If interactions are neglected, spin only plays a trivial role since the electron spin polarization, \mathcal{P} , can be determined from

$$\mathcal{P} = \frac{(N_{\uparrow} - N_{\downarrow})}{(N_{\uparrow} + N_{\downarrow})}, \quad (1.1)$$

where N_{\uparrow} (N_{\downarrow}) is the number of occupied spin up (spin down) LLs by electrons. From this equation, we can infer that if an even number of levels are filled then $\mathcal{P} = 0$, while for an odd number of filled LLs $\mathcal{P} = 1/\nu$ where ν is the filling factor or number of filled levels. By increasing the magnetic field, it is possible to also increase the degeneracy of each Landau level to a degree where all of the electrons occupy only the lowest Landau level (LLL). The degeneracy of each LL per unit area per spin is simply given by eB/h , where e is the charge of the electron, B is the magnetic field and h is Planck's constant. In the LLL, complete polarization of the electrons is expected and thereby spin becomes irrelevant. In reality however, if electron-electron interactions are considered spin is reestablished as a relevant degree of freedom and fascinating phenomena emerge in the LLL. In the following, we list four examples:

- **Spin phase transitions in the fractional quantum Hall effect:** If electron-electron interactions are considered in the LLL, new ground states appear when these particles are occupying certain rational, fractions with odd denominators of the available states. In this fractional quantum Hall effect (FQHE) regime, the formation of many-body ground states is dependent on the spin polarization which is determined by the interplay between the Coulomb and Zeeman energies. Transitions between ground states of different spin polarization exist at several fractional filling factors. At some transitions, domains of different polarization, similar to a ferromagnet, are believed to exist.
- **Polarization of composite fermions:** In the theory of the FQHE, the strongly correlated electrons can be transformed into a system of weakly interacting particles referred to as composite fermions (CF) which experience an effective magnetic field different from the external field. These new quasiparticles will condense into many-body ground states occupying integer values of new CF LLs similar to the IQHE regime of electrons. The polarization of these entities can then be obtained from equation 1.1 where now n_{\uparrow} (n_{\downarrow}) is the number of occupied spin up (spin down) LLs by CFs. Spin phase transitions are naturally understood in the CF model.
- **Skyrmions and spin reversed excitations:** Exactly at full electron occupation of the LLL (filling factor $\nu = 1$) the ground state is completely polarized even in the absence of a Zeeman energy. The excitations of the $\nu = 1$ ground state are not single spin flips, but rather involve several spins which gradually reverse over a certain spatial extent due to the competition that exists between the Zeeman and exchange energies. The $\nu = 1$ topological excitations with underlying spin-texture have been named skyrmions due to their similarity with objects in the skyrme model of nuclear physics. Additionally, in the FQHE, the fractionally charged Laughlin quasiparticle ground state excitations also involve spin reversal.

- **Interactions between nuclear and electron spins:** In GaAs, the spin of the electrons can couple to the spin of the nuclei via the Fermi contact term of the hyperfine interaction. Polarized nuclei will then affect the electron system by creating a local hyperfine magnetic field which acts on the electron spins. Likewise, polarized electrons create a local magnetic field acting on the nuclear spins.

In our work, we research various aspects of the above mentioned phenomena by means of two experimental techniques: electrical transport and nuclear magnetic resonance. Our original incentive, however, was to explore the anomaly found in the FQHE regime characterized by a large peak in the longitudinal resistance at the minimum of filling factor $\nu = 2/3$, referred to as the huge longitudinal resistance (HLR) peak. In previous works [4, 5], long equilibration times of the longitudinal resistance indicated that the nuclear system plays an essential role in the existence of the HLR anomaly. Resistance detected (RD)NMR experiments were successful in proving that this was in fact the case. In addition, it was experimentally determined that a large current density was necessary to stimulate the appearance of the HLR. A model was also presented associating the HLR and a transition between ground states of different spin polarizations, where domains were believed to form. Nevertheless, many questions remained unanswered. For example, the HLR exists at magnetic field values where a spin polarization transition was not expected. Furthermore, the role of the current was not well understood, there was a lack in evidence of domain existence and a four-fold anomalous splitting of the NMR lines was observed, which could not be explained by conventional electron-nuclear interaction mechanisms leading to the conjecture of a new type of interaction [6].

In this dissertation, in collaboration with the thesis work presented by S. Kraus in reference [7], a connection was established between the HLR and the spin phase transition at filling factor $\nu = 2/3$. The link between them became clear after finite thickness and g-factor corrections were included in the calculation of the Coulomb and Zeeman energies. Hence, some of our studies are concerned with establishing similarities and differences between the $2/3$ transition and the HLR. This necessarily includes the study of the interaction between electrons and nuclei since both effects are intrinsically related. Consequently, in addition to magnetotransport experiments, we also perform NMR and resistance detected NMR measurements. One main objective is to clarify the reason behind the four-fold splitting of the RDNMR lines. Therefore, we present a technique developed in this work which combines conventional NMR methods with RDNMR, enabling us to directly measure the electron spin polarization of the system. Applied to the $2/3$ transition, this proved to be very beneficial in understanding the nature of the HLR peak and also to study properties of spin phase transitions in general. In this thesis, however, we go beyond the study of transitions and apply our NMR technique to investigate other spin phenomena occurring in the FQHE. This serves the purpose of both exploring the interactions that exist between the electrons and nuclei and also to acquire a better understanding of the

electron system in a 2DES by measuring the electron spin polarization via a shift in the NMR spectra. Our work is presented in six chapters:

In chapter 2, we introduce the concepts necessary to understand the results presented in this thesis. It is divided into four parts. In the first part, a review of two-dimensional electron systems and classical magnetotransport is presented. A quantum mechanical approach of magnetotransport is also needed in order to understand the quantum Hall effect. The integer quantum Hall effect (IQHE) is shortly discussed in the second part followed by a more extensive description of the fractional quantum Hall effect (FQHE) in the third part of the chapter, where we introduce Laughlin's trial wavefunction and the composite fermion (CF) picture. In the last section, we handle the spin degree of freedom in the FQHE in detail. Here, spin phase transitions between electron ground states of different polarizations are particularly examined. A brief excursion into the composite fermion picture allows us to naturally understand the nature of these transitions. Especially the polarization for the half filled Landau level is important as it will be needed in the interpretation of the spin polarization measurements presented in chapter 5. In the same section, we differentiate between an activation and a polarization CF mass. After a section on skyrmions and quasiparticle charged excitations, we explain the hyperfine interaction which is responsible for the correlation between electrons and nuclei. We finish the chapter by dealing with the two experimental methods used in our thesis to study spin phenomena in the QHE; transport and NMR (including resistance detected NMR). In the latter, a spectrum of the anomalous four-fold splitting is shown.

Before presenting our transport results in chapter 4, we show the sample structures employed in our experiments in chapter 3. The experimental setups needed for transport and NMR are also introduced there.

Due to the different experimental techniques employed, we separate the results part of our thesis into two chapters: The transport experiments are presented in chapter 4 while the results from NMR measurements are treated in chapter 5.

In chapter 4, we concentrate exclusively on the unpolarized-polarized phase transition which occurs at $2/3$ filling of the lowest Landau level. In transport, this transition is identified by a peak in the longitudinal resistivity at the $2/3$ FQH ground state minimum. In the first section, we show that a small peak in the longitudinal resistivity at low current densities develops into the HLR anomaly by increasing the current. Therefore, it is necessary to distinguish between the low current and the high current regimes when dealing with the $2/3$ transition. In both cases, however, the transition occurs at a critical ratio of the Coulomb to Zeeman energies which can be tuned by either tilting the sample with respect to the magnetic field direction or by varying the density. Such measurements are presented in section 4.2, including a phase diagram of the $2/3$ ground state polarization, where the phase transition boundary is indicated by the HLR peak. Important differences between the low current and high current peak are also discussed

in sections 4.3 and 4.4, leading to a model of the physics involved in both regimes (section 4.5). In the rest of the chapter, we analyze further properties of the $2/3$ transition as a function of current intensity and frequency as well as time dependence and temperature. From these measurements some new insights have been obtained, which have allowed us to build up on the model of section 4.5. The results are analyzed in conjunction with the NMR measurements in the last chapter of the thesis.

The main results of this contribution are presented in chapter 5. It deals with NMR studies of various spin phenomena in the LLL. They can be generally summarized in four parts. Firstly, we take advantage of the interaction that exists between the nuclear and the electron systems in order to measure the electron spin polarization at several spin phase transitions. A method developed in this work is presented here in which resistance detected (RD)NMR and conventional NMR techniques were combined to measure the electron polarization. Besides probing the polarizations expected from the CF theory at various fillings, we investigate the existence of domains at the transitions. Secondly, we continue our research at $\nu = 2/3$, in addition to the transport measurements, and establish important differences between the low and high current regimes observed with NMR. Thirdly, we study samples under the influence of strain which exhibit a quadrupole splitting of the NMR lines and in this way clarify the four-fold splitting anomaly in the HLR regime. Finally, we exploit the excitations of several FQHE ground states and of filling factor $\nu = 1$ in the LLL. We close the chapter by offering an outlook on possible experiments in which measuring the electron spin polarization might assist in understanding further phenomena occurring in the FQHE regime.

In the last chapter we summarize our results and discuss the conclusions obtained from the vast number of experiments conducted at the $2/3$ spin phase transition and at other spin phenomena.

Chapter 2

The Quantum Hall Effect

Some of the basic concepts of a two-dimensional electron system (2DES) [8] are introduced in this chapter. The first section deals with the experimental realization of a 2DES. It is necessary to review the classical and quantum-mechanical transport characteristics of electrons which are electrostatically confined to two dimensions and subjected to a magnetic field B . This will help us to introduce the basic concepts necessary to understand the quantum Hall effect. Section 1.2 presents a short description of the integer quantum Hall effect (IQHE) followed by the fractional quantum Hall effect (FQHE) in section 3. The composite fermion (CF) picture has been an elegant approach to explain the FQHE and will be briefly discussed in that section. The last section of the chapter studies the spin degree of freedom in the FQHE. This includes the existence of ground states with different spin configurations and transitions between these states, spin in the CF picture, the polarization of the half-filled lowest Landau level, skyrmions and quasiparticle excitations and electron-nuclear interactions. The section will end by presenting some of the measuring techniques used to study these phenomena. All of the experimental results presented in this thesis are concerned with spin in the FQHE.

2.1 The Classical Hall Effect

2.1.1 The Two-Dimensional Electron System

Several techniques have been implemented to construct a 2-dimensional electron system. The Metall-Oxide-Semiconductor Field Effect Transistor (MOSFET) and semiconductor heterojunctions are two examples of 2DES where the QHE has been observed. The best quality samples have been obtained with heterojunctions based on the semiconductor/semiconductor interface GaAs/Al_xGa_{1-x}As. These are usually grown by Molecular Beam Epitaxy (MBE) ¹,

¹Molecular Beam Epitaxy (MBE) consists of an epitaxial growth of crystalline layers, which are evaporated at a typical rate of 1 atomic layer per second on top of a crystalline substrate. Ultra high vacuum (UHV) conditions

where one atomic layer can be grown at a time. This enables the realization of perfectly ordered crystalline material. Furthermore, the AlGaAs/GaAs interface is nearly free of disorder because the lattice constants of these materials are almost identical. Since AlGaAs has a larger band gap than GaAs, the conduction and valence bands are bent and a triangular potential is formed at the interface if the system is suitably doped. This is shown in the schematic illustration of Fig. 2.1(a).

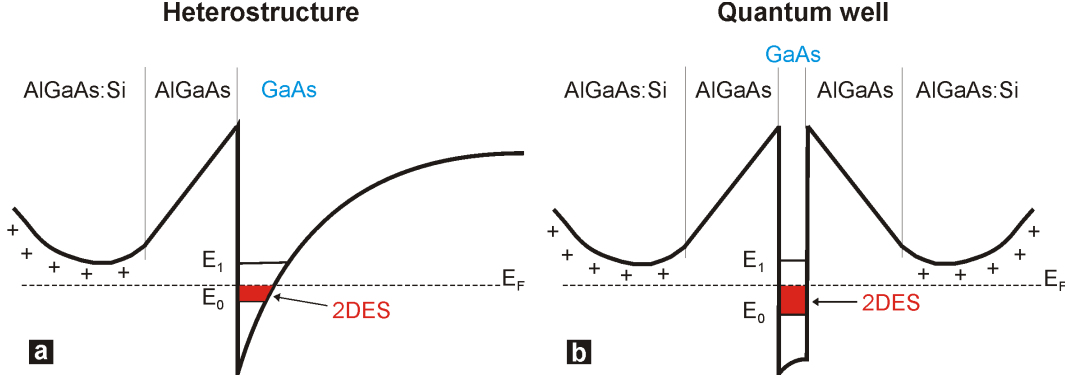


Figure 2.1: The conduction band of an AlGaAs/GaAs heterostructure (a) and quantum well (b) are schematically shown. A 2DES forms in the GaAs layer with quantized energies in the z -direction. At low temperatures ($k_B T \ll \Delta E_{\text{subband}}$) only the lowest subband is populated. The electrons, supplied from a Si-donor layer, fill the 2DES up to E_F .

The electrons are trapped in the potential and a 2DES forms in the GaAs layer since they are only free to move in the xy -plane while their energies are quantized in the z -direction (perpendicular to the interface). The energy spectrum is given by: $E = E_z^i + \frac{\hbar^2 k_x^2}{2m^*} + \frac{\hbar^2 k_y^2}{2m^*}$, where m^* is the effective mass of the electrons ($m_{\text{GaAs}}^* \approx 0.067m_e$; m_e is the free electron mass) [10]. At sufficiently low temperatures, i.e. if $k_B T \ll \Delta E$ (subband energy spacing), and low densities, the electrons only occupy the lowest subband (k_B is the Boltzmann constant). An ionized Si-donor layer, which is placed away from the interface in order to minimize scattering (modulation doping), provides the electrons of the 2DES [11]. The assumption of a parabolic energy dispersion for the conduction band yields a constant density of states for the lowest subband:

$$D(\varepsilon) = dN(E)/dE = \frac{g_s m^*}{2\pi\hbar^2}, \quad (2.1)$$

where the g_s is the spin degeneracy. The Fermi energy is then proportional to the density n_e of the 2DES:

$$E_F = \frac{\pi\hbar^2}{m^*} n_e. \quad (2.2)$$

are required in order to reduce the number of impurities in the crystal [9].

Electrons can also be confined to a potential well, referred to as a quantum well (QW), if AlGaAs/GaAs/AlGaAs is grown. In this case, the 2DES forms in the GaAs layer sandwiched between the AlGaAs layers, as shown in Fig. 2.1(b).

2.1.2 Classical Magnetotransport

In this section, we review the classical description of electric magnetotransport of a 2DES. This is important in order to introduce the concepts necessary to determine properties of the system, such as mobility and density [12].

In a typical Hall bar geometry, illustrated in Fig. 2.2, a current I is applied between the source and drain of a 2DES sample of width W and length L . In the presence of a magnetic

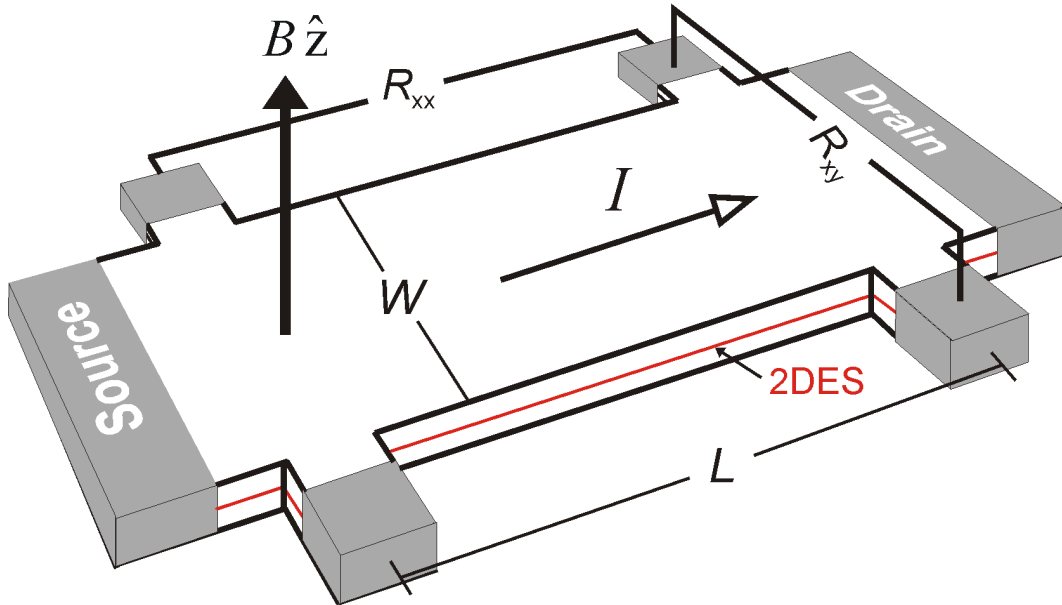


Figure 2.2: For magnetotransport measurements, a Hall bar-shaped sample of width W and length L can be used. The current flows from source to drain and the longitudinal voltage V_{xx} , and transverse or Hall voltage V_{xy} , are measured. A magnetic field is usually applied in the z -direction, perpendicular to the 2DES.

field B , directed perpendicular to the 2DES, the electrons moving between the source and drain will deflect sideways due to the Lorentz force. The accumulated carriers on the side create a voltage, referred to as Hall voltage V_H , transverse to the current direction². The transverse or Hall resistance value R_{xy} (or R_H) is simply given by the relation $R_{xy} = V_{xy}/I$. Likewise, the longitudinal resistance $R_{xx} = V_{xx}/I$.

²The Hall effect was discovered in 1879 by Edwin Hall by running a current through a thin sheet of gold.

The ability of the electrons to move through the crystal is affected by scattering processes with phonons, impurities or with other electrons. The Drude-model includes the influence of scattering by considering the electrons as classical particles bouncing off elastically with impurities. This “friction” force imposed on the carriers impedes them from accelerating from source to drain, leading to a stationary drift velocity, \mathbf{v}_D . In the absence of a magnetic field, this drift velocity is given by: $\mathbf{v}_D = -e\tau\mathbf{E}/m^*$, where e is the electron charge, \mathbf{E} the electric field and τ the collision or scattering time. The mobility can now be defined as: $\mu_e = e\tau/m^*$. It renders important information about the quality of the sample³. In the temperature regime where our experiments have been performed ($T < 4K$) the mobility is only weakly temperature dependent and mainly affected by random-impurity scattering.

Introducing the Lorentz force into the Drude model by turning on the magnetic field yields the following equation of motion:

$$m \frac{d\mathbf{v}_D}{dt} = -e\mathbf{E} - e \frac{\mathbf{v}_D}{c} \times \mathbf{B} - m \frac{\mathbf{v}_D}{\tau}, \quad (2.3)$$

where $m \frac{d\mathbf{v}_D}{dt} = 0$ for the stationary case. The drift velocity can also be expressed in terms of a current density \mathbf{j} as follows: $\mathbf{v}_D = \mathbf{j}/en_e$. From the relation $\mathbf{E} = \hat{\rho}\mathbf{j}$ or equivalently $\mathbf{j} = \hat{\sigma}\mathbf{E}$, where $\hat{\rho}$ is the resistivity tensor and $\hat{\sigma}$ the conductivity tensor, we obtain:

$$\rho_{xx} = \frac{1}{en_e\mu_e} \quad \text{and} \quad \rho_{xy} = \frac{B}{n_e e}. \quad (2.4)$$

Here, ρ_{xx} is the longitudinal resistivity and ρ_{xy} the transverse or Hall resistivity. The resistances (what is actually measured in an experiment) will be related to the resistivities in the following way: $R_{xx} = \rho_{xx} \cdot L/W$ and $R_{xy} = \rho_{xy}$. These formulas were used to calculate the mobility and density of the samples used in this thesis.

Furthermore, the conductivity can be obtained from the inverse of the resistivity tensor. Assuming an isotropic system (Onsager relation), i. e. $\rho_{xx} = \rho_{yy}$ and $\rho_{yx} = -\rho_{xy}$, we can write:

$$\hat{\sigma} = \hat{\rho}^{-1} = \frac{1}{\rho_{xx}^2 + \rho_{xy}^2} \begin{pmatrix} \rho_{xx} & -\rho_{xy} \\ \rho_{xy} & \rho_{xx} \end{pmatrix}. \quad (2.5)$$

It is interesting to notice that if $\rho_{xx} \rightarrow 0$ then $\sigma_{xx} \rightarrow 0$ whenever $\rho_{xy} \neq 0$. This will be important in explaining the integer quantum Hall effect.

2.2 The Integer Quantum Hall Effect

2.2.1 Landau Quantization

If an electron is able to complete a full cyclotron path without scattering, it will interfere with itself and the classical Drude picture is no longer valid. This is the case for high mobility

³The best AlGaAs/GaAs 2DES heterostructures which have been grown exhibit mobilities of the order $30 \cdot 10^6 \text{ cm}^2/\text{Vs}$ [13].

samples in the presence of a sufficiently strong magnetic field at low temperatures. Therefore, a quantum mechanical solution to the problem becomes unavoidable [14].

The Schrödinger equation for a free electron, i.e. ignoring all electron-electron interactions, subjected to a magnetic field is given by the well known expression:

$$\frac{1}{2m^*} (\mathbf{p} + e\mathbf{A})^2 \Psi_N(x, y) = E_N \Psi_N(x, y). \quad (2.6)$$

Here m^* is the effective mass of the electron and the vector potential \mathbf{A} is related to the magnetic field as $\mathbf{B} = \nabla \times \mathbf{A}$. If the Landau gauge is chosen, i.e. $\mathbf{A} = xB\hat{y}$ which obeys $\nabla \times \mathbf{A} = B\hat{z}$, the eigenfunctions can be written as a product of a plane wave extending in the y-direction and the eigenfunction of the time-independent Schrödinger equation: $\Psi_N = e^{ik_y y} \phi_N(x)$. The eigenfunctions $\phi_N(x)$ are the solution of the quantum mechanical harmonic oscillator problem. Hence, the total eigenfunctions Ψ_N are:

$$\Psi_N = e^{ik_y y} \exp\left[-\frac{(x - x_0)^2}{2\ell_B^2}\right] H_N\left[\frac{(x - x_0)}{\ell_B}\right]. \quad (2.7)$$

H_N are the Hermite polynomials and ℓ_B is the magnetic length defined as $\ell_B = \sqrt{\frac{\hbar}{eB}}$. From this solution, it becomes clear that the wavefunctions are extended in y but localized in x, centered around the coordinate $x_0 = -k_y \ell_B^2$. The cyclotron radius, which indicates the spread of the electron wavefunction in the x-direction, is determined by the magnetic length. The energy eigenvalues are a discrete set of ladder-levels referred to as Landau levels (LLs):

$$\varepsilon_N = \hbar\omega_c \left(N + \frac{1}{2}\right), \quad (2.8)$$

where $N = 0, 1, 2, \dots$ is the Landau level index and $\omega_c = \frac{eB}{m^*}$ is the cyclotron frequency. We can include the spin degree of freedom by adding the Zeeman energy term E_Z to equation 2.8:

$$E_N = \hbar\omega_c \left(N + \frac{1}{2}\right) + g^* \mu_B B s. \quad (2.9)$$

The reduced g-factor of GaAs $g^* \approx -0.44$, μ_B is the Bohr magneton, B the magnetic field and s the spin quantum number $= \pm 1/2$. Figure 2.3 shows how the energy spectrum of a 2DES, which forms a Fermi sea at $B = 0$ (a), splits into a series of discrete Landau levels, separated by the energy $\hbar\omega_c$ (b), when subjected to a finite magnetic field. These levels split again due to spin by the energy E_Z (c). The energy eigenvalues are obtained regardless of the gauge chosen for the vector potential \mathbf{A} . Also, the center coordinate of the wavefunctions x_0 is independent of (x, y) , which means that each electron will have the same energy and the degeneracy of a single LL will depend on the number of states that can be packed into that level. The degeneracy per unit area per spin is $n_L = eB/h$. Thus, the stronger the magnetic field, the larger the degeneracy. The filling factor ν can be defined as the ratio between the total number of electrons, N_e , and the degree of degeneracy in each LL, n_L , for a sample of area A :

$$\nu = \frac{N_e}{n_L A} = \frac{n_e}{n_L} = \frac{n_e h}{eB}. \quad (2.10)$$

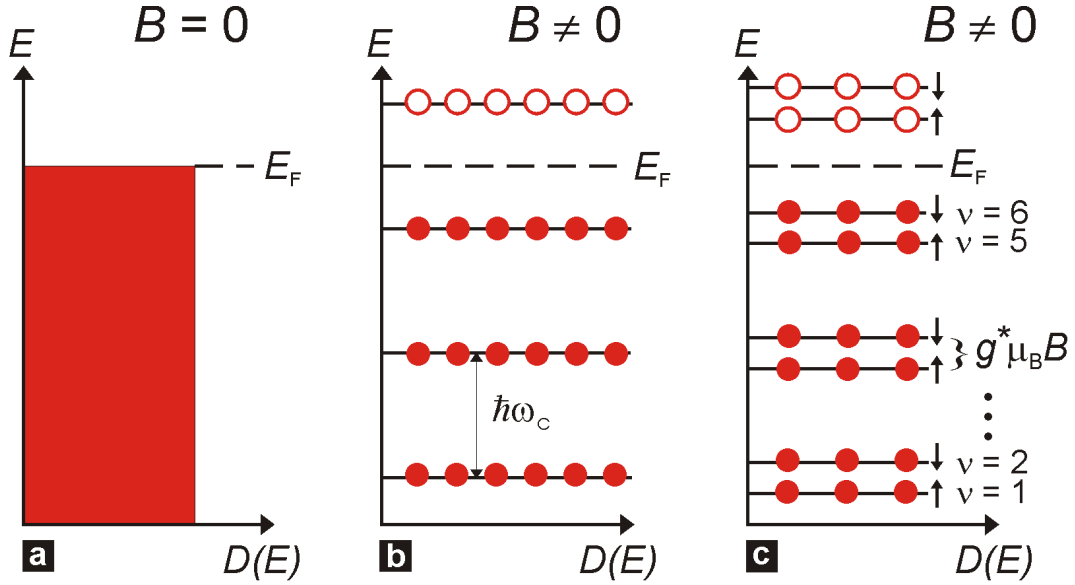


Figure 2.3: a) A 2DES forms a Fermi-sea filled up to E_F at $B = 0$. b) In the presence of a B -field, the 2DES splits into a series of Landau levels (LLs) with discrete energy values. c) Each LL is further spin-split into 2 levels separated by the Zeeman energy. In this example $\nu = 6$ since 6 levels are filled with electrons.

Alternatively, the magnetic field can be discretized in units of magnetic flux quanta Φ_0 . The filling factor ν can then be described as the ratio of electrons and the total number of magnetic flux quanta penetrating the sample of area A : $\nu = \frac{N_e}{\Phi/\Phi_0} = \frac{n_e h}{eB}$, since $\Phi = BA$ and Φ_0 is the ratio between the Planck's constant h and the electron charge e .

Ideally, the density of states (DOS) of each level will be a singular δ -function similar to the DOS of a quasi zero-dimensional system known as quantum dot: $D_E = \delta(E - E_{N,s})$. In reality, the delta-like LLs are broadened due to imperfections in the sample. This disorder-induced broadening plays an essential role in the IQHE.

2.2.2 Quantum Mechanical Magnetotransport

The quantum mechanical properties of a 2DES in a magnetic field have an immense impact on its transport behavior. It is most convenient to analyze these transport characteristics by using our measurements presented in Fig. 2.4. In this graph, the longitudinal resistivity ρ_{xx} (black curve) and the Hall resistivity ρ_{xy} (red curve) are plotted vs magnetic field B ⁴. At low fields ($B < 0.2$ T), ρ_{xy} increases linearly with B while ρ_{xx} remains constant, as expected from the classical magnetotransport theory of a 2DES. However at higher fields, a series of plateaus

⁴The sample was grown by M. Henini in Nottingham university. It has a mobility of $\mu = 1.0 \cdot 10^6$ cm²/Vs at a density of $n = 2.56 \times 10^{11}$ cm⁻².

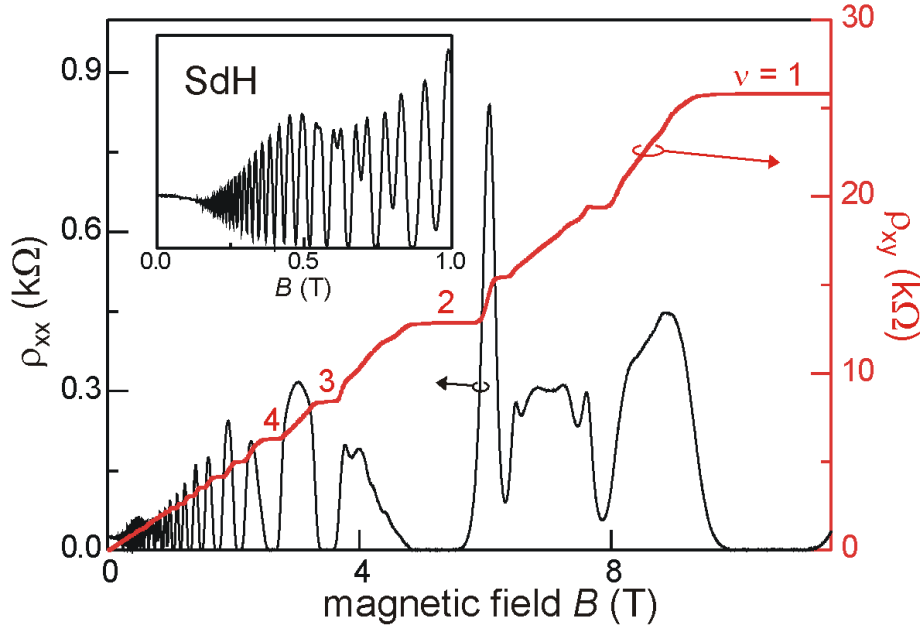


Figure 2.4: IQHE: At high magnetic fields the Hall resistance R_{xy} (red curve) is characterized by plateaus quantized to $(1/\nu)h/e^2$ for integer filling values ν , accompanied by a vanishing longitudinal resistance R_{xx} (black curve). The plateaus at fractional values of ν are due to electron-electron interactions. The FQHE is explained in section 2.3. Inset: SdH oscillations in R_{xx} at low fields (Sample from wafer NU1154).

in the Hall resistivity, accompanied by a vanishing longitudinal resistivity becomes the most striking features in the curve. The resistivity value of these steps is given by:

$$\rho_{xy} = \left(\frac{1}{\nu}\right) \frac{h}{e^2} \quad (2.11)$$

for an integer filling factor ν . This phenomenon, discovered by Klaus von Klitzing, is known as the integer quantum Hall effect (IQHE) [15, 16]. The resistance value at filling factor 1 is thus known as the von Klitzing constant ($R_K = 25,812.807\dots \Omega$) and is used as the standard unit of resistance since it can be measured to a precision of up to 10^{-8} [17, 18]. It is dependent only on the natural constants e and h and is not affected by any sample parameters. The fine structure constant $\alpha = \frac{1}{2}\mu_0 c (R_K)^{-1}$, which depends on the permeability constant in vacuum μ_0 , the speed of light c and the R_K constant, can be determined by measuring the quantized Hall resistance [19]. The oscillations in ρ_{xx} at low fields where there are no plateaus, known as Shubnikov-de Haas (SdH) oscillations, are periodic in $1/B$ and inversely proportional to

the density: $\Delta(1/B) = g_s e / h n_e$ (g_s is the spin degeneracy). The inset of 2.4 shows the SdH oscillations at low magnetic fields ($B < 1$ T). The splitting of the lines which initiates at $B \approx 0.5$ T is due to spin.

Even though the IQHE was discovered almost 25 years ago, there are still many questions which remain unanswered concerning its nature. Several successful approaches and formalisms, however, have been put forward which accurately describe many of the observed phenomena (for a review see [8, 10, 12, 20, 21]). In general, all of these approaches include Landau level formation, low temperatures ($k_B T \ll \hbar \omega_c$) and the existence of localized states. In this work we have chosen the percolation picture due to its intuitive nature [22, 23]. This picture will be introduced in the remaining of the section.

So far, we have only considered the DOS of the LLs to be δ -like functions, see Fig. 2.5(a). However in reality, the LLs will be broadened by disorder. The tails of the LLs now consist of localized states (i.e. states in which electrons are confined to a small region in space and do not carry current across the sample) and current-carrying or extended states at the center of the levels [Fig. 2.5(b)]. In general, a quantized Hall plateau in ρ_{xy} and a vanishing ρ_{xx} occurs

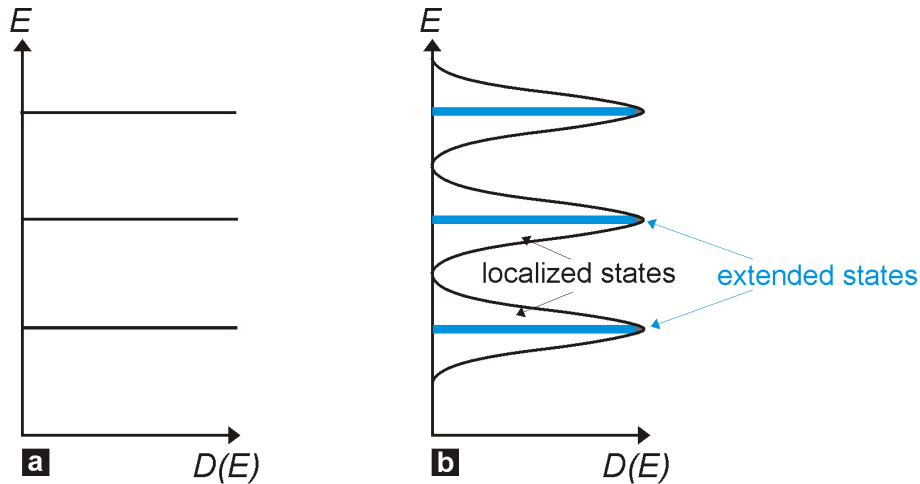


Figure 2.5: Energy vs density of states (DOS) of a 2DES. (a) LLs represented by δ -like functions. (b) The presence of disorder broadens the levels. Localized states are found at the tails and extended states (blue) in the center of these broadened LLs. Localization is essential for measuring the QHE.

whenever the Fermi energy lies at the cyclotron gap between LLs. The localized states pin this energy at the gap, also referred to as the mobility gap, for a certain range of magnetic field values and the plateaus acquire a finite width. Therefore, the existence of localized states is essential in observing the ρ_{xy} plateaus in the QHE. If the Fermi energy lies in the extended states part of the LL, then ρ_{xx} will take on finite values and ρ_{xy} deviates from the quantized value. This is easily visualized in the percolation picture as follows: In the presence

of a smoothly varying random disorder potential, i.e. when the magnetic length is much shorter than the disorder lengthscale, the electron states will lie on contour lines of constant energy present in the random potential landscape. This situation is shown schematically in Fig. 2.6, where the left side shows the confining potential for a sample of width W (shown for the N th LL) while the right side indicates a contour map of the potential landscape. As we increase

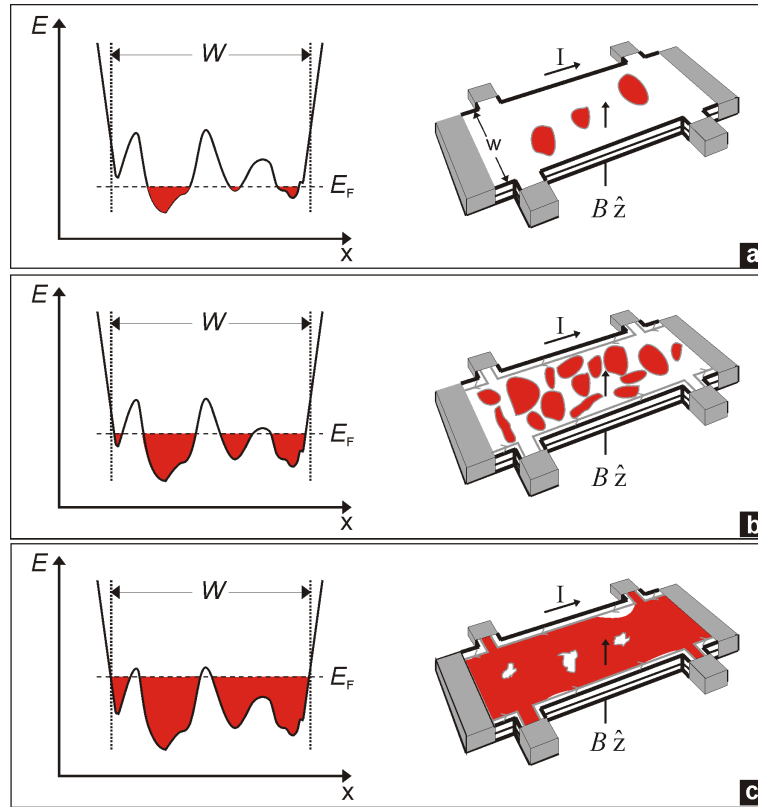


Figure 2.6: Left: Confinement potential for sample of width W . Right: Contour maps of the potential landscape. Red areas indicate filled states and white areas empty states. (a) The Fermi energy, E_F , is at the low-energy tail of the LL (localized states). Electrons occupy only deep valleys without backscattering (ρ_{xy} is quantized, $\rho_{xx} = 0$). (b) E_F is at the center of the LL (extended states). Electrons backscatter from one edge to the other (ρ_{xy} is not quantized, $\rho_{xx} \neq 0$). (c) E_F is at the high-energy tail of the LL (localized states). Current flows on energy contours of mountain tops and edge states without backscattering (ρ_{xy} is quantized, $\rho_{xx} = 0$).

the magnetic field at constant density and occupy a single LL with electrons, the Fermi energy moves across the broadened level. At the low-energy tail, electrons first start occupying the deep valleys [Fig. 2.6(a)]; they are localized and do not contribute to transport. At this point ρ_{xx} vanishes and ρ_{xy} is quantized. As the magnetic field is further increased, the occupied valleys

grow larger until their shorelines, where the electrons can move, percolate from one side of the sample to the other, see Fig. 2.6(b). Electrons can now move across the sample and scatter back to the source. This backscattering process impedes transmission of the electrons from source to drain and thereby is responsible for ρ_{xx} to take on finite values and ρ_{xy} to deviate from the quantized value. At this point, the Fermi energy lies in the extended states part of the LL. Note that at the sample boundaries, the LL energy rises and intersects the Fermi energy. Electrons can also circulate along those so-called edge states and the direction of flow is opposite at the two sample edges [24]. By further increasing the field, the electrons will now occupy most of the sample except for the top of the potential hills [Fig. 2.6(c)]. The shore lines are now either encircling these tops or at the sample edges. In this case, backscattering is again suppressed and ρ_{xx} vanishes while ρ_{xy} is quantized.

Alternatively, Landau and Büttiker have developed a formalism in order to explain the IQHE by only employing edge states [25]: One can imagine that the number of edge states in the sample will depend on the number of Landau-levels intersecting the Fermi-energy. These states will carry current, each contributing an amount of e^2/h to the total conductivity. For example at filling factor $\nu = 2$, there will be two edge states present in the sample. If the Fermi energy is situated in the mobility gap, then the sample bulk is *incompressible*, i.e. a region where adding an extra electron costs a finite energy, and the current is carried between source and drain at the edges without backscattering. As a consequence ρ_{xx} vanishes and $\rho_{xy} = h/i e^2$, where i is the number of edge states. If the Fermi energy is situated in the center of a LL (in the extended states), the sample bulk becomes *compressible* (adding an extra electron only costs a very small amount of energy) and backscattering occurs. Since the Landauer-Büttiker formalism is mostly concerned with edge states, it considers the system to be quasi one-dimensional. This approach has been very successful in describing numerous experiments [26, 27, 28].

Until now, we have neglected electron-electron interactions in explaining the IQHE. Even though the non-interacting single-particle model is very powerful in describing many of the observed phenomena, it is by no means complete. For example in the IQHE, screening of the disorder potential caused by Coulomb interactions between the electrons is also important in understanding the nature of the localized states as shown in several experimental and theoretical works [29, 30, 31, 32]. In addition, the existence of fractional quantized values of the Hall resistance is caused by strong electron correlations. The topic of the next section is the fractional quantum Hall effect, which was discovered by Störmer and Tsui and explained by Laughlin.

2.3 The Fractional Quantum Hall Effect

Shortly after the discovery of the IQHE in a Si-MOSFET, the FQHE was first observed in an AlGaAs/GaAs heterostructure by Störmer and Tsui [33, 34, 35]. Figure 2.7 shows a typical plot

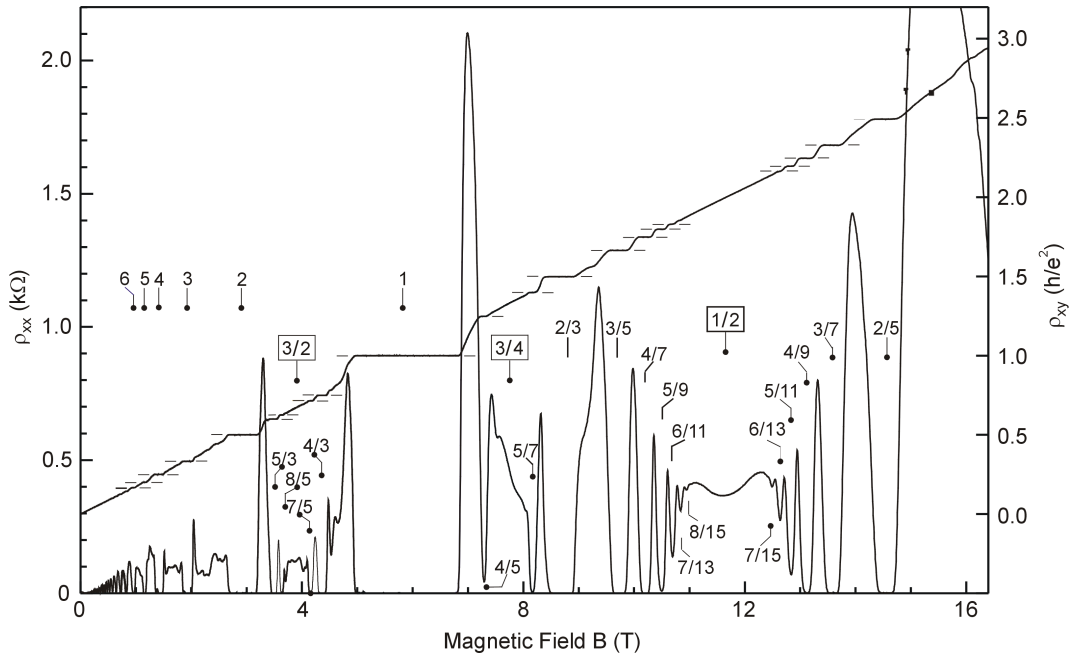


Figure 2.7: FQHE: In the lowest Landau level (LLL), a number of plateaus at fractional values of h/fe^2 appear in the Hall resistance, accompanied by a vanishing longitudinal resistivity. These fractional quantum Hall states are caused by Coulomb interactions between the electrons in a strongly correlated system. These measurements were performed by J.H. Smet and the sample grown by W. Wegscheider.

of the longitudinal resistivity and the Hall resistance vs the magnetic field for a high-mobility sample. This curve is characterized by plateaus in ρ_{xy} quantized to values of h/fe^2 , where f is an exact rational value with an odd denominator, accompanied by a vanishing ρ_{xx} . In the LLL, these fractions occur at certain sequences, which can be summarized by the following equations:

$$f = \frac{b}{2pb \pm 1} \quad (2.12)$$

and

$$f = 1 - \frac{b}{2pb \pm 1}, \quad (2.13)$$

which are related by particle-hole symmetry. Here, p and b are both integer numbers. All of these fractional states are characterized by having odd denominators, being symmetric around $\nu = 1/2$, having a larger gap for small denominators and occurring only in very high mobility samples at low temperatures (few mK). The existence of fractional QH states was completely unexpected, since in the single particle picture no gap should exist below $\nu = 1$. However, the FQHE can be understood if electron-electron interactions are taken into account. As a result,

the Hamiltonian of equation 2.6 must now include electron correlations:

$$\hat{H} = \frac{1}{2m^*} (-i\hbar\nabla + e\mathbf{A}(\mathbf{r}_j))^2 + \frac{e^2}{4\pi\epsilon_0} \sum_{j < k} \frac{1}{|\mathbf{r}_j - \mathbf{r}_k|} + \sum_j U(\mathbf{r}_j) + g\mu_B \mathbf{B} \cdot \mathbf{S}. \quad (2.14)$$

In the formula, we have added the Coulomb interaction energy (second term on the right side), the positive background and disorder potential (third term) and the Zeeman energy (last term) [21, 36]. Laughlin's trial wavefunction approach includes electron-electron interactions, though neglecting disorder and the spin degree of freedom in the LLL. This is handled in the next section.

2.3.1 Laughlin's Trial Wavefunction

Several approaches were undertaken in order to understand the problem of interactions in the LLL [37, 38, 39]. Laughlin's proposal of a trial wavefunction proved to be very successful in describing the strong electron correlations describing the $\nu = 1/m$ QH ground states with m being an odd integer [40, 41]. This trial wavefunction is given by the following expression:

$$\Psi_{1/m} = \prod_{i < j} (z_i - z_j)^m \exp \left[-\frac{1}{4\ell_B^2} \sum_i |z_i|^2 \right]. \quad (2.15)$$

In this formula, $z_{i,j}$ is the position of an electron denoted as a complex number and $m = 2p + 1$ where p is an integer. There are certain restrictions to the wavefunctions. For example, p must be an integer in order for the $\Psi_{1/m}$ to be analytic and hence m is necessarily an odd integer. This forces the orbital part of the wavefunction to be antisymmetric and the spin part to be symmetric. It was assumed that since the electrons are only occupying the lowest spin split LL, the spin degree of freedom would be frozen, i.e. polarized. This consideration is important in this thesis because, in the next section, it will become clear that this assumption only holds for $1/m$ QH ground states. However at other fractional filling factors, partial or zero polarization ground states do exist. Transition between ground states of different spin polarization is a major part of this work.

Returning to Laughlin's wavefunction, we can analyze the equation 2.15 in two parts. The second part of the equation is merely the Gaussian wavefunction of the problem without interactions. More interesting is the first part of the equation, the so-called Jastrow-type term. This term includes the $e^- - e^-$ interactions and can be more easily explained by specifically considering the ground state at filling $\nu = 1/3$. For this special case, $m = 3$ because $m = 1/\nu$. The term $z_i - z_j$ describes the interaction of electron i with all other electrons. Since at this filling factor there are 3 flux quanta per electron, the wavefunction of electron i will have 3 zeros for every other electron j it interacts with⁵. One zero (flux quantum) is located at the position of the

⁵The wavefunction will have 3 vortices, which in principle can be considered as zeros in the wavefunction. In a simplified intuitive picture, a vortex can be modelled as a flux quantum.

electron j due to Pauli's exclusion principle. The other two zeros, however, can be located anywhere. Nevertheless, it is energetically most favorable for the other two zeros to also be at the position of electron j . As Halperin stated, "the wavefunction does not waste any zeros" [42,43]. An electron will then see a 3-fold zero at the position of the other electrons and the only way to minimize the Coulomb repulsion energy is to rearrange themselves in such a manner as to be the furthest away from each other as possible. Figure 2.8 shows Monte-Carlo simulations illustrating the arrangement of 1000 electrons for an uncorrelated distribution (a) and a strongly correlated system (b). This arrangement of the particles is feasible since at $\nu = 1/3$ only $1/3$ of

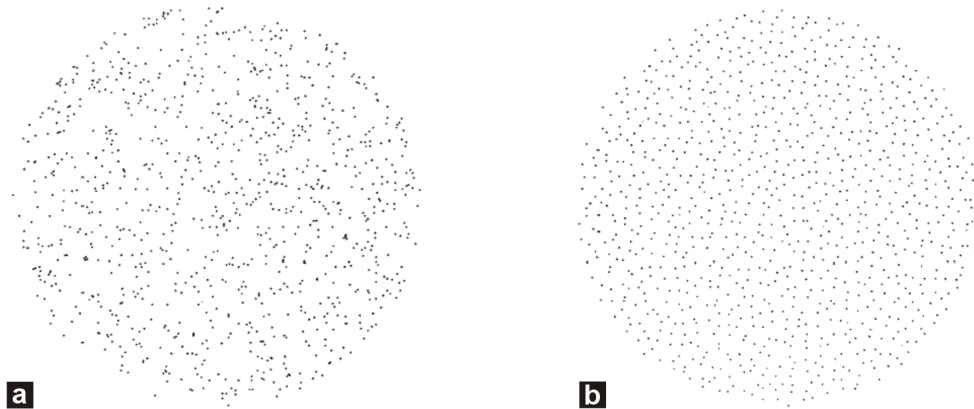


Figure 2.8: Monte-Carlo simulations of 1000 electrons for an uncorrelated distribution (a) and a strongly correlated system (Laughlin wavefunction for $m = 3$), where the Jastrow-type term has been included (b). This figure is adapted from reference [22].

the LL is filled and the electrons have enough space to "redistribute" themselves. Another way to understand this behavior is by looking at equation 2.15. If there are three zeros at the position of electron j , the exponential of the Jastrow-term is also 3. The wavefunction will decay extremely rapidly for any two particles approaching each other, thereby keeping the electrons as far as possible. Laughlin's trial wavefunction method was well corroborated by Monte-Carlo and other numerical calculations and set the base for understanding the FQHE.

Laughlin's fractionally charged quasiparticles

So far, we have presented the necessary wavefunction that explains the FQH ground states at $\nu = 1/m$. Since at these filling factors $\rho_{xx} \rightarrow 0$, gapped elementary excitations should exist. Here, the question arises, what these gapped excitations are. Laughlin showed that they are fractionally charged quasiparticles [40, 41]. This can be understood by again considering $\nu = 1/3$ as an example. If we move away from exactly $\nu = 1/3$ by either slightly increasing ($\nu <$

$1/3$) or decreasing ($\nu > 1/3$) the magnetic field (or changing the density), we can introduce or remove a single quantum of magnetic flux, respectively. Since 3 flux quanta exist per electron of charge e , it is then equivalent to say that an introduction or removal of a flux quantum means adding either a quasihole or a quasielectron of fractional charge $e^* = e/3$. The excitation gap is then given by the necessary energy required to include the quasiparticle. In general, quasiparticle excitations have charge $e^* = e/m$ and do not obey either Bose-Einstein nor Fermi-Dirac statistics, but rather anyonic statistics. The quasihole wavefunction, for example, can be written as:

$$\Psi_{gh} = \prod_i (z_i - z_0) \Psi_{1/m} \quad (2.16)$$

in which a flux quantum is introduced at z_0 [39]. Shot-noise and tunnel experiments, which have satisfactorily proven the existence of fractional charged excitations, were essential in supporting Laughlin's theory [44, 45]. Quasiparticle excitations will be addressed in section 5.5 of this thesis.

One major drawback of Laughlin's approach is that it only accounts for the $1/m$ FQH ground states. The wavefunctions for the other fractions (see Fig. 2.7 and equations 2.12 and 2.13), such as $\nu = 2/3$, are not considered if Laughlin's Ansatz is used. Many of the missing fractions could be accounted for by the hierarchy approach, in which higher order FQHE states are constructed with Laughlin's quasiparticles instead of electrons [43, 46, 47]. Nonetheless, this approach turned out to be incomplete in many ways. For example, it failed to describe the experimental data, in which some states are more stable than others. A very elegant and natural way of describing all of the FQHE states in the LLL is Jain's composite fermion picture described in the next section.

2.3.2 Composite Fermion (CF) Picture

The resemblance between the IQHE and the FQHE seen in experiment hinted to the idea that many of the phenomena occurring in the FQHE could be explained by transforming the strongly interacting system of electrons into a weakly interacting system of some new quasi-particles. Jain's success in identifying *composite fermions* quasi-particles as the real particles of the system in the FQHE was a major achievement in this field [48]. In the following, we describe the basic concepts of this model: If an even number ($2p$) of vortices of the many-body wavefunction are captured by an electron, a new quasiparticle, referred to as a composite fermion (CF) is formed [36, 48, 49]⁶. In a simplified picture, we can say that $2p$ point flux quanta are attached to an electron. At $\nu = 1/2$, $p = 1$ and for this special case each electron carries exactly 2 flux quanta. In this section, we will mainly discuss this particular case. The electrons effectively avoid each other by attaching to these flux quanta and the strongly correlated electron system

⁶If an odd number of vortices is captured by an electron, the resulting quasiparticle is a composite boson.

changes to a weakly interacting CF-system. The composite particles experience an effective magnetic field, which is given by:

$$B_{\text{eff}} = B_{\text{ext}} - 2n_e\phi_0. \quad (2.17)$$

Here, B_{ext} is the external magnetic field and n_e the electron density. Generally speaking, it is possible to interpret the effective magnetic field as follows: An electron is attached to 2 “fictitious” flux quanta which are oriented opposite to the external magnetic field. These mostly cancel the real magnetic field resulting in B_{eff} . Alternatively, one can picture an electron “capturing” two real flux quanta from the external magnetic field, thus reducing its value to B_{eff} .

More accurately, B_{eff} is obtained by determining the phase produced by a CF moving around a closed loop of area A : $2\pi \left(\frac{B_{\text{ext}}A}{\phi_0} - 2N_{\text{enc}} \right)$. The left term is the Aharonov-Bohm phase due to the external magnetic field while the right term is the phase produced by N_{enc} which is the number of flux quanta of the other composite particles enclosed during the loop. In the mean-field approximation, the flux quanta can be “spread” out so that $N_{\text{enc}} = n_eA$. Equating this phase to a new Aharonov-Bohm phase produced by the effective magnetic field, i.e. $\frac{2\pi B_{\text{eff}}A}{\phi_0} = 2\pi \left(\frac{B_{\text{ext}}A}{\phi_0} - 2n_eA \right)$, renders equation 2.17. At $\nu = 1/2$, $B_{\text{eff}} = 0$ and a CF Fermi sea forms. The composite fermions fill the sea up to the Fermi-energy, E_F . The Fermi wave vector is given by the following relation: $k_{F,\text{CF}} = (4\pi n_e)^{1/2}$ [50]. B_{eff} deviates from 0 as one moves away from $\nu = 1/2$ and it is negative for $\nu > 1/2$ and positive for $\nu < 1/2$. Consequently, composite fermions occupy CF-LL which are energetically separated by $\hbar\omega_c^*$. The CF cyclotron frequency is then: $\omega_c^* = \frac{eB_{\text{eff}}}{m_{\text{CF}}^*}$, where m_{CF}^* is the CF-effective mass. Consequently, the CF-filling factor can be obtained from the electron filling factor by using the following relation:

$$\nu = \frac{\nu_{\text{CF}}}{2\nu_{\text{CF}} \pm 1}. \quad (2.18)$$

This is obtained by replacing B by B_{eff} in equation 2.10. For example, $\nu = 2/3$ and $\nu = 2/5$ become $\nu_{\text{CF}} = 2$ for negative or positive B_{eff} , respectively. Likewise $\nu = 3/5, 3/7$ turn into $\nu_{\text{CF}} = 3$ and $4/7, 4/9$ into 4 (see section 5.2.4).

The CF model explains the experimental results astonishingly well. All of the fractional states can be well understood with this model. Even the recently discovered FQHE fractions (for example $\nu = 4/11$ and $\nu = 5/13$) could be explained as FQH states of CFs [51, 52]. Comparing again Fig. 2.7, we see that ρ_{xx} shows SdH oscillations which are symmetrical around $\nu = 1/2$. This resembles the case for electrons around $B = 0$. In general, the FQHE of strongly-correlated electrons can be considered to be the IQHE of weakly interacting composite fermions. The CF-model is schematically represented in Fig. 2.9⁷.

⁷We have restricted our discussion to the LLL, however CFs also exist at $\nu = 3/2$. At $\nu = 5/2$ and $7/2$, a composite fermion pair forms at these states resulting in a minimum in ρ_{xx} (see section 5.6). At higher LLs, e.g. $\nu = 9/2, 11/2, \dots$, a charge density wave describes these ground states. In transport, they are characterized by anisotropic peaks depending on the crystallographic direction [53, 54].

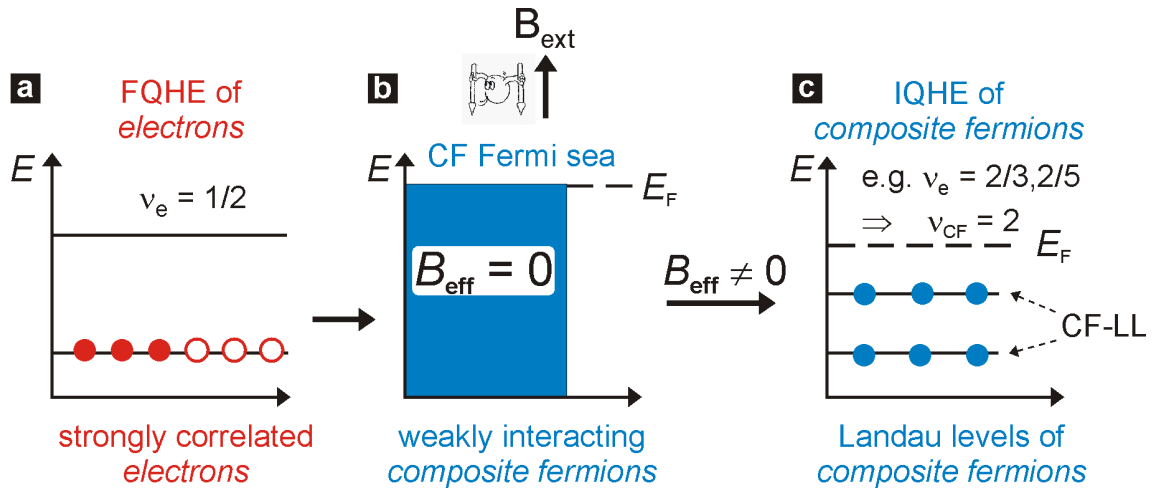


Figure 2.9: Composite Fermion (CF) model. If the LLL is only half filled ($\nu = 1/2$), the strongly correlated electronic system (a) can be transformed into a weakly interacting system of CFs by attaching two flux quanta to an electron (b). At this filling factor, the CFs experience a zero effective magnetic field and form a CF Fermi sea. Deviating from $\nu = 1/2$, $B_{\text{eff}} \neq 0$ and CFs occupy CF-LLs separated by $\hbar\omega_c^*$ (c). A CF filling factor can be obtained from the electronic filling factor (e.g. $\nu = 2/3$ and $2/5$ become $\nu_{\text{CF}} = 2$) via equation 2.18.

2.4 The Spin Degree of Freedom in the Lowest Landau Level

If only the lowest spin-split LL is occupied by electrons, it is natural to assume that the spin degree of freedom is effectively frozen out since the system is expected to be fully polarized. Therefore, one of the requirements for Laughlin's trial wavefunction is that its orbital part is antisymmetric under particle exchange due to the symmetric nature of the spin part. As previously mentioned, this assumption successfully describes the $\nu = 1/m$ QH groundstates. For example at $\nu = 1$ and $\nu = 1/3$, the only possible groundstate has complete spin polarization. However, spin has proven to be responsible for a rich number of phenomena occurring in the LLL. For instance at all fractional filling factors different from $\nu = 1/m$, ground states of various spin polarizations exist. Transitions between these states have been detected in numerous experiments [5,55,56,57,58,59]. Also, the CF Fermi sea at $\nu = 1/2$ is no longer completely polarized whenever the CF Fermi energy is greater than the Zeeman splitting [60,61,62]. Furthermore, the lowest energy charged excitations of the $\nu = 1$ quantum Hall ferromagnetic state are charged excitations with an underlying spin texture known as Skyrmions [22, 63, 64, 65, 66, 67]. These topological objects were first measured by means of optical pumped nuclear magnetic resonance (OPNMR) experiments (see section 2.4.4) [68]. Also, the quasiparticle-quasihole excitations of several ground states in the FQH regime are spin-reversed [8, 69]. Finally, the electron spin

may couple to the nuclear spin via the hyperfine interaction [70, 71]. This leads to unexpected behavior of the electronic system measured in transport experiments [5, 58, 59, 72]. Moreover, the electron spin polarization can be directly determined from NMR experiments [68, 73].

In the next subsections we briefly deal with these spin-related phenomena individually. They are necessary to understand the transport and NMR experiments carried out in this work. We end the section by reviewing several experimental techniques and experiments used to study spin in the LLL. We focus particularly on transport and NMR.

2.4.1 Spin Phase Transitions

The existence of ground states with partial or no spin polarization in the LLL was first pointed out by B.I. Halperin soon after the discovery of the FQHE. He noted that since in GaAs the electron reduced mass is much smaller than the free electron mass ($m^* = 0.067m_e$) and the effective g-factor is $g^* = 0.44$ instead of 2.03 (free electrons), then the Zeeman energy E_Z is about 60 times smaller than the cyclotron energy. Furthermore, E_Z is similar to the quasiparticle energies (≈ 5 K at 10 T) at several ground states of the FQHE, which depend on the exchange part of the Coulomb energy, approximately given by $E_C[K] = 50K \cdot \sqrt{B[\text{T}]}$ [23]. The favorable ground state polarization is thus dependent on the interplay between the Zeeman and Coulomb energies and the assumption of only completely polarized groundstates is incorrect since partial or unpolarized states exist in this regime.

Halperin constructed a trial wavefunction to include the spin degree of freedom [42]⁸: For example at $\nu = 2/3$, this wavefunction is given by:

$$\Psi = \prod_{i < j} (z_i - z_j)^3 \prod_{k < m} (\tilde{z}_k - \tilde{z}_m)^3 \prod_{i, k} (z_i - \tilde{z}_k)^2 \exp \left[-\frac{1}{4\ell_B^2} \sum_i |z_i|^2 \right] \exp \left[-\frac{1}{4\ell_B^2} \sum_k |\tilde{z}_k|^2 \right]. \quad (2.19)$$

The coordinates z and \tilde{z} represent spin down and spin up electrons, respectively. This formula fulfills all the necessary requirements: the wavefunction is antisymmetry under particle exchange, electrons of equal spin are kept further separated than electrons with opposite spin (exponent of Jastrow terms) and all electrons are located in the LLL. Numerical calculations by Chakraborty *et al.* [8] indicated that unpolarized or partially polarized states are in some cases energetically more favorable than fully polarized states. Their results for $\nu = 2/5$ and $2/3$ are displayed in Fig. 2.10. Here, the excitation energies are plotted vs magnetic field. In both cases, an unpolarized state is expected to be energetically favorable at sufficiently low B -fields while a polarized state should exist at higher fields. The transition from an spin unpolarized to a spin-polarized state is significantly different, however, for both filling factors. For $\nu = 2/3$, a gapless region was calculated, and consequently a non-zero R_{xx} is expected at intermediate magnetic

⁸Such a wavefunction is also applied to CF-pairing at $\nu = 5/2, 7/2$ and in bilayer systems, in which the coordinate z represents one layer and \tilde{z} the other layer [21].

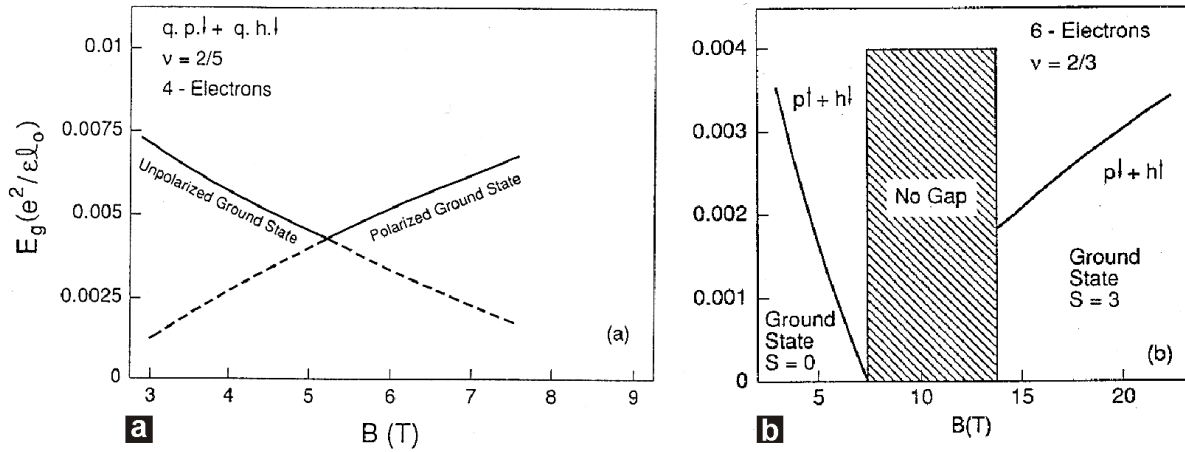


Figure 2.10: Numerical calculations of the quasiparticle excitation energy vs B -field at filling factors $2/5$ (a) and $2/3$ (b). For both cases, an unpolarized ground state is expected for small B and a polarized state for large B . A gapless region is calculated for $\nu = 2/3$ (hatched). The figure is adapted from reference [8].

fields, whereas at $\nu = 2/5$ a gap is always present. Eisenstein *et al.* first discovered such a spin phase transition in the FQHE experimentally (Fig. 2.11). In their activation measurements at $\nu = 8/5$, which is the particle-hole conjugate of $\nu = 2/5$, two different slopes of the excitation energy are seen: the first slope is negative and occurs at $B < 5.3$ T and the second positive and occurs at $B > 5.3$ T. The different slopes at the two magnetic field regions indicate different quasiparticle Zeeman splittings and hence ground state polarizations [Fig. 2.11 (a)]. Figure 2.11 (b) shows a plot of R_{xx} vs B_{\perp} performed at filling factor $\nu = 2/3$. Here, the sample was tilted with respect to the external magnetic field direction. In this way, B_{\perp} remains constant while B_{tot} increases. At this filling factor, a non-vanishing R_{xx} at intermediate tilt-angles reveals the spin unpolarized-polarized phase transition. The electron-nuclear hyperfine interaction also plays a major role in the $\nu = 2/3$ transition [6] and will be extensively discussed in chapters 4 and 5.

It is important to note that since the favorable ground state depends on the interplay between Zeeman and Coulomb energies, the parameter which determines the ground state is the ratio between these energies defined as $\eta = \frac{E_Z}{E_C}$. The transitions occur at a critical value of this ratio, η_c ⁹. Since $E_Z \propto B$ and $E_C \propto \sqrt{B}$, transitions between states can be tuned either by introducing a parallel B -field through tilting of the sample ($E_Z \propto B_{\text{tot}}$ and $E_C \propto \sqrt{B_{\perp}}$) or by varying the density (E_Z is constant and $E_C \propto \sqrt{n}$) through the use of a gate (see section 4.2). If a quantum well is used, in order to correctly determine the value of η , it is necessary to

⁹This value varies slightly in different samples.

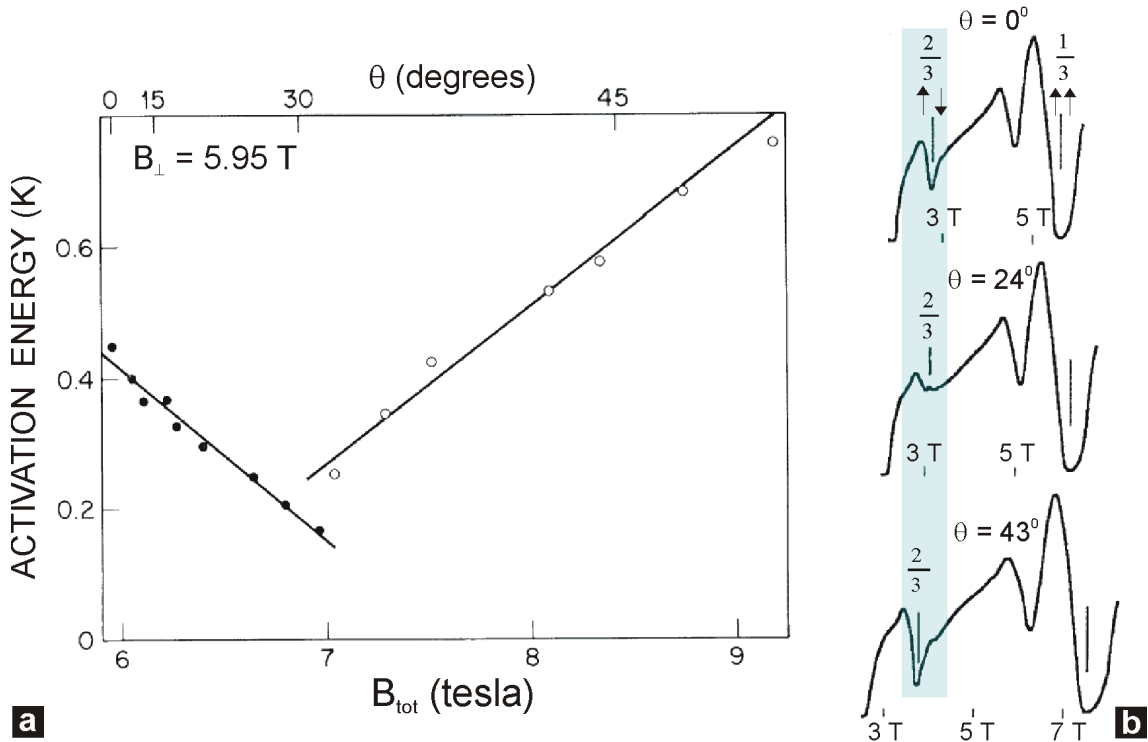


Figure 2.11: Spin phase transitions in the FQHE. The left figure (a) shows activation measurements of the $\nu = 8/5$ state, which is the particle-hole conjugate of $\nu = 2/5$. The different slopes give evidence for two different quasiparticle excitation energies and hence two ground state polarizations. The right figure (b) shows tilted B -field experiments for $\nu = 2/3$. The disappearance and reentrant behavior of the R_{xx} minimum is consistent with an unpolarized-polarized phase transition. Figures taken from references [74] and [75], respectively.

introduce finite thickness and g -factor corrections in the Coulomb energy and Zeeman energy calculations, respectively. The g -factor is given by:

$$g(B, N) = g_0 - c(N + \frac{1}{2})B, \quad (2.20)$$

where $g_0 = 0.4$ and $c = 0.0115 \text{ T}^{-1}$ for a 15 nm QW, B is the magnetic field and N the Landau level number [76]. These correction are due to the non-parabolicity of the band structure in GaAs [77]. The Coulomb energy can be calculated according to:

$$E_C = \frac{e^2}{4\pi\epsilon\ell_B^{\text{eff}}}. \quad (2.21)$$

In this expression, $\ell_B^{\text{eff}} = \sqrt{\ell_B^2 + \lambda^2}$ is the effective magnetic length and λ is the FWHM of the wavefunction which depends on the QW thickness [78, 79].

Even though the spin phase transitions can be satisfactorily understood by only considering the strongly correlated electron system, the weakly interacting CF-picture provides a more elegant, intuitive and accurate way of understanding this phenomenon. In this model, the expected ground state polarizations are obtained naturally, as we will explain in the following.

2.4.2 Spin in the CF Picture

In Fig. 2.9, we schematically showed that if $\nu \neq 1/2$, the CF Fermi sea develops into a discrete series of LLs energetically separated by $\hbar\omega_c^*$. If we introduce the spin degree of freedom, we can further split these levels by the Zeeman energy $g^*\mu_B B$ as in the case of the IQHE. The latter splitting, however, depends on the external magnetic field and not on B_{eff} . Drawing again the CF-LLs, this time as a function of density (or equivalently B_{tot} at tilted fields), and including the spin-splitting, the crossings between ground states become obvious. This is plotted in Fig.

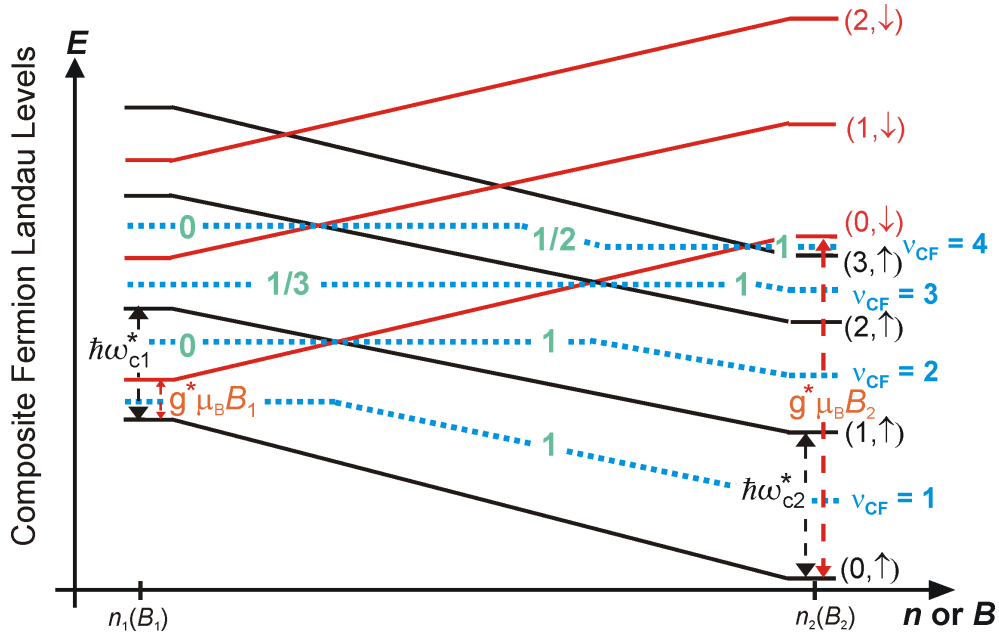


Figure 2.12: Spin-split composite fermion Landau levels. Since the CF-cyclotron energy increases as \sqrt{n} or \sqrt{B} and the Zeeman energy as n or B , crossings between ground states of different polarization exist. The blue-dotted line represents the Fermi level. For simplicity, we have connected $n_1(B_1)$ and $n_2(B_2)$ with straight lines. The polarization can be determined from $\mathcal{P} = \frac{N_{\uparrow} - N_{\downarrow}}{N_{\uparrow} + N_{\downarrow}}$. At $\nu_{\text{CF}} = 2$ ($\nu = 2/3$), a transition occurs from $\mathcal{P} = 0$ to $\mathcal{P} = 1$ at $\Delta_{\text{CF}} = E_Z$. At $\nu_{\text{CF}} = 3$ ($\nu = 3/5$) and $\nu_{\text{CF}} = 4$ ($\nu = 4/7$) transitions occur from $\mathcal{P} = 1/3$ to $\mathcal{P} = 1$ and $\mathcal{P} = 0$ to $\mathcal{P} = 1/2$ to $\mathcal{P} = 1$, respectively.

2.12 for the CF LLs $N = 0, 1$ and 2 . The spin up level is depicted black, the spin down is

shown in red and the Fermi energy is blue. The splitting between two levels of same spin, for example $N = (0, \uparrow)$ and $N = (1, \uparrow)$ is given by the CF cyclotron energy $\hbar\omega_{c1}^*$ at the density n_1 (or field B_1). The splitting between levels of different spin, e.g. $N = (0, \uparrow)$ and $N = (0, \downarrow)$ is the Zeeman energy ($g^*\mu_B B_1$ at n_1). Considering the case of fixed filling factor $\nu_{CF} = 2$ as an example, we see that at low densities or fields $\hbar\omega_{c1}^* > g^*\mu_B B_1$. The two CF-LLs have different spin orientation and the polarization is therefore zero. The polarization is given by the following expression:

$$\mathcal{P} = \frac{N_{\uparrow} - N_{\downarrow}}{N_{\uparrow} + N_{\downarrow}}. \quad (2.22)$$

Increasing the density has a different effect on both energy scales. While the Zeeman splitting increases linearly with the density n , the CF cyclotron energy increases as \sqrt{n} ($m_{CF} \propto \sqrt{n}$). Therefore, at higher densities, $\hbar\omega_{c2}^* < g\mu_B B_2$ and the two occupied CF-LLs have the same spin orientation, i.e. the system is polarized¹⁰. A transition between $N = (0, \downarrow)$ and $N = (1, \uparrow)$ occurs whenever the CF cyclotron Δ_{CF} and the Zeeman energies are the same¹¹:

$$\Delta_{CF} = \frac{\hbar e}{m_{CF}^p} |B_{\text{eff}}| = E_Z = g_{CF}^* \mu_B B_{\text{ext}}. \quad (2.23)$$

In this equation, m_{CF}^p is the CF polarization mass, which will be introduced in section 2.4.3 and B_{eff} is given by equation 2.17. The CF g -factor g_{CF}^* has been measured to be largely the g -factor of the electrons g^* , which means that CFs are only weakly interacting [81]. In references [7], [82] and [83], it is shown that the critical value of spin transitions in the FQHE is more accurately described by the CF picture than by the Coulomb to Zeeman energy ratio of the electrons.

In the LLL, the CF filling factor $\nu_{CF} = 2$ equals the electron filling factor $\nu = 2/3$ and $2/5$ of electrons. In Fig. 2.12, we have also displayed examples for $\nu_{CF} = 1, 3$ and 4 . These relate to electron filling factors $\nu = 1/3$, $\nu = 3/5$ (also $3/7$) and for $\nu = 4/7$ (also $4/9$), respectively. Filling factor $\nu_{CF} = 1$ can only be spin polarized as expected from Laughlin's trial wavefunction, $\nu_{CF} = 2$ has a transition from $\mathcal{P} = 0$ to $\mathcal{P} = 1$, $\nu_{CF} = 3$ from $\mathcal{P} = 1/3$ to $\mathcal{P} = 1$ and $\nu_{CF} = 4$ has two transitions: $\mathcal{P} = 0$ to $\mathcal{P} = 1/2$ and $\mathcal{P} = 1/2$ to $\mathcal{P} = 1$ at higher fields. These spin transitions between CF groundstates of different polarizations were confirmed by Kukushkin *et al.* by carrying out optical experiments. The electron spin polarization, \mathcal{P} , was obtained from luminescence experiments by measuring the degree of circularly polarized light emitted from time resolved radiative recombination of 2D electrons with photoexcited holes bound to acceptors [60]¹². The samples used were high-quality single GaAs/AlGaAs

¹⁰Since the CF spin and the electron spin are the same, it is equivalent to refer to a CF or electron spin polarization [80].

¹¹For simplicity, we have drawn straight lines from B_1 (n_1) to B_2 (n_2). It is however important to remember that the CF cyclotron energy increases as \sqrt{B} (\sqrt{n}).

¹²The experimental method is described in reference [84]. It is beyond the scope of this thesis to explain these experiments in more detail.

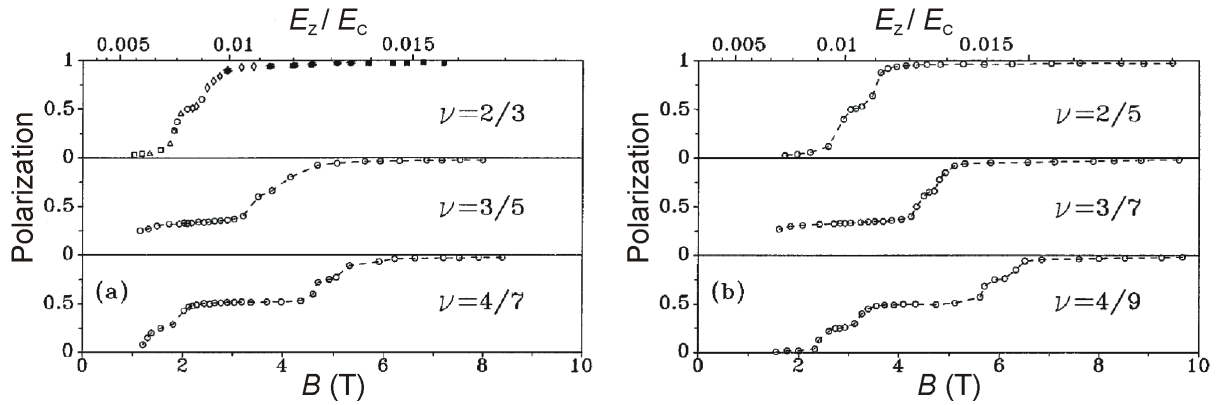


Figure 2.13: Spin phase transitions in the FQHE. The electron spin polarization was measured by means of optical measurements. The transitions expected from the composite fermion theory are observed in these experiments. Some small polarization plateaus appear which are not explained by the simple CF model (e.g. $\mathcal{P} = 1/2$ at $\nu = 2/3$). The data was taken from reference [60].

heterojunctions. The small polarization plateau seen at unexpected values, such as $\mathcal{P} = 1/2$ at $\nu = 2/3$ cannot be explained by the weakly interacting CF-model. CF interactions might play a role in these cases [85].

2.4.3 Polarization at $\nu = 1/2$

At $\nu = 1/2$, despite the fact that $B_{\text{eff}} = 0$, the spins of the CFs still experience a Zeeman energy from the external magnetic field. Therefore, in the limit of vanishing temperature, the $\nu = 1/2$ CF Fermi sea is expected to be completely polarized when the Zeeman energy $E_Z > E_F$, where E_F is the CF Fermi energy (see also section 5.2.2). If $E_Z < E_F$ however, the CF Fermi sea is only partially polarized. A smooth transition from a partially to a completely polarized system takes place at a critical ratio η when the Zeeman and Fermi energies are equal. The polarization at $\nu = 1/2$ was measured by means of optical experiments by Kukushkin *et al.* [60] and NMR experiments by Freytag *et al.* [62]. The most important results are presented in Figs. 2.14 (a) and 2.14 (b), respectively. In the top figure, the electron spin polarization, \mathcal{P} , is plotted vs magnetic field at fixed filling factor $\nu = 1/2$. These measurements were obtained with the same optical technique described above. From the graph, it is evident that the electron system is fully polarized at a B -fields larger than approximately 9.3 ± 0.5 T. At lower fields the system starts to depolarize. Likewise, in the NMR experiments presented in Fig. 2.14 (b), the electron system is fully polarized ($\mathcal{P} = 1$) at $B > 10$ T, while at lower fields $\mathcal{P} < 1$. This plot of polarization vs magnetic field was obtained by measuring the Knight shift from NMR experiments carried out on multiple GaAs/AlGaAs quantum wells (see next section). The

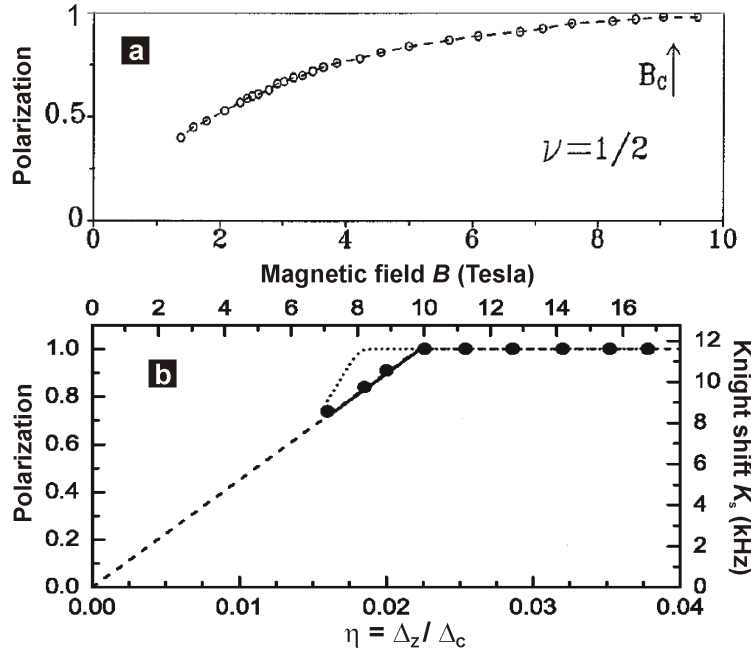


Figure 2.14: Spin polarization at filling factor $\nu = 1/2$. The CF sea at $1/2$ is completely spin polarized if $E_F > E_Z$. This happens at approximately $B = 9.5$ T. At lower fields the polarization of the system is less than one. The polarization was extracted from optical measurements (Figure (a) taken from reference [60]) and from NMR experiments performed on a multiple quantum wells sample (Figure (b) adapted from reference [62])

transition should occur at $\hbar^2 k_{F,CF}^2 / 2m_{CF}^* = g_{CF}^* \mu_B B_c$, where m_{CF}^* is the CF mass and $k_{F,CF}$ is the CF wavevector a previously described. Assuming a parabolic dispersion law for composite fermions, the CF mass was determined from these experiments. It is however necessary to distinguish between the mass obtained from activation measurements (activation mass, m_{CF}^a) and polarization experiments (polarization mass, m_{CF}^p)¹³.

Activation and polarization mass of CFs

A CF mass is in general dependent on the experiment performed. For example, the CF mass determined from polarization measurements is much larger than the one determined from activation experiments, and these two masses are different from a bare CF cyclotron mass. This is however not surprising considering that the LLL Hamiltonian does not contain a mass (the

¹³The CF-polarization mass obtained from the experiments in reference [60] is $m_{CF}^p = 2.27m_e$. This was determined by assuming: 1) $g_{CF}^* = g_e^*$, 2) $n_{CF} = n_e$, 3) E_Z is independent of m_{CF}^p and 4) a parabolic dispersion law for CFs.

kinetic energy is a constant in the LLL) and a CF mass is not a renormalized value but is obtained entirely from interactions. Nevertheless, it is convenient to define an effective CF mass, whenever the CF picture is used. One type of CF mass can be phenomenologically defined from activation measurements and it is given by:

$$\frac{m_{\text{CF}}^{\text{a}}}{m_e} \approx 0.08\sqrt{B(\text{T})}. \quad (2.24)$$

Instead, the mass obtained from polarization measurements can be determined from the following expression:

$$\frac{m_{\text{CF}}^{\text{p}}}{m_e} \approx 0.60\sqrt{B(\text{T})}. \quad (2.25)$$

These values are different because the activation energy used to calculate equation 2.24 includes the bare cyclotron energy and the self interaction energies of the created CF particle-hole pair [80]¹⁴. The polarization mass (eq. 2.25), on the other hand, was determined from the energy splitting between two states of different polarization. Hence, this is the value which should be used for experiments involving spin polarization. The electron spin polarization at filling factor $\nu = 1/2$ will be addressed again in section 5.2.2 of this work.

2.4.4 Skyrmions and Quasiparticle Excitations

The $\nu = 1$ QH state remains spin polarized even in the absence of a Zeeman energy ($g^* \rightarrow 0$). An energy gap between the states of different polarization remains due to the Coulomb exchange energy which tries to keep the electron spins oriented in the same direction. The system is thus stabilized in a ferromagnetic state and the term Quantum Hall Ferromagnet (QHF) is appropriately used to describe the $\nu = 1$ state. Electron-electron interactions play a major role in this state. In the limit of vanishing Zeeman energy, the lowest-lying charged energy excitations of the QHF state are topological objects with an underlying spin-texture. Such an excitation, referred to as a skyrmion, is schematically drawn in Fig. 2.15¹⁵. Skyrmions are characterized by having their spin turned downward at the center and gradually turning upward at a distance far from the center. At intermediate distances, all the spins point in the xy-plane and exhibit a vortex-like winding configuration. A skyrmion is energetically more favorable than a single spin flip whenever the Coulomb exchange energy is large in comparison to the Zeeman energy because it prefers locally aligned spins. The energy necessary to create an excitation is given by the sum of the Zeeman and Coulomb exchange energies:

$$E = E_Z + E_{\text{exch}} = g^* \mu_B B + \rho_s E_C k^2. \quad (2.26)$$

¹⁴The “bare” cyclotron mass has been determined from cyclotron resonance experiments [86].

¹⁵The concept of a skyrmion was borrowed from the skyrme crystal model of nuclear physics [87].

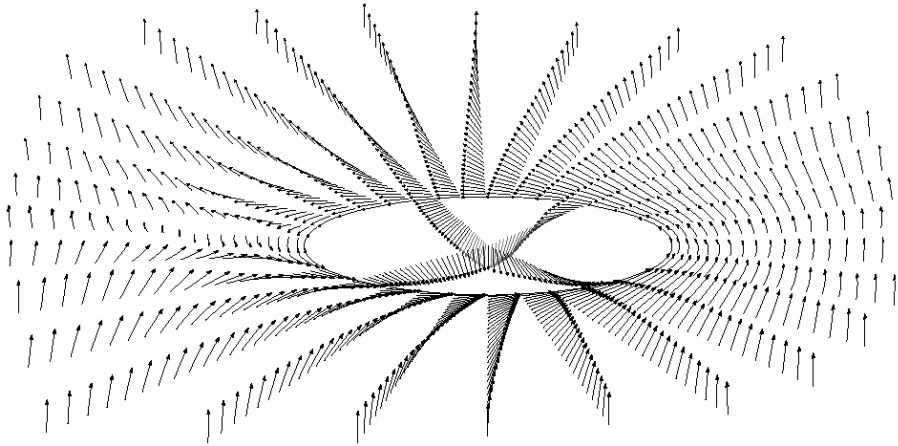


Figure 2.15: The lowest-lying energy excitations of the QHF state $\nu = 1$ at vanishing Zeeman energy are topological objects with an underlying spin-texture known as skyrmions. These structures are characterized by gradually flipping numerous electron spins but yet carrying exactly one unit of charge. The spin points downwards at the center and upwards at a distance far from the center. At some intermediate distance the spin points in the xy -plane. The existence and size of a skyrmion are determined by the interplay between E_Z and E_C .

Here, ρ_s is the “spin stiffness” and k the wavevector. The size of a skyrmion and the number of spin reversals are then determined by the interplay between these two energies. At $E_Z = 0$, the skyrmion should be infinite. Increasing the Zeeman energy shrinks the skyrmion in order to balance the Zeeman and Coulomb energies. At large E_Z , the single particle model is restored and the excitations are single spin flips. Skyrmions in a QHF carry a charge which is equal to $\pm e$ at filling factor 1. Exactly at the filling factor, skyrmions freeze out at sufficiently low temperatures. Deviating from $\nu = 1$ creates a skyrmion for $\nu > 1$ or an antiskyrmion for $\nu < 1$. The number of skyrmions/antiskyrmions equals the number of added/removed charges.

Experimentally, it makes sense to measure the electron spin polarization around $\nu = 1$ in order to study skyrmionic excitations since these involve flipping of electron spins. Barrett *et al.* were the first group to obtain direct experimental evidence for the existence of skyrmions by performing optically pumped NMR (OPNMR) experiments. The most important results are presented in Fig. 2.16 (a). In this graph, the Knight shift is plotted vs filling factor. In the next section we will see that the Knight shift, which is the shift of the nuclear spin precession or Larmor resonance frequency, is directly proportional to the electron spin polarization \mathcal{P} . At exactly $\nu = 1$, the Knight shift is maximum corresponding to $\mathcal{P} = 1$. On both sides of $\nu = 1$ the polarization decreases rapidly. This result agrees well with the theoretical prediction that

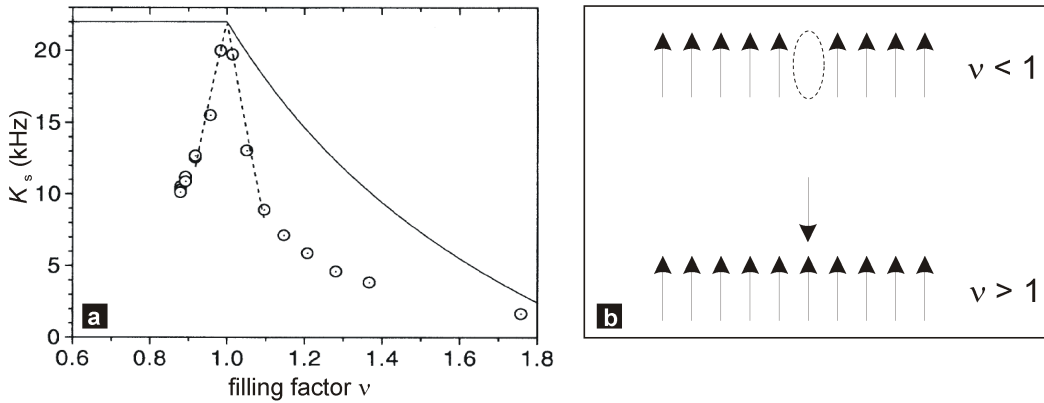


Figure 2.16: The existence of skyrmions was first proved by means of optically pumped NMR experiments [68]. Figure (a) shows that at exactly $\nu = 1$, $\mathcal{P} = 1$, but it deviates from this value on both sides of $\nu = 1$ as expected for skyrmions. For a non-interacting system the expected polarization is shown by the solid line. Figure (b) schematically shows that if Coulomb exchange were neglected, one would expect the system to unpolarize for $\nu > 1$, but should remain fully polarized at $\nu < 1$ (adapted from [22])

finite-size skyrmions with a total spin of ≈ 3.6 exist around $\nu = 1$ ¹⁶. The solid line shows the expected Knight shift for the non-interacting system, i.e. if Coulomb exchange were neglected and the excitations were just a single spin flip. This can be easily understood by using Fig. 2.16 (b). For this case we would expect a fully polarized system for $\nu < 1$, since the introduction of a hole would not change the polarization, whereas if an electron is introduced, the polarization should decrease as $\mathcal{P} = (2 - \nu)/\nu$ for $1 < \nu < 2$ until reaching 0 at $\nu = 2$. The measurements shown in Fig. (a) were performed at $B = 7.05$ T. However skyrmions are not expected to occur at this B -field value since Kukushkin *et al.* ruled out the existence of skyrmions at fields greater than 4 T by determining the polarization with luminescence experiments [88]. This apparent contradiction might be due to a shift in the electron Zeeman energy caused by an additional local magnetic field created by dynamically polarized nuclei which act on the electron spin, known as hyperfine field. The coupling of the electronic and nuclear system is the topic of the next subsection. In principle, skyrmions should also exist around the QHF state $\nu = 1/3$ [64]. Even though there has been some indication that they exist in this regime [89], some experiments have not revealed their existence [23, 52]. This might be due to the much larger spin stiffness at $1/3$.

Some of the quasiparticle excitations in the FQHE, for example at $\nu = 2/3$, might be spin

¹⁶Even though a skyrmion should be a spatially unbounded, infinite spin excitation, in the QHF one speaks of skyrmions whenever the number of reversed spins per quasiparticle is greater than 1.

reversed [see Fig. 2.10 (b)]. Here, the spin degree of freedom also plays an important role. Skyrmonic and quasiparticle excitation measurements will be presented in section 5.5.

2.4.5 Interactions between Electrons and Nuclei

The electronic system alone cannot explain certain phenomena occurring in the LLL. The coupling between electrons and nuclei should be taken into account. The importance of the nuclear system in two-dimensional systems has been established in numerous experiments [5, 58, 73, 90, 91, 92, 93]. In general, electrons and nuclei couple via the hyperfine interaction. It is thus important to understand the consequences of this interaction in more detail.

Hyperfine Interaction

If a nucleus has a spin \mathbf{I} , then it can interact with an electron spin \mathbf{S} , through the hyperfine interaction written as:

$$H = A_{\text{HF}} \mathbf{I} \cdot \mathbf{S} \quad (2.27)$$

The hyperfine constant has two contributions, $A_{\text{HF}} = A_s + A_p$. The first contribution arises from the electron wavefunction which has a non-zero probability of being located at the nuclear site, usually from s-type wavefunctions. This term is known as the Fermi contact interaction:

$$A_s = \frac{\mu_0}{4\pi} \cdot \frac{8\pi}{3} \cdot (g_e \mu_B) (g_N \mu_N) |\psi(0)|^2 \quad (2.28)$$

Here, g_e , g_N are the free electron g -factor and the nuclear g -factor respectively, μ_N the nuclear magneton, μ_B the Bohr magneton, μ_0 the permeability constant and $|\psi(0)|^2$ the probability of finding an electron at a nuclear site.

The second contribution comes from wavefunctions which have an angular momentum and vanish at the nuclear site such as p-wavefunctions:

$$A_p = \frac{\mu_0}{4\pi} \cdot \frac{2}{5} \cdot (g_e \mu_B) (g_N \mu_N) \left\langle \frac{1}{r^3} \right\rangle \langle 3 \cos^2 \theta - 1 \rangle \quad (2.29)$$

where θ is the angle between the magnetic field and the p-wavefunction lobe [94]. The term $\left\langle \frac{1}{r^3} \right\rangle$ is an averaging over the electronic wave function and it vanishes at $\psi(0)$. Since in GaAs the electrons contributing to transport are situated in the conduction band, they have s-type wavefunctions. Therefore, only the Fermi contact term is relevant in this case (equation 2.28).

In principle, the hyperfine coupling between electrons and nuclei is important in two ways: First, whenever the nuclei are polarized, they create a local magnetic field, referred to as the nuclear hyperfine field B_N , which acts exclusively on the electronic spin (i.e. not on the orbital motion). The spin of an electron “feels” this internal magnetic field given by:

$$\mathbf{B}_N = \frac{2\mu_0}{3} \cdot \frac{g_e}{g^*} \hbar \sum_i a_i \gamma_{Ni} \mathbf{I}_i |\Psi(\mathbf{r}_i)|^2 \quad (2.30)$$

summing over the nuclei i at position r_i [90]. This expression was obtained by averaging over all nuclear isotopes with respect to their abundance a_i . In GaAs, the abundances for the three isotopes present are 60.4% for ^{69}Ga , 39.6% for ^{71}Ga and 100% for ^{75}As . The equation also contains g^* which is the effective g -factor of the electrons in GaAs and $\gamma_N = \frac{g_N \mu_N}{\hbar}$ referred to as the gyromagnetic ratio. Alternatively, B_N can be written in terms of the hyperfine constant as: $B_N = \frac{A_{\text{HF}} \langle I_z \rangle}{g^* \mu_B}$. As a result of the nuclear hyperfine field, the Zeeman energy changes to $g^* \mu_B (B_{\text{ext}} + B_N)$. The change in the electron spin resonance (ESR) frequency due to the nuclear hyperfine field is known as the Overhauser shift [95]. Since spin phenomena in the LLL, such as spin phase transitions or Skyrmions depend on the ratio η , which contains the Zeeman energy (see sections 2.4.1 and 2.4.4), they are strongly affected by the hyperfine coupling. The nuclei can be polarized either thermally or through electron spin flip nuclear spin flop processes. Usually the thermal polarization is negligible, but at the low temperatures and high magnetic fields (at $T \approx 20$ mK and $B = 10$ T) where some of our experiments were performed, about 15% of the nuclei are polarized. We will return to this point in chapter 5. Flip-flop processes can be easier visualized by rewriting equation 2.27 into

$$H = A_{\text{HF}} \left\{ \frac{1}{2} (\mathbf{I}_+ \cdot \mathbf{S}_- + \mathbf{I}_- \cdot \mathbf{S}_+) + \mathbf{I}_z \cdot \mathbf{S}_z \right\}. \quad (2.31)$$

The last term is the effective Zeeman interaction between the electron and nuclear spins. In the first two terms, \mathbf{I}_+ ($-$) and \mathbf{S}_+ ($-$) are the raising (lowering) operators for a nuclear and electron spin, respectively. They represent simultaneous electron flip nuclear flop processes: $\Delta S = \pm 1$ is accompanied by a $\Delta I = \mp 1$. The nuclear system is thus driven out of thermal equilibrium and the enhanced nuclear polarization or hyperpolarization via these processes is called the Overhauser effect. Dynamical nuclear polarization (DNP) can be achieved by optically exciting the electronic system with circularly polarized light (optical pumping) [96] or by current-induced nuclear spin polarization ([5, 91]) just to mention two techniques amongst others reported in the literature ([97, 98]).

Besides the nuclear hyperfine field created by polarized nuclei, the polarized electrons also create a local magnetic field acting on the nuclear spins. Summing over the electrons j , the field acting upon the i th nucleus is:

$$\mathbf{B}_e^i = -\frac{2\mu_0}{3} \cdot g_e \mu_B \sum_j \mathbf{S}_j |\Psi(\mathbf{r}_j)|^2. \quad (2.32)$$

This is the second important effect of the hyperfine coupling. Due to the additional magnetic field, the nuclear Zeeman splitting changes by $\hbar \gamma_N \mathbf{B}_e$. This change causes a shift in the NMR Larmor resonance frequency of the nuclei referred to as the Knight shift K_s in 2DES¹⁷. Since

¹⁷The Knight shift is usually defined as the frequency shift due to \mathbf{B}_e divided by the zero-shift reference frequency given in % or ppm units. However in 2DES, it has become common practice to define the Knight shift as the shifted frequency in terms of kHz.

K_s is proportional to the electron polarization \mathcal{P} , NMR is a powerful technique to determine this value (see section 5.2). In the next subsection we describe the two experimental techniques, NMR and transport, used in this thesis to study the electron-nucleus coupling in the FQHE.

2.4.6 Measuring Techniques

Various techniques have been implemented to study the spin degree of freedom in the FQHE. The optical measurements shown in Figs. 2.13 and 2.14(a), as well as heat capacity [99], magnetization [100, 101], surface acoustic waves (see appendix A), transport [55], optically pumped (OP)NMR [96], optically detected (OD)NMR [88, 102], multiple quantum well (MQW)NMR [73] and resistance detected (RD)NMR [6, 58] measurements have all provided an insight into spin phenomena in the LLL. In this section, we concentrate on transport and NMR.

Transport

From Fig. 2.11(b), we have seen that the importance of spin in the FQHE has been revealed in transport by a non-vanishing longitudinal resistance at $\nu = 2/3$. Furthermore, the coupling between electrons and nuclei has been determined by considering the large time constants involved in the settling of the resistance. For example at $\nu = 2/3$, an anomalously large peak in R_{xx} was measured by Kronmüller *et al.* (Fig. 2.17) [5].

In the figure, the longitudinal resistance is plotted vs magnetic field. The fractional filling factor $\nu = 2/3$ appears around $B = 8$ T. By reducing the field sweep rate near filling factor $2/3$, a large peak develops in R_{xx} . This peak is referred to as the huge longitudinal resistance or HLR peak. The inset on the left corner shows the time it takes the peak to settle to equilibrium after the B -field has been stopped. It is on the order of several minutes or even hours which is typical for effects involving nuclear magnetic moments. Further work on the HLR has revealed that this peak indicates the transition between the spin-unpolarized and spin-polarized ground states of $\nu = 2/3$ [59]. Also the peak evolves from a small longitudinal resistance (SLR) to a HLR peak by increasing the current. A model explaining these phenomena has been recently established. Transport studies of the $\nu = 2/3$ transition peak is a major part of this thesis. Our results are presented in chapter 4.

Since spin phase transitions depend on the critical ratio E_Z/E_C , a change in the Zeeman energy due to a nuclear hyperfine field B_N shifts these transitions to other values of the external B -field. Recently, the shifting of the $\nu = 2/3$ transition has been used as a “detector” to determine B_N as a function of filling factor in the QHE [98].

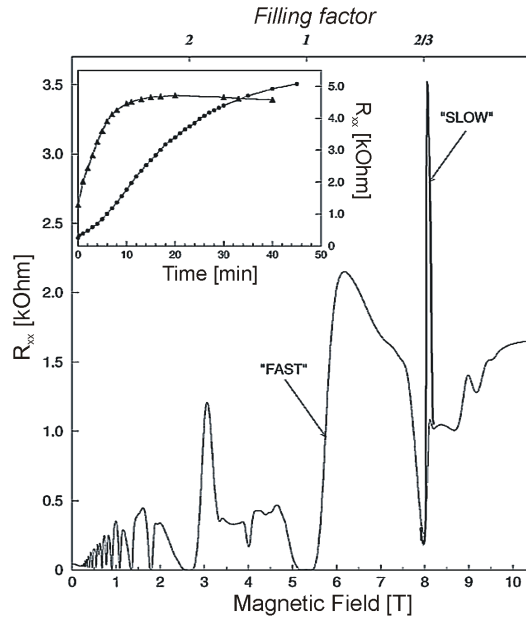


Figure 2.17: The large peak in the longitudinal resistance around $\nu = 2/3$ is referred to as the huge longitudinal resistance (HLR) peak [5]. It appears if the B -field sweep rate is drastically reduced. The inset shows that it takes several minutes for the peak to saturate. This is caused by the interaction between the nuclear and electronic systems via the hyperfine interaction.

NMR

Nuclear magnetic resonance is an important tool to study the electron spin polarization \mathcal{P} of a 2DES. This is mainly because the electron polarization is directly proportional to the Knight shift which can be determined from the spectroscopical information ($\mathcal{P} \propto K_s$). However, obtaining a signal from a single quantum well is a great experimental challenge. The sensitivity of an NMR experiment depends on the product of the number of nuclei in the system and on their average nuclear spin polarization. Unfortunately, there are very few nuclei located in the quantum well compared to the number of nuclei in the rest of the sample, i.e. barriers and substrate. Furthermore, the average polarization of the nuclear spins in the quantum well is usually small. In order to overcome these problems, several techniques have been implemented. For example, the average nuclear polarization can be increased by optically pumped (OP)NMR in which electron-hole pairs are generated by near infrared laser irradiation [96]. In this way, a non-equilibrium spin polarization of the electrons is created which in turn polarizes the nuclei via the hyperfine interaction. The resulting dynamical nuclear polarization (DNP) enables one to study the electron-nuclear coupling in a 2DES [96, 103, 104, 105]. This technique was used in the measurements shown in Fig. 2.16. However, it has the disadvantage of bringing the system

out of equilibrium.

Furthermore, the number of nuclear spins has been increased by using multiple quantum well (MQW) samples. Here, several GaAs quantum wells are stacked on top of each other. MQW were used for example in the OPNMR experiments presented in Fig. 2.16, and by Freytag *et al.* in polarization experiments performed in the LLL [see Fig. 2.14 (b)] [23]. This technique, however, has the disadvantage that the charge carrier density is fixed and that growing many identical layers is challenging. In chapter 5 we present a new method which we have developed, where conventional NMR and resistance detected NMR (see next subsection) are measured, in order to quantitatively determine the electron spin polarization in a single 2DES.

Resistance Detected (RD)NMR

Transport and NMR techniques can be combined in the so-called resistance detected (RD)NMR [6]. This method has been used to establish the interaction between nuclei and electrons in the

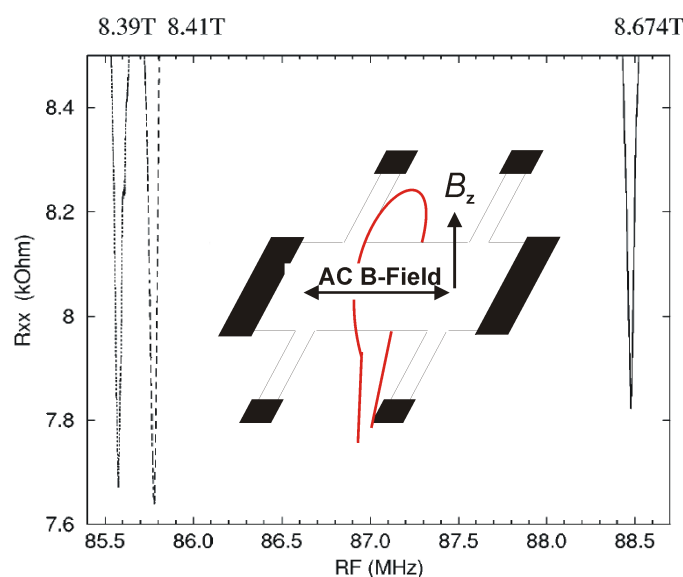


Figure 2.18: RDNMR measurements on the HLR peak. The dips in R_{xx} occur at the Larmor resonance frequency of ^{69}Ga . These experiments proved the existence of electron-nuclear spin interactions in the FQHE (adapted from [6]). Inset: NMR coil (one loop) was wound around a Hall bar.

FQHE. It consists of irradiating the sample with a radio frequency (RF) tuned to the Larmor frequency of the nuclei in question (^{69}Ga , ^{71}Ga or ^{75}As , in GaAs) while monitoring the changes in R_{xx} . Figure 2.18 shows RDNMR measurements on the HLR peak at three different magnetic fields for three different carrier densities. The resonance frequency is tuned to the ^{69}Ga nuclei. A single turn NMR coil was used in the experiments. The dip in the R_{xx} value indicated that

the nuclear system interacts with the electronic system in the HLR regime.

A closer look at the RDNMR spectra of the three nuclear isotopes revealed a four-fold splitting of the lines, see Fig. 2.19. None of the established interaction mechanism, such as

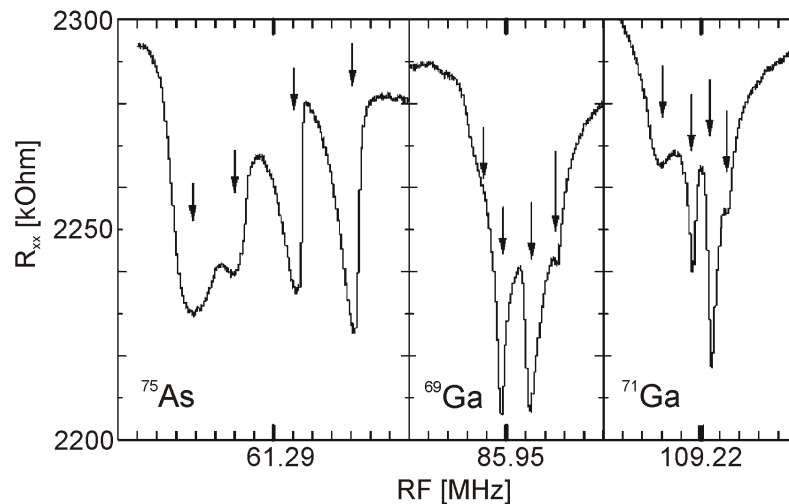


Figure 2.19: An anomalous four-fold splitting of the RDNMR lines was measured by Kronmüller *et al.* in the HLR regime [6]. In section 5.4, we clarify the reason for such a splitting.

quadrupole effects, dipolar coupling or hyperfine interactions, were able to explain such an anomaly in the RDNMR experiments. It was therefore speculated that a new electron-nuclear interaction could exist in the FQHE regime. In section 5.4, we study the four-fold splitting and explain the reason for such an anomaly.

In the next chapter, we present the high mobility, narrow quantum wells which were used in this thesis. Furthermore, we describe the experimental setup required for the experiments.

Chapter 3

Samples and Experimental Setup

3.1 The Samples

The samples used for the transport measurements consist of single, narrow (14 and 15 nm) GaAs quantum wells sandwiched between $\text{Al}_x\text{Ga}_{1-x}\text{As}$ layers. In all the samples used in this work, the aluminium content was 33% ($x = 0.33$).

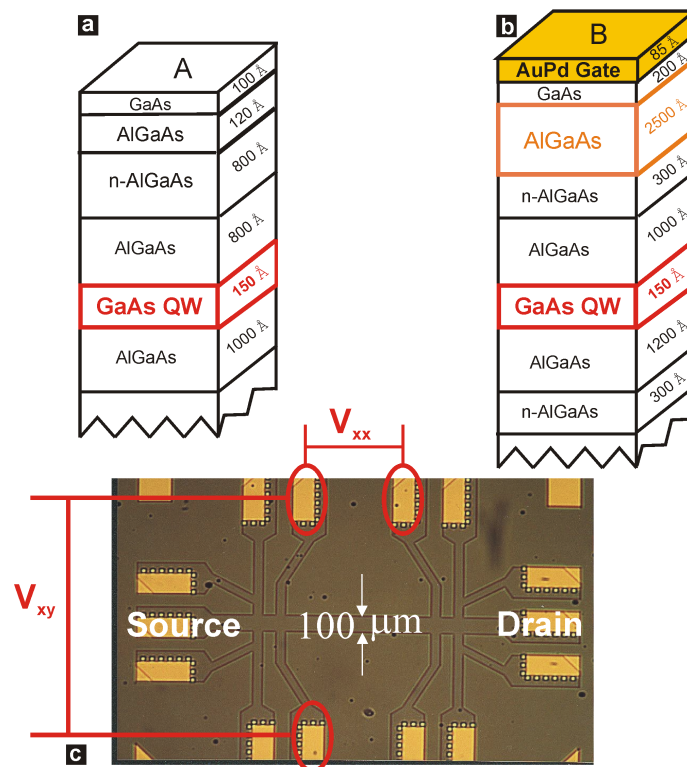


Figure 3.1: Schematical drawing of a type A sample (a) and a type B sample (b). A photograph of a typical Hall bar used in our transport experiments (c).

Type	Wafer, d QW (nm)	Density ($\times 10^{11} \text{cm}^{-2}$)	mobility ($\times 10^6 \text{cm}^2/\text{Vs}$)	V_{gate} (V)
A	100797.3 (15)	0.9 - 1.3 illumination	1.5 @ $n = 1.3 \times 10^{11} \text{cm}^{-2}$	no gate
A	052098.2 (14)	0.74-1.77 illumination	1.8@ $n = 1.3 \times 10^{11} \text{cm}^{-2}$	no gate
A	052098.4 (15)	1.5-2.0 illumination	2.1 @ $n = 2.0 \times 10^{11} \text{cm}^{-2}$	no gate
B	020502.1 (15)	0.8-2.1 frontgate	1.6 @ $n = 1.5 \times 10^{11} \text{cm}^{-2}$	(-0.6 - 0)
—	NU1154 (15) (15)	2.56 no illumin.	1.0 @ $n = 2.6 \times 10^{11} \text{cm}^{-2}$	no gate no gate
—	120700.1 (15/22/15)	0.5-2.2 backgate	1.3 @ $n = 1.6 \times 10^{11} \text{cm}^{-2}$	see reference [7]

Table 3.1: Some of the wafers used in this thesis are listed here. Samples of type A correspond to Fig. 3.1(a) and of type B correspond to Fig. (b).

Figures 3.1 (a) and (b) schematically show two characteristic samples used for our experiments. Sample A is single-sided doped and contains no electrons without illumination. The carriers can be introduced into the well by firstly illuminating the sample at ^4He temperature, then heating it up until the thermal energy is high enough for the carriers to tunnel from the doping layer into the well (> 15 mK) and electrons start populating the well, and finally cooling it down to ^3He or dilution refrigerator temperatures (see next section). This sample shows a typical mobility of $\mu \approx 1.8 \cdot 10^6 \text{cm}^2/\text{Vs}$ at a density of $1.3 \times 10^{11} \text{cm}^{-2}$ (further details are presented in Reference [4]). Sample B is symmetrically doped and has an intrinsic density of $n = 2.03 \times 10^{11} \text{cm}^{-2}$ without illumination. A thick AlGaAs cap layer (250 nm) was grown in order to evaporate a metallic gate without affecting the quality of the 2DES. The density can be varied between $2.03 \times 10^{11} \text{cm}^{-2}$ and $0.8 \times 10^{11} \text{cm}^{-2}$ by means of a 8.5 nm thin AuPd front gate. This covered the whole density range of the $\nu = 2/3$ transition. Table 3.1 lists the most important wafers used in this thesis. The type of sample correlates with the structures drawn in Fig. 3.1.

An example of a typical Hall bar used in this work is shown in Fig. 3.1(c) (see also reference [7]). The current was applied between the source and drain and the longitudinal and Hall voltages were measured. The length to width ratios L/W of the Hall bars employed in the measurements were 5, 6, 7, 8.5 and 9.5. The usual width of our Hall bars is $100 \mu\text{m}$, however, we also used other widths ranging from $80 \mu\text{m}$ to 1.5mm in various experiments. This will be specified in the corresponding figures. The procedure for structuring the Hall bar and evaporating the contacts and front gate for a sample of type B is described in appendix B. In

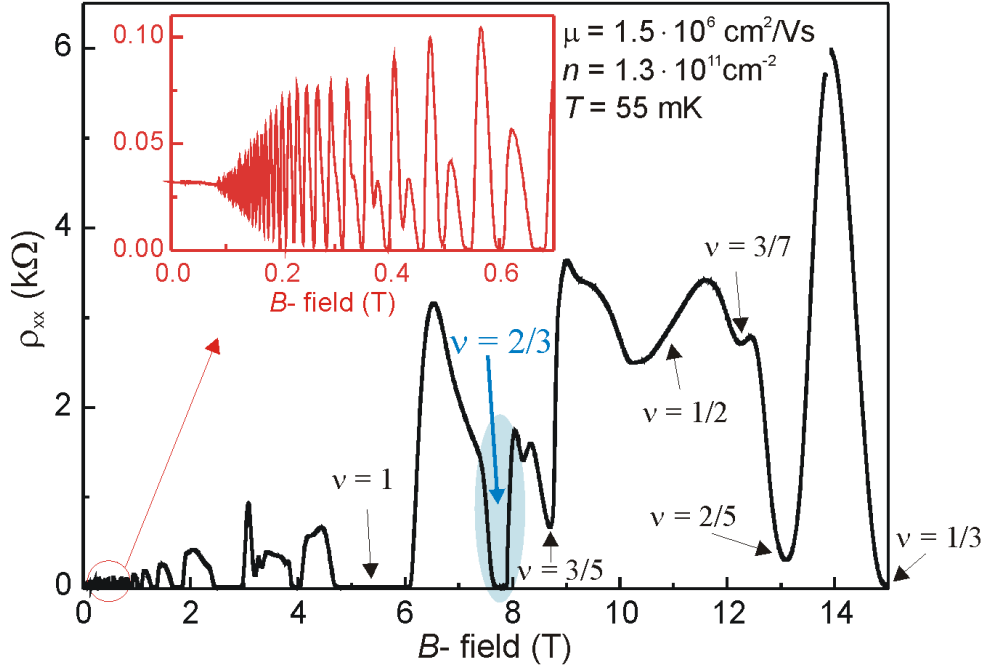


Figure 3.2: Typical ρ_{xx} vs B -field plot at $n = 1.3 \times 10^{11} \text{ cm}^{-2}$ and $T = 55 \text{ mK}$ in a B-type sample. Inset: SdH oscillations and spin splitting at lower B -fields (Sample from wafer 020501.1).

Fig. 3.2, we present a plot of the longitudinal resistivity vs B -field using a sample of type B at $T = 55 \text{ mK}$. Several filling factors, such as $\nu = 2/3, 2/5, 3/5, 3/7, 1/3$ etc. can be observed. The Shubnikov-de Haas maxima begin to spin-split at $B \approx 0.3 \text{ T}$ (see inset). In this graph, $n = 1.3 \times 10^{11} \text{ cm}^{-2}$ and $\mu = 1.5 \cdot 10^6 \text{ cm}^2/\text{Vs}$. A significant part of our measurements were performed at the $\nu = 2/3$ ground state highlighted in blue.

3.2 Experimental Setup

The experiments presented in this work were mostly performed on two types of cryogenic system: A ^3He system and a dilution refrigerator.

^3He system

We used two different ^3He inserts:

1) An Oxford Instruments HelioxVL insert in which the sample is mounted at the end of a cold finger in vacuum. The ^3He liquid is pumped by an internal activated charcoal sorption pump in order to reach base temperatures of $T \approx 250 \text{ mK}$ [106].

2) Custom-built ^3He insert in which the sample is immersed in the liquid with a base temperature of 350 mK.

Both inserts have a rotation mechanism useful for in-situ tilted B -field experiments.

$^3\text{He}/^4\text{He}$ dilution refrigerator

In general two types of dilution refrigerator inserts were employed:

1) An Oxford KelvinoxTLM dilution refrigerator with two different inserts: a standard Oxford insert with base temperatures of ≈ 20 mK ([106]) and a low temperature insert designed by J. Göres [54] capable of reaching temperatures below 15 mK used for the activation measurements of section 4.7 .

2) An NMR dilution refrigerator constructed for a 15/17 T, 52 mm bore superconducting magnet with a homogeneity of ≈ 5 ppm per cm^3 located at the High Magnetic Field Laboratory in Grenoble (GHMFL) [23]. High stability (≈ 1 ppm) was achieved by using a Bruker 21/120 SC6 power supply. The lowest base temperature reached in the fridge was $T \approx 35$ mK. Most of the NMR results presented in chapter 5 were obtained in this system.

3.2.1 Quasi-DC Transport

Except for the DC-current experiments shown section 4.6.2, we used a standard lock-in technique at low frequencies for the electrical transport measurements. Typical frequency values used were between 7 and 23 Hz. A sinusoidal AC current, ranging from 0.5 nA to 1.4 μA (depending on the Hall bar width), was supplied by a Hewlett Packard 3325B or a Stanford DS345 synthesized function generator connected in series to a 10 M Ω resistor. The longitudinal and Hall voltages were measured simultaneously with two different lock-in devices, EG&G Princeton 5210 and Stanford SR830, linked to digital multimeters (DMM) such as the Keithley 2000. A standard four point configuration was used for the longitudinal resistance measurements by having different voltage probe contacts than the source and drain [see Fig. 3.1(c)]. All of the instruments were separated from ground with the use of isolating transformers and optocouplers. This enabled us to have a well-defined ground at the 2DES usually from a single device. The gate voltages were applied by a D/A converter.

3.2.2 NMR

In order to measure the electron spin polarization of a single QW in the FQHE regime (see section 5.2), several experimental requirements had to be fulfilled. It was necessary to simultaneously conduct electrical transport and NMR measurements at $^3\text{He}/^4\text{He}$ dilution refrigerator temperatures in homogeneous ($< 10^5$ ppm) and high (up to 18 T) magnetic fields. Therefore, we opted for carrying out part of our experiments at the NMR facility of the GHMFL.

The scheme presented in Fig. 3.3 depicts the sample preparation needed for the experiments. In general, the structured sample is bonded to a chip carrier (1) and then inserted into a copper

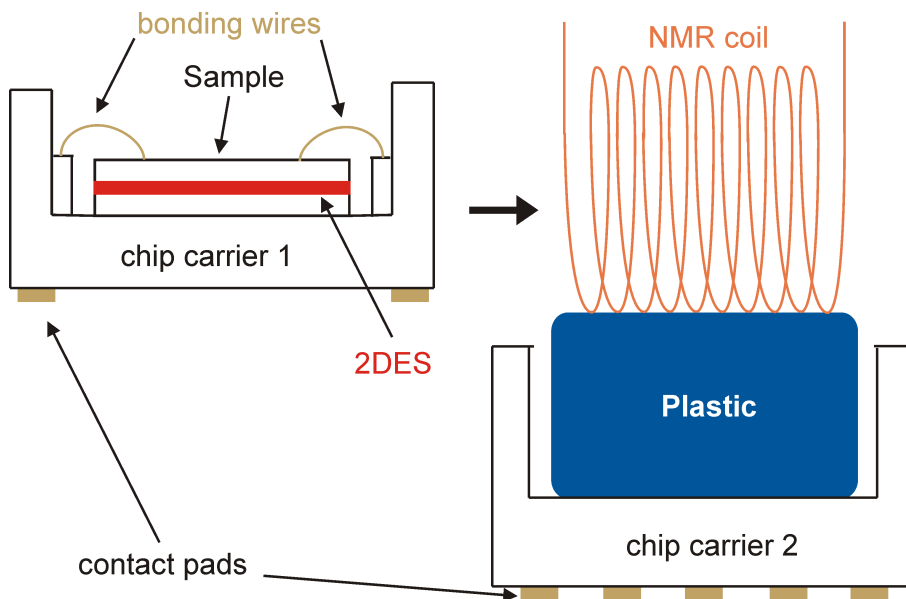


Figure 3.3: Schematical drawing of the sample preparation. The sample is firstly bonded into chip carrier 1 and then inserted into an NMR coil which is glued to chip carrier 2.

NMR coil which is glued to another chip carrier (2). Special care is taken to arrange the bond wires parallel to the RF magnetic field lines. Both chip carriers are then connected together and chip carrier 2 is plugged into the sample holder. A photograph of the sample is shown in Fig. 3.4. The bonded sample, the two chip carriers and the copper NMR coil (9 wounds) are clearly seen. This setup enabled us to increase the RF magnetic field homogeneity across the sample in comparison to a single turn NMR coil. RF field uniformity was particularly beneficial in obtaining a reference signal from the substrate nuclei by means of pulsed NMR experiments (see section 5.1). Additionally, heating effects were reduced by immersing the sample into the mixture and keeping the amplitude of the RF signal below -16 dBm. The cooling power of the fridge is $\approx 120 \mu\text{W}$ at $T = 100$ mK. Furthermore, a plastic mixing chamber was used to avoid eddy currents while sweeping the magnetic field or RF irradiation. By comparing transport measurements without an RF-signal and with an on-resonance signal, we could establish an increase in temperature of only 10 mK.

In order for the system to effectively absorb the RF field produced by the NMR coil and to detect the NMR signal originating from the substrate nuclei, it is important that the coil resonates at the Larmor frequency, ω_L , of the nuclei investigated. Usually a coil is formed from capacitive and inductive elements and its resonant frequency is given by $\omega_R = 1/\sqrt{L_i C}$,

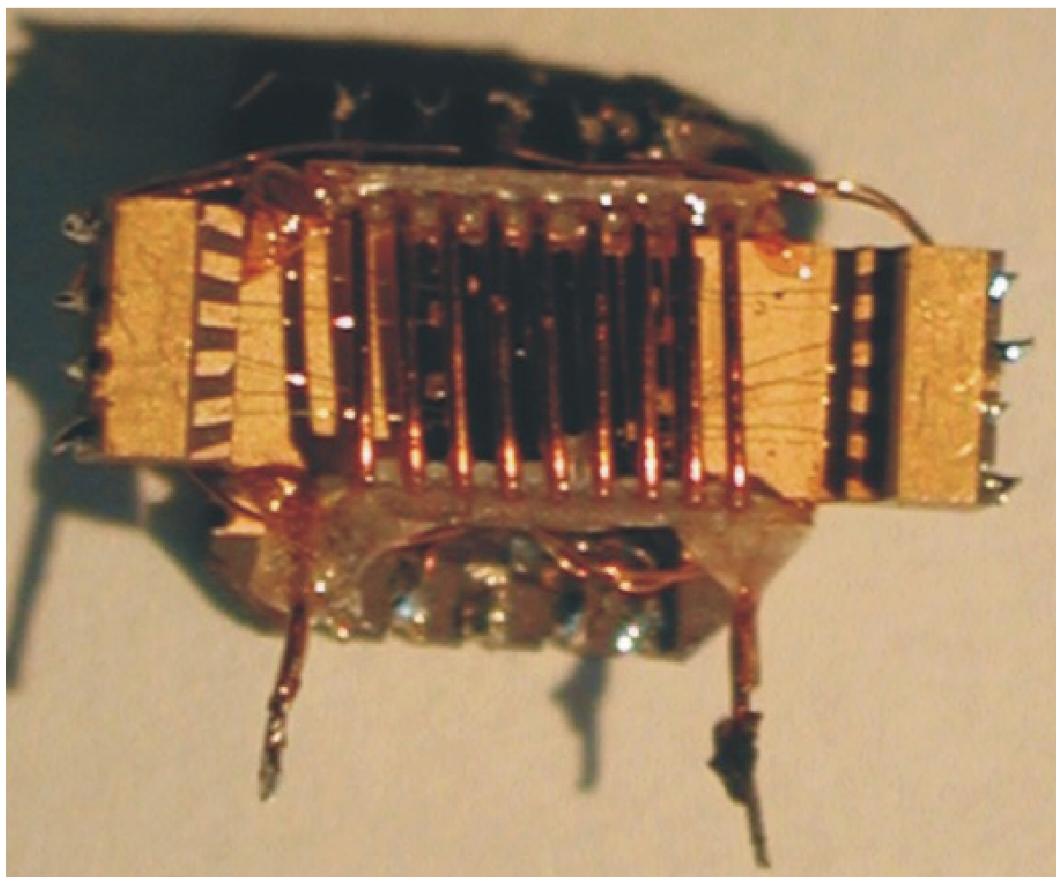


Figure 3.4: Photograph of the NMR coil wound around the bonded sample. By using this setup, a homogeneous RF magnetic field was accomplished across the sample.

where L_i is the inductance and C the capacitance of the LC circuit. In addition to frequency tuning, losses of the RF-power going into and out of the circuit can be reduced by matching the impedance of the LC circuit to the typical 50Ω input and output impedance value of the RF components and transmission lines.

However, for a simpler use with the dilution refrigerator, we employed the so-called *top-tuning* technique in which all variable components are located outside the cryostat. The circuit used in our experiments is shown in Fig. 3.5. It consists of one variable capacitor (between $C = 5$ and 600 pF) for impedance matching and variable length of the transmission line (blue, dotted line) for frequency tuning. Since the line is part of the circuit, this technique presents some loss of the signal to noise ratio. Nevertheless, it proved to be sufficient and more adequate due to its simplicity for our experiments in which tuning was mainly necessary for the pulsed, but not for the RDNMR experiments. We were able to detect the NMR signal from the substrate nuclei even with a small rf power (< -16 dBm).

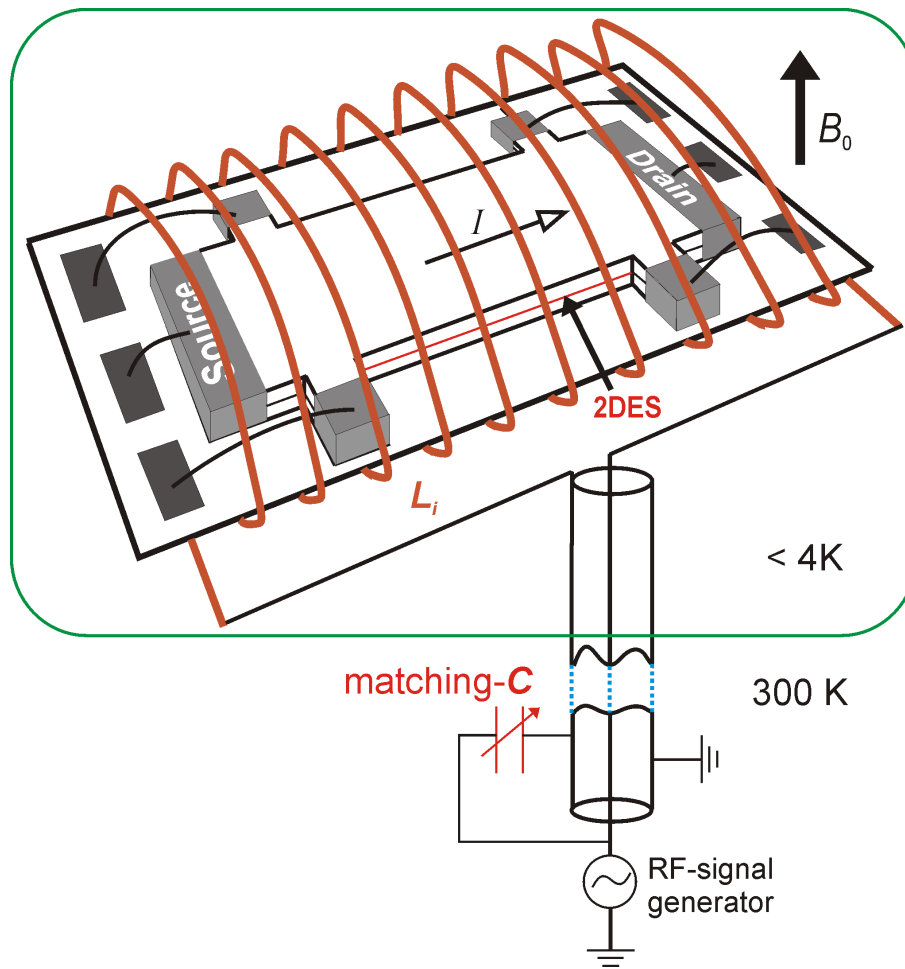


Figure 3.5: An NMR coil wound around the contacted Hall bar structure was tuned to the Larmor resonance frequency of the nuclei investigated. In the *top-tuning* technique, shown in the drawing, a variable capacitor located outside the cryostat is used to match the impedance to 50Ω . The frequency is tuned by varying the length of the transmission line. By using this setup, we were able to conduct NMR and transport experiments simultaneously.

In the figure, we also show a top view of the Hall bar structured 2DES bonded to the chip carrier and wound by a copper NMR coil. The coil was directly attached to low-loss coaxial cables. Semi-rigid copper coaxes were used from 300 K to 4 K, and cryogenic, silver-plated, copper-beryllium coaxes ($R_{DC} < 50 \Omega/\text{m}$) from the 4 K plate to the mixing chamber for a better thermalization. In the continuous wave (CW) NMR experiments (see chapter 5), the RF signal was supplied by a Hewlett-Packard 8657A signal generator while the pulsed signal was provided from a custom-built spectrometer. This setup was necessary for some of the measurements presented in chapter 5.

Chapter 4

Transport Studies of the $\nu = 2/3$ Spin Phase Transition

This chapter deals with transport studies of spin phase transitions in the FQHE. Transitions between ground states of different polarization are observed at filling factors $\nu = 2/3, 3/5$ and $4/7$ ($\nu_{CF} = 2, 3$ and 4 , respectively). In particular, we focus on $\nu = 2/3$ which shows a transition from an unpolarized ($\mathcal{P} = 0$) to a fully polarized ($\mathcal{P} = 1$) state as schematically drawn in Fig. 4.1.

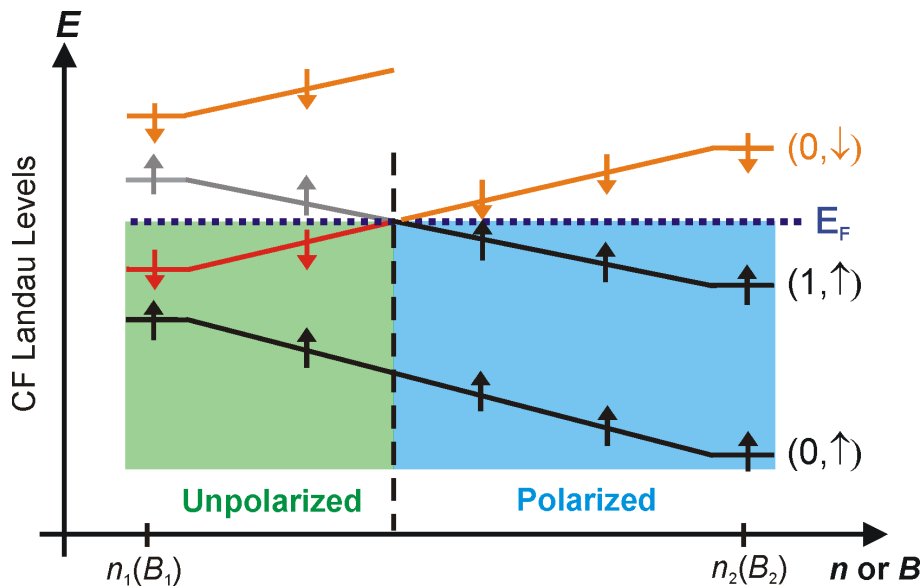


Figure 4.1: CF Landau levels: The spin unpolarized-polarized transition at $\nu = 2/3$ is studied in this chapter by means of transport experiments.

In transport, the phase transition is observed by a resistance peak in the longitudinal resistivity at the $\nu = 2/3$ minimum. At small currents, a small longitudinal resistance (SLR) peak

appears in the ρ_{xx} minimum while at high currents a huge longitudinal resistance (HLR) is measured. This situation is depicted in Fig. 4.2. In (a), the magnetic field was swept and plotted vs

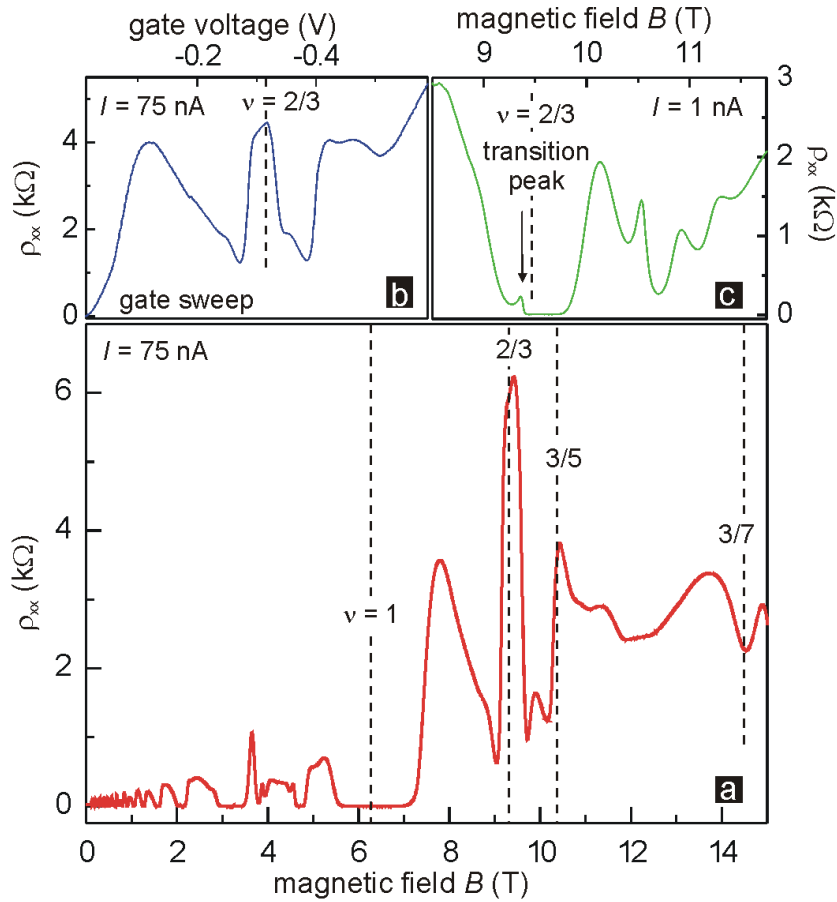


Figure 4.2: (a) Plot of the longitudinal resistivity vs B -field for a sample from wafer 020502.1 at a density of $n = 1.55 \times 10^{11} \text{cm}^{-2}$. The B -field was swept slowly ($dB/dt = 0.02 \text{ T/min}$) at the fixed gate voltage $V_g = -0.3 \text{ V}$. (b) The gate voltage was swept at constant B -field ($B = 9.25 \text{ T}$) and $I = 75 \text{ nA}$. (c) A B -field sweep is shown at low currents ($I = 1 \text{ nA}$). The measurements were performed in a $^3\text{He}/^4\text{He}$ dilution refrigerator at $T = 50 \text{ mK}$.

ρ_{xx} by applying a large current ($I = 75 \text{ nA}$). A large peak is observed at filling factor $\nu = 2/3$. In Fig. (b), the gate voltage is swept at constant B -field ($B = 9.25 \text{ T}$) and plotted vs ρ_{xx} at the same current value. The HLR is also present in this plot. At low currents on the other hand ($I = 1 \text{ nA}$), the transition peak is characterized by a small peak in ρ_{xx} as seen in the B -field sweep shown in Fig. (c). One objective of this chapter is to establish the connection between the spin phase transition and the huge longitudinal resistance (HLR) anomaly peak. Therefore, it is important to firstly present the similarities and differences between the low current (or SLR)

and high current (or HLR) regime. The two experimental techniques employed to measure the transition, i.e. tilted B -field and density tuning experiments, are shown and discussed in section 4.2. By combining both of these methods, we could map a phase diagram of the $\nu = 2/3$ ground state as a function of Coulomb and Zeeman energies. The hysteresis and time dependence are analyzed in section 4.3 and the Hall resistance is shortly discussed in section 4.4. After explaining the model used to describe the phenomenon responsible for the existence of a peak at the transition in section 4.5, in which both current regimes are discussed, we analyze its dependence on various parameters such as time, frequency and current. Finally, temperature measurements were necessary in order to understand the mechanism leading to dissipation in more detail.

4.1 The Low and High Current Regimes

In transport experiments, the spin unpolarized-polarized phase transition at filling factor $\nu = 2/3$ is characterized by a peak in the longitudinal resistivity, where usually vanishing resistance is measured instead. This has been reported in numerous works [5, 8, 55, 58, 59, 72]. At the transition, density fluctuations caused by disorder are believed to induce domains of different spin configuration. Scattering along domain walls across the sample is a possible cause for extra dissipation observed in transport [5, 57, 58, 59, 107]. Surprisingly, the phase transition peak changes drastically if the current is increased: the small resistance peak (SLR) in ρ_{xx} develops into a large and broad peak as illustrated in Fig. 4.3. From this graph, we can infer that the huge longitudinal resistance peak, known as the HLR, always occurs at the spin phase transition. Four traces of the longitudinal resistivity vs filling factor ν in the vicinity of $2/3$ are shown. In all four curves, the magnetic field is kept constant ($B = 8.1$ T) while the gate voltage is swept. A sample of type B, presented in Fig. 3.1, was used in these experiments. The black solid line represents a sweep from higher to lower filling factor for a current of $I = 1$ nA (small current regime). The small peak indicates the unpolarized-polarized spin phase transition. The dashed line shows the gate sweep in the opposite direction. A very small hysteresis is seen in the curve. The red curves show the HLR peak at a current of $I = 40$ nA in both sweep directions in the large current regime. A pronounced hysteresis as well as saturation times of the order of minutes characterize this large peak. It was thus necessary both to increase the current and reduce the gate voltage sweep rate from 0.6 V/s, used for the small current peak, to 0.0024 V/s in order to observe the high current peak.

More precisely, it is the current density rather than the current which is the critical parameter to induce the HLR. Figure 4.4 shows the large current resistance peak measured by using a 1.5 mm wide hall bar. The HLR transition peak fully develops in such a structure only after increasing the current to 1.4 μ A.

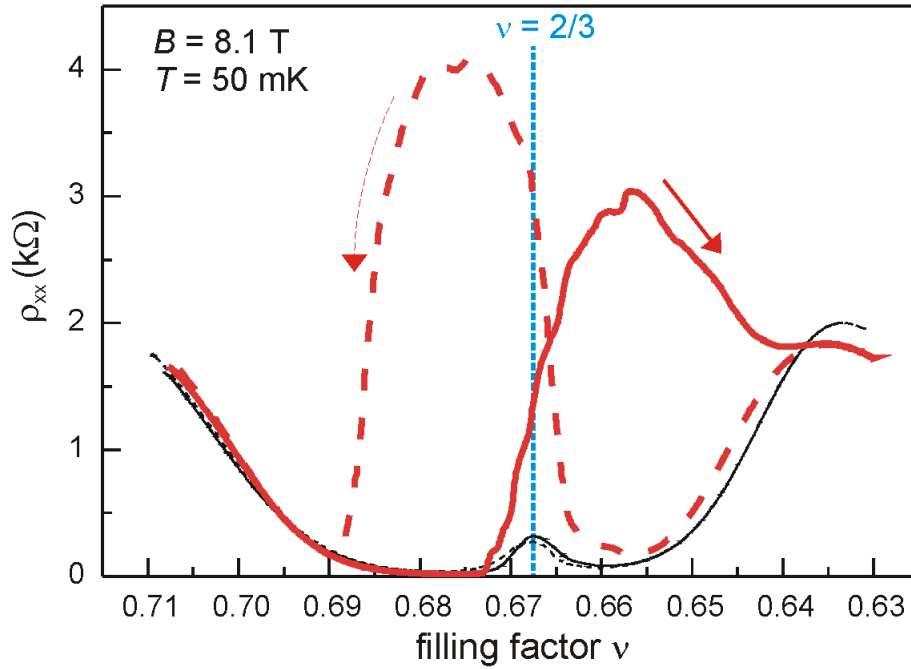


Figure 4.3: Plot of ρ_{xx} vs filling factor around $\nu = 2/3$. The black traces represent a sweep from higher to lower filling factor (solid line) and from lower to higher filling factor (dashed line) at $I = 1$ nA while the red traces show a plot at $I = 40$ nA (Sample from wafer 020502.1).

Since the existing ground state depends primarily on the interplay between the Zeeman and Coulomb energies, the transition will occur at a certain critical ratio η_c of these energies. In the next section, we present two experimental techniques in which the ratio η was varied in the vicinity of the $2/3$ phase transition.

4.2 Phase Diagram of the $\nu = 2/3$ Ground State

Experimentally, it is possible to choose the polarization of the ground state at filling factor $\nu = 2/3$ by tuning the ratio $\eta = E_Z/E_C$. At low B -fields, i.e. low values of η , the unpolarized ground state is favored, while at high B -fields (high η values) the polarized state is present. Since the Zeeman energy $E_Z \propto B$ and the Coulomb energy $E_C \propto \sqrt{B}$, a transition between states can be obtained either by tilting the direction of the sample with respect to the magnetic field or by sweeping the electron density.

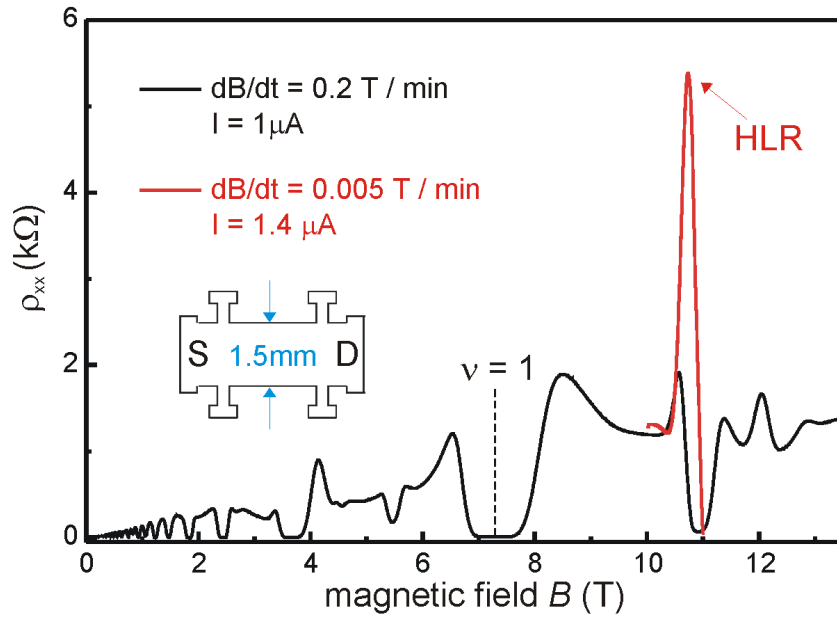


Figure 4.4: A 1.5 mm Hall bar was used to measure the longitudinal resistivity as a function of magnetic field B . The graph shows a fast sweep of the B -field at $I = 1 \mu\text{A}$ (black curve) and a slow sweep at $I = 1.4 \mu\text{A}$ (red curve). The current density is the critical parameter to induce the HLR (Sample from 052098.4).

4.2.1 Tilted B -field Experiments

If a sample at fixed density is tilted relative to the direction of the magnetic field B_z by an angle θ , a filling factor occurs at the same B_{\perp} value at all angles, but at higher B_{tot} since this value increases according to $B_{\text{tot}} = B_{\perp} / \cos \theta$. As a result, the Zeeman energy rises as a function of the tilt-angle ($E_z \propto B_{\text{tot}}$) while the Coulomb energy remains constant ($E_C \propto \sqrt{B_{\perp}}$). Therefore by tilting the sample it is possible to tune the ground state polarization of the filling factor $\nu = 2/3$ due to its dependence on $\eta = E_z / E_C$. Figures 4.5(a) and (b) show plots of ρ_{xx} vs B_{\perp} zoomed on the $\nu = 2/3$ minimum. These measurements were performed at $T = 250$ mK and a density of $n = 1.2 \times 10^{11} \text{cm}^{-2}$ using a 14 nm QW of type A [Fig. 3.1(a)]. The four curves, which are offset vertically for clarity, represent four different tilt-angles θ . A schematic diagram of the tilted sample is depicted at the top of Fig. 4.5(a). Plots (a) and (b) were measured in the low and high current regimes, respectively. In Fig. (a), the vanishing ρ_{xx} at $\theta = 0^\circ$ is caused by the gapped $\nu = 2/3$ ground state, which in this case is unpolarized ($\eta < \eta_c$). As the sample is tilted, B_{tot} increases while B_{\perp} remains constant and a small peak appears in the ρ_{xx} minimum (see blue arrows) revealing the unpolarized-polarized transition at η_c . This situation occurs when both states are brought close to degeneracy. The ρ_{xx} minimum reenters at higher tilt-angles ($\eta > \eta_c$) indicating a polarized ground state.

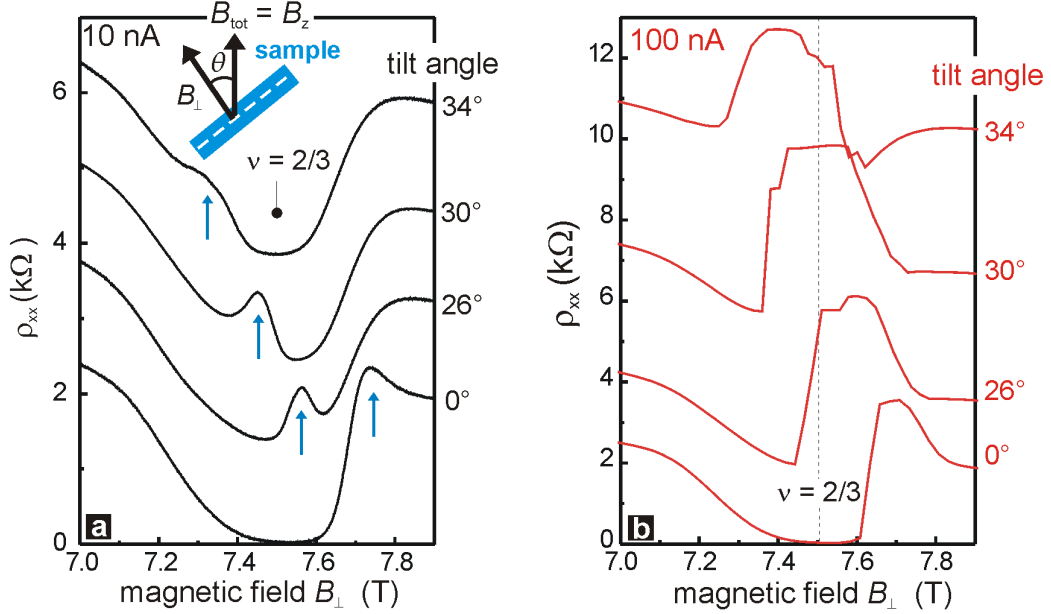


Figure 4.5: The Zeeman to Coulomb ratio η can be tuned by means of tilted B -field experiments. The SLR at low currents [Fig. (a)] and the HLR at high currents [Fig. (b)] are observed at different angles (Sample from 052098.2).

In the high current regime (100 nA), the transition peak develops into the huge longitudinal resistance (HLR) peak [Fig. 4.5(b)]. The HLR appears at the same η_c value as the small current peak, but extends over the whole range of the $2/3$ minimum. The height and width of the HLR are caused by a current-induced nuclear spin polarization (see section 4.5). These measurements were done using a so-called settling-time technique. This consists of sweeping the B -field in steps of 50 mT at a rate of 0.5 T/min and then waiting a certain amount of time (settling time) until the resistance value reaches equilibrium, i.e. until $\Delta\rho_{xx}/\Delta t < 1 \text{ } \Omega/5 \text{ s}$. Subsequently, the magnetic field can be swept to the next value. The value of $\Delta\rho_{xx}/\Delta t$ is determined by the noise in the system. This technique was used due to the long equilibration times involved in the HLR regime. The time dependence, hysteresis, as well as a model for HLR are presented in section 4.3 and 4.5.

A complete range of angles is shown in Figs. 4.6(a) and (b). Here, the two color plots show ρ_{xx} versus B_{perp} and $\cos(\Theta)$ ¹. For these measurements, a symmetrically doped 15 nm QW was used ($\mu \approx 1.3 \cdot 10^6 \text{ cm}^2/\text{Vs}$ at $n = 1.6 \times 10^{11} \text{ cm}^{-2}$). Details of this structure are published

¹In the experiments shown in Figs. 4.6 and 4.8, Θ is defined as the angle between the direction parallel to the 2DES and B_z .

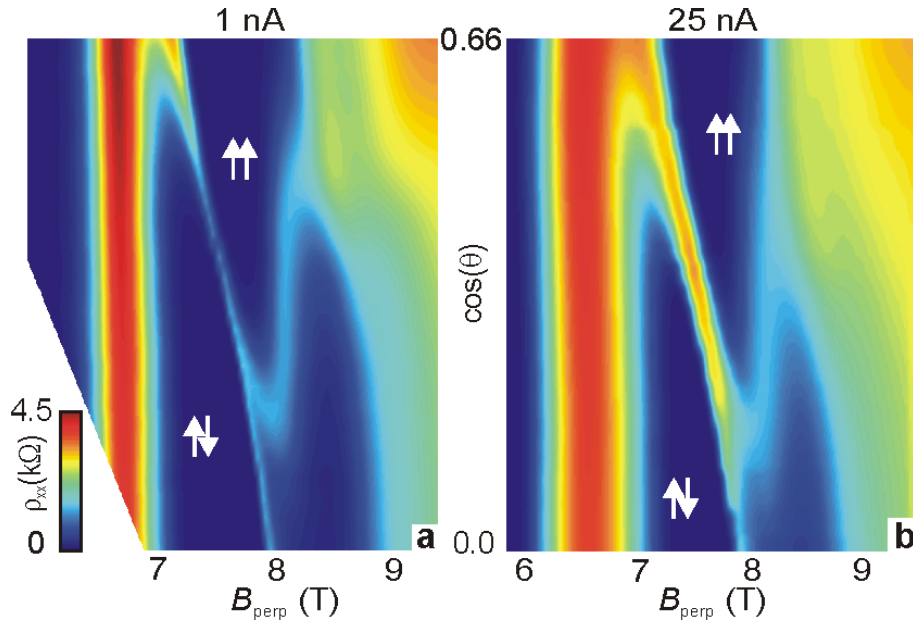


Figure 4.6: Color plot of the $\nu = 2/3$ transition at low currents (a) and high currents (b) derived from tilted B -field experiments. Figure adapted from Reference [59] (Sample from 120700.1).

elsewhere [7, 59]. The curves used for the color plot 4.6(a) were measured in the low current regime (1 nA). The thin blue line around $B_{\perp} = 7.5$ T is caused by the small longitudinal resistance peak signaling the spin unpolarized-polarized phase transition. In the high current regime [Fig. 4.6(b)], i.e. at $I = 25$ nA, the SLR peak develops into the HLR, depicted as a thick, red line.

4.2.2 Density Sweep

The spin polarization of the ground state can also be chosen by tuning the density n of the sample. In Figs. 4.7(a) and (b), ρ_{xx} is plotted versus ν at four different values of the magnetic field ($B = 7.8, 8.0, 8.5$ and 9.0 T). The figures are again vertically offset for clarity. These curves were measured by sweeping the gate voltage in order to go from a high to a low filling factor at $I = 5$ nA [Fig. (a)] and $I = 40$ nA [Fig. (b)], respectively. In this case, $\eta \propto \frac{B}{\sqrt{\nu}}$ at constant magnetic field B and a transition occurs from an unpolarized to a polarized state. The small peak reveals this transition in the low current regime while the large HLR peak in the high current regime. The green curve in Fig. (b) taken at $B = 11$ T does not show any peak since the system is fully polarized.

A complete set of densities is presented in the color plots of Figs. 4.8(a) and (b). In these experiments, the same sample was used as the one described in Fig. 4.6. Similar to the tilted field

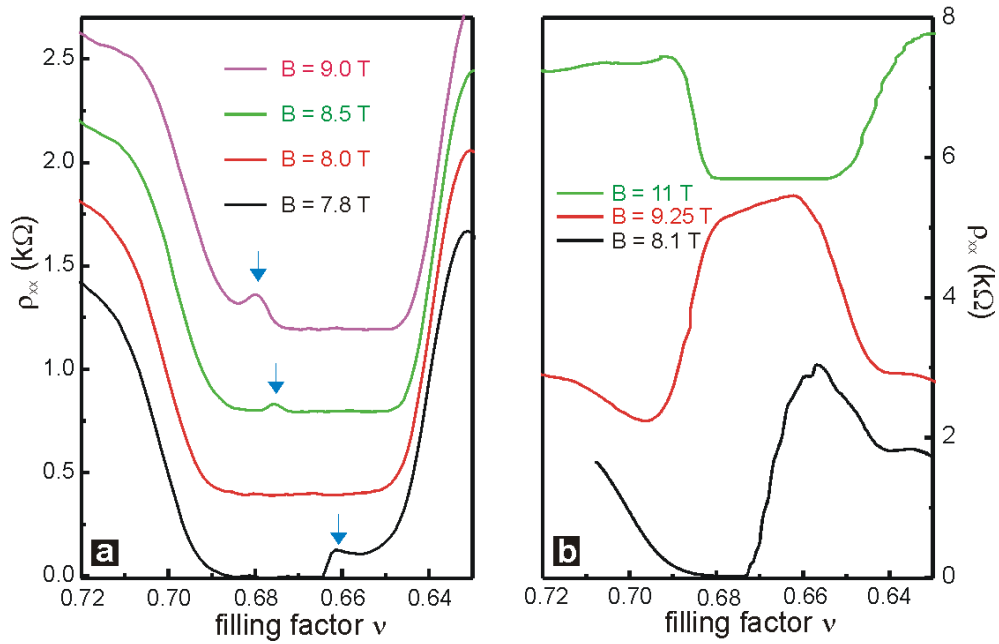


Figure 4.7: ρ_{xx} vs ν at different B -fields. The SLR (a) and HLR (b) can also be induced by varying η via density sweeps (Sample from 020502.1).

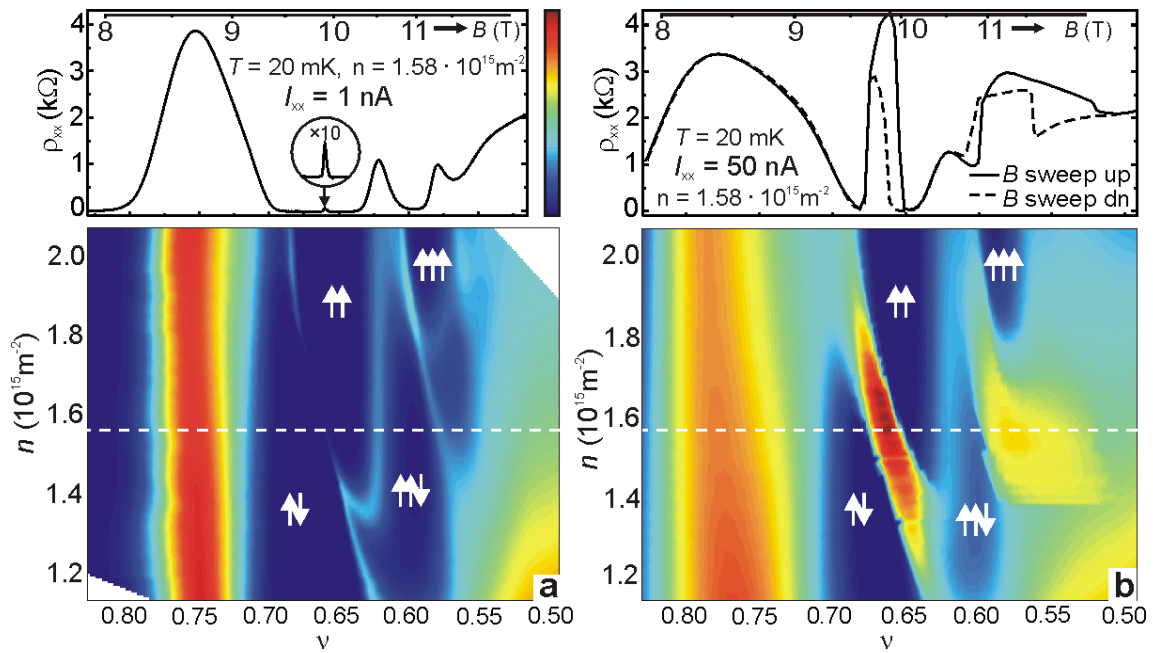


Figure 4.8: Color plot of density sweeps in the low current (a) and high current (b) transition regimes. Figure adapted from Reference [59] (Sample from 120700.1).

experiments, the thin blue line indicates the transition at low currents (1 nA) which develops into the HLR at high currents (40 nA). The two top insets depict ρ_{xx} versus ν and B for the density value marked by a white dashed line in the color plots. These curves were measured by sweeping the magnetic field around filling factor $\nu = 2/3$ at the desired density value, which was varied by means of a gate. In the high current regime a hysteresis is observed between the magnetic field up and down sweeps. This will be discussed in the next section.

4.2.3 Phase Diagram

A phase diagram of the $\nu = 2/3$ ground state is presented in Fig. 4.9. This plot has been extracted from tilted magnetic field sweeps at various densities ranging between $n = 0.74 \times 10^{11} \text{ cm}^{-2}$ and $n = 1.77 \times 10^{11} \text{ cm}^{-2}$ using a sample of type A [3.1(a)]. The data points indicate the B_{tot} vs B_{\perp} values at which a ρ_{xx} transition peak is measured in the HLR regime². The color scale on the top left indicates the value of the measured difference in longitudinal resistance (ΔR_{xx}) between a fast and a slow sweep. From B_{\perp} and B_{tot} , we calculated E_{Zeeman} (right axis) and E_{Coulomb} (top axis), respectively. The red curves (solid and dashed) show the lines of constant $\eta = E_Z/E_C = 0.019 \pm 0.002$ which were calculated to fit the experimental results. These values were obtained after using equations (2.20) and (2.21), in which the Zeeman and Coulomb energy were corrected for a 15 nm QW³. This regime depicts the boundary between the unpolarized and the fully polarized $\nu = 2/3$ ground state polarization for a 15 nm QW. For comparison, we have plotted the same η regime for a wide 30 nm QW, drawn as a black line, and observe that in such a well the transition would be expected at a lower magnetic field value⁴. From the diagram we can observe that most of the data points lie inside the calculated phase transition boundary. Therefore, the assertion that η is the critical parameter which determines the ground state is in good agreement with the experimental results. Nevertheless, a better description of the transition is given by using the CF model [7, 82, 83]. The orange dashed line seen in Fig. 4.9 was calculated by equating the Zeeman energy and the CF cyclotron energy as presented in equation 2.23. The CF polarization mass at a density of $n_0 = 1.18 \times 10^{11} \text{ cm}^{-2}$ (at which the HLR was strongest) was determined to be $m_{\text{CF}}^{\text{p}}(n_0) = 1.65 m_e$. The transition peak develops at $\nu = 2/3$ at this density only after tilting the sample by $\theta = 28^\circ$ ($B_{\perp} = 7.4$ T and

²There is no data available below $B_{\perp} = 4.6$ T since the lowest achievable density in this sample is $n = 0.74 \times 10^{11} \text{ cm}^{-2}$. Moreover, due to the hysteresis and width of the HLR peak, B_{tot} and B_{\perp} are average values over the region where the HLR exists.

³For the FWHM value, we used $\lambda = 8.9$ acquired from calculations presented in Reference [79].

⁴For a 30 nm QW, we used $\lambda = 16.2 \cdot 10^{-9}$ m. We have opted for comparing with a 30 nm QW instead of a heterostructure since in the latter case the FWHM depends on density and on sample specific parameters such as doping concentration [79].

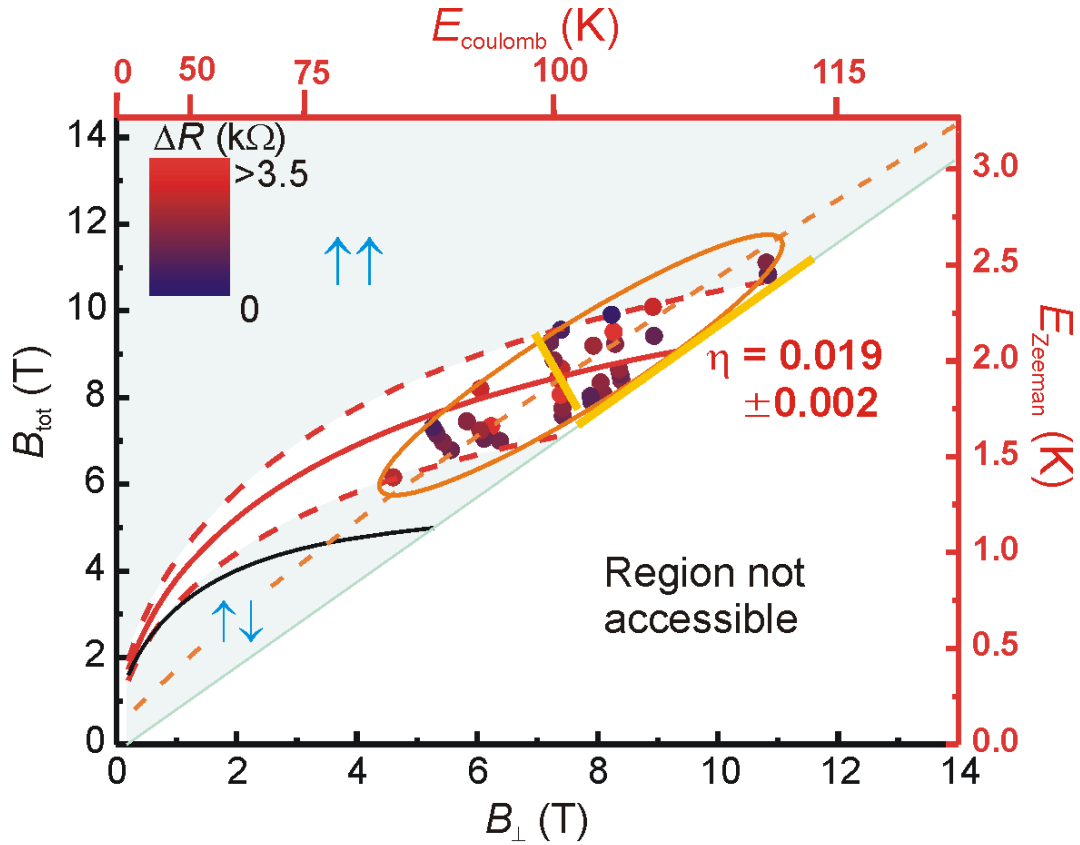


Figure 4.9: Phase diagram of the $\nu = 2/3$ ground state. The dots indicate the B_{tot} vs B_{\perp} value where the maximum of the transition occurs. From the data points, a critical value $\nu = 0.019 \pm 0.002$ for the $\downarrow\uparrow - \uparrow\uparrow$ transition can be determined (red lines). The black line shows the same $\eta_c = 0.019$ expected for a 35 nm QW. The yellow lines were extracted from Figs. 4.6 and 4.8. The dashed, orange line was calculated via equation 2.23 using the CF model. (Sample from 052098.2)

$B_{\text{tot}} = 8.45$ T). The mass was obtained from the following expression:

$$m_{\text{CF}}^{\text{p}} = \frac{\hbar e |B_{\text{eff}}| m_e}{g^* \mu_{\text{B}} B_{\text{tot}} m_e} = \frac{2 |B_{\text{eff}}| m_e}{g^* B_{\text{tot}}}, \quad (4.1)$$

where $|B_{\text{eff}}| = |B_{\perp}(\nu) - B_{\perp}(\nu = 1/2)|$. In our calculations, we have again corrected the g -factor with equation 2.20. From eq. 2.25, we know that $m_{\text{CF}}^{\text{p}}/m_e \propto \sqrt{B}$, which using $m_{\text{CF}}^{\text{p}}(n_0)$ yields $m_{\text{CF}}^{\text{p}}/m_e = 0.53 B_{\text{tot}}/\sqrt{B_{\perp}}$. Here, we have rewritten \sqrt{B} into $B_{\text{tot}}/\sqrt{B_{\perp}}$ since we are conducting tilted B -field experiments. The prefactor is slightly smaller, but in fair agreement, with the theoretical expected value 0.6 [80] (see also section 2.4.3). All of the measured data points can be enclosed in an ellipse and from the diagram we can realize that the calculated dashed line passes through the center of the ellipse. The CF picture offers an excellent descrip-

tion of spin phase transitions in the FQHE regime as it has also been corroborated by the NMR experiments presented in the next chapter.

4.3 Hysteresis and Time Dependence of the Transition

The transition resistances show clear differences in its hysteretic and time evolution behavior depending on the current. In this section, we study these differences in both the low and high current regimes.

Low Current Regime

Figures 4.10(a) and (b) show two gate sweeps around filling factor $\nu = 2/3$. In the solid

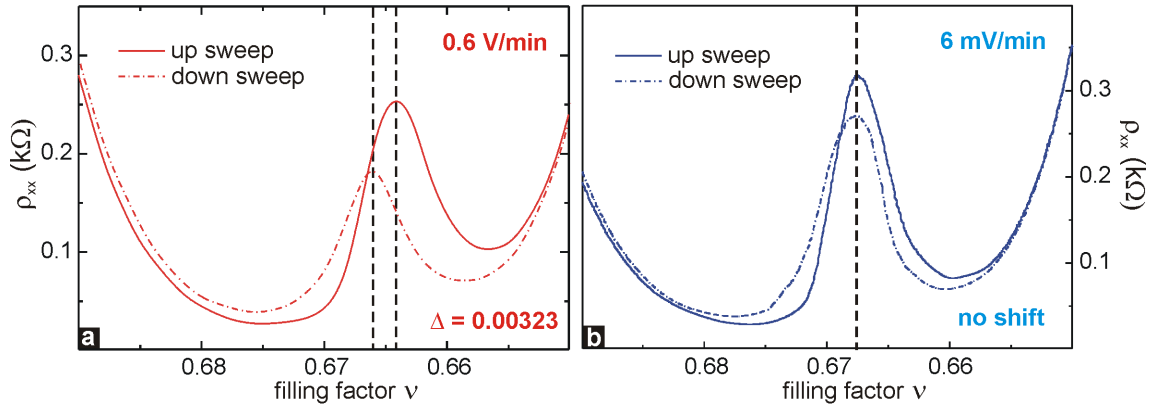


Figure 4.10: Density sweeps in the SLR regime. The small hysteresis observed for a gate voltage sweep rate of $dV/dt = 0.6\text{V}/\text{min}$ (a) vanishes after reducing dV/dt to $6\text{ mV}/\text{min}$ (b). The amplitude of the peak only increases very slightly after reducing the sweep rate (Sample from 020502.1).

curve, the gate voltage was swept in order to go from a high to a low filling factor and in the dashed line it was swept in the opposite direction. The gate voltage sweep was reduced from $dV/dt = 0.6\text{ V}/\text{min}$ in Fig. 4.10(a) to $dV/dt = 6\text{ mV}/\text{min}$ in Fig. 4.10(b). The small hysteresis observed in the first figure ($\Delta\nu = 0.00323$) vanishes after the sweep rate is reduced⁵. Furthermore the amplitude of the peak increases very slightly after reducing the sweep rate. These measurements were done at $T \approx 70\text{ mK}$. In reference [7] it was shown that a hysteresis is observed in the low current regime only below this temperature. The hysteresis mentioned

⁵At the edges of the peak, the hysteresis is only due to the integration time of the Lock-ins and not from the physical system.

there is not caused by the nuclear system but rather by the exchange energy of the electrons (see Fig. 4.25).

High Current Regime

The situation changes drastically at high currents. A long time dependence and a remarkable hysteresis are present in this regime even above $T = 70$ mK. In order to study this situation more carefully, we have used the time settling technique described in section 4.5 for both upward and downward sweeps of the magnetic field. The three plots presented in Fig. 4.11 (a-c) show ρ_{xx} vs B -field at $\theta = 15^\circ$, 30° and 34° , respectively, at $T = 250$ mK. The black curves

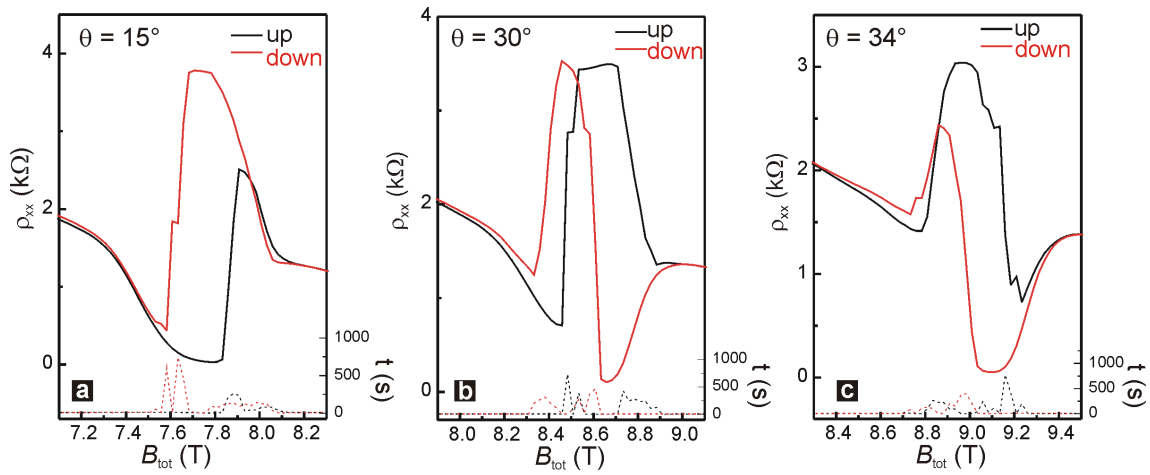


Figure 4.11: The HLR shows a pronounced hysteresis between the up sweeps (black) and down sweeps (red). The hysteresis reverses as the angle is increased in tilted B -field experiments (a \rightarrow c). The samples are from 052098.2.

were measured by sweeping the field upwards, while the red curves were taken during downward sweeps. In all three plots, we can observe a pronounced hysteresis which is notoriously different for the three angles. At $\theta = 15^\circ$, the up-sweep HLR curve is narrower than the down-sweep curve. At $\theta = 30^\circ$, both the up and down sweep HLR curves are very similar and at $\theta = 34^\circ$ the up-sweep curve is broader than the down sweep curve. The different hysteresis can be explained as follows: As seen in the black curves of Figs. 4.11 (a-c), the HLR starts to develop at a certain value of the magnetic field. This value corresponds to the critical Zeeman to Coulomb energy ratio (η_c) of the spin phase transition. The HLR then extends over the whole width of the $2/3$ minimum and finally disappears at the high B -field side of the minimum. The peak which develops during the down sweep of the B -field (red curves) also sets in at η_c and also extends over the complete width of the $2/3$ minimum vanishing at the low B -field side of the minimum. The hysteresis reverses because η_c shifts to a lower value of B_\perp as the angle

is increased. That is, at $\theta = 15^\circ$ the HLR develops on the high B -field side of the $\nu = 2/3$ minimum, at $\theta = 30^\circ$ it initiates near the center of the minimum and at $\theta = 34^\circ$ it begins on the low B -field side. Hence, the HLR switches from being narrow to being broad with increasing tilt angle for the upward sweeps and viceversa for the downward sweeps⁶. The possible reason for the peak broadness will be discussed in the next section (Model of the HLR). The dotted lines seen at the bottom of Figs. (a-c) show the settling time needed for the curves to reach equilibrium. The long time constants of the order minutes or even hours are due to the involvement of the nuclear system in the HLR effect.

The time dependence can also be studied by recording the time it takes the HLR to relax back after switching off the current, see Figs. 4.12(a) and (b). The experiments were performed

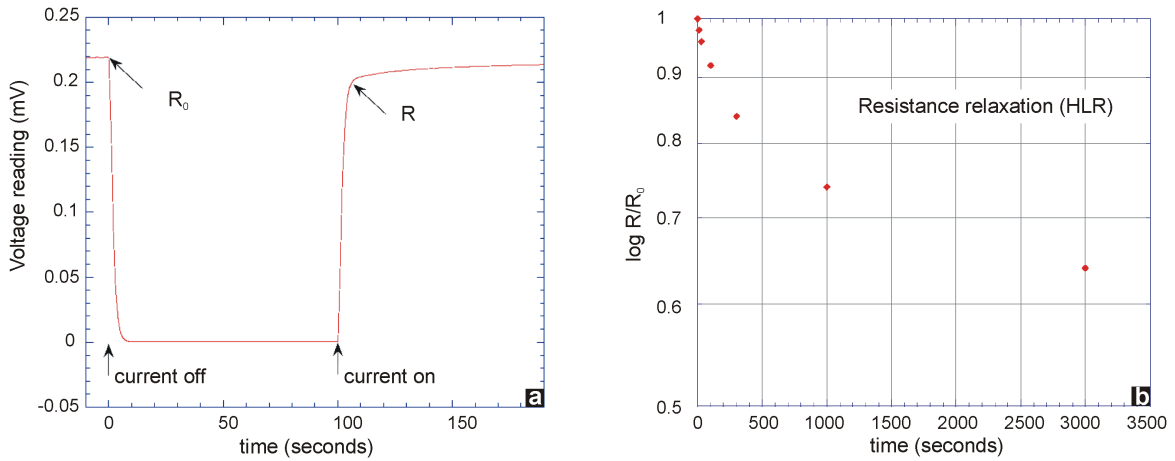


Figure 4.12: The time evolution of the HLR is studied by switching the current off and on as plotted in Fig. 4.10(a). The recovery of the HLR is plotted as $\ln R/R_0$ vs t in Fig. 4.10(b).

as follows: The magnetic field was swept upwards until η_c was reached. It was then stopped and a certain amount of time was allowed for the resistance R_{xx} to increase to its equilibrium value R_0 . Afterwards, the current was switched off and then turned back on after an arbitrary waiting time t . The new resistance value was recorded immediately after switching the current back on. Fig. 4.12(a) shows an example of such a measurement done at $T \approx 40$ mK in a 17 nm QW of a type A sample. Here, the current was switched off for approximately 100 s. The HLR resistance was about 90% of its original value after switching on the current again. This

⁶In reference [59], a different behavior of the HLR hysteresis was observed. During a down sweep, the resistance did not extend to the end of the minimum, but only until the beginning of the transition. We do not know the exact cause for these differences, but it might be that there is a stronger coupling between the electrons and nuclei in our system.

procedure was repeated for various waiting times and the logarithm of the ratio R/R_0 is plotted versus time in Fig. 4.12(b). The resistance relaxation times obtained range from ≈ 10 minutes to even hours. These are typical nuclear relaxation times in GaAs. The experiments shown here are thus essential in determining the order of magnitude of the relaxation times present in the system. However, they do not render the exact T_1 spin-lattice relaxation time since its value depends on other factors such as current and the magnetic field in which the experiments were carried out.

4.4 Hall Resistance

So far we have only considered the longitudinal resistance while studying the spin phase transition at $\nu = 2/3$. In this section, we also investigate the Hall resistance R_{xy} during the phase transition in both the low and high current regimes presented in Figs. 4.13 (a) and (b), respectively. In the left figure, R_{xy} has been measured at $I = 1$ nA and $T < 20$ mK by sweeping the

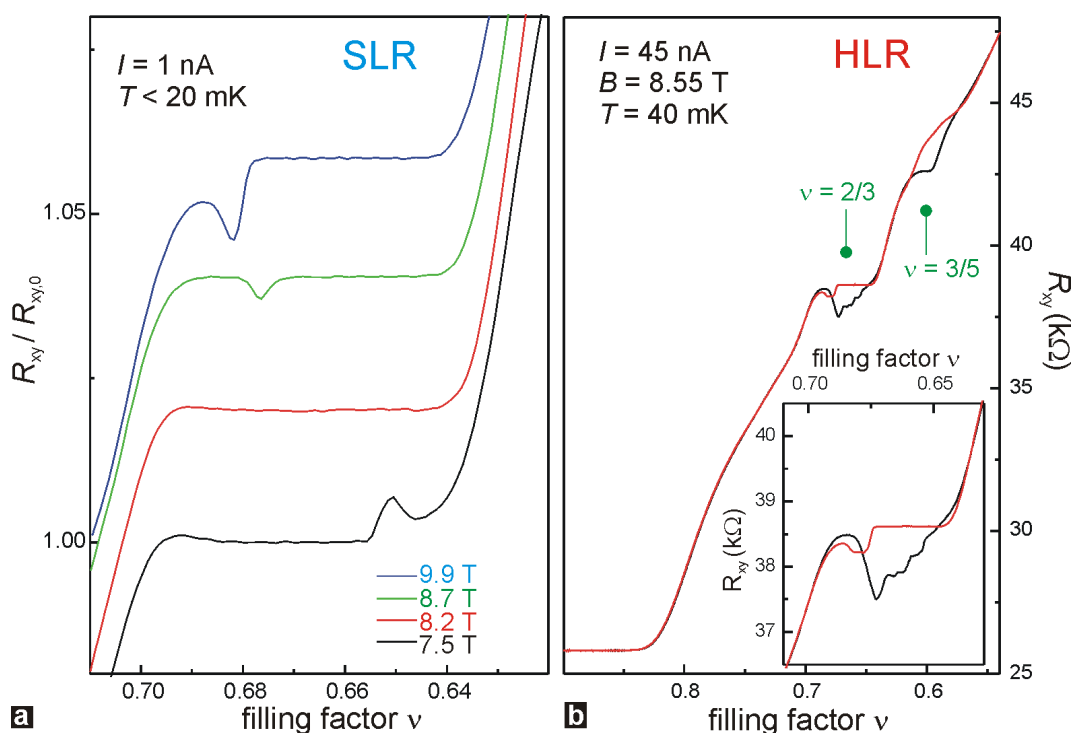


Figure 4.13: Plots of the Hall resistance vs filling factor in the low current (a) and high current (b) regimes. The deviation from exact quantization indicates dissipative transport which occurs during spin phase transitions (Sample from 020502.1).

gate voltage at four different values of the magnetic field. For this purpose, we employed samples of type B [Fig. 3.1(b)]. The curves have been normalized to $3R_K/2$ and offset vertically

for clarity. The small deviation from exact quantization indicates dissipative transport at the $\nu = 2/3$ ground state. This occurs simultaneously with the small peak in ρ_{xx} which characterizes the spin phase transition. What is interesting here is the sign in the change of the resistance. On the high filling factor side, that is at $\nu > 2/3$, R_{xy} decreases (blue and green curves) while at $\nu < 2/3$ it increases (black curves) and at $\nu = 2/3$ it vanishes (red curves). This might imply that the Hall resistance tries to reach its classical value as it departs from its quantization.

In the HLR regime at $\nu = 2/3$, R_{xy} deviates from exact quantization more strongly than in the low current regime. Also, a marked hysteresis is present as seen in Fig. 4.13(b) in which the black curve is a gate sweep from high to low filling factor and the red curve in the opposite direction. A similar effect is seen at the $\nu = 3/5$ spin transition. The inset zooms in at filling factor $2/3$. The Hall resistance in the high current regime has also been presented in reference [108]. The information obtained from the experiments shown in sections 4.1-4.4, as well as work performed on quantum Hall ferromagnets (QHF) has led us to present a model explaining the dissipation mechanism at the $\nu = 2/3$ transition. This model is discussed in the following section.

4.5 Model of the Transition

Resistance spikes have been observed at the transition between two crossing Landau levels in several systems. In the IQHE, resistance peaks were measured in InGaAs/InP heterostructures [109], SiGe [110], AlAs [111, 112], wide GaAs QWs and in bilayer systems [79, 113], while in the FQHE they were measured in single heterostructures and QW at several filling factors such as $\nu = 2/3, 2/5, 3/5, 4/7$ etc. [5, 55, 56, 58, 59, 75]. In transport, hysteretic transport of the resistance spikes have been addressed in terms of QH ferromagnetism of pseudospin states [58, 114]. In general, only the two crossing levels, which can differ in Landau level orbital or spin indices, subband, or valleys, are taken into consideration. The two levels can then be assigned pseudospin up and pseudospin down and the electron-electron interactions lead to magnetic anisotropy. The system can show either easy-plane pseudospin anisotropy (the pseudospin orientation magnetization is preferred in a plane of orientations) and resemble an XY ferromagnet, easy-axis anisotropy (the pseudospin orientation can only take on discrete values along a certain axis) such as an Ising ferromagnet or isotropic ferromagnet (all orientations are possible). QHFs can be classified as follows: If the two pseudospin LLs only differ in the real spin component, that is same subband and same LL orbital quantum number N , the ferromagnetic state is isotropic. The $\nu = 1$ single layer QHF presented in section 2.4.4 is an example of such a system. If the pseudospin states of the crossing LLs differ in real spin and orbital quantum number, but are from same subbands, the ferromagnet is characterized by easy-axis anisotropy. Pseudospins from different subbands can have any of the three pseu-

dospin anisotropies. A summary of possible QHFs is schematically displayed in figure 7 of reference [115].

In this work, we are interested in the single layer $\nu = 2/3$ ($\nu_{\text{CF}} = 2$) transition, where the two levels involved are the spin up state of the lowest CF-LL and the spin down of the second CF-LL. Therefore, easy-axis anisotropy characteristics have been identified in transport where a finite peak in the ρ_{xx} resistance and hysteresis occur. In the following, we will present a model of transport at this transition by considering some the concepts of easy-axis QHFs in combination with the results described in the first sections of this chapter: Usually, if the Fermi energy lies in the localized states between LLs no backscattering is possible. The system is incompressible in the bulk and the longitudinal resistivity goes to zero while the Hall resistivity is quantized. At the crossing of two LLs, the gap should disappear, the Fermi energy would then be in the extended states and ρ_{xx} should be finite across the minimum. However, in experiment, we do not observe a complete vanishing of the ρ_{xx} minimum, but rather a sharp peak which does not cover the whole extent of the minimum⁷. This unexpected behavior occurs because since the intra-LL exchange energy is stronger than the inter-LL exchange energy, the system prefers to stay in one of the two possible states (spin up or down) instead of in a linear superposition of the states. Furthermore, the presence of disorder forces the system to break up into domains of different polarizations. Hence, disorder plays a major role since there will be density fluctuations and the parts of the sample with a lower density will be unpolarized while the parts with higher density will be polarized. A schematic diagram of the domains is presented in Fig. 4.14. The dissipation in transport happens due to reflections at the domain walls separating the regions of both polarizations which cause backscattering. At low currents, i.e. in the SLR regime, backscattering of current-carrying quasiparticles reflecting along the domain walls cause a peak in ρ_{xx} . This situation changes if the current is increased. Electrons will acquire enough energy to scatter between the domain walls and as a result spin-flips are necessary. In order to conserve momentum, spin reversal processes can be mediated via spin-orbit coupling, phonon emission or electron-nuclear hyperfine interaction. Experiments have revealed that the latter interaction is dominant in the high current or HLR regime. Electron spin-flips are accompanied by nuclear spin-flop processes which create an enhanced or dynamical nuclear spin polarization (DNP). The DNP will take place underneath the domain walls and it will act back on the electronic system changing its Zeeman energy. This will create an additional disorder of the electronic system and the domain structure will change. Since the resistance increases substantially, it is natural that either the amount of domain walls increases (smaller domains) or the walls become larger and thus the amount of scattering excitations also increases. Flip-flop processes are usually not possible due to the much larger electron spin than nuclear spin splitting. However, at the transition the electronic levels are almost degenerate and the electrons and nuclei can couple.

⁷This situation only applies for the low current regime.

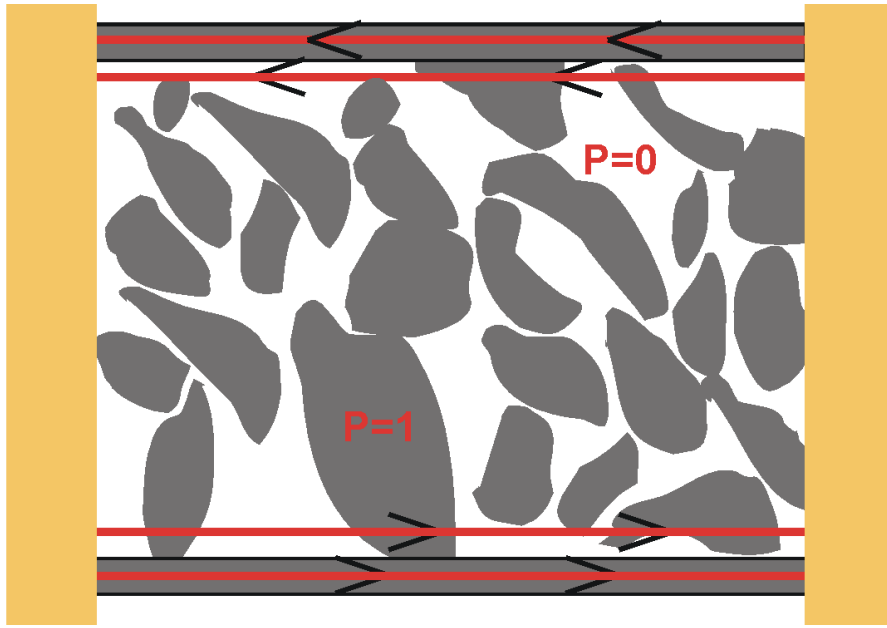


Figure 4.14: At the transition, domains of different spin polarization ($\mathcal{P} = 0$ and $\mathcal{P} = 1$ at $\nu = 2/3$) are believed to form. Dissipation in the longitudinal resistivity is probably due to backscattering of the charge-carrying quasiparticles reflecting at the domain walls.

Another possibility is that not only a single spin flip but rather collective low-energy excitations involving several spins, similar to skyrmions trapped at the domain walls, exist at the transition. This issue is studied in more detail in section 4.7.2.

In addition to the increment in the amplitude of the HLR peak, its width also increases drastically. From Fig. 4.3, we can see that the ρ_{xx} peak extends over the whole range of the $\nu = 2/3$ minimum. The broadening may be caused by a shifting of the peak due to the hyperfine field created by the current-induced dynamically polarized nuclei. Electrons crossing from an unpolarized to a polarized domain flip their spin upward resulting in a downward flop of the nuclear spin. Consequently, the nuclear hyperfine field B_N is negative and the peak shifts towards a higher magnetic field (i.e. lower ν if the B -field is held constant and the density is changed). On the other hand, electrons crossing from a polarized to an unpolarized domain have the opposite effect, B_N is then positive and the peak shifts towards lower magnetic fields (higher ν). The hysteresis of Fig. 4.11 indicates that B_N can be either positive or negative and this is strongly dependent on the sweep direction, that is on the previous history of the system. It still remains unclear why the amplitude of the HLR peak during a B -field down sweep (decreasing ν in a density sweep) is larger than the peak during the B -field up sweep (increasing ν in a density sweep), see Figs. 4.11 (a-c). This is the case for all tilt-angles if we consider the amplitude of the peak to be $\Delta\rho_{xx}$, i.e. the difference in ρ_{xx} before and after the peak has set in. Such a

difference in amplitude between up and down sweeps has also been observed in hysteretic peaks of level crossings in AlAs samples [111, 112]. It has been explained that the magnetization of the electronic system takes on different values on both sides of the transition thereby leading to a different domain structure and resistance values. Furthermore, the screening properties depend on whether the $N = 0$ or $N = 1$ CF-LL is filled [107]. Unfortunately, the exact mechanism which leads to such a huge peak has not been thoroughly understood.

The behavior of the transition peak also depends on other numerous factors which have not been included in this model. For example, ρ_{xx} has a different time evolution depending on whether an AC or DC current is applied to the system. Also, sample specific characteristics such as disorder or strain could alter the absolute value of the resistance⁸. In the rest of the chapter, we will present various experiments which have been useful in understanding the mechanism leading to dissipation. These include current and frequency dependent measurements (AC and DC) as well as the temperature behavior of the resistance near and at the transition. At the end of section 4.7, we will discuss an improvement of the model.

4.6 Time, Frequency and Current Dependence at the Transition

All of the experiments presented so far were conducted using an AC current. In this section, besides studying the AC dependence in more detail, we also compare results between AC, DC and differential resistance (AC + DC) measurements in the SLR and HLR regimes. The samples used for these studies are from wafer 052098.2 [see Fig. 3.1(a)].

4.6.1 AC measurements: Time and Current Dependence

The time dependence of the SLR and HLR peak at several values of an AC current is shown in Fig. 4.15. The three sets of data (blue dots, green squares and red triangles) were obtained by following the three sequences depicted in Fig. 4.15(b)⁹. The blue dots were measured by setting the AC current to a specific value for approximately 10 s and then recording the ρ_{xx} value. The density and tilt-angle were chosen in order to have the HLR and SLR peaks at the same B-field values near the center of the $\nu = 2/3$ minimum. After the 10 s the current was driven back to zero and left at this value for ≈ 5 min. Then, the next current value was set and again ρ_{xx} recorded after 10 s at the new current value. From graph 4.15(a) we can

⁸Samples under strain show a larger HLR peak (approximately $2k\Omega$ larger) than samples which are not subjected to strain [see Fig. 5.19(d)].

⁹These measurements were performed in cooperation with S. Kraus and S. Lok and have also been published in references [7] and [59].

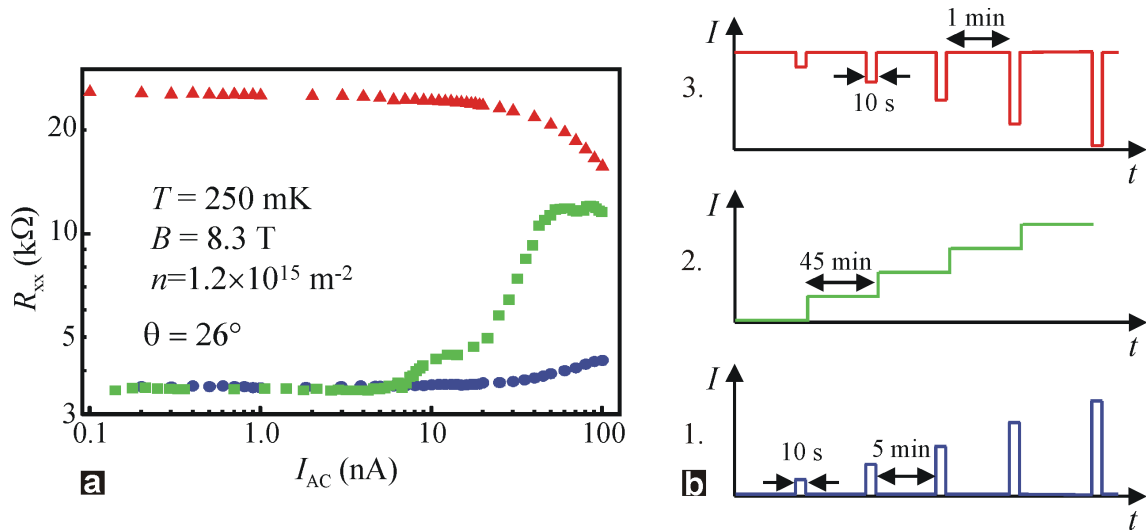


Figure 4.15: (a) Time and AC current dependence measurements at the low current regime (blue), high current regime (red) and intermediate regime (green). (b) I vs t sequence used to determine the data points in Fig. (a). The graphs are also plotted in references [7] and [59].

infer that ρ_{xx} does not change substantially for $I < 20$ nA. For greater values, the resistivity changes because the HLR sets in, even after this short time. Nevertheless, the blue curve proves the linearity of the I-V characteristic in the SLR regime. The second experiment dealt with studying the current threshold necessary for the HLR to develop. It consisted of stepping the current value and recording ρ_{xx} after 45 minutes for each value. The green squares indicate that after ≈ 10 nA the resistance starts increasing and at $I > 20$ nA, it strongly increases until reaching a maximum value at $I > 40$ nA¹⁰. The current dependence of the HLR is clearly established here. In the third sequence of measurements, the I-V characteristic of the HLR was analyzed in order to investigate if the large peak is caused by a non-linear behavior of the system due to the high currents involved. The red triangles were plotted after turning on the current to 100 nA and letting the resistance saturate after 45 minutes. Ten second excursions to various lower current values were undertaken in which ρ_{xx} was recorded. The current was reset to 100 nA for 1 minute after each point. An almost constant resistivity value is observed for $I < 30$ nA. The decrease in ρ_{xx} for higher values of the current is probably due to heating effects. This experiment rules out non-linear effects as the cause for the HLR build up and corroborate that the interplay between the electronic and nuclear system is mostly responsible for the appearance of the large peak.

¹⁰A 80 μm Hall bar was used for these experiments.

4.6.2 DC and Differential Resistance Measurements

The DC current behavior of the transition peak in both current regimes is investigated in this section. The slow B -field sweeps shown in Fig. 4.16(a) in the SLR regime reveal that AC (black curve) and DC (red curve) currents lead to the same resistance values and no hysteresis is observed. While this is true for low currents, the situation drastically changes for high currents.

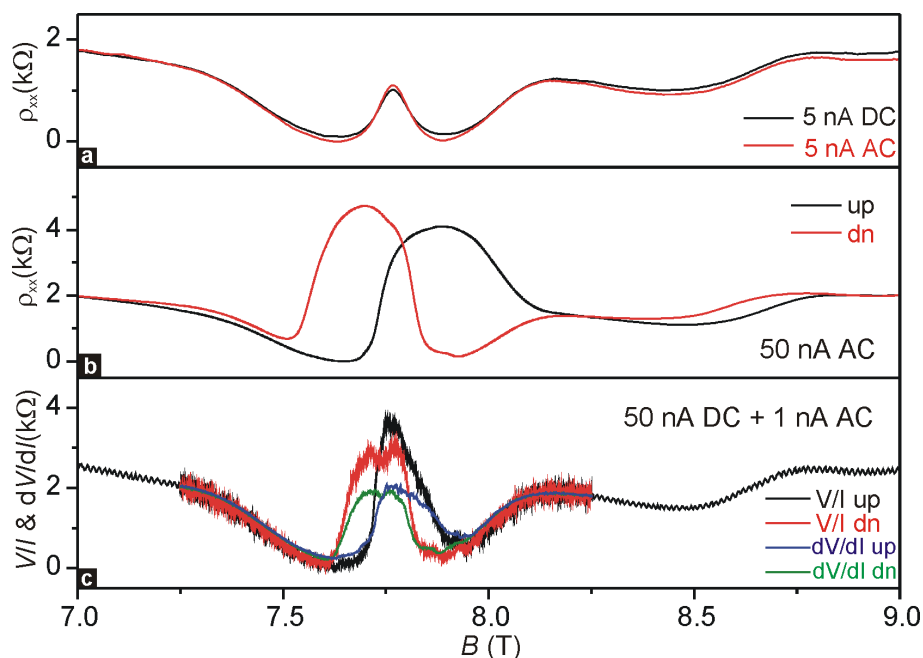


Figure 4.16: (a) AC (red) and DC (black) measurements in the SLR regime. (b) AC measurements for an upward B -field sweep (black) and downward sweep (red). (c) Up (black) and down (red) B -field sweeps for a DC current in the HLR regime and differential resistance measurements (dV/dI) for $I = 50$ nA DC + 1 nA AC currents (up sweep blue and down sweep green).

ρ_{xx} is plotted vs B for an AC current in Fig. 4.16(b) and for a DC current in Fig. 4.16(c), both in the HLR regime. The black curves represent an upward sweep of the B -field and the red curves a downward sweep. Even though a DC current also induces a huge peak in ρ_{xx} if the field is swept slowly, its amplitude and width are slightly smaller than for an AC current. The DC-HLR is also not affected by changing the current direction from a negative DC [Fig. 4.17(a)] to a positive DC [Fig. 4.17(b)], for a wide Hall bar ($400\mu\text{m}$) in which we have used the time settling technique described in section 4.2.1. Again, the bottom curves show the HLR equilibration times. Returning to Figs. 4.16(b) and (c), we can observe that in both AC and DC measurements, a marked hysteresis is present. In Fig. 4.16(c), the differential resistances dV/dI were also plotted for an upward sweep (blue curve) and downward sweep (green curve) of the

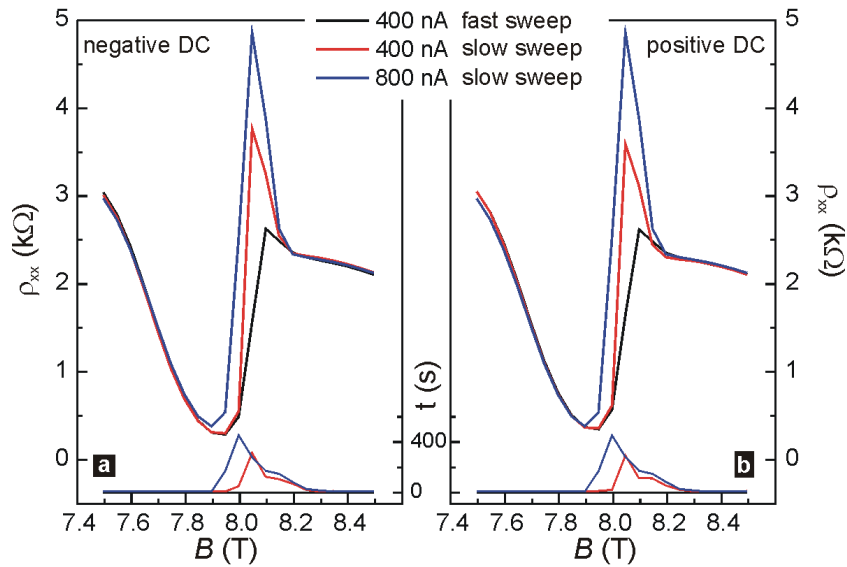


Figure 4.17: Magnetic field sweeps in the HLR regime for a negative (a) and a positive (b) DC current.

B -field. They were measured by superimposing a 1 nA AC current to a 50 nA DC current. It is seen that the main features of the HLR, such as hysteresis, time dependence and huge amplitude, remain the same in the differential resistance.

The time evolution of the HLR peak, on the other hand, shows significant differences depending on the type of current involved. The temporal behavior of the ρ_{xx} resistance is depicted in Fig. 4.18. In this experiment, firstly the B -field was swept to $B = 7.77$ T, in order to be at the center of the SLR peak, without an applied current. After a few seconds the current was increased to $I = 50$ nA and ρ_{xx} was monitored for several hours. The black curve in 4.18(a) shows the time development of the HLR by applying an AC current. The resistance increases within minutes to ≈ 4.9 k Ω and then saturates at this value. The top figure [4.18(b), green curve] actually reveals that the resistance does not completely saturate but slightly rises although very slowly. The jumps in the resistance might be caused by a rearrangement of domains which lead to so-called ‘‘Barkhausen effects’’ reported in Reference [58]. On the other hand, if a DC current is employed [Fig. 4.18(a), red curve] the longitudinal resistance rises faster than the AC resistance, reaches a maximum after some minutes and decreases again to its original value. The decrease is not monotonous but rather shows a logarithmic behavior. We checked that the decrease of ρ_{xx} is not merely due to a slowly shifting of the peak to another magnetic field value by reducing the current and quickly sweeping the B -field over the $\nu = 2/3$ transition. Thus, the unexpected time behavior for a DC current differs considerably from the AC time evolution of the HLR. In order to study this situation more carefully, we have carried out very low frequency measurements (mHz). That is, we induce the HLR with a positive DC

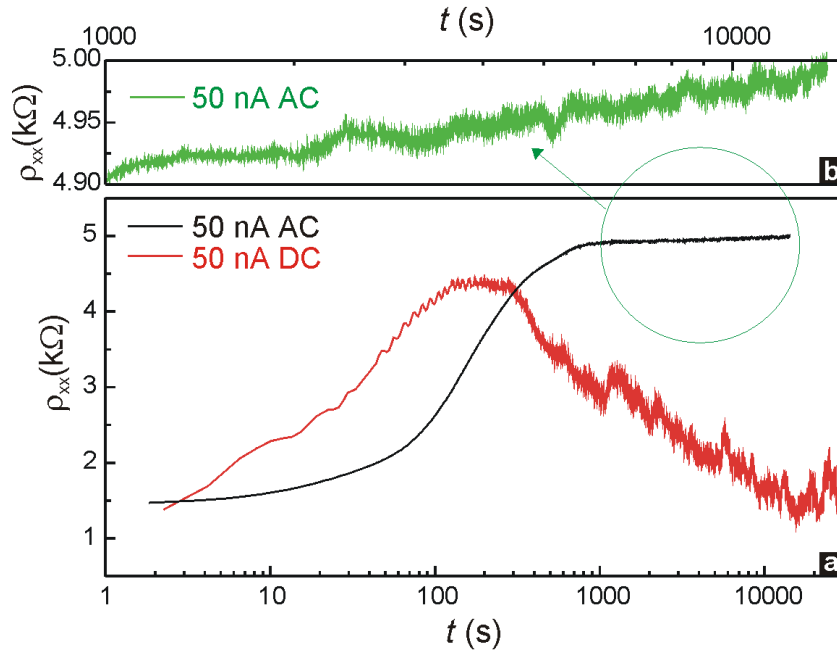


Figure 4.18: (a) Time evolution of the HLR for an AC (black) and DC (red) current. (b) Logarithmic time development of the AC-HLR.

current and monitor the resistance for several hours before reversing the polarity of the DC current. Figure 4.19 illustrates that the DC resistance drops with time, but as soon as the current is reversed, a sharp peak in ρ_{xx} appears. Most likely, the domain structure is influenced by the AC current differently than for the DC current¹¹. Beside the DC and low frequency transport measurements, we also carried out surface acoustic waves (SAW) experiments in order to study the high frequency regime. We present preliminary results, which were obtained in cooperation with the University of Nottingham, in Appendix A of this work.

4.6.3 Conclusions

There are two principal results which can be concluded from the experiments of this section. Firstly, non-linear transport can be definitely ruled out at the transition in both the SLR and HLR regimes. The anomalous huge resistance peak is mostly caused by the interaction between electron and nuclear spins. Secondly, whereas the B -field sweeps do not differ considerably between an AC, DC (independent of current direction) or differential resistance current, the time evolution of the HLR peak is strongly dependent on the type of current used. The HLR

¹¹Occasionally, ρ_{xx} suddenly jumps without reversing the polarity. Such a situation can be seen at $t \approx 460$ s. These changes are much slower than the resistance spikes at the polarity reversal points and occur randomly due to the dynamical nature of the domains. Similar jumps have been observed for a constant AC current (not shown).

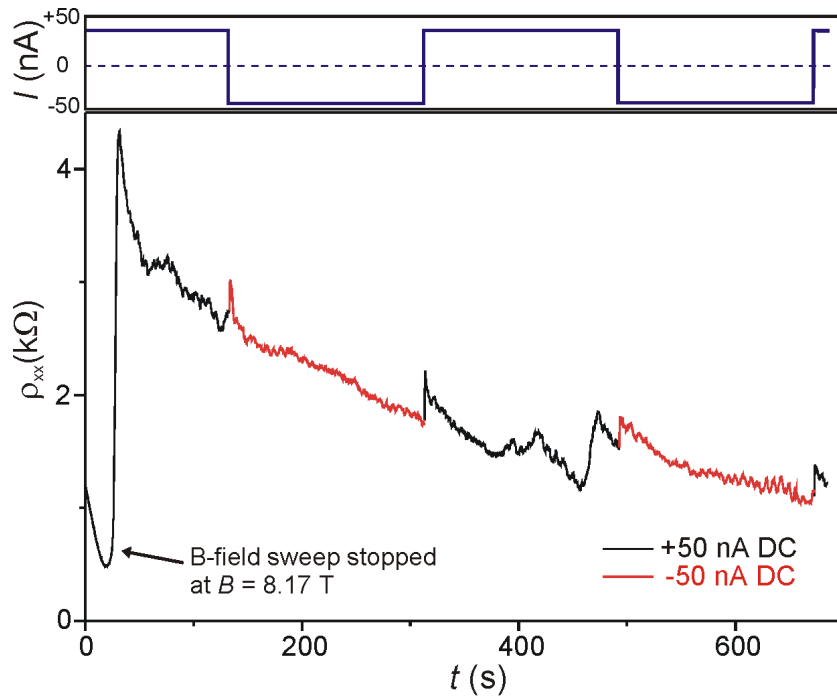


Figure 4.19: The DC polarity has been reversed after several hours and the ρ_{xx} monitored during this time. A spike appears in the resistivity every time the polarity is reversed.

reaches equilibrium and saturates after several minutes if an AC current is applied, while with a DC current it reaches a maximum after several minutes and then collapses again. This situation might indicate that the inhomogeneous hyperfine field B_N created by the polarized nuclei and needed for the existence of the HLR can only be stabilized with a changing current direction. On the other hand, a current flowing in only one direction will create the inhomogeneous B_N , but will eventually disappear with time. Further experiments are needed in order to understand this behavior.

4.7 Activation Measurements

An important issue concerning the $\nu = 2/3$ transition is to understand in more detail the mechanism which leads to dissipation in transport. For this reason, we decided to study the behavior of the peak as a function of temperature. In order to avoid dynamical nuclear spin polarization effects, we restrained our experiments to the SLR regime. (The sample used here is from wafer 020502.1).

4.7.1 Temperature Dependence

The longitudinal resistivity ρ_{xx} is plotted vs magnetic field at the constant filling factor $\nu = 2/3$ for several temperatures ranging from 22 to 810 mK. It is important to note that we have used

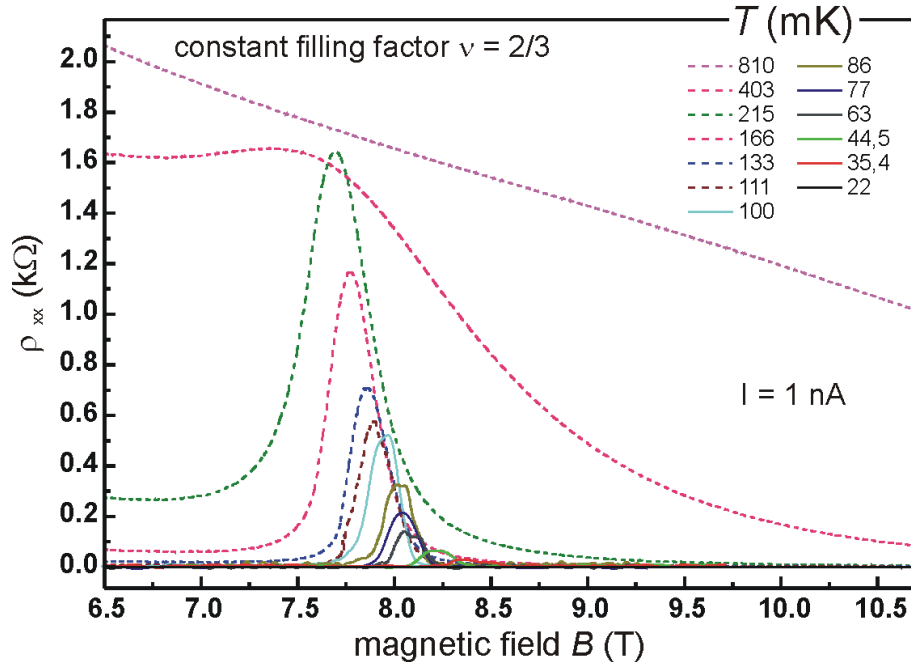


Figure 4.20: Temperature dependent measurements of the SLR transition peak ranging from 22 mK to 810 mK. At the lowest temperatures the peak completely vanishes.

a small AC current ($I = 1$ nA) in order to remain in the SLR regime. Since we are at constant filling, it was necessary to sweep both the magnetic field and the gate voltage simultaneously. Exploiting the linear relation between density and gate voltage, which was determined prior to the experiments, we were able to use equation 2.10 in order to stay at constant $\nu = 2/3$. Therefore each value of the magnetic field is at a different density. The solid curves were obtained by using the low temperature insert described in Reference [54] and the high temperature curves (dashed lines) were measured with a standard insert as described in section 3.2. After each temperature was reached, we waited sufficiently long for the electronic system to be in thermal equilibrium with the external bath.

In Fig. 4.20, we clearly see the transition peak appearing between ≈ 7.5 and 8.4 T. There are two general behaviors which can be observed from the data: A shifting of the peak to lower magnetic fields at increasing temperatures and a decrease of the peak's amplitude at lower temperatures until it completely vanishes at $T \approx 22$ mK. The shifting of the ρ_{xx} peak is merely due to a change in E_Z after the thermal nuclear polarization is randomized at higher temperatures:

$\eta_c \propto \frac{B_{\text{ext}} + B_N}{\sqrt{B_{\text{ext}}}}$ and B_N increases with temperature ($B_N^{\text{thermal}} < 0$) thus B_{ext} decreases.

The temperature dependence of the peak's amplitude hints to activated transport and therefore a remaining gap at the transition. In the next section, we determine the value of the activation gap at and away from the transition at $\nu = 2/3$, followed by an analysis and discussion of the data.

4.7.2 Activation Gap

The resistivity value at the maximum of the transition peak is plotted vs temperature in Fig. 4.21(a). The low temperature points ($T < 100$ mK) are shown in the inset. In Fig. 4.21(b),

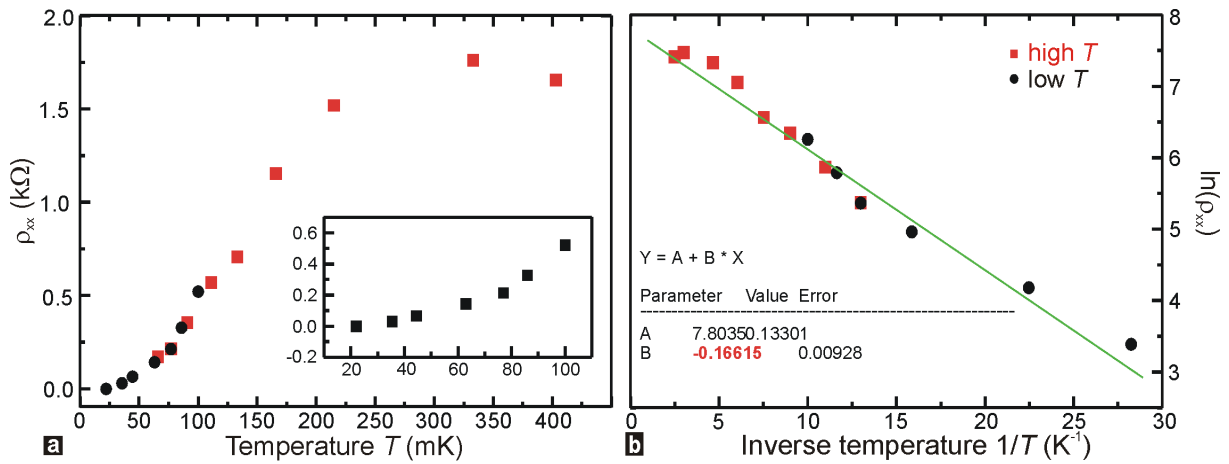


Figure 4.21: (a) Plot of the ρ_{xx} values vs temperature at the maximum of the transition peaks. Inset: Low temperature points ($T < 100$ mK). (b) Arrhenius plot ($\ln \rho_{xx}$ vs $1/T$) of the same data points. The linear fit reveals the smallest activation gap energy value at the transition: $\Delta = 320$ mK.

we plot the same points but as $\ln \rho_{xx} (\propto \frac{\Delta}{2k_B T})$ vs $1/T$ (Arrhenius plot). From the linear fit, we determined the value of the activation gap at the transition to be $\Delta = 320$ mK. We should mention that since the activation gap is dependent on the magnetic field and the peak shifts with increasing temperature due to the nuclear hyperfine field, an inevitable error is introduced in the gap calculation. The error is small however compared to the gap value.

The activation energy was also determined for several magnetic fields between 6.5 T and 9.5 T. In order to calculate Δ for the B -field range where the transition occurs ($7 \text{ T} < B < 9 \text{ T}$), we shifted the curves so that the peak maximum of every curve could be at the same B -field value (Fig. 4.22). Here, ρ_{xx} is plotted vs B^* , where $B^* = 0$ was taken to be at $B = 8 \text{ T}$. In Fig. 4.23 we plot two sets of data: the black dots indicate the gap after shifting the curves while the red squares are the Δ values for curves which have not been shifted and are outside the

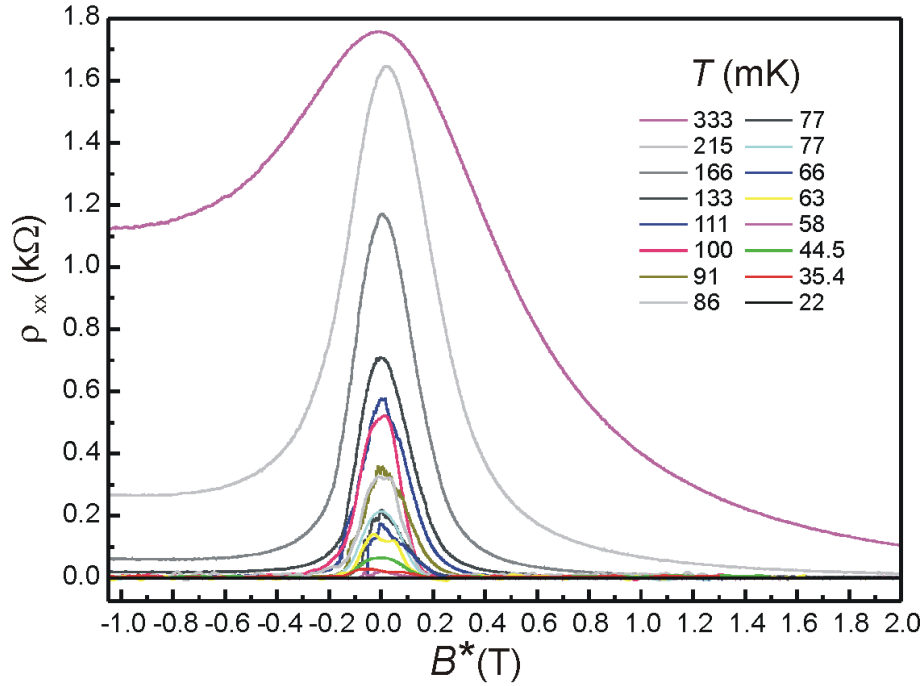


Figure 4.22: The curves have been shifted so that all ρ_{xx} peak maxima appear at $B = 8 \text{ T} \equiv B^* = 0$.

transition region. By adjusting the red data, we conclude that we have committed about a 10% error by shifting the curves. Here, we can clearly observe a strong decrease of the gap at the transition. The smallest gap value is 320 mK as previously shown. In the following we will analyze the origin of the activation gap.

Analysis and Discussion of the Activation Data

At the beginning of the chapter, we schematically showed the spin phase transition as a simple crossing between two CF LLs. This would imply, however, that the energy gap completely vanishes at the transition. This is contrary to the results obtained from the activation measurements presented above. Therefore, the level crossing could be redrawn as shown in Fig. 4.24. The gap Δ is the energy separating the levels at the transition. Nonetheless such an anticrossing behavior is not expected at the $\nu = 2/3$ transition due to the following reasons: An activation gap could exist, for example, if spin-orbit interactions (generally believed to be irrelevant in GaAs [116]) would be important. This would imply, however, a suppression of electron-nuclear spin flip-flop processes since the spin-orbit coupling would provide an alternative path for electron spins to flip while still conserving angular momentum. This situation is not observed in our experiments where nuclear effects play an essential role. Furthermore, spin-orbit interactions would mix the two spin states and domains of two distinct electron spin polarizations would not be able

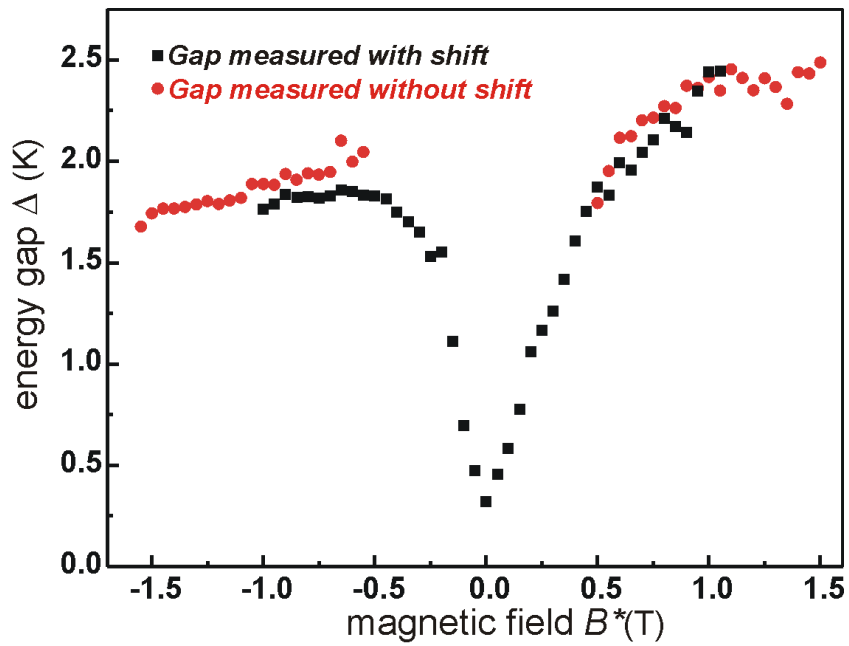


Figure 4.23: Activation energy gap Δ vs B^* at constant filling $\nu = 2/3$. The energy derived from the shifted curves (Fig. 4.22) are shown in black and from non-shifted curves in red (Fig. 4.20).

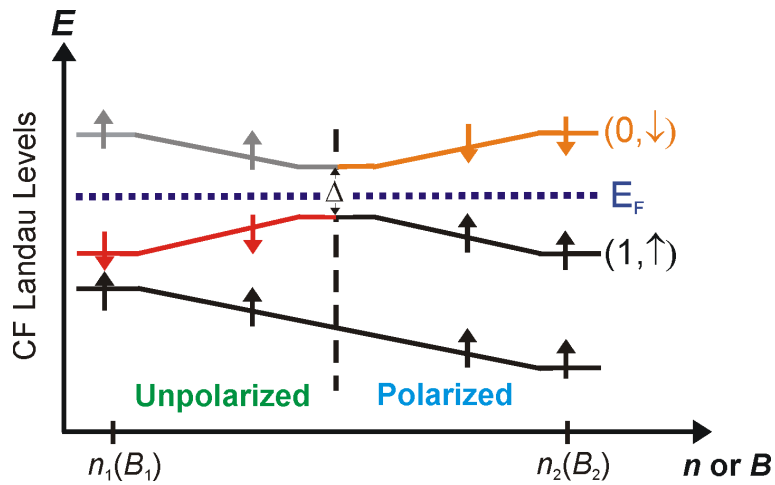


Figure 4.24: Schematic diagram of the crossing between two CF LLs at $\nu_{CF} = 2$ with an activation energy gap Δ remaining.

to form. As we will see in the next chapter, we have measured the existence of unpolarized and polarized domains at the $2/3$ transition with nuclear magnetic resonance. Nevertheless, it is possible that a gap exists if the exchange interaction between the electrons is considered, i.e. if one deviates from the non-interaction picture. In a simplified diagram, we could again draw

the level crossing, but this time the CF levels are shifted by the exchange energy ΔE_{exch} , see Fig. 4.25. The transition does not occur at the level coincidence but slightly away. This could

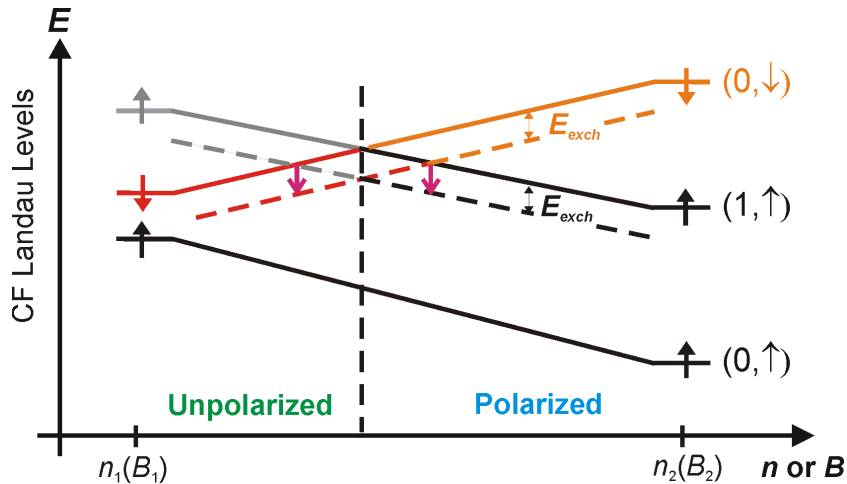


Figure 4.25: Schematic diagram of the CF LL crossing. Here, we have included a shifting of the energy levels due to exchange energy. A gap and hysteresis are measured in experiment.

lead to a measuring of an activation gap and to the hysteresis observed below 70 mK (see reference [7]). The energy gap value measured in our experiments is in good agreement with the one determined by Engel *et al.* [117] at the same transition ($\Delta = 250$ mK). However, recent experiments by Hashimoto *et al.* have shown an activation gap of only $\Delta \approx 93$ mK [118]. It is still unclear whether the gap that we are measuring is only due to exchange interactions.

Another important observation in our measurements is the complete disappearance of the resistance peak in ρ_{xx} at the lowest temperatures of our measurements ($T \approx 22$ mK). Even though this behavior might be caused by the activation gap, it has been predicted that domains could become smaller and more dilute with decreasing temperatures [107]. Below a certain temperature, domain walls no longer overlap therefore suppressing backscattering and, as a result, dissipation.

Finally, from Fig.4.23, we can observe a relatively abrupt decrease of the activation gap at the transition. A similar behavior was reported in the IQHE when two pseudospin levels coincide [119]. In those experiments, conducted by Muraki *et al.*, they mention that at crossings where easy-axis anisotropy is expected, a sharp peak in ρ_{xx} , accompanied by an abrupt decrease in the activation energy gap, should be observed. Moreover, they argue that a reduced gap at the transition might provide an indication for low-lying energy excitations which could resemble a skyrmion trapped at walls between domains of different polarization.

In analogy to this work, we perform a similar analysis of our data. The $\nu = 2/3$ spin phase transition can be modelled as a crossing between the spin-down state of the lowest CF

LL with the spin-up of the second CF LL, so that the pseudospin is just the real spin of the system. Level coincidence occurs when the Zeeman energy equals the CF cyclotron energy, i.e. $E_Z = \hbar\omega_{c,CF}$. Since the former energy is proportional to the B -field while the latter is $\propto \sqrt{B}$, a transition occurs by increasing the magnetic field (or density), see inset of Fig. 4.26. In a first approximation, we can regard the CF cyclotron energy to be equivalent to the electron Coulomb interaction energy E_C . A transition will then occur at $E_Z = \eta_c E_C$, as previously stated at the beginning of the chapter. For the measurements presented here, η_c was calculated to be 0.0188 after including finite-thickness and g -factor corrections. Away from the transition, the coinciding levels split by the difference between E_Z and E_C , i.e. $\Delta E_{\text{split}} = g\mu_B B - \frac{\eta_c e^2}{4\pi\epsilon\epsilon_B^{\text{eff}}}$.

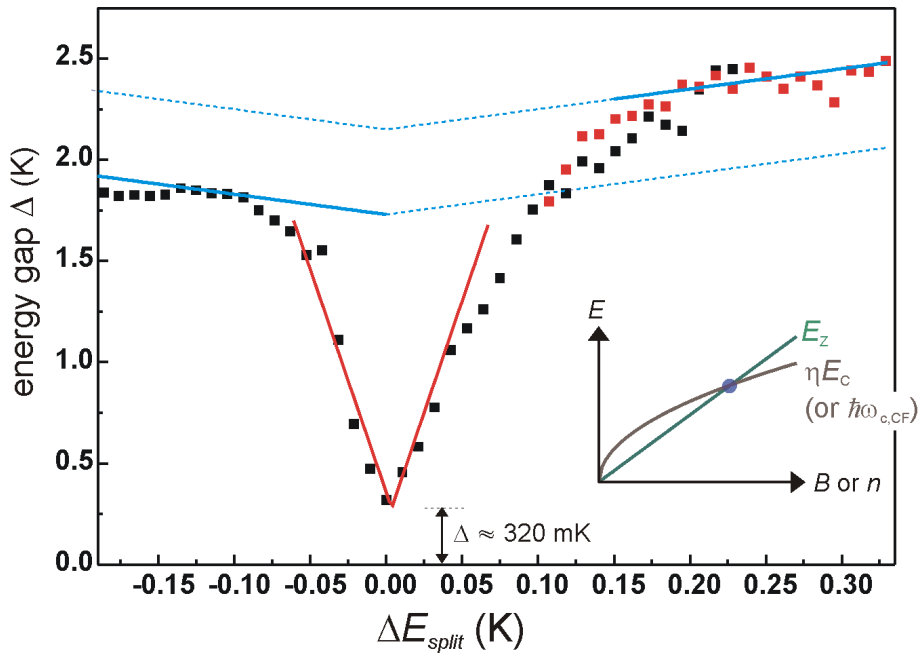


Figure 4.26: Activation energy gap Δ vs ΔE_{split} (energy separation of the crossing levels) at constant filling $\nu = 2/3$. The blue curves indicate the expected slopes for a single spin flip while the red curve presents a larger slope (≈ 22) implying that at the transition several spin flips might be involved.

In Fig. 4.26, we plotted the activation energy gap Δ vs the calculated energy level splitting ΔE_{split} . In such a plot, a slope of one, depicted as a blue line in the figure, indicates the energy required for a single spin flip [120]. This is in good agreement with the points away from the transition. At the transition, on the other hand, the slope becomes much steeper (≈ 22), implying that several spins per unit charge could be involved at the level coincidence.

From these measurements, we might conclude that low-lying energy excitations, resembling skyrmions inside the domain walls, might exist at the $\nu = 2/3$ transition. Building up on the model discussed in section 4.5, we could speculate that these excitations could then travel across

the sample dissipating energy and thus contributing to the resistance peak in ρ_{xx} . The nuclear system would then become polarized due to spin flip-flop processes mediated by these excitations. At low currents, the number of excitations could be small, leading to a small resistance peak and a negligible induced nuclear spin polarization—only the thermal polarization would then play a significant role in this regime. On the other hand, a large current would increase the number of excitations, thus increasing the amount of flip-flop processes and as a consequence also the induced nuclear spin polarization. The HLR could then be caused both by an increased number of excitations and the inhomogeneous magnetic hyperfine field as discussed in section 4.5.

4.7.3 B_N Determination

In the previous section we showed that by raising the temperature, the transition peak shifts to a lower critical field magnetic field B_c . This shift is depicted in Fig. 4.27(a) by plotting B_c of the $\nu = 2/3$ transition peak vs temperature. The nuclear hyperfine field can then be determined

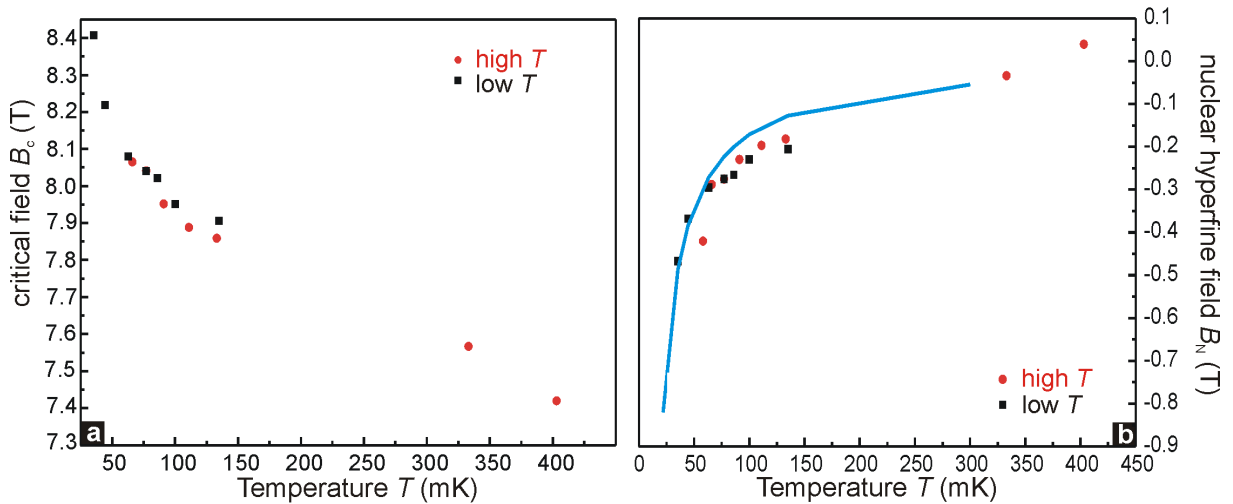


Figure 4.27: (a) Critical magnetic field B_c of the transition vs temperature. (b) The nuclear hyperfine field B_N was determined from B_c and plotted vs T . At the lowest temperatures ($T \approx 22$ mK) the thermal $B_N \approx -0.5$ T.

from B_c by making use of the following relations:

$$\frac{B_c + B_N}{\sqrt{B_c}} \approx \eta_c \text{ and } \lim_{T \rightarrow \infty} B_N = 0. \quad (4.2)$$

The second term indicates the vanishing of the thermal nuclear polarization at high temperatures ($B_N \approx 0$ at $T \geq 600$ mK). Since we know that the critical ratio η_c should be almost the same

at these low temperatures, we can extract B_N by using the formula: $\eta_c(T \rightarrow \infty) = \eta_c$, which yields $B_N = \sqrt{B_c(T \rightarrow \infty)B_c} - B_c$.

We have plotted B_N vs temperature in Fig. 4.27(b). The nuclear hyperfine field at the lowest temperature where a peak still appeared in the resistance ($T = 35$ mK) is approximately -0.5 T. This is a substantial value since it is about 6% of the external magnetic field ($B_{\text{ext}} \approx 8$ T).

In reference [59], S. Kraus measured a nuclear hyperfine field of about -0.45 T at very similar temperatures. S. Kraus also calculated the expected hyperfine field which would exist due solely to the average thermal nuclear spin polarization. In this work, we have used Gibb's distribution, as described in reference [59], to determine the nuclear spin polarization¹². The calculated hyperfine field due to a thermal nuclear polarization is plotted vs temperature in Fig. 4.27(b) as a blue curve. We see a good agreement with the experimental data.

Summarizing this chapter, we have studied the $\nu = 2/3$ unpolarized-polarized phase transition characterized by a peak in the minimum of the longitudinal resistivity as a function of density, tilt-angle, current, frequency, time and temperature. We have demonstrated that the HLR peak can be considered as the high current regime of the transition. Some similarities but also striking differences exist between a low current and the HLR regime. We have discussed most of them in this chapter. We proposed a model to explain the mechanism leading to the different results. In both regimes, the presence of polarization domains seem to be crucial for dissipation. In the case of the HLR, a current-induced dynamic nuclear polarization (CIDNP) influences the domain structure considerably, thus strongly enhancing dissipation. At low currents, the transition is only affected by the thermal polarization at the lowest temperatures.

Temperature activation measurements reveal that a gap remains at the transition and that possibly low-energy excitations in which several spin flips are involved might be favored instead of a single spin flip. In this chapter, we showed that the HLR evolves differently in time, if an AC or DC current is used. Furthermore, we proved that the high current resistance peak is not caused by non-linear effects, but it is the interplay between the electrons and the nuclei which is responsible for such an effect. In the next chapter, we take advantage of the nuclear-electron interaction in order to further study the electron spin polarization at the transition and to corroborate some of our assertions by using NMR. Additionally, we also study the $\nu = 3/5$ and $4/7$ transitions as well as low energy excitations around $\nu = 1$ and $1/3$.

¹²The following information was needed for the calculations: Paget *et al.* has listed the maximum hyperfine field for each of the three nuclei in GaAs [121]. $B_N^{69\text{Ga}} = -1.365$ T, $B_N^{71\text{Ga}} = -1.17$ T and $B_N^{75\text{As}} = -2.76$ T. This is taking into consideration that all the spins are in the lowest level and the average spin polarization is $\langle I \rangle = 3/2$.

Chapter 5

NMR Studies of the Lowest Landau Level

In the previous chapter, we investigated spin phase transitions, particularly at $\nu = 2/3$, with magnetotransport. An important distinction was made between the low current and high current or HLR regimes where we discovered important differences. In both regimes, the nuclear system takes on a crucial role since it strongly affects the transport characteristics of the system. Electrons and nuclei communicate via the hyperfine interaction by coupling their spins. In this chapter, we take advantage of this coupling in order to study more aspects of the spin phase transition at $\nu = 2/3$ and other filling factors, as well as diverse spin-related phenomena in the FQHE such as skyrmionic and spin-reversed quasiparticle excitations by using nuclear magnetic resonance (NMR)¹.

We opted for this technique because NMR spectroscopy is a powerful experimental tool which exploits the interactions between electrons and nuclei in order to examine the electronic and structural properties of a wide range of physical systems [70, 71]. In a 2DES, however, the sensitivity of the NMR signal amplitude, which is proportional to the product of the number of nuclear spins and their average spin polarization, is greatly restricted. A technique known as resistance detected (RD)NMR (see section 2.4.6) has been employed to qualitatively study nuclear-electron interactions in a single 2DES in the FQHE [6, 58]. Recently, there have also been major efforts to quantitatively study QH systems by measuring the electron spin polarization in multiple quantum wells (MQW) or optically pumping the nuclear system (OP-NMR) [73, 96]. Thus the NMR signal to noise ratio improves considerably as the number of nuclei and the average nuclear polarization are respectively increased.

In this work, we have developed a technique in which the electron spin polarization can be quantitatively measured in a *single* 2DES by combining RDNMR and NMR. Measuring a single layer enabled us to overcome the problems present in the MQW and OPNMR techniques, such as a fixed density, identical growth of many layers and driving the system out of its equilibrium

¹Samples from wafer 020502.1 were used in all of the experiments presented in the chapter except for Figs. 5.20 and 5.23.

state. Before presenting this technique in sections 5.2.1 and 5.2.2, we firstly introduce some of the NMR basics (section 5.1) required to understand the experiments discussed in this chapter. The rest of the chapter is generally outlined in five parts. Firstly, we present measurements of the electron spin polarization at the $\nu = 2/3, 3/5$ and $4/7$ transitions in sections 5.2.3 and 5.2.4. In section 5.3, we focus on the $\nu = 2/3$ transition and investigate important differences existing between the low and high current regimes. A description of stressed samples which show a quadrupole splitting is necessary and thus discussed in section 5.4. These results were useful in solving the four-fold splitting anomaly in RDNMR experiments reported at the $\nu = 2/3$ transition in previous works [6]. Furthermore, we report on an anomalous line shape of the RDNMR spectrum in the vicinity of filling factors 1, $1/3$ and $2/3$. We finally close the chapter by presenting some recent progress and an outlook on possible future NMR experiments in the FQHE regime.

5.1 NMR Basics

Nuclear magnetic resonance or NMR can be used to study any system which has a non-zero nuclear spin. The total magnetic moment of a nucleus μ_I is given by:

$$\mu_I = \gamma_N \hbar \mathbf{I} \quad (5.1)$$

where $\hbar = h/2\pi$ is Planck's constant, \mathbf{I} is the nuclear spin operator and γ_N is the so-called gyromagnetic ratio. The value of γ_N is known for almost every non-zero spin nuclear system. In GaAs there are the three nuclear isotopes: ^{71}Ga , ^{69}Ga and ^{75}As .

In the presence of a magnetic field B , the nuclear spin interacts with the field and the Hamiltonian is simply written as:

$$H_N = -\mu_I \cdot B = -\gamma_N \hbar \mathbf{I} \cdot \mathbf{B}. \quad (5.2)$$

Moreover, if the field points in the z-direction the Hamiltonian reduces to:

$$H_N = -\gamma_N \hbar I_z B_z. \quad (5.3)$$

The eigenvalues of H_N are multiples of the I_z eigenvalues m_z which may take any of the $2I + 1$ values $m_z = I, I - 1, \dots, I$:

$$E_N = -\gamma_N \hbar m_z B_z. \quad (5.4)$$

In other words by turning on a magnetic field in the z-direction, the system will split up in $2I + 1$ energy levels separated by the nuclear Zeeman energy:

$$\Delta_N = E_N - E_{N+1} = \hbar \omega_L = \gamma_N \hbar B_z. \quad (5.5)$$

In this equation, $\omega_L = \gamma_N B_z$ is called the Larmor resonance frequency and is equivalent to the classical precession frequency of a nuclear magnetic moment subjected to a magnetic field.

In Fig. 5.1(a), we have drawn the nuclear Zeeman energy splitting for the simplest $I = 1/2$ case. The nuclear spin up state is energetically more favorable to populate than the spin down

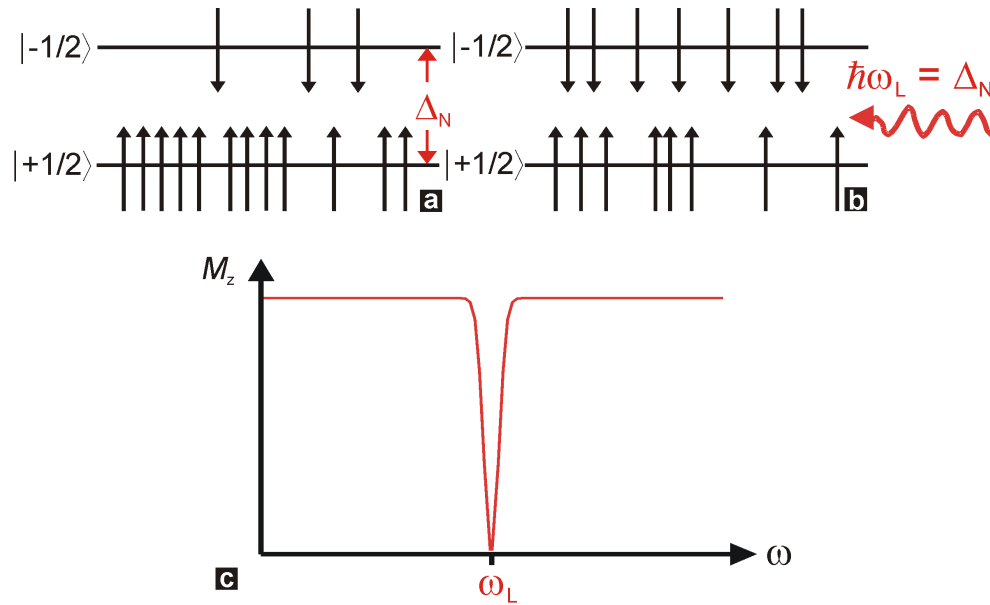


Figure 5.1: (a) Schematic diagram for the energy splitting Δ_N of a nucleus with spin $I = 1/2$ in the presence of a magnetic field B_z . (b) Applying an RF signal tuned to the Larmor resonance frequency ω_L induces transitions between the levels. (c) In a continuous wave (CW) experiment, the magnetization in z -direction, M_z , decreases as the Larmor frequency is reached.

state. The number of nuclei populating the levels $|+1/2\rangle$ and $|-1/2\rangle$, that is N_+ and N_- respectively, is determined by the Boltzmann factor:

$$\frac{N_-}{N_+} = \exp \frac{-\Delta_N}{k_B T} = \exp \frac{-\gamma_N \hbar B_z}{k_B T} \quad (5.6)$$

in which k_B is the Boltzmann constant and T the temperature. At high temperatures ($k_B T \gg \Delta_N$) the ratio N_-/N_+ is approximately unity so both levels are nearly equally populated. At low temperatures and high magnetic fields, on the other hand, the thermal nuclear polarization becomes considerable ($\approx 15\%$ at $T = 20$ mK and $B = 10$ T). If we consider the whole ensemble of spins, the excess of spin up nuclei will amount to a net magnetization M_0 pointing in the same direction as the external magnetic field B_z . The total magnetization M_0 is then equal to M_z and for a two level system is given by:

$$M_0 = \frac{1}{2} (N_- - N_+) \hbar \gamma_N = \frac{1}{2} \hbar \gamma_N N \tanh \frac{\hbar \gamma_N B_z}{2 k_B T}, \quad (5.7)$$

where $N = N_- + N_+$. The polarization is expressed in equation 2.22.

NMR spectroscopy consists of irradiating the sample with a radio frequency tuned to the Larmor frequency of the nuclei in question:

$$f = \gamma_N B_z. \quad (5.8)$$

If an alternating magnetic field $B_1(t)$ is perpendicular to the direction of the static magnetic field B_z , transitions will occur between adjacent energy levels; transition rules only allow for $\Delta m = \pm 1$. Since there is the same probability for nuclei to move from $|+1/2\rangle$ to $|-1/2\rangle$ as viceversa, the rf-radiation reduces the total M_z magnetization since both levels become more equally populated, see Fig. 5.1(b).

In general, an NMR experiment can be performed with a continuous rf wave (CW) or a pulsed rf signal. In a CW experiment either the magnetic field is swept at constant rf or the frequency is swept at constant B -field. We have schematically plotted the magnetization in the z -direction M_z vs rf for a frequency sweep CW experiment in Fig. 5.1(c). It is expected that M_z decreases as the Larmor frequency is reached. Experimentally, a change in M_z is usually detected by the loss of energy in the rf-coil due to the absorption. After the frequency is no longer in resonance, the system reestablishes its equilibrium magnetization after a certain time T_1 known as the longitudinal or spin-lattice relaxation time. The equation which describes the recovery of M_z is:

$$M_z = M_0 \left(1 - \exp\left(-\frac{t}{T_1}\right) \right) \quad (5.9)$$

Characteristic times for T_1 range from ms to even hours or days. These will strongly depend on the interaction between the nuclear system and the “reservoir.” That is, it involves the transfer of energy to the lattice via conduction electrons, phonons etc.

At the present time, it is common practice to perform pulsed rather than CW NMR experiments. They consist of exposing the sample to an rf pulse of certain duration τ_p , tuned close to the Larmor resonance frequency which creates an alternating magnetic field B_1 . The magnetization, originally pointing in the z -direction, will tip towards the xy -plane. An x and y component of the magnetization ($M_{x,y}$) appears as depicted in Fig. 5.2(a). The tipping angle ϕ depends on the duration and magnitude of B_1 :

$$\phi = 2\pi\gamma\tau_p B_1 \quad (5.10)$$

A $\pi/2$ pulse, for example, means that the magnetization is entirely tipped to the xy -plane and $M_z = 0$.

If one detects either the M_x or M_y as a function of time, a damped oscillation of the magnetization, known as free induction decay (FID) signal, is obtained [Fig. 5.2(b)]. The time it takes for the FID signal to decay is called the transverse or spin-spin relaxation time T_2 . It is normally much shorter than the T_1 time and typically ranges from μs to ms. The equation

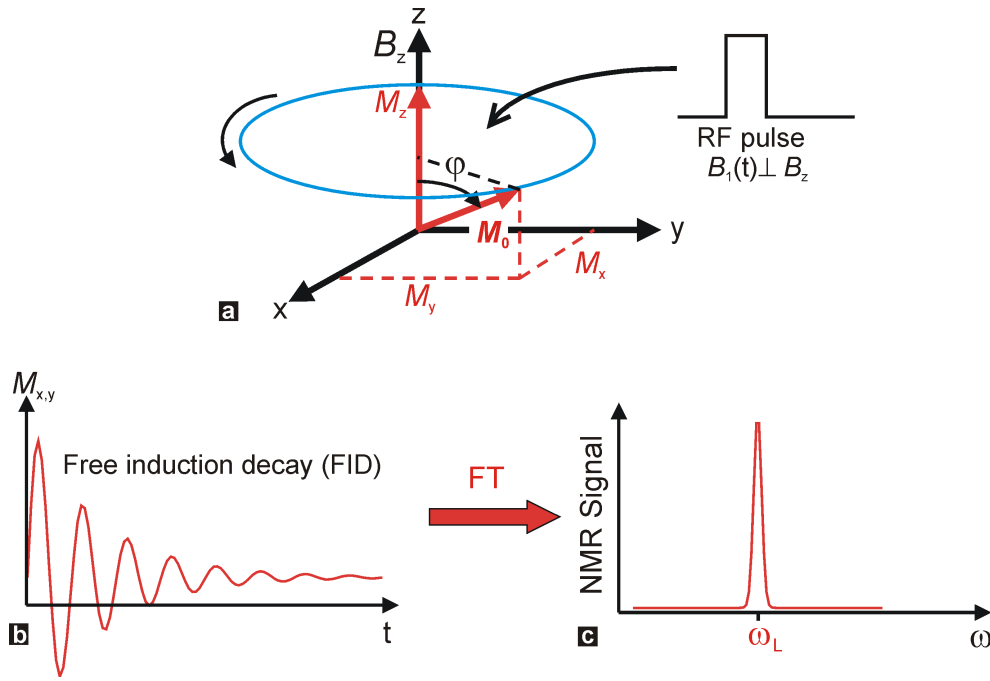


Figure 5.2: (a) If an RF-pulse tuned to ω_L is applied perpendicular to the direction of the static magnetic field B_z , the M_z magnetization tips into the xy -plane by an angle ϕ . An oscillating free induction decay (FID) signal of the M_x or M_y magnetization is observed in the NMR spectrum. (c) The Fourier transform of the FID gives a peak at the resonance frequency.

which describes the transverse relaxation process, that is the time required for $M_{x,y}$ to return to equilibrium, can be written as:

$$M_{x,y} = M_{x0,y0} \exp\left(-\frac{t}{T_2}\right) \quad (5.11)$$

The $M_{x,y}$ decays rapidly because spins of different nuclei precess at slightly different frequencies. This dephasing of the spin precession is basically due to two reasons: Firstly, inhomogeneities in the external magnetic field B_0 causes each nucleus to experience a slightly different magnetic field and secondly, spin-spin couplings, in which one nucleus produces a small local magnetic field on the other nuclei ($B_{loc} \sim \mu_1/r^3$, dipole-dipole coupling), produces different precession frequencies. A T_2^* relaxation time is obtained by adding these two processes²:

$$\frac{1}{T_2^*} = \frac{1}{T_2} + \frac{1}{T_{2,inhom.}} \quad (5.12)$$

²Whenever the dephasing time T_2 is fast, it is preferred to perform a spin-echo experiment. This consists of pulsing the magnetization by 90° into the xy -plane, followed by a 180° after a time τ which tilts the magnetization from the $+y$ to the $-y$ axis. The dephased spins will partially come back into phase after a time 2τ thus producing an echo signal [23, 122]. This method was not employed in this thesis.

The Fourier transform (FT) of the FID signal results in a resonance peak at ω_L as shown in Fig. 5.2(c). The Larmor frequency of the nuclei and the NMR line shapes can be strongly affected if interactions of the nuclei with its surroundings are considered. These interactions could be nuclear spin-spin couplings (dipole-dipole interaction), spin-orbit interactions (chemical shift) and electron spin-nuclear spin couplings (hyperfine interaction) [70, 71]. While dipole interactions merely broaden the NMR signal, and the spin-orbit effects are usually tiny in 2DES systems, the hyperfine interaction results in a shift of the ω_L (Knight shift) which is proportional to the electron spin polarization \mathcal{P} . Therefore, NMR is an ideal technique to study \mathcal{P} in a 2DES. In the following sections, we will present measurements of the electron spin polarization at various filling factors in the FQH regime.

5.2 Measurements of the Electron Spin Polarization

In section 2.4.5 we explained that the hyperfine interaction is responsible for coupling the nuclear with the electronic system in a 2DES, see equation 2.27. In GaAs, the Fermi contact term (eq. 2.28) is predominant and mostly responsible for the coupling of the systems. Considering the local magnetic field B_e which is created by polarized electrons acting on the nuclear spins (eq. 2.32), we can rewrite equation 5.5 as follows:

$$\hbar\omega_L = \gamma_N \hbar (B_z + B_e). \quad (5.13)$$

As a result, the Larmor resonance frequency shifts by $\gamma_N B_e$. The Knight shift, K_s , is usually defined as the shift in Larmor frequency divided by the bare Larmor frequency ($\gamma_N B_z$) and given in ppm. In 2DES however, the Knight shift is defined only as the shift in ω_L given in kHz.

The electron spin polarization \mathcal{P} , which is proportional to the Knight shift, can then be determined from NMR spectroscopy via the Knight shift via the following equation:

$$\mathcal{P}(\nu, T) = K_s / K_{s,\max}(\mathcal{P} = 1). \quad (5.14)$$

Here, $K_{s,\max}(\mathcal{P} = 1)$ is the maximum Knight shift obtained from nuclei interacting with a fully polarized electron system and \mathcal{P} depends on filling factor and temperature³. Furthermore, the Knight shift is proportional to the electron density n and inversely proportional to the quantum well thickness w :

$$K_s = \frac{n \mathcal{P} A_{\text{eff}}}{w}. \quad (5.15)$$

A_{eff} is defined as an effective hyperfine coupling constant which can be calculated or experimentally determined as it has been done from OPNMR measurements in MQW structures [123, 124]. In the next two sections, we will show how we combined RDNMR with NMR techniques and used $\nu = 1/2$ to determine K_s for any achievable electron density in our single, narrow QW structure.

³At phase transitions, it is also dependent on η as we have previously remarked.

5.2.1 The RDNMR/NMR Technique

In order to overcome the problem of having a very low sensitivity, which is the case when a conventional NMR experiment is carried out on a single QW, we have developed a method of combining resistance detected (RD)NMR with standard NMR techniques. In the following, we describe this method in detail: The degree of electron spin polarization can be directly determined by measuring the Knight shift of the Larmor resonance frequency caused by the interaction between the nuclei and the conduction electrons in the GaAs QW. This shift can be obtained by comparing the resonance signal of the nuclei interacting with electrons and the unshifted resonance signal from nuclei which are not interacting with electrons. This technique is illustrated in Fig. 5.3. Firstly, the magnetic field is swept until the filling factor of interest is

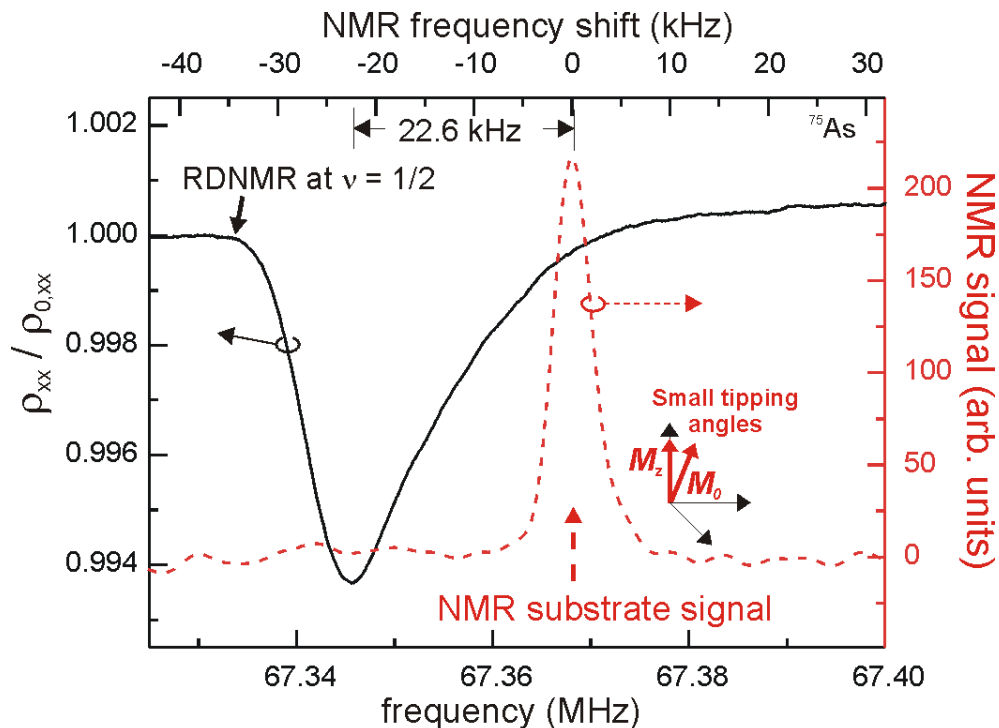


Figure 5.3: The black, solid line represents ρ_{xx} vs RF-frequency at $\nu = 1/2$. The red, dashed line shows the Fourier transform of the FID signal from the substrate. Small tipping angles of the magnetization were used for the FID as schematically shown. The experiments were performed at $B = 9.25$ T and $T = 55$ mK. The density was held constant at $n = 1.12 \times 10^{11} \text{cm}^{-2}$ during the RDNMR measurements in order to be at $\nu = 1/2$.

reached. Keeping the magnetic field and the gate voltage constant at that filling, we monitor the changes in the longitudinal resistivity ρ_{xx} as a function of the frequency of incident RF radiation. The radio frequency is swept through the Larmor frequency of the ^{75}As , ^{69}Ga or ^{71}Ga

nuclei with a much slower speed than the relaxation rate at the corresponding filling factor⁴. Most of our NMR experiments were performed on ⁷⁵As nuclei since it is a pure isotope with 100% abundance while the Ga nuclei have two isotopes, ⁶⁹Ga and ⁷¹Ga, with 60.4% and 39.6% abundance, respectively [90]. It is important to maintain the amplitude of the RF-signal low (≈ 20 dBm) to avoid heating effects (see section 3.2.2). In particular, the experiments shown in Fig. 5.3 were conducted at constant filling factor $\nu = 1/2$. At a density of $n = 1.12 \times 10^{11} \text{ cm}^{-2}$, $\nu = 1/2$ occurs at $B = 9.25 \text{ T}$. The temperature, $T = 55 \text{ mK}$, was determined by comparing transport experiments at this value without an RF-signal and at $T = 50 \text{ mK}$ with an applied, on-resonance RF-signal. In the black solid curve of the figure, we plotted ρ_{xx} vs RF-frequency and observe a single dip in the longitudinal resistivity as we approach the Larmor frequency of the ⁷⁵As nuclei⁵. The change in resistivity is due to the Overhauser shift, since the Zeeman energy E_Z changes by depolarizing the nuclei as explained in section 2.4.5⁶. RDNMR has been employed on a wide range of experiments in the QHE regime, where the coupling between the nuclear and electronic system has been qualitatively shown [6, 58, 72, 90, 91, 92, 125]. Nevertheless, in order to know quantitatively the degree of electron spin polarization, it is necessary to determine a zero-shift reference resonance frequency from nuclei which are not interacting with electrons. For this purpose, we carried out a standard pulsed NMR experiment on the sample to obtain the FID signal from the substrate. Since the nuclei located in the substrate are not interacting with conduction electrons (the conduction band is empty there) their NMR resonance signal serves as a zero Knight-shift reference. The red dashed line in Fig. 5.3 shows the Fourier transformed signal of the FID. Note that in agreement with previous studies, no quadrupole splitting of the GaAs substrate NMR line is observed (see section 5.4) [96, 103]. To obtain the FID signal, small tipping angles ($< 1\%$) were used in order to avoid saturation, as depicted in the inset of the figure. This was done mainly because the relaxation time T_1 of substrate nuclei at low temperatures is of the order of hours or even days. The signal to noise ratio was increased by integrating up to 128 FID's in the reference spectra. From the figure, we see that the RDNMR resonance line is shifted by $\approx 22.6 \text{ kHz}$ with respect to the reference line. The difference in the resonance frequency equals the Knight-shift

⁴At some filling factors, the equilibration times may be very long. For example at the $\nu = 2/3$ phase transition in the HLR regime, a full sweep may take a few hours in order to maintain a quasi-static situation.

⁵Our results obtained for the ⁶⁹Ga and ⁷¹Ga exhibit qualitatively the same behavior. Quantitatively the resonance frequency changes due to the different gyromagnetic ratios and the Knight shift scales by $\gamma_N(^{69}\text{Ga})/\gamma_N(^{75}\text{As})$ and $\gamma_N(^{71}\text{Ga})/\gamma_N(^{75}\text{As})$ with respect to $K_S(^{75}\text{As})$.

⁶The sign and shape of the RDNMR line is dependent on the filling factor. We will see in the following sections that at spin phase transitions a change of R_{xx} is caused by a change in the value of η_c which involves E_Z . At other filling factors, for example at odd IQH fillings, where $R_{xx} \propto \exp -\frac{\Delta}{2k_B T}$, a change in E_Z causes a change in Δ and thus in R_{xx} . At $\nu = 1/2$ the situation is more complicated, but here too a change in E_Z alters R_{xx} . The sign and amplitude of ΔR_{xx} is not yet fully understood. However, this is of no immediate relevance to the experiments presented here.

of the RDNMR signal, coming from the nuclei in the QW, with respect to the zero-shift NMR substrate reference signal. We can also infer from the graph that there is only a small error bar for the determination of the Knight shift. Since the degree of electron polarization can be obtained via equation 5.14, we can determine $\mathcal{P}(\nu, T)$ quantitatively if we know the maximum Knight shift expected for a fully polarized system, $K_{s,\max}(\mathcal{P} = 1)$. In the following, we will describe how we used Knight shift measurements at filling factor $\nu = 1/2$ at various densities to accomplish this task.

5.2.2 Calibration Curve at $\nu = 1/2$

The maximum Knight shift due to a completely polarized electron system can be determined by measuring the Knight shift for different densities at filling factor $\nu = 1/2$. Ideally, the fractional quantum Hall ferromagnet state $\nu = 1/3$ could be used for the $\mathcal{P} = 1$ reference for any density. However, since we are conducting an RDNMR experiment, we need a finite value of ρ_{xx} . Therefore we opted for filling factor $\nu = 1/2$, where all the electrons should be spin polarized above some critical magnetic field B_c (see section 2.4.3). This situation occurs

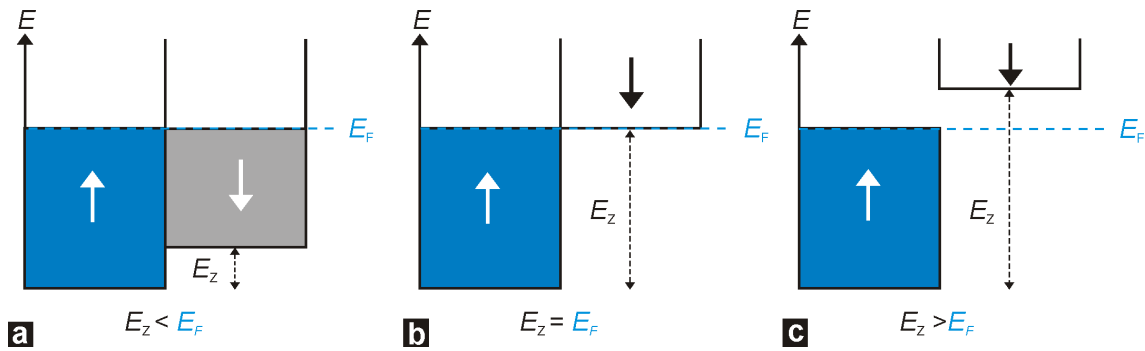


Figure 5.4: Schematic diagram of the spin up and spin down energy bands at $\nu = 1/2$ for $E_Z < E_F$ (a), $E_Z = E_F$ (b) and $E_Z > E_F$ (c).

because even though CFs experience $B_{\text{eff}} = 0$ at $\nu = 1/2$ the Zeeman energy still acts on their spin thereby shifting the energy bands for spin up and spin down. In other words, B_{eff} only affects the orbital part of the angular momentum and not the spin. The CFs will then be expected to be fully polarized for $E_Z > E_F$, where E_F is the CF Fermi energy. The spin up and spin down energy bands at $\nu = 1/2$ are schematically shown in Fig. 5.4 for $E_Z < E_F$ (a), $E_Z = E_F$ (b) and $E_Z > E_F$ (c). The blue color represents filled spin up states and the grey color filled down states. In this discussion, it is important to note that electrons and CFs have the same spin and therefore the CF or electron spin polarization is equivalent [80].

In Fig. 5.5, we show a plot of the Knight shift as a function of density at constant filling factor $\nu = 1/2$. We achieved this by changing simultaneously gate voltage and magnetic field

to maintain fixed filling $\nu = 1/2$. The inset depicts a gate voltage sweep at $B = 15$ T in which

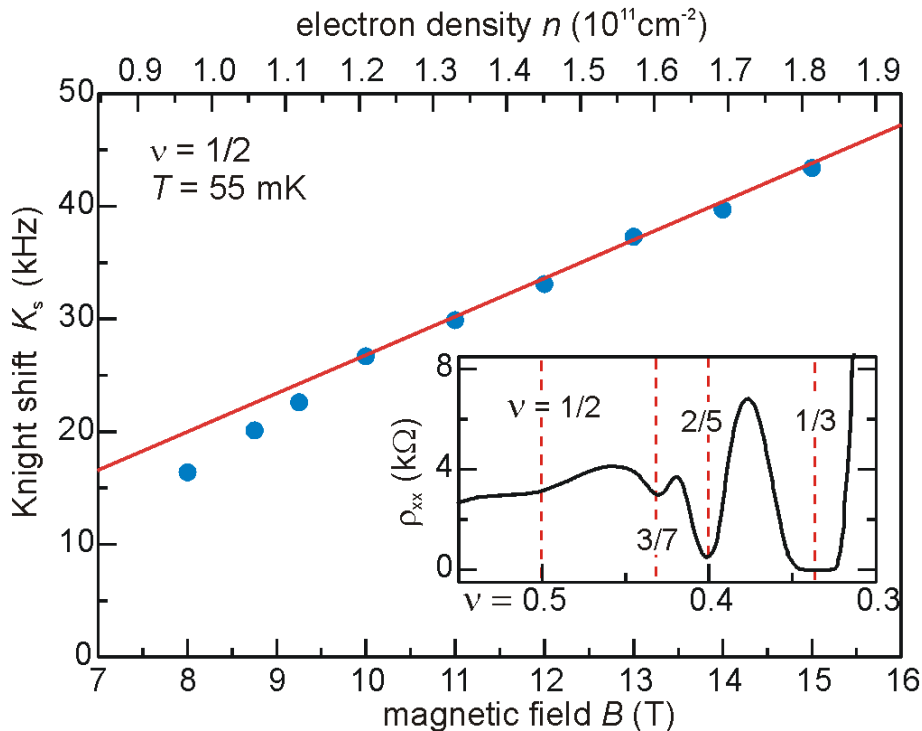


Figure 5.5: Knight shift K_s vs density for constant filling $\nu = 1/2$. The straight line in red indicates the expected Knight shift for a fully polarized electron system. Below $B_c \approx 10$ T, the system is no longer completely polarized. This “calibration curve” was used to study the spin phase transition at $\nu = 2/3, 3/5$ and $4/7$. The inset shows ρ_{xx} vs ν at $B = 15$ T.

fractional filling factors $\nu = 1/2, 3/7, 2/5$ and $1/3$ are seen. In the main figure, the data points which are above $B \approx 10$ T fall on a straight line in agreement with equation 5.15⁷. Below 10 T the data points deviate from a straight line indicating a depolarization of the electronic system at low densities as expected⁸. An extrapolation of the linear region to lower fields allows us to know $K_s(\mathcal{P} = 1)$ at any achievable density in our sample. The $\nu = 1/2$ calibration curve was very useful to determine the electron spin polarization at the phase transitions of fillings $2/3, 3/5$ and $4/7$.

⁷We should point out that there is an offset for $K_{S,\max}(n) \rightarrow 0$, which results most probably from a change in the electron probability density across the QW at very low densities. However, in the density regime that we are interested in, this “calibration curve” holds very well.

⁸The $\nu = 1/2$ state has two Fermi surfaces, for each spin orientation, if it is not completely polarized. The difference between the areas of the spin up and the spin down Fermi disks render the spin polarization. [60, 61, 62, 126].

Calculation of η_c and m_{CF}^{p}

Apart from using the results presented in Fig.5.5 as a calibration curve for $K_{\text{s,max}}(\mathcal{P} = 1)$, we can also calculate $\eta_c = E_Z/E_C$ and m_{CF}^{p} in order to compare it with previous results. In Figs. 2.14(a) and (b) [60,62] of section 2.4.3, we showed two experiments where the spin polarization at $\nu = 1/2$ was measured. In Fig.2.14(a) the polarization was obtained by optical experiments while in 2.14(b) it was extracted by applying NMR in multiple quantum wells. In both cases, a smooth transition from a partial to a complete polarization is observed at ≈ 9.3 T and ≈ 10 T, respectively. In the latter experiments, a 35 nm QW was used and the sample was tilted with respect to B_z in order to measure \mathcal{P} at various fields. Even though we also measure $B_c = 10$ T, a more accurate comparison can be made by calculating η_c and including finite thickness and g -factor corrections. By using equations 2.20 and 2.21, we have computed $\eta_c = 0.021$ which is in very good agreement with $\eta_c = 0.022$ extracted from Fig.2.14(a).

If the CF model is used, the system undergoes a transition when the CF Fermi energy equals the Zeeman energy [see Fig. 5.4(b)], that is $(\hbar^2 k^2)/(2m_{\text{CF}}^{\text{p}}) = g^* \mu_B B$, where the wavevector of a Fermi surface at $\nu = 1/2$ is given by $k_{\text{c,CF}} = (4\pi n_{\text{CF}})^{1/2}$ [126]. The polarization CF mass, which differs from an activation CF mass (see section 2.4.3), can be calculated to be $m_{\text{CF}}^{\text{p}} = 2.92m_e$, where the g -factor has again be corrected. It is important to note that this value applies only to $\nu = 1/2$ and $B = 10$ T. Assuming a \sqrt{B} dependence of the mass, we can obtain $\frac{m_{\text{CF}}^{\text{p}}}{m_e} \approx 0.92\sqrt{B(\text{T})}$. This value is about 1.5 times larger than the one obtained from the calculations of Park and Jain [80] given in equation 2.25. The prefactor, however, is a sample dependent parameter, which was affected by the g -factor corrections due to the narrow quantum wells. Finally, we would like to reiterate that the CF mass extracted from these experiments is a CF polarization mass which is about 10 times larger than the expected activation CF mass.

5.2.3 Study of the Electron Spin Polarization at the $\nu = 2/3$ Transition

We have studied the electron spin polarization at the $\nu = 2/3$ transition by using the RD-NMR/NMR technique previously described. In this section, we present our main results which apply to both the low and high current regimes. Additional results which establish important differences between these regimes will be presented in section 5.3.

The solid black line of Fig. 5.6 shows an RDNMR plot of the longitudinal resistivity ρ_{xx} vs NMR frequency shift at a constant magnetic field $B = 8.1$ T and constant density $n = 1.35 \times 10^{11} \text{cm}^{-2}$ ($V_{\text{gate}} = -0.417$ V). These values were chosen in order to be at the top of the unpolarized-polarized transition peak. The current was set at $I = 40$ nA so that the HLR peak develops after several minutes. Furthermore, the gate was swept from a low to a high filling factor as depicted by the red dashed curve in Fig. 4.3. The NMR substrate signal, which represents the zero-shift reference, is also plotted in Fig. 5.6 (red dashed curve). The NMR

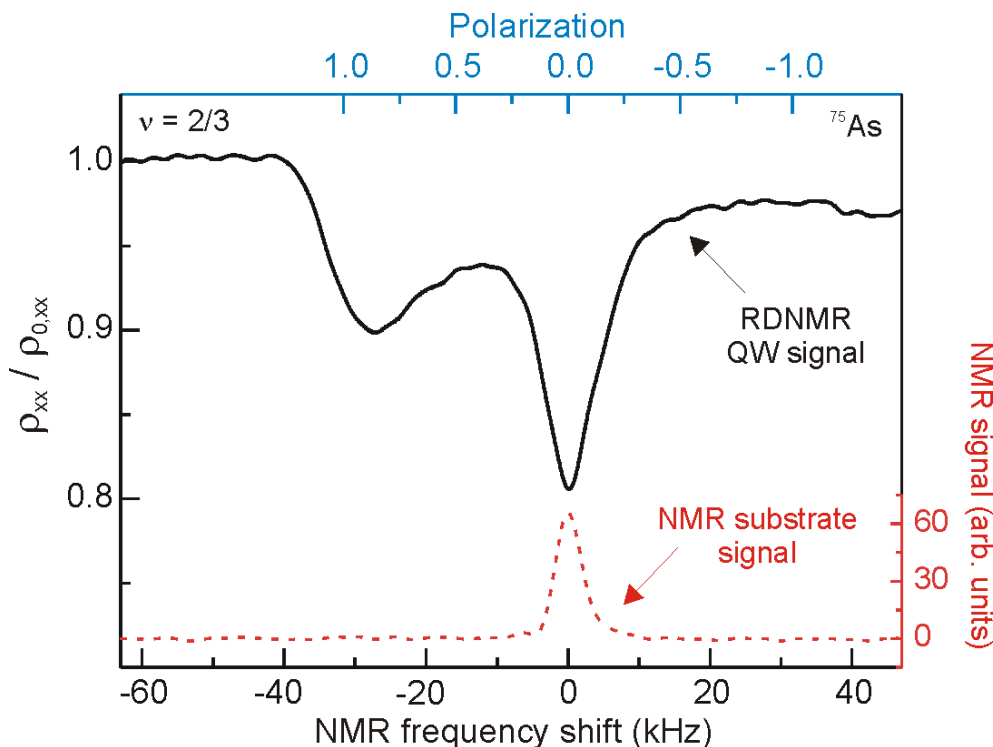


Figure 5.6: RDNMR/NMR technique applied to the high current spin phase transition at $\nu = 2/3$. The black, solid line shows ρ_{xx} vs NMR frequency shift (polarization) and the red, dashed line the substrate reference signal. In the solid line, two resonances are observed at $\mathcal{P} = 0$ and $\mathcal{P} = 1$. These measurements were carried out at $B = 8.1$ T, $I = 40$ nA, $n = 1.35 \times 10^{11} \text{cm}^{-2}$ and $T = 55$ mK.

frequency shift given in kHz is taken relative to the NMR substrate signal f_0 (NMR frequency shift [kHz] = $f - f_0$). We have also used the $\nu = 1/2$ calibration curve of the previous section (Fig. 5.5) to rescale the x-axis from frequency to polarization and included it in the figure as the top blue axis. In the RDNMR curve, two well resolved resonance lines are seen. The minima of these two lines are separated by 31.6 kHz. The right line clearly appears at the same resonance frequency as the substrate reference signal. By looking at the polarization axis, it is evident that this separation agrees very well with the expected Knight shift for a fully polarized electron system. This is an indication that the two contributions to the RDNMR signal come from nuclei interacting with the two different types of electronic domains. The Larmor frequency of the nuclei which interact with fully polarized electrons shifts by $K_{s,\text{max}}(\mathcal{P} = 1)$, whereas the frequency of nuclei which interact with unpolarized electrons remains at the same position of the substrate reference signal. Hence, this plot shows direct *spectroscopic evidence* of an inhomogeneous state in a 2D electron system and of domain formation at the $\nu = 2/3$ transition.

static or slowly fluctuating domains

A domain structure can only be revealed by a local probe like NMR. The local information persists, even if fluctuations are considered, provided that the domains are static on the time scale of the measurements $t \approx 1/K_{s,\max} \approx 20 \mu\text{s}$ (inverse linewidth). In the simplest case, there are only two types of static domains with polarization $\mathcal{P} = 0$ and $\mathcal{P} = 1$ and the nuclei interacting with different domains will experience a different Knight shift, $K_s(\mathcal{P} = 0) = 0$ and $K_s(\mathcal{P} = 1) = K_{s,\max}$, leading to two distinct lines. This is schematically represented in Fig. 5.8(a). On the other hand, if the domains would fluctuate at a similar rate as the time scale of

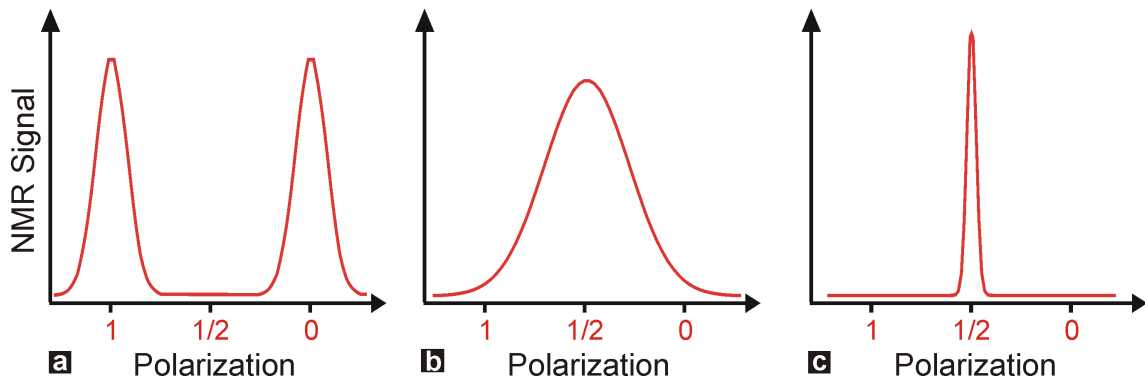


Figure 5.7: (a) Static domains or very slowly fluctuating domains lead to distinct lines. (b) If the $\mathcal{P} = 0$ and $\mathcal{P} = 1$ domains at the $\nu = 2/3$ spin phase transition would fluctuate at a similar rate as the time scale of the measurements (inverse linewidth), the NMR line would broaden between $K_s(\mathcal{P} = 0)$ and $K_{s,\max}(\mathcal{P} = 1)$ as schematically shown. (c) Faster fluctuations of the domains than the NMR time scale leads to motional narrowing and an average polarization around $\mathcal{P} = 1/2$ (Schematic diagram).

the measurements, some nuclei would only experience domains of polarization $\mathcal{P} = 0$, some only $\mathcal{P} = 1$ domains and some would experience both domains, thus broadening the NMR line and part of the information would be lost, see Fig. 5.8(b).

If the fluctuations were faster than the NMR time scales, all nuclei would experience an average polarization $\langle \mathcal{P} \rangle = (A_1 \mathcal{P}_1 + A_2 \mathcal{P}_2) / (A_1 + A_2)$, where A_i is the area of domain i and the NMR then turns into a global probe. This situation, referred to as *motional narrowing*, leads to a single NMR line centered at $\mathcal{P} = 1/2$, schematically drawn in Fig. 5.8(c). In these experiments, the two lines of the $\nu = 2/3$ are well resolved indicating a static domain structure or at least domains fluctuating slowly [23, 96, 103, 127]. In reality, a line corresponding to a nonzero polarization \mathcal{P}_1 is broadened between between $\mathcal{P} = 0$ and $\mathcal{P} = \mathcal{P}_1$ due to the density profile of the electrons across the width of the quantum well. This situation has been calculated in reference [128] and is depicted in Fig. 5.8. The electron density profile (a) has been computed

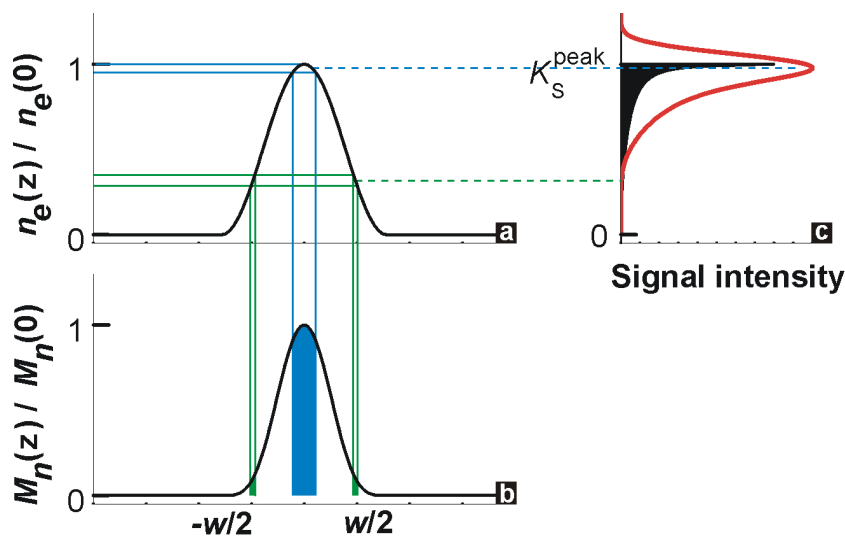


Figure 5.8: The electron density profile (a) and the resulting nuclear z -magnetization profile (b) were calculated for a quantum well of thickness w . From this information, an intrinsic NMR line shape was computed (black curve in c) and convoluted by a Gaussian distribution (red curve in c). A broadening of the nonzero polarization NMR lines is caused by the density profile across the width of the QW.

for a quantum well of thickness w by a self-consistent bandstructure calculation. The resulting nuclear magnetization profile, $M_n(z)$ is presented in (b). The black filled curve in Figure (c) shows the intrinsic NMR line obtained from such an electron density and magnetization profile. The NMR signal intensity at a certain frequency is proportional to the number of nuclei resonating at that frequency and their population excess. Since the Knight shift is proportional to the electron density, a maximum shift of the line is caused by the electrons in the center of the quantum well (blue dashed line). Near the edges of the well, the electron density decreases and so does the Knight shift (green dashed line). A convolution of the intrinsic line shape and a Gaussian function, needed due to a broadening of the NMR lines caused by nuclear dipolar interactions, is shown in Fig. (c) as a red curve. These calculations explain the broadened spectrum of the nonzero lines observed in our experiments (see for example Fig. 5.3).

5.2.4 Study of the Transitions at $\nu = 3/5$ and $4/7$

In this section, we apply the same RDNMR/NMR technique to study the spin phase transitions at $\nu = 3/5$ ($\nu_{\text{CF}} = 3$) and $\nu = 4/7$ ($\nu_{\text{CF}} = 4$). In Fig. 5.9, we plot ρ_{xx} vs NMR frequency shift at the $\nu = 3/5$ transition peak, depicted as a black line. The red dashed curve is again the

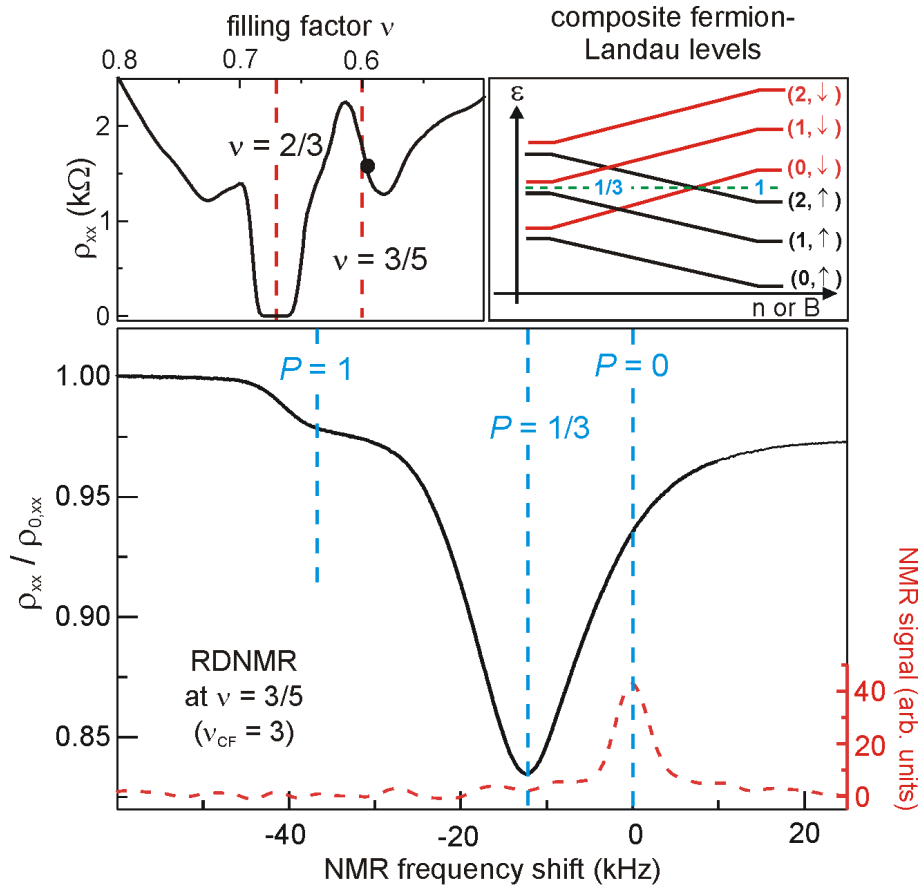


Figure 5.9: The gate voltage sweep depicted in the top left panel and the RDNMR measurement of the main graph were performed at $B = 10$ T. The spin transition for the $\nu = 3/5$ state is observed in transport (top left panel). The $\mathcal{P} = 1/3$ to $\mathcal{P} = 1$ transition for $\nu = 3/5$ ($\nu_{CF} = 3$), as expected from the CF picture (top right panel), is measured by RDNMR (black, solid line)/NMR (red, dashed line).

substrate reference signal. The top left panel shows a gate voltage sweep at a fixed magnetic field ($B = 10$ T) plotted as ρ_{xx} vs filling factor at a current of $I = 50$ nA. A large broad peak characterizes the spin phase transition similar to the HLR transition at $\nu = 2/3$. The black dot on the curve signalizes the position where we have stopped the gate sweep to carry out the RDNMR experiment. From the main graph, we observe that two resonance lines are present, both shifted from the zero-shift reference substrate signal. The left line is shifted by roughly 36.7 kHz and the right line by ≈ 12.2 kHz. Using again the calibration curve in Fig. 5.5, we can infer that the two shifts correspond to polarizations $\mathcal{P} = 1$ and $\mathcal{P} = 1/3$, respectively, at a density of approximately $n = 1.5 \times 10^{11} \text{ cm}^{-2}$, as expected from the composite fermion model. This can be easily understood by looking at the composite fermion-Landau level diagram in the top right panel, where the green dashed line represents the Fermi energy at $\nu_{CF} = 3$. The

different strength of the absorption lines is strongly dependent on the position of the transition peak where the RDNMR was carried out (see next section).

The top left panel of Fig. 5.10 shows a gate voltage sweep at a fixed magnetic field $B = 12$ T. The $\nu = 4/7$ spin phase transition is also characterized by a large peak. The black

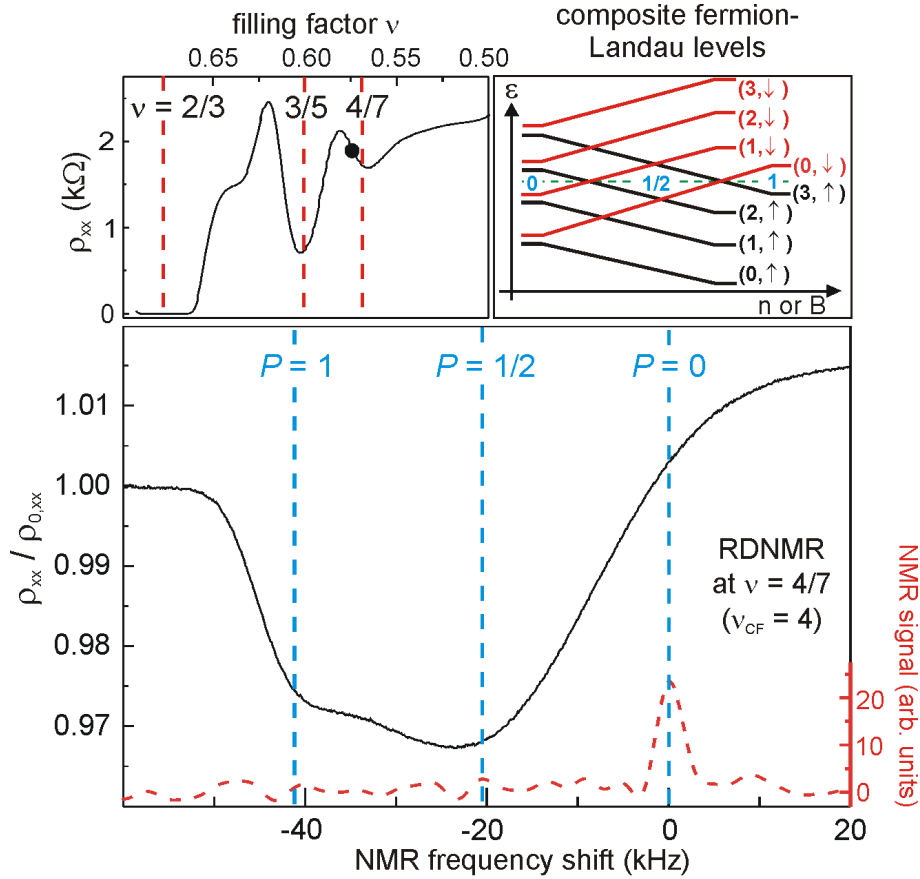


Figure 5.10: Gate voltage sweep (left, top panel) and RDNMR plot (main graph) at $B = 12$ T. A spin transition at $\nu = 4/7$ is also evident from the transport data. The CF picture predicts a transition from $\mathcal{P} = 0$ to $\mathcal{P} = 1/2$ and from $\mathcal{P} = 1/2$ to $\mathcal{P} = 1$ at $\nu = 4/7$ ($\nu_{\text{CF}} = 4$) as seen in the right, top panel. The latter transition is measured by the RDNMR (black, solid line)/NMR (red, dashed line) technique.

dot on the curve marks the position where the RDNMR measurement of the main figure was taken. We observe again two minima but this time separated from the reference signal by ≈ 41 and ≈ 22 kHz, respectively. This corresponds to the polarizations $\mathcal{P} = 1/2$ and $\mathcal{P} = 1$ for a density of $n = 1.67 \times 10^{11} \text{ cm}^{-2}$. From the top right panel, it becomes obvious that in these experiments we are measuring the $\mathcal{P} = 1/2$ to $\mathcal{P} = 1$ transition expected at high B -fields for $\nu_{\text{CF}} = 4$. These experiments elucidate the power of the developed technique. Apart from

confirming the composite fermion spin polarization measurements of Kukushkin *et al.* [60], it provides local information.

Here, it is important to mention that in our experiments we do not observe any features at intermediate polarization values which have been measured in previous works. For example at filling factor $\nu = 2/3$, a $\mathcal{P} = 1/2$ state has been revealed by optical experiments [60], (see Fig. 2.13). Likewise an electron spin polarization state of $\mathcal{P} = 3/4$ has been reported at the same filling factor from NMR experiments done on multiple quantum wells [73]. These states of partial polarization at $2/3$ are not yet understood and cannot be explained by the simple non-interacting CF model. We should note, however, that the samples and experimental methods used in those works are different than the ones presented here. In the optical measurements by Kukushkin *et al.*, the authors used a single-sided heterostructure with a much lower density in which the spin phase transitions occur at lower magnetic fields ($B = 2.3$ T at $\nu = 2/3$). Furthermore, they measure a signal which is proportional to $\sum_i A_i \mathcal{P}_i$, where A_i is the area of polarization \mathcal{P}_i measured by the laser spot. In our experiments, on the other hand, we detect changes of the longitudinal resistance and therefore do not measure a global polarization, but rather a signal proportional to $\sum_i a_i \mathcal{P}_i$, where a_i are coefficients dependent on the scattering mechanism leading to a resistance peak in transport. In the conventional NMR measurements presented in reference [73] they used 100 multiple quantum wells (each 30 nm) stacked on top of each other in order to increase the number of nuclei contributing to the signal. The question remains if all the layers are identical and therefore have the same polarization. These differences might lead to the discrepancies obtained in the results.

5.2.5 Conclusions

The conclusions drawn from the experiments presented in this section can be summarized as follows: We developed a technique in which the electron spin polarization, \mathcal{P} , can be measured in a single quantum well. So far, measurements of \mathcal{P} in two-dimensional systems had only been conducted on multiple quantum wells or with techniques which involved the hyperpolarization of the nuclei via optical methods. This technique was very useful in studying spin phase transitions in various FQH states. Measurements at $\nu = 1/2$ allowed us to both obtain a reference curve for the maximum Knight shift as a function of density (expected from a fully polarized system) as well as investigating the polarization of this state as a function of magnetic field. From the latter information we could extract a value for the composite fermion polarization mass.

The RDNMR/NMR technique discussed in this section was applied successfully to the spin phase transition at $\nu = 2/3$. Two distinct lines in the RDNMR spectrum indicate that the nuclear system interacts with electron domains of polarization zero and one. This spectroscopic evidence of domain formation at the transition is the most important result of the section. Mea-

measurements conducted at other filling factors, namely $\nu = 3/5$ and $\nu = 4/7$, also reveal domain formation, but more importantly confirm the expected polarization of composite fermions. In our discussion of the NMR measurements at $2/3$, we have not differentiated between the high and low current regimes as in the previous chapter. This is the topic of the next section.

5.3 The Low Current vs the High Current Regime at $\nu = 2/3$

The $\nu = 2/3$ transition in the HLR and SLR regimes are studied separately in this section by means of RDNMR. We also present measurements of the transition at a higher temperature and finally, we investigate the time evolution of the transition peak at different currents by switching the onresonance RF-signal on and off.

5.3.1 The High Current Regime

We performed RDNMR at different positions of the high current transition peak near $\nu = 2/3$. The results, plotted in Fig. 5.11, were obtained after sweeping the gate in order to go from a low to a high filling factor [Fig. (a)], and from a high to a low filling factor [Fig. (b)], as indicated by the arrows on the top panels. Qualitatively, the results are independent of the sweep direction. The curves shown in the main figures are RDNMR frequency sweeps for different constant gate voltages at $B = 8.1$ T. We have plotted ρ_{xx} vs polarization and the curves are vertically offset for clarity. The upper left panels of both figures show the gate voltage sweeps already plotted in Fig. 4.3. The numbered colors on the graph correspond to the position on the transition peak where we carried out the RDNMR experiments of the main plot.

There are several interesting phenomena which can be inferred from this picture. Firstly, the two resonance lines at $\mathcal{P} = 0$ and $\mathcal{P} = 1$ indicate the presence of domains, as mentioned above. Secondly, there is a remarkable change in amplitude between the $\mathcal{P} = 1$ and the $\mathcal{P} = 0$ resonances at different positions on the resistance peak. On the higher filling factor side, the $\mathcal{P} = 1$ resonance line is stronger than the $\mathcal{P} = 0$ line (red curve 2 and green curve 3). As we progress along the ρ_{xx} curve and move to lower filling factors, the $\mathcal{P} = 1$ line becomes much weaker and eventually disappears, while the $\mathcal{P} = 0$ line gains in strength [violet curve 4 and orange curve 5, and the magenta curve 6 in Fig. (b)]. This might seem counter-intuitive at first because the transition occurs from a spin-unpolarized ground state at high filling factor to a spin-polarized ground state at low filling factor ($\eta \propto B/\sqrt{\nu}$ at constant B). Hence, the $\mathcal{P} = 1$ domains should be dominant on the low filling factor side and the $\mathcal{P} = 0$ domains on the high filling factor side of the transition peak. This situation is easier visualized with the aid of Fig. 5.12. However, we should recall that the width of the ρ_{xx} peak is caused by a current-induced nuclear spin polarization, since the transition is Overhauser-shifted from the

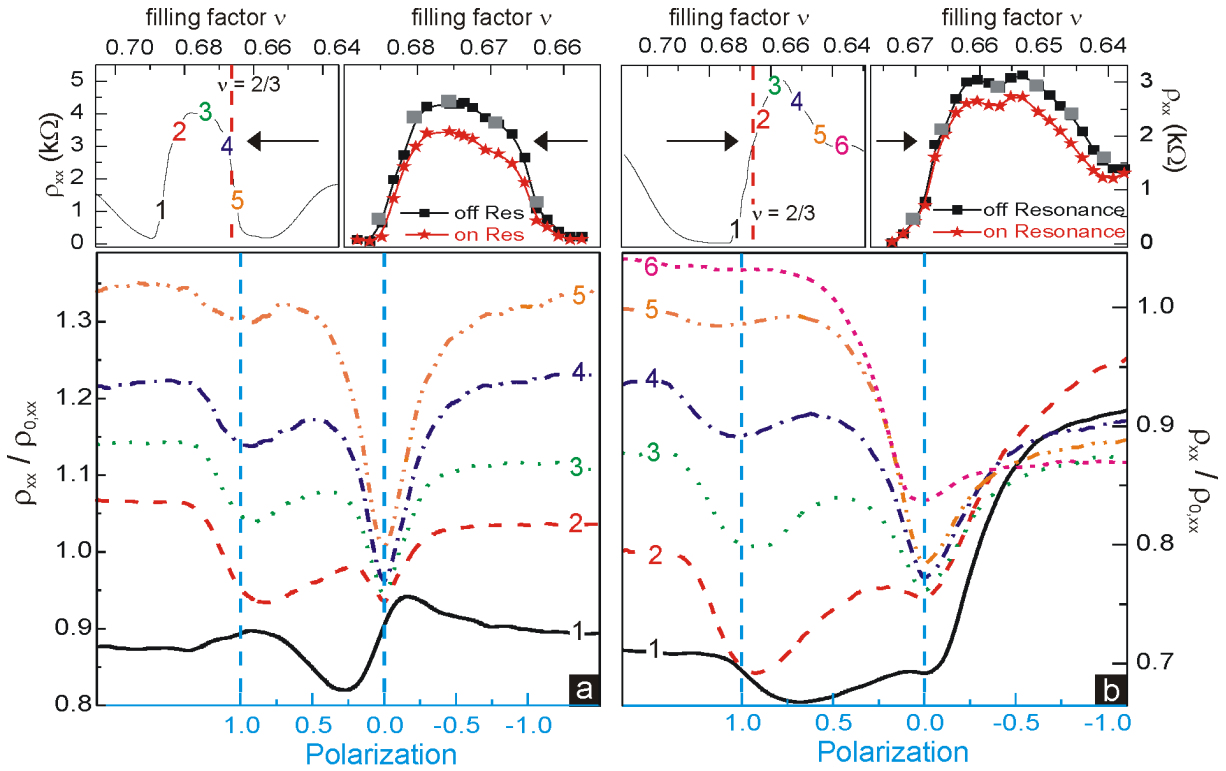


Figure 5.11: Study of the RDNMR resonance lines at different gate voltages ($B = 8.1$ T, $T = 55$ mK and $I = 40$ nA). In (a) the gate voltage has been swept from low to high filling factor and in (b) from high to low. The main figures represent RDNMR measurements for several constant gate voltage values. The upper left panels of both figures show the gate voltage sweeps also shown in Fig. 4.3. The colored numbers indicate the position on the peak, where the RDNMR was carried out (main figure). The upper right panels compare the ρ_{xx} values for the on and off-resonance case.

original value η_0 . That means that on the high filling factor side of the peak, the *minority phase* domains, in this case the polarized domains, will be stabilized by the non-equilibrium current-induced nuclear spin polarization. By randomizing the nuclei with the RF-signal, we shift the transition back to η_0 and the minority phase domains vanish. As a result, the resistance transition peak diminishes, leading to the resonance dip observed in ρ_{xx} . Likewise, on the low filling factor side, the unpolarized domains are the minority phase and the contribution of the $\mathcal{P} = 0$ line is strongest (curves 4 and 5). Thus, in our experiments, we are detecting the changes in the minority phases rather than the changes in the majority phases. The same situation occurs at the $\nu = 3/5$ transition in which the strongest dip originates from the minority phase domains, see Fig. 5.9. It is therefore important to remark that by doing RDNMR experiments we are not carrying out a thermodynamical measurement, as in a conventional NMR experiment. It

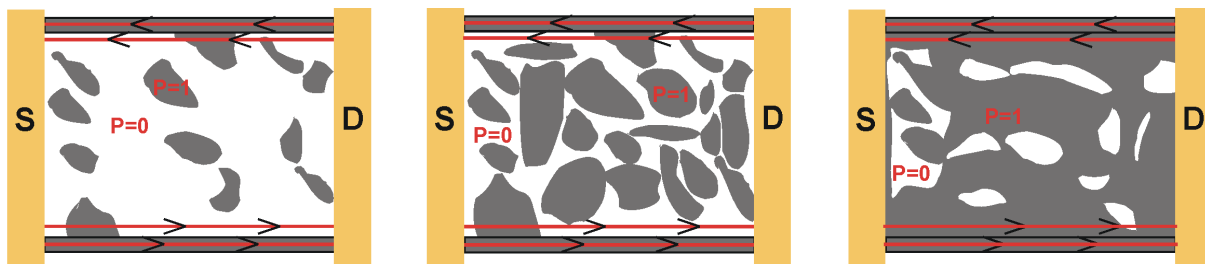


Figure 5.12: (a) On the high filling factor side of the transition peak, the unpolarized region dominates and the $\mathcal{P} = 0$ domains should be in the majority. (b) In the center of the peak, both phases should be equal and in the low filling factor side, the $\mathcal{P} = 1$ domains are expected to be the majority.

is difficult to analyze the data in more detail since a theoretical description of the mechanism responsible for the large resistance peak has not been presented to date.

The third interesting observation in this graph can be seen from the top right panels of both figures. Here, we have plotted the value of ρ_{xx} off-resonance, i.e. ρ_{xx} at constant B -field and V_{gate} values with the RF-source on but away from the Larmor resonance frequency (black squares), and the ρ_{xx} on-resonance, i.e. whenever the RF-frequency equals the Larmor frequency of the nuclei (red stars). Consequently, non-resonant heating effects could be ruled out by comparing the on and off-resonance signals⁹. The data were obtained by performing RDNMR measurements at different gate voltages, covering the whole width of the HLR peak. Evidently, ρ_{xx} is smaller for the on-resonance signal than for the off-resonance signal. This situation is true for the whole extent of the ρ_{xx} peak. Therefore, we can be certain that a mere shift in the peak, due the Overhauser effect, cannot be the only reason for the resistance change in the on-resonance condition. Otherwise, we would expect ρ_{xx} to decrease on one side of the peak and increase on the other (see section 5.3.2). This shows that the amplitude of ρ_{xx} is strongly affected by randomizing the nuclei. The inhomogeneous nuclear spin polarization created by the high driving current is thus destroyed and order is partially restored in the electronic system.

Finally, the anomalous, “dispersion-like” line shape of the black curve 1 in both main figures cannot be understood in terms of two differently polarized domains. It occurs on the high filling factor side whenever the peak develops only to a small value [Fig. 5.11(b)] or has not yet completely vanished [5.11(a)]. Similar line shapes have also been observed around filling factors $\nu = 1, 1/3$, and $2/5$ as well as $2/3, 3/5$, and $4/7$ away from the spin transition. This will be addressed section 5.5. In the following, we focus on the low current regime at the $\nu = 2/3$

⁹Even though there is an increase in the nuclear spin temperature whenever we change their magnetization, it does not affect the electronic system since these two systems are very weakly coupled. Therefore, we can safely say that the electronic system is being measured isothermally.

transition.

5.3.2 The Low Current Regime

We have also studied the spin phase transition at $\nu = 2/3$ in the low current regime. Figure 5.13 is the analog to Fig. 5.11 but for $I = 1$ nA. In Figure 5.13(a) the gate has been swept in order to go from low to high filling factor and in 5.13(b) from high to low filling factor, as indicated by the arrows. The left top panels show gate voltage sweeps at a fixed magnetic field

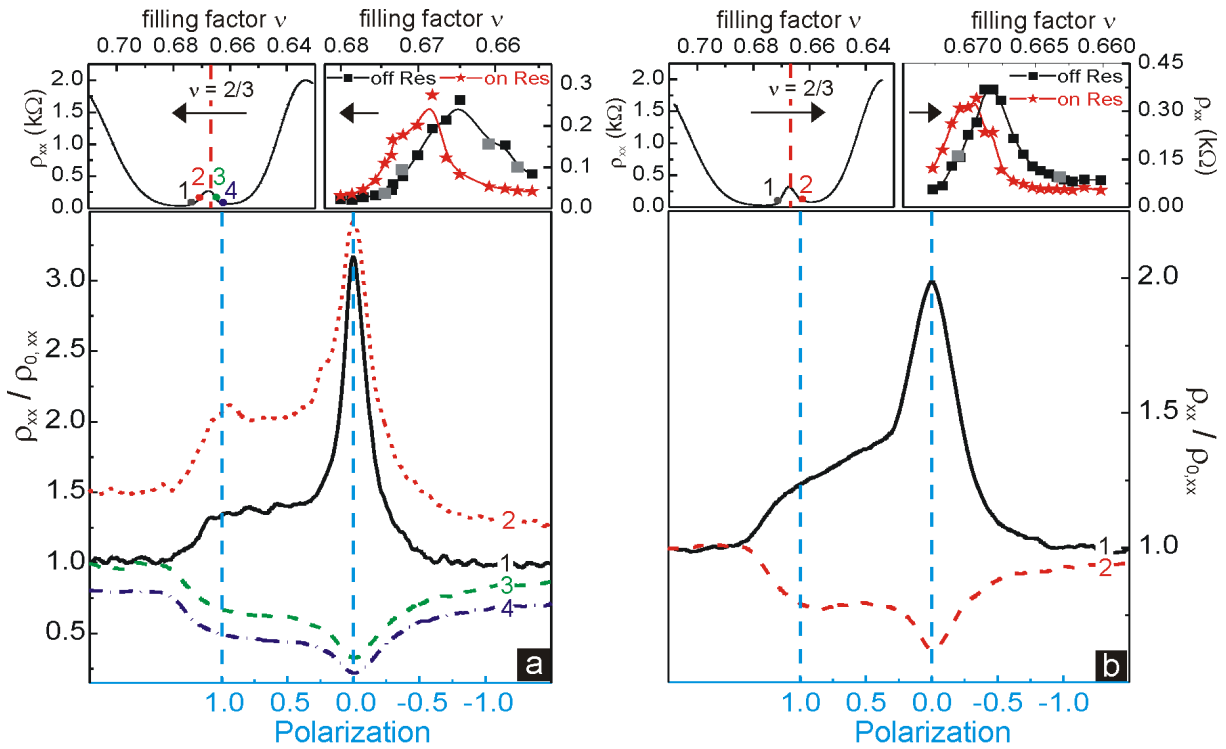


Figure 5.13: RDNMR experiments at the $\nu = 2/3$ spin transition in the low current regime for a gate sweep from low to high filling factor (a) and from high to low (b). The top left panels of both figures show the gate voltage sweeps and the right panels show the off- and on-resonance signals of ρ_{xx} (see also Fig. 5.11). These measurements were performed at $B = 8.1$ T and $T = 55$ mK.

of 8.1 T. The small peak at the $\nu = 2/3$ minimum indicates the spin unpolarized-polarized phase transition. The colored numbers show the position on the peak, where we stopped the gate voltage and swept the RF-signal. Some similarities can be seen between the high and low current regimes. For example, the two resonance lines at $\mathcal{P} = 0$ and $\mathcal{P} = 1$ in the RDNMR spectrum prove the interaction of electrons and nuclei and the existence of domains with these

two polarizations also in the low current regime¹⁰. However, some differences between both current regimes are also apparent. The value of ρ_{xx} increases as we reach the Larmor frequency of the nuclei if the gate is stopped on the high filling factor side of the peak. On the other hand, if the gate is stopped on the low filling factor side, ρ_{xx} decreases. On the right top panels, we again plot the value of ρ_{xx} off-resonance (black rectangles) and on-resonance (red stars). From these graphs, it is obvious that the changes in ρ_{xx} at a low current are due to an Overhauser shifting of the peak resulting from a negative hyperfine field. This clearly distinguishes the low from the high current regime, where this shift is masked by the global decrease of the resistance (Fig. 5.11). We note that at low currents the amplitude of the peak remains the same for the off and on-resonance case. This behavior strongly suggests a homogeneous nuclear polarization across the sample according to the thermal Boltzmann distribution and that the on-resonance applied RF-signal simply destroys part of the thermal nuclear spin polarization.

From the shifting of the peak, we can estimate the change in nuclear hyperfine magnetic field, B_N , due to the RF signal. By referring to equation 2.10, we obtain $\Delta B_N = \frac{nh}{e} \left(\frac{1}{\nu_1} - \frac{1}{\nu_2} \right) = 45$ mT for the sweep presented in Fig. 5.13(a) and 20 mT for the sweep shown in Fig. 5.13(b). After consulting Fig. 4.27, we expect a thermal B_N of about 360 mT at $T = 55$ mK. Hence, we depolarize 12% (6% in the other sweep direction) of the nuclei with the RF-signal, which results in a Zeeman energy change of approximately $0.9 \mu\text{eV} \equiv 10.5$ mK ($0.42 \mu\text{eV} \equiv 4.9$ mK for the other sweep direction).

5.3.3 Temperature and Time Dependence of the SLR and HLR Transitions

T = 250 mK

Since we presume that the SLR peak is only influenced by the thermal nuclear spin polarization, we would not expect an NMR signal to be detected if the temperature is high enough for the average thermal polarization to be insignificant. On the other hand, the HLR is influenced by a current-induced nuclear spin polarization and a signal should be measured even at higher temperatures. In order to verify this, we repeated the RDNMR experiments at $T = 250$ mK, where the nuclear thermal polarization is very low. As expected, we could not measure a signal at low currents at this temperature. At high currents, on the contrary, we obtained qualitatively the same results as in the low temperature experiments shown in Fig. 5.11. An RDNMR plot at $T = 250$ mK and $I = 100$ nA is presented in Fig. 5.14. Here, we see that the two resonance lines are separated by ≈ 29 kHz, which is expected for $K_{s,\text{max}}$ from the calibration curve of Fig. 5.5. The two distinct lines indicate that the domains are probably also static at this temperature. The fact that at $T = 250$ mK we could only observe changes in the RDNMR spectrum in

¹⁰Here again, both sweep directions show qualitatively almost the same behavior [see Figs. 5.13(a) and 5.13(b)]

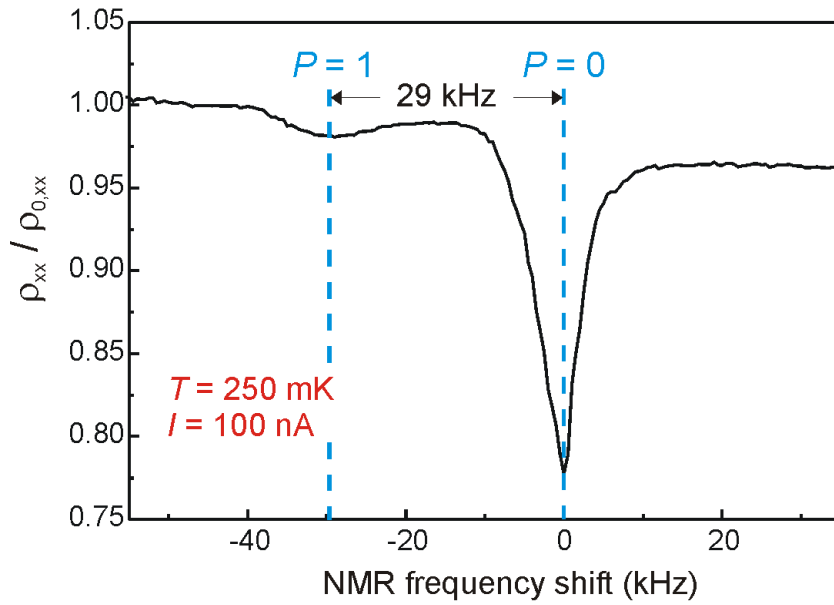


Figure 5.14: RDNMR measurement on the HLR peak at $T = 250$ mK. At this temperature no signal was observed in the SLR regime.

the high current regime but not at low currents reiterates our assertion that the HLR is mainly caused by an induced nuclear spin polarization. The SLR, however, is only affected by a thermal nuclear spin polarization which is only about 1% at $T = 250$ mK and $B = 10$ T. Hence, no effects are seen at this temperature in the low current regime.

Time evolution

Additional information about the electron-nuclear coupling can be obtained by studying the time behavior of the transition peak at different currents. The relaxation times of the longitudinal resistance peak at the transition are investigated for several currents between 0.7 and 42 nA by using an RF signal. The experiments were performed as follows: At a specific current value, the gate was swept to $\nu = 2/3$ at a constant magnetic field value, see Fig. 5.15(a). After reaching $2/3$, the gate sweep was stopped and the longitudinal resistivity, ρ_{xx} , was monitored as a function of time. We chose the necessary density and B -field ($n = 1.29 \times 10^{11}$ cm $^{-2}$ and $B = 8$ T) in order for both the SLR and HLR peaks to exist at exactly $\nu = 2/3$. During this process, an RF signal was irradiating the sample but at a frequency away from the Larmor frequency of the ^{75}As nuclei at 8 T (off-resonance). After the resistance reached equilibrium, we tuned the RF signal on resonance for 33 minutes while recording ρ_{xx} and then tuned the frequency off resonance again. This situation is depicted in Figs. 5.15(b) and (c) for two currents: $I = 4.9$ nA, in which the transition peak is in the SLR regime (b) and for $I = 42$ nA in the HLR regime (c).

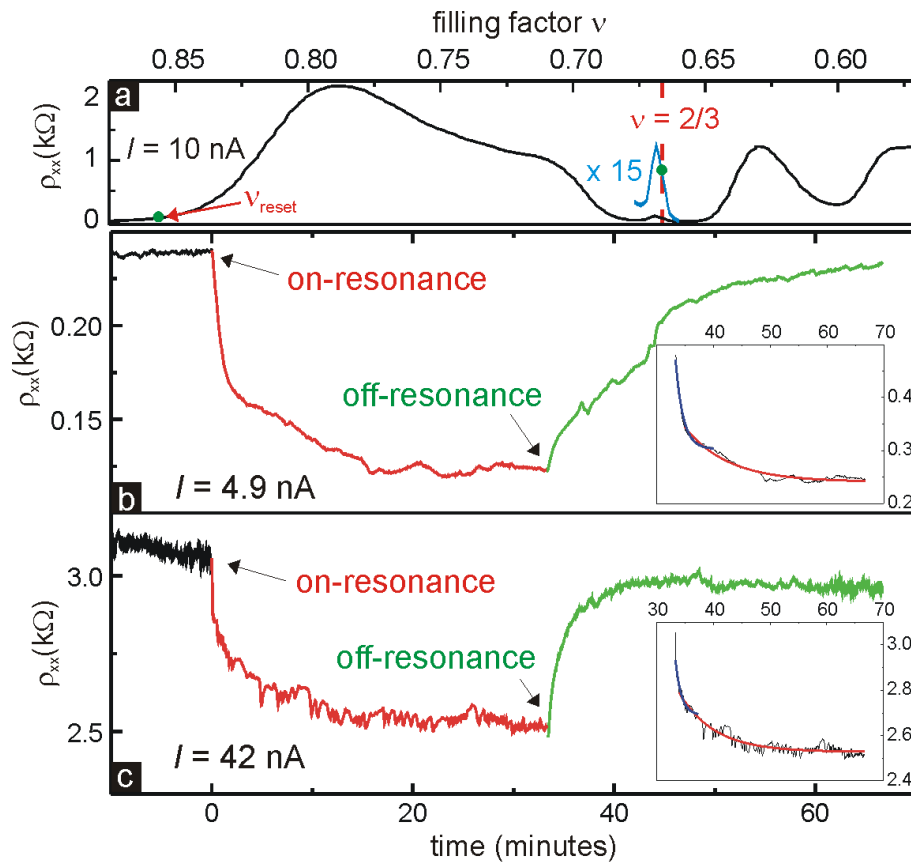


Figure 5.15: (a) Gate voltage sweep at $I = 10$ nA and $B = 8$ T. The blue curve is magnified 15 times and $\nu_{\text{reset}} \approx 0.87$. Time evolution of the SLR (b) and HLR (c) peaks after setting the RF signal on-resonance (red curves) and again off-resonance (green curves).

After the measurement of each current value, we swept the gate back to $\nu_{\text{reset}} \approx 0.87$, changed the current, waited at that filling factor for 30 minutes in order to reset the system, and then swept back to $\nu = 2/3$ [see Fig. (a)]. In both regimes, the resistance drops exponentially after tuning the RF on resonance (red curves). At low currents, the SLR resistance peak decreases due to a shifting of the transition peak, while at high currents, the HLR is partially destroyed (see Figs. 5.11 and 5.13). By fitting an exponential function to the decreasing, on-resonance resistance, depicted in the insets of both figures, it is possible to determine the relaxation time T_1 . The exponential fit, shown as a red curve in the insets, renders $T_1 = 7.61 \pm 0.5$ min for the low current regime [Fig.(a)] and $T_1 = 6.2 \pm 0.3$ min for the high current regime [Fig.(b)]. If we only consider the first 5 minutes after switching on the RF signal, however, we obtain a faster time constant than if we also consider latter times. This situation is in good agreement with the current switching experiments presented in the previous chapter (Fig. 4.12). The expo-

ponential fit of the first 5 minutes (blue curves of insets) yields: $T_1(\text{SLR}) = 1.35 \pm 0.2$ min and $T_1(\text{HLR}) = 1.06 \pm 0.15$ min. Surprisingly, the relaxation times obtained are very similar for all studied currents in both regimes and hence no T_1 current dependence can be clearly observed.

For that reason, we decided to study the time dependence of the resistance as a function of current more carefully after setting the RF signal again off resonance [green curve in Figs. 5.15(b) and (c)] and analyzing the relaxation of the peak back to its original value. Once more, the peak rises exponentially and for most current values, two different time constants T_1 were determined again. In this case, however, we could distinguish between a short time constant $T_1(\text{short})$, which is independent of the current applied, and a longer constant $T_1(\text{long})$ which is current dependent. The time relaxation constant is plotted vs current in Fig.5.16 [$T_1(\text{short})$ in blue and $T_1(\text{long})$ in red]. The inset shows a representative ρ_{xx} vs time plot (green) and the fitted curve (black) after the RF has been set off resonance at $I = 14.1$ nA. The reason for

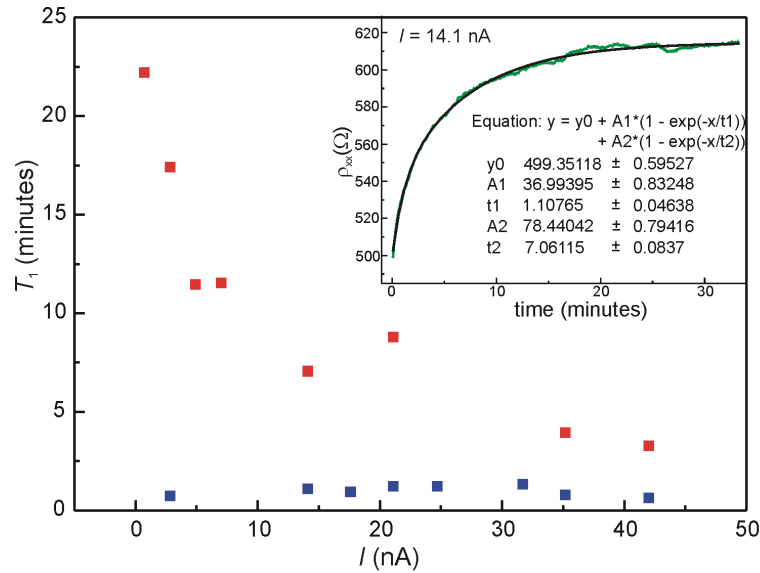


Figure 5.16: Time relaxation constant T_1 vs current after the RF has been set off resonance. The blue symbols are a short T_1 and the red symbols are a long T_1 obtained from a an exponential fit of the curves. Inset: Longitudinal resistivity ρ_{xx} vs time at $I = 14.1$ nA (green curve). The black line is an exponential fit to the data.

having at least two time constants in these experiments might be due to the fact that the change in resistance is caused by several factors. In addition to the nuclear relaxation, switching the RF signal on and off resonance might provoke small changes in the temperature, which would cause the peak to shift (at low currents) or to alter its amplitude (at high currents). Furthermore, it has been shown in section 4.6, figure 4.18 that the HLR resistance continues to rise even after many hours, due the dynamic nature of the domain structure, which may lead to extremely long time

constants. It could therefore be that the short relaxation time constant, which is independent of the current, might not be connected with the nuclear system, whereas the long relaxation time, which is current dependent, could actually be the T_1 of the nuclei. The enhancement of the relaxation rate (T_1^{-1}) with increasing current shows once more that the nuclear and electron spins are more strongly coupled at high currents. The dependence of T_1 on the current, which seems to be exponential, might provide important information about the dissipation mechanism of the transition peak.

5.3.4 Conclusions

In conclusion, the RDNMR results obtained in this section support some of the ideas developed in the previous chapter concerning the low and high current regimes at $2/3$. For example, the formation of domains could be proven in both current regimes. Also, the RDNMR experiments taken at different positions of the transition peak proved that the HLR is caused by an inhomogeneous nuclear hyperfine field (the peak is always destroyed with RF-irradiation) while the SLR peak is only affected by a homogeneous nuclear field (shifting of the peak with RF). Experiments at $T = 250$ mK strengthened this conclusion. It was also observed from the amplitude of the two resonance lines that the non-equilibrium nuclear spin polarization in the HLR regime is stabilized by the minority phase domains. In the SLR, on the other hand, the amplitude of the lines remains constant independent on whether RDNMR was performed on the high or low filling factor side of the peak. From this information, we can infer that in the HLR regime a peak in ρ_{xx} is formed, even if one domain is more abundant than the other, while the SLR is only seen when both domains types are equally represented. The time relaxation measurements show a current-independent and a current-dependent time constant. The latter might deliver interesting information regarding the mechanism leading to dissipation.

5.4 Samples under Strain: Quadrupole Splitting

In section 2.4.6, we showed that Kronmüller *et al.* reported an anomalous four-fold splitting of the RDNMR lines in the HLR regime (see reference [6]). So far, all the RDNMR curves presented in this chapter have not revealed such an anomaly. In this section, we will clarify the reason for the four-fold splitting. For that purpose, it is necessary to briefly introduce the quadrupole interaction.

Besides the hyperfine interaction with electrons, nuclei can also interact with an electric field gradient EFG if they possess a nuclear quadrupole moment Q_N . Nuclei with a spin $I > 1/2$, such as ^{69}Ga , ^{71}Ga and ^{75}As with $I = 3/2$, have a non-spherical charge distribution and thus a finite Q_N . An EFG can exist due to intrinsic properties such as the surrounding electron charge

distribution. The interaction between the nuclear quadrupole moment and the EFG, $\Delta\mathbf{E}$, can be expressed by the following Hamiltonian [70]:

$$H_Q = \frac{1}{6} \sum_{i,j} Q_{i,j} \Delta\mathbf{E}_{i,j}. \quad (5.16)$$

Here, $\Delta\mathbf{E}_{i,j}$ is a tensor quantity which can also be written as:

$$\Delta\mathbf{E}_{i,j} = \frac{\partial^2 V}{\partial x_i \partial x_j}, \quad (5.17)$$

where $x_i (i = 1, 2, 3)$ are the coordinates x , y and z and V is the electrostatic potential. By choosing an appropriate coordinate system, it is possible to represent the EFG by three principal axes: V_{xx} , V_{yy} and V_{zz} .

If the nucleus is at a site of cubic symmetry, which is usually the case in GaAs, then $V_{xx} = V_{yy} = V_{zz}$, which in combination with the solution to the Laplace equation ($\sum_i V_{ii} = 0$) yields zero for all three derivatives from equation 5.17. Therefore, the nucleus is not affected by quadrupole effects in this case. The allowed transitions $\Delta m_I = \pm 1$ are all of the same energy and only one line appears at $\gamma_N B_z$ (for zero Knight shift) in the NMR spectrum as illustrated in Fig. 5.17(a) for a nucleus with spin $I = 3/2$.

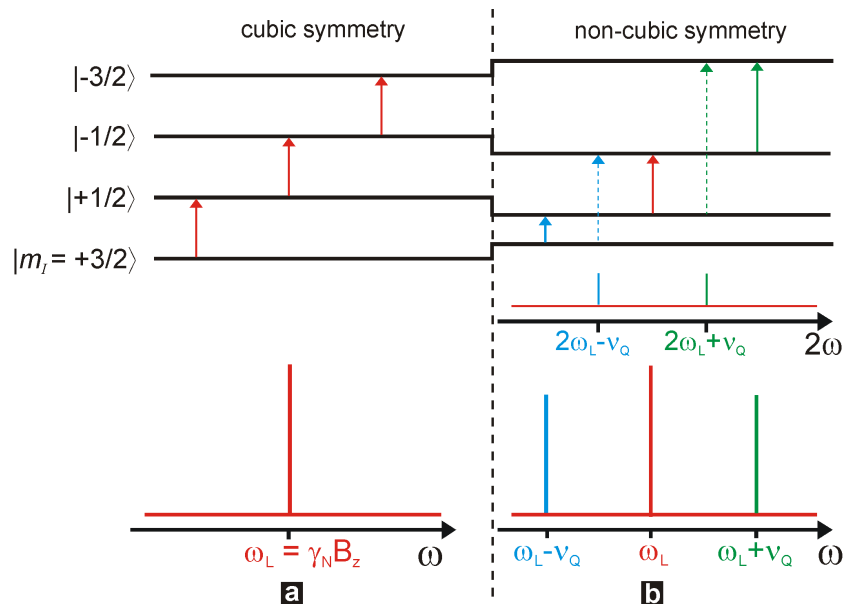


Figure 5.17: Schematic energy diagram for a nucleus with spin $I = 3/2$. (a) If the nucleus is located in a lattice of cubic-symmetry, the three $\Delta m_I = \pm 1$ transitions are identical and no quadrupole splitting is observed in the NMR spectrum. (b) If the cubic symmetry is broken, two satellite peaks at $\omega_L \pm \nu_Q$ appear due to the quadrupole interaction. Also $m_I = \pm 2$ transitions are allowed.

On the other hand, if the cubic symmetry is broken, for example caused by a distortion of the crystal lattice due to a strained sample, the EFG couples to the nuclear quadrupole moment Q_N . In general, the energy splitting due to the quadrupole interaction is given by:

$$\Delta E_Q = \frac{h\nu_Q}{2} \left(m_I^2 - \frac{I}{3}(I+1) \right), \quad (5.18)$$

in which ν_Q is the so-called “quadrupole frequency:”

$$\nu_Q = \frac{3eQ_N V_{zz}}{2I(2I-1)h}. \quad (5.19)$$

These formulas were derived for $\Delta_N \gg \Delta E_Q$ in first order perturbation theory¹¹. In particular, for $I = 3/2$ the NMR lines split into three as shown in Fig. 5.17(b). The central transition (red), i.e. $|m_I = 1/2\rangle \rightarrow |m_I = -1/2\rangle$ remains unaffected, but two satellite lines appear, shifted from the central line by $-\nu_Q$ (blue) and $+\nu_Q$ (green) for the $|m_I = 3/2\rangle \rightarrow |m_I = 1/2\rangle$ and $|m_I = -1/2\rangle \rightarrow |m_I = -3/2\rangle$ transitions, respectively. Due to the coupling between the quadrupole moment of the nuclei in the non-cubic lattice sites and the EFG, the transition selection rules $\Delta m_I \pm 1$ are lifted, thus enabling $\Delta m_I \pm 2$ transitions. If an rf-signal is applied at twice the Larmor frequency, resonance lines may be observed at $f = 2\omega_L \pm \nu_Q$.

In the measurements discussed so far, no quadrupole effects were observed. In this section, we present results obtained from samples which are subjected to strain and therefore show a quadrupole splitting of the NMR lines. In Fig. 5.18, we show two RDNMR spectra at $\nu = 1/2$ for two different samples of the same wafer [see Fig. 3.1(b)]. In (a) we replot the same curve presented in Fig. 5.3 where only one NMR line, Knight shifted from the substrate reference signal, is observed. In Figure (b) we perform again the same RDNMR experiment at similar B -field and density values ($B \approx 9.2$ T and $n = 1.11 \times 10^{11} \text{ cm}^{-2}$), but with a sample mounted differently to the chip carrier than one used for the spectrum in figure (a). Three resonance lines are observed in the RDNMR spectrum (blue curve) as opposed to the one resonance line previously measured. The central line in spectrum (b) is shifted from the substrate reference signal (red curve) by approximately the same amount as in figure (a) and the two additional resonances are equally separated (≈ 17 kHz) from the central line. From this information, we can conclude that the three-fold splitting of the lines can be attributed to the nuclear quadrupole interaction, which is most likely caused by an external strain due to the mounting of the sample¹².

After conducting the measurements at $\nu = 1/2$, we changed the density to $n = 1.49 \times 10^{11} \text{ cm}^{-2}$, at constant B -field (9.2 T) in order to go to filling factor $\nu = 2/3$. At this density, the unpolarized-polarized transition is present in our sample. In Fig. 5.19(b), we show RDNMR

¹¹This formula is obtained by assuming axial symmetry so that $V_{xx} = V_{yy}$ which is the case even for strained GaAs. The reader may consult the following references for a complete derivation of equation 5.18: [70, 71, 129].

¹²The strained samples were mounted to the chip carrier by using a rubber-based glue (“Fixogum”), while the non-strained samples were attached to the carrier with polymethyl methacrylate (PMMA).

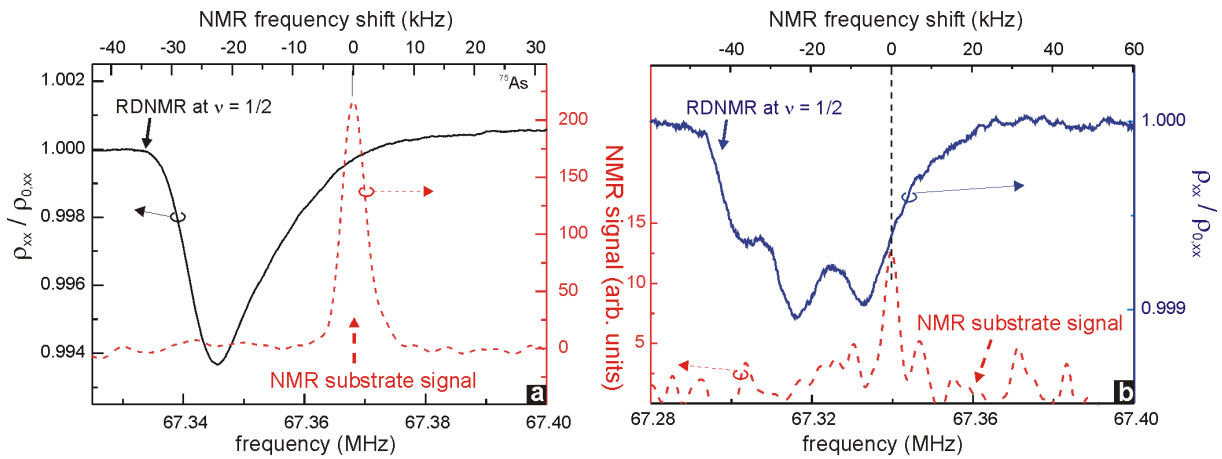


Figure 5.18: (a) In a sample without strain, the RDNMR spectrum at $\nu = 1/2$ (black line) only shows one resonance line (same spectrum showed in Fig. 5.3). (b) On the other hand, in a sample under strain, three resonance lines appear in the spectrum due to the quadrupole interaction. Both samples are from the same wafer (020502.1), but mounted differently on the chip carrier.

spectra obtained at the $\nu = 2/3$ spin transition peak in the high current regime. In Figure 5.19(c), we have replotted the measurement at $\nu = 1/2$ for comparison. The black curve in (b) reveals five features instead of the usual two lines as seen in Fig. 5.6. The substrate reference signal (red curve in Fig.(a) with maximum at $f_0 = 67.340$ MHz) coincides with one of the resonance lines of the black curve, Fig. 5.19(b), which can now be identified as the zero-shift resonance. All lines are equidistant and separated by ≈ 17 kHz. Experiments at $2f_0$ show two weak resonance lines, which are separated by ≈ 34 kHz and lie at exactly $2f_0 \pm 17$ kHz [yellow curve in Fig.5.19(a)]. This spectrum can be interpreted as follows: Each of the two resonance lines obtained from nuclei interacting with electrons in $\mathcal{P} = 0$ and $\mathcal{P} = 1$ domains, as presented in Fig. 5.6, split into three lines by virtue of the quadrupole interaction. The $\mathcal{P} = 1$ line is Knight shifted from the $\mathcal{P} = 0$ line by ≈ 34 kHz as expected from the calibration curve of Fig. 5.5 for a density of $n = 1.49 \times 10^{11} \text{ cm}^{-2}$. The quadrupole splitting is $\Delta E_Q \approx 17$ kHz for this sample and therefore two of the lines coincide, resulting in five instead of six lines. The first three features at lower frequency are much weaker than the last two resonance lines since the measurements were conducted on a position of the transition peak where the $\mathcal{P} = 0$ resonance is better developed than the $\mathcal{P} = 1$ as in curve 5 of Figs. 5.11(a) and (b). The experiment at filling factor $\nu = 1/2$ [blue curve in Fig. 5.19(c)] shows that while the quadrupole splitting is independent of the density (ΔE_Q is still 17 kHz), the Knight shift is now ≈ 23 kHz as expected for $n = 1.11 \times 10^{11} \text{ cm}^{-2}$. The results at $\nu = 1/2$ corroborate the interpretation of the spectrum at the $\nu = 2/3$ transition.

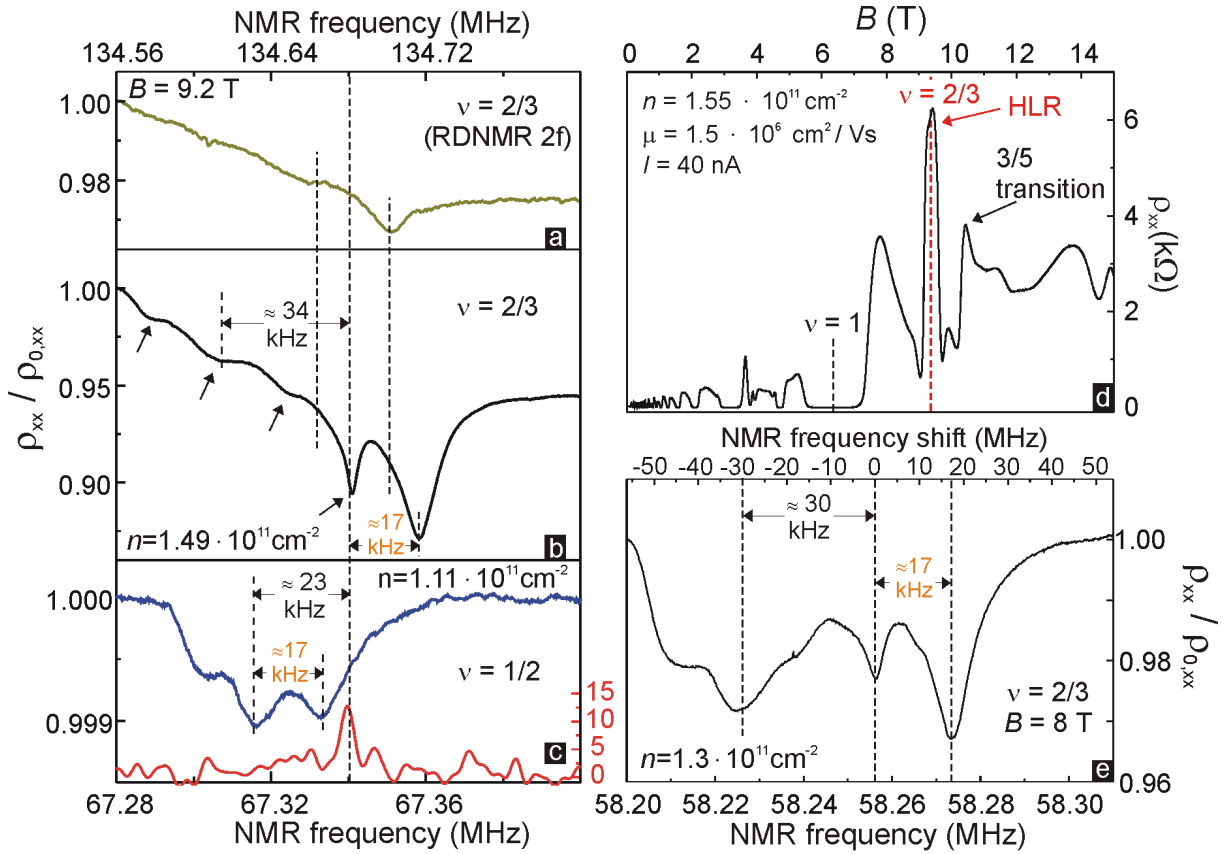


Figure 5.19: RDNMR measurements on the HLR peak around the resonance frequency f (b) of the ^{75}Ga nuclei and twice the frequency $2f$ (a) at $B \approx 9.2$ T and $n = 1.49 \times 10^{11} \text{ cm}^{-2}$ for a strained sample. RDNMR at $\nu = 1/2$ [blue curve in (c)] at $n = 1.11 \times 10^{11} \text{ cm}^{-2}$ and NMR signal (red curve) of the substrate. (d) ρ_{xx} vs B -field in the HLR regime. (e) RDNMR on the HLR at $B = 8$ T and $n = 1.3 \times 10^{11} \text{ cm}^{-2}$. All measurements were performed at $T = 55$ mK.

A sample under the influence of strain also affects the transport features of the high current $\nu = 2/3$ transition peak. In Fig. 5.19(d), we see that ρ_{xx} increases to more than 6 k Ω while for a sample without strain, ρ_{xx} is considerably smaller (only ≈ 4 k Ω as observed in Fig. 4.3). Finally, we repeated the RDNMR experiment for a smaller density ($n = 1.3 \times 10^{11} \text{ cm}^{-2}$) and magnetic field ($B = 8$ T) for a situation in which the $\mathcal{P} = 0$ and $\mathcal{P} = 1$ are similarly strong [Fig. 5.19(e)]. While the Knight shift decreased to ≈ 30 kHz, in agreement with the calibration curve 5.5 for this density, ΔE_Q remained at 17 kHz. The spectrum shows four clear resonance lines and a very weak feature at -17 kHz.

If the strain on the sample increases, then the quadrupole splitting also increases [105]. Furthermore, if the splitting is comparable to the Knight shift, a situation can occur in which several resonance lines overlap yielding four lines in the spectrum. This is indeed the case for the curi-

ous four-fold splitting reported earlier in the HLR regime. In Fig. 5.20, we plot RDNMR measurements performed on the high current transition peak at $B \approx 8.1$ T and $n = 1.3 \times 10^{11} \text{ cm}^{-2}$ in which an original type A sample was employed [Fig. 3.1(a)]. Plot 5.20(b) clearly shows four

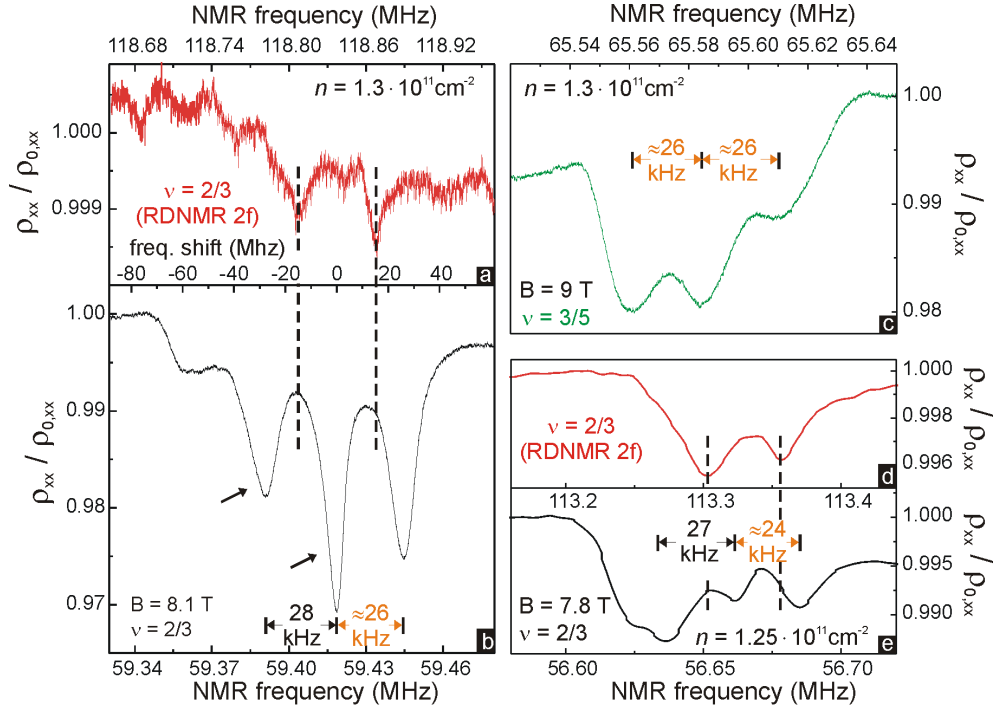


Figure 5.20: RDNMR on the HLR peak at f (b,e) and $2f$ (a,d) of a (15,14) nm QW using two samples type A sample under strain. [For Figs. (a-c), a sample from 100797.3 was used and for (d-e) a sample from 052098.2.] (c) RDNMR performed on the $\nu = 3/5$ spin phase transition peak.

resonance lines, where the last three lines are nicely developed. The double resonance, $2f$, measurements indicate that the lines are quadrupole split by ≈ 26 kHz¹³. Moreover, the expected Knight shift for the $\mathcal{P} = 1$ line is ≈ 28 kHz. There are two overlapping features, marked by the arrows in the figure, so that instead of six lines, four lines are present. The RDNMR spectrum at the $\nu = 3/5$ transition ($B = 9$ T) shows a three-fold splitting of the $\mathcal{P} = 1/3$ resonance line. The splitting $\Delta E_Q = 26$ kHz is independent of the magnetic field as expected.

In some samples, the $\Delta m_I = \pm 2$ lines at $2f_0 \pm \nu_Q$ are strongly developed. In Figs. 5.20(d) and (e), we show the $2f$ and f RDNMR measurements, respectively, for a 14 nm QW of type A at constant field $B = 7.8$ T. The expected $K_{s,\max} = 27$ kHz at $n = 1.25 \times 10^{11} \text{ cm}^{-2}$ and a quadrupole splitting $\Delta E_Q \approx 24$ kHz are both observed. Hence, four lines become visible in the RDNMR spectrum. These experiments show that the quadrupole interaction, due to strain

¹³The density is similar to the one used in the experiments reported in reference [6].

caused by the mounting of the sample, is the origin of the four-fold splitting previously reported in the HLR regime [6].

tilted B -field

Another way to verify that the splitting of the lines is due to the quadrupole interaction is by carrying out tilted B -field RDNMR experiments. Equation 5.18 can be generalized for this situation by considering a magnetic field in the z -direction which differs from the direction of the principal axis of the electric field gradient tensor z' by the tilt-angle θ [70]:

$$\Delta E_Q = \frac{h\nu_Q}{2} \left(\frac{3 \cos^2 \theta - 1}{2} \right) \left(m_I^2 - \frac{I}{3}(I + 1) \right). \quad (5.20)$$

What is important in this equation is the $\frac{3 \cos^2 \theta - 1}{2}$ dependence. The quadrupole splitting ΔE_Q decreases with the angle until it completely vanishes at $\theta = 54.7^\circ$. At higher angles the splitting should increase again until reaching $\pm \frac{\nu_Q}{2}$. Also, the NMR resonance line broadens since all possible orientations of the nuclear spins relative to the external B -field may exist between 0 and θ . These experimental findings have been corroborated by simulations presented in reference [23]. In the RDNMR experiments at tilted B -field depicted in Fig. 5.21, we observe that the four-fold splitting at 0° [Fig.(a)], also shown in Fig. 5.20(e), slightly reduces at 11° [Fig.(b)], finally becoming one broad line at 20° [Fig.(c)] with a FWHM ≈ 40 kHz. The measurements were obtained by using the time-settling technique described in section 4.2.1. In figures (d)-(e), the same results were obtained in a 15 nm type A sample, but using an 800 μm wide Hall bar for the measurements. The four-fold splitting is clearly seen in this case. The measured Knight shift is ≈ 31 kHz (as expected for $n = 1.35 \times 10^{11} \text{cm}^{-2}$) while $\Delta E_Q \approx 27$ kHz [Fig. 5.21(f)]. At 15° , ΔE_Q reduces to 21 kHz and the four lines seem to develop into five lines although they are difficult to resolve, see Fig. 5.21(e). At higher tilt-angles [32° , Fig. 5.21(d)] only one broad resonance line appears with a FWHM ≈ 30 kHz. This behavior is expected if the quadrupole interaction is responsible for the splitting of the lines and therefore strengthens our interpretation that ΔE_Q is responsible for the anomalous four lines previously observed.

5.5 Anomalous NMR Line Shape around $\nu = 1, 1/3$ and $2/3$

Spin phase transitions are not the only example where the spin degree of freedom is important in the FQH regime. Theoretical and experimental works have shown that at sufficiently low Zeeman energy, the lowest lying energy excitations around the QH ferromagnetic state $\nu = 1$ are topological excitations referred to as skyrmions. In RDNMR experiments, skyrmions have been speculated to be responsible for an anomalous line shape observed around $\nu = 1$ [93]. Even though the CF skyrmion analog should exist around $\nu = 1/3$ at vanishing Zeeman energy [89],

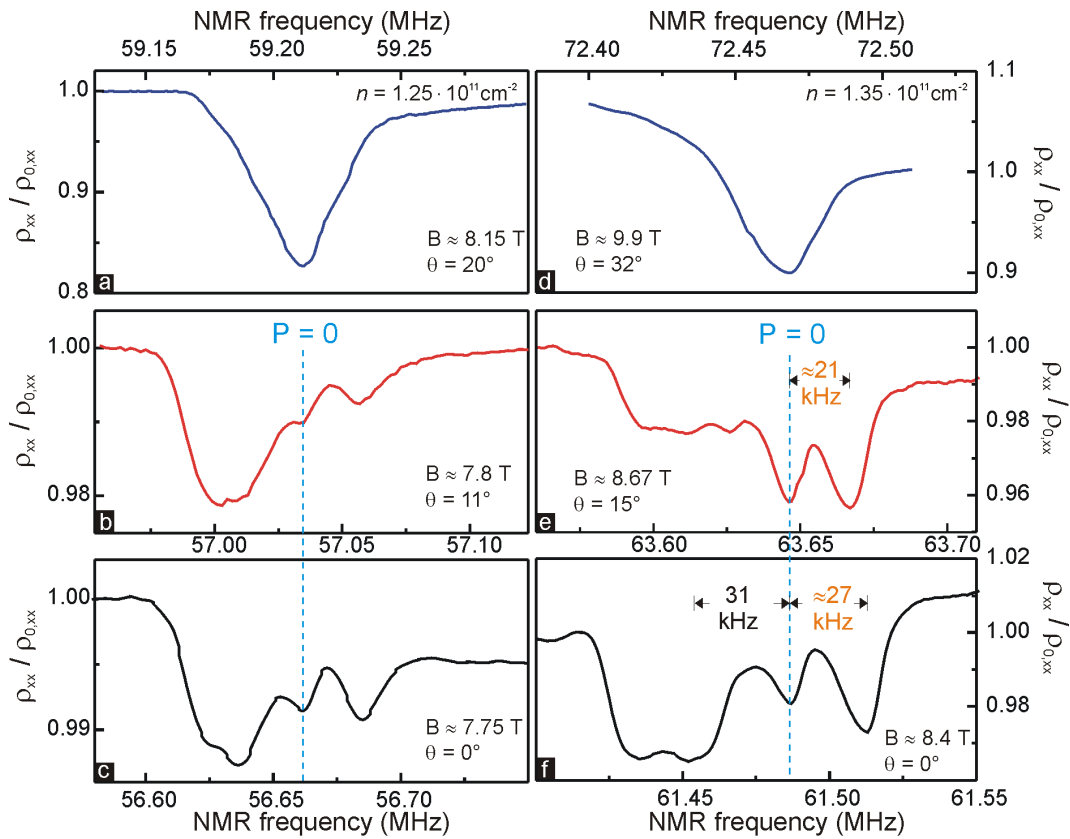


Figure 5.21: Tilted B -field RDNMR measurements on the HLR peak of a strained sample at 0° (a), 11° (b) and 20° (c) for a 14 nm QW using an $80\mu\text{m}$ wide Hall bar. A 15 nm QW was employed for the experiments shown in figures (d)-(f), but an $800\mu\text{m}$ wide Hall bar was used instead.

their existence was not revealed in various experiments [23, 130]. With this in mind, we carried out RDNMR measurements at filling factors close to $\nu = 1$ and $\nu = 1/3$. Figures 5.22(a) and 5.22(d) display a gate sweep at $B = 8$ T and $B = 15$ T, respectively. In the first figure, the ρ_{xx} minimum for $\nu = 1, 2/3$ and $3/5$ are visible. In the second figure, filling factors $\nu = 3/7, 2/5$ and $1/3$ are clearly identified. Figure 5.22(c) shows RDNMR measurements taken at filling factors $\nu = 0.76, 0.78, 0.8, 0.83$, i.e. in the vicinity of $\nu = 1$ as indicated by the color dots on the transport curve [5.22(a)]. The four curves, which colors correspond to the dot's colors, have been offset for clarity. The magnetic field was kept constant at $B = 6.75$ T for all four rf-sweeps. Interesting in this plot is the development of an anomalous line shape. Initially ρ_{xx} decreases, then increases and finally returns to its original value. Also, a third line, indicated by arrows, appears as we approach $\nu = 1$. It is shifted towards negative polarizations (dashed line indicates the position of $\mathcal{P} = 0$). This “dispersion-like” line shape is very different to the data of the $\nu = 2/3, 3/5$ and $4/7$ spin phase transitions as well as near filling factor $\nu = 1/2$ [Fig. 5.22(f)].

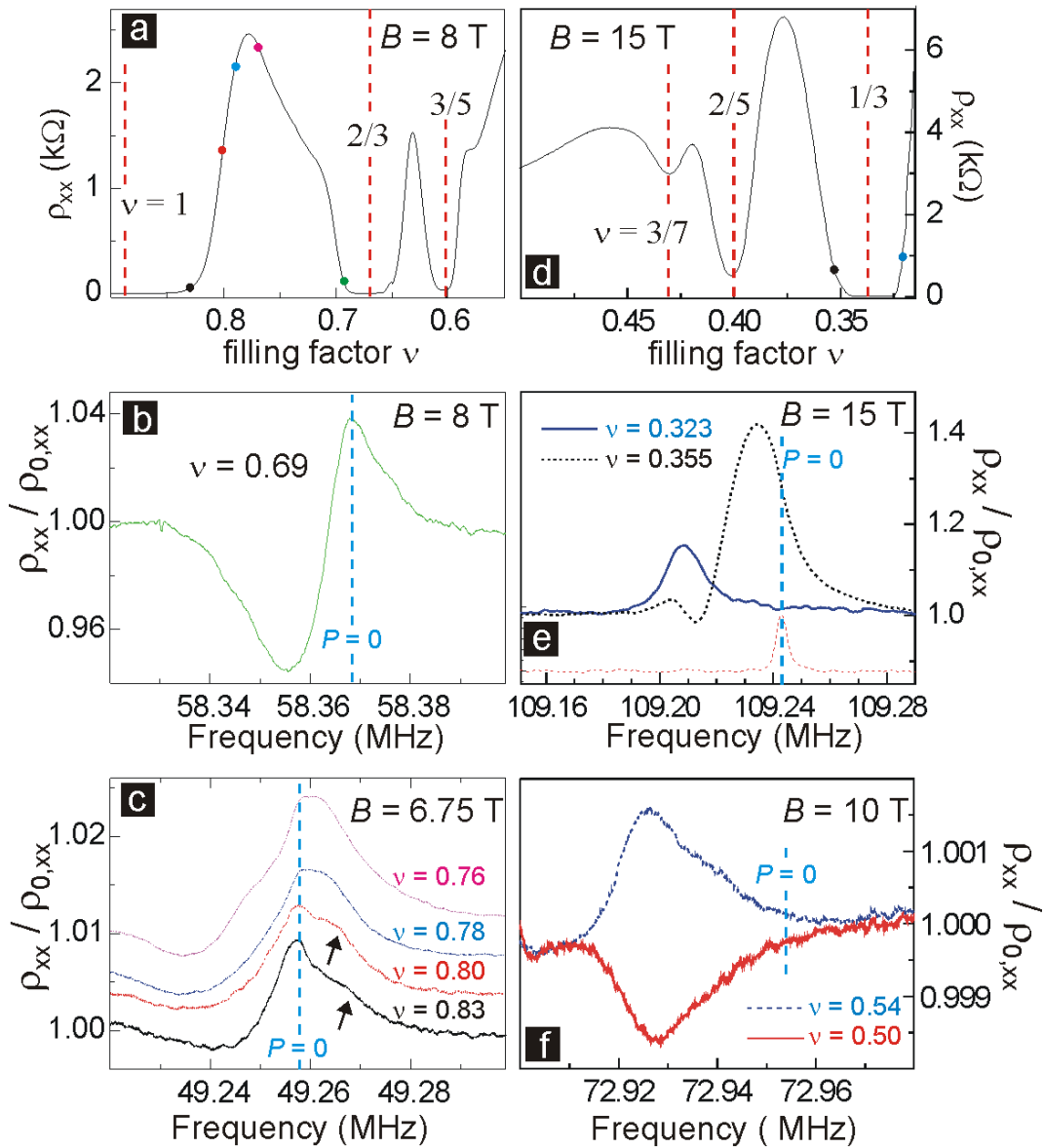


Figure 5.22: Gate voltage sweeps at $B = 8$ T (a) and $B = 15$ T (d), respectively. The black dots indicate the position where RDNMR experiments were performed. An anomalous line shape was observed in the RDNMR experiments at the high filling factor side of $\nu = 2/3$ [at $\nu = 0.69$, Fig.(b)], at the high filling factor side of $\nu = 1/3$ [at $\nu = 0.355$, plotted as a dashed curve in Fig.(e)], and at the low filling factor side of $\nu = 1$ [(Fig.(c)]. A conventional line shape is seen at the low filling factor side of $\nu = 1/3$ [at $\nu = 0.323$, plotted as a solid line in Fig.(e)], and of $\nu = 2/3$ (not shown), at the spin-phase transitions and at other filling factors, e.g. $\nu = 0.5$ and 0.54 [Fig.(f)].

Such anomalous line shapes are similar to the ones reported in the literature [93]. In order to clarify the question whether these lines may provide evidence for the existence of a skyrme crystal, we also carried out RDNMR experiments near filling factor $\nu = 1/3$ [at $\nu = 0.323$ and 0.355 shown in Fig. 5.22(e)]. On the high filling factor side of $\nu = 1/3$, a similar, anomalous resonance line is present [black, dashed curve in Fig. 5.22(e)]. This curve was measured at $B = 15$ T and $\nu = 0.355$. However, it is highly unlikely that this line shape indicates the existence of skyrmions around $\nu = 1/3$ due to several reasons: Firstly, if we compare it to the one observed at $\nu = 0.323$ [blue, solid line in Fig. 5.22(e)], i.e. for the case of quasi-hole excitations ($\nu < 1/3$), we do not observe the anomalous line shape but rather a conventional one. If skyrmions would exist in this region, the “unconventional” line should be present on either side of $\nu = 1/3$. Secondly, the ratio between the Zeeman to Coulomb energies ($\eta = 0.027$) is excessively large compared to the low spin-stiffness at this filling factor¹⁴. Optical experiments have shown that even at $\nu = 1$, where the spin stiffness is about thirty times larger [64, 131], skyrmions only exist below a critical $\eta_c = 0.011$ [88]. Moreover, the η values for the RDNMR measurements close to $\nu = 1$ at $B = 6.75$ T ($\eta = 0.017$) and around $\nu = 2/3$ at $B = 8$ T ($\eta = 0.019$) exceed η_c . Thirdly, RDNMR experiments near filling factor $\nu = 2/3$ [Fig. 5.22(b)] also display an anomalous line shape. This measurement was performed on the high filling factor side of $\nu = 2/3$ [the gate voltage and magnetic field were stopped at $\nu = 0.69$; the green dot in Fig. 5.22(a)] and at a constant field of $B = 8$ T. Since at this field, the QH ground state is unpolarized, the existence of skyrmions can be ruled out. The same situation also exists around $\nu = 2/5, 3/5$, and $4/7$ (not shown here). Figure 5.22(f) shows RDNMR lines for the filling factors $\nu = 0.5$ (red, solid line) and 0.54 (blue, dashed line)¹⁵. An increase in ρ_{xx} for the latter case and a decrease for the former case are seen. Important to notice here is the normal line shape obtained. This plot indicates that the details of the change in resistance depend sensitively on the particular choice of filling factor. The change in Zeeman energy due to rf-irradiation may increase as well as decrease the resistance. This may be the cause for the “strange” line shape near $\nu = 1, 2/3$ and $1/3$, since unpolarized and polarized regions may cause a different response on the resistance (for example decreasing for polarized regions and increasing for unpolarized ones).

From our data, we can infer that skyrmions are not likely to be the origin of the anomalous “dispersion-like” line shape. Instead, it seems that a coupling of the nuclear system with quasi-particle excitations (spin-aligned or spin-reversed), which exist around all filling factors investigated, might be responsible. It is probable that the line shape arises from a non-uniform response of the system to changes in E_Z . It remains unclear why, in contrast to $\nu = 1$, for fractional filling factors the anomalous line shape occurs only at the high filling factor flank

¹⁴The values of η have been corrected for finite thickness effects by using equations 2.20 and 2.21.

¹⁵Previous measurements done around $\nu = 1/2$ show that the NMR behavior at $\nu > 1/2$ and $\nu < 1/2$ is quite complex. It depends on parameters such as temperature, tilt-angle, magnetic field, etc. [62].

(quasi-electron excitations) and not at the opposite flank (quasi-hole excitations).

5.6 Outlook

The RDNMR/NMR technique introduced in this chapter can be extended to study additional spin phenomena present in the QHE. Until now, we have restricted our technique to spin transitions and low-energy collective excitations occurring in the lowest Landau level. In the higher Landau levels, a different situation prevails as new QH states appear, see Fig. 5.23. For example

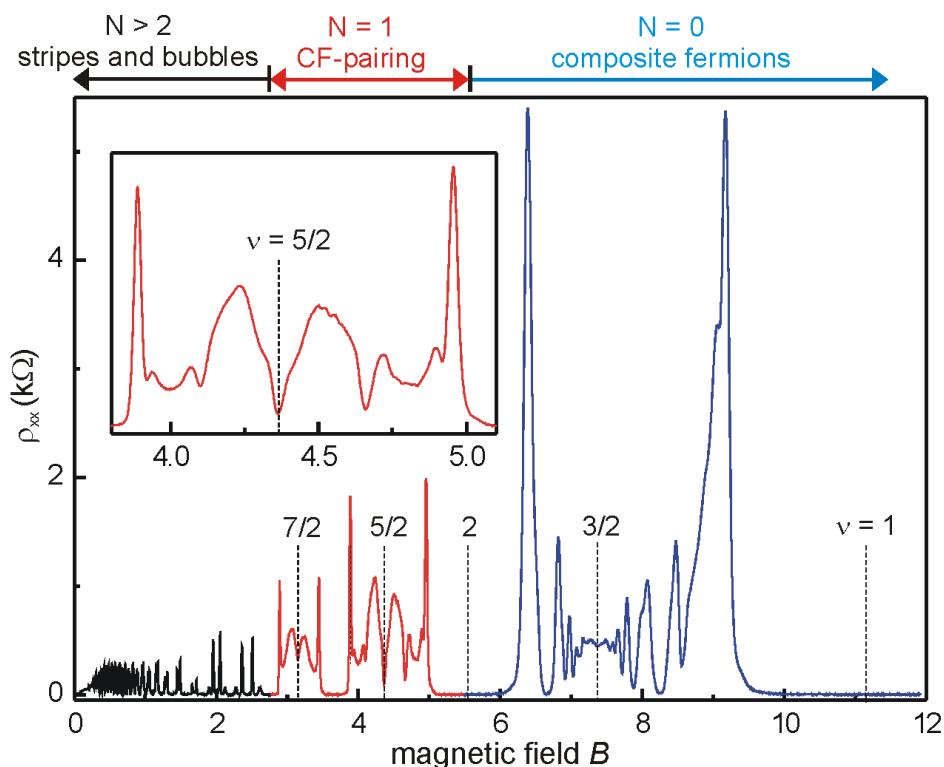


Figure 5.23: The FQHE at higher LLs. The even-denominator FQHE states at $N = 1$ ($\nu = 5/2$ and $\nu = 7/2$) are believed to be caused by pairing of CFs. The polarization and as a result the nature of the wavefunction remains an enigma. Sample from a heterostructure with a mobility of $\mu \approx 9.0 \cdot 10^6 \text{cm}^2/\text{Vs}$ at $n = 2.7 \times 10^{11} \text{cm}^{-2}$ (Wafer 496 from Umansky).

for $N \geq 2$, collective anisotropic ground states, in which the competition between the Coulomb and exchange energies forces electrons to cluster in “stripe” and “bubble” patterns, have been measured near even denominator filling factors (e.g. $\nu = 9/2$ and $11/2$) [53, 54, 132]. In the first excited LL, $N = 1$, FQHE states with even denominator were discovered at $\nu = 5/2$

and $7/2$, differing from the $\nu = 1/2$ and $\nu = 3/2$ metallic states in the LLL (see inset of Fig. 5.23) [133, 134]. A spin-singlet wavefunction was proposed [135] based on the idea of electron-pairing [42]. This unpolarized wavefunction seemed to be supported by the rapid collapse of the state at tilted B -fields [136]. However, subsequent numerical calculations indicated that a spin-polarized paired-wavefunction might be energetically more favorable than the spin-singlet state [137]. Even though recent work suggests that phase transitions might occur between a CF-pairing state to an anisotropic phase, similar to the $N \geq 2$ LLs states ([138, 139]), the polarization of the state remains an enigma. The technique developed in this work could be used to measure the Knight shift at $\nu = 5/2$ and $7/2$ (or near the fillings if the resistance vanishes) in order to determine the electron spin polarization and hence the nature of these QH states.

More recently, possible evidence for excitonic condensation has been observed in electron-electron bilayer systems at certain ratios of the QW center-to-center separation and magnetic length (d/ℓ_B), when each of the two layers are at half filling [140, 141]. As we have seen in this chapter, the electron spin polarization plays an important role at filling factor $\nu = 1/2$. However, in a closely spaced bilayer system, where the total filling factor $\nu_T = 1$, one would expect the system to be fully polarized. It has been suggested in reference [142], that studying the electron spin polarization might render important information concerning this condensate state. A possible application of the technique developed in this work could be to measure \mathcal{P} in this regime.

Chapter 6

Conclusions and Summary

The objective of this thesis is to study spin phenomena occurring in the lowest Landau level (LLL) of the quantum Hall effect. In principle, one would expect all of the electrons in the LLL to be fully polarized thus freezing out the spin degree of freedom. However, due to the strong correlation which exists between the electrons at filling factors $\nu \leq 1$, new incompressible quantum Hall states with vanishing longitudinal and quantized Hall resistances appear at certain fractions of the available states. In this fractional quantum Hall effect (FQHE), the many-body wavefunction of the ground states and their excitations will depend on the spin polarization of the system. Hence, spin is reestablished as an important degree of freedom in the LLL. Spin phenomena in this regime include spin phase transitions of several FQHE ground states, spin-reversed and topological excitations with an underlying spin-texture referred to as skyrmions, polarization of composite fermions (CFs) and interactions between nuclear and electron spins.

In our work, we employed two different experimental techniques: magnetotransport and nuclear magnetic resonance (NMR) to investigate these phenomena. The latter technique proved to be particularly useful in studying interactions between electrons and nuclei. In fact, NMR is an important tool to study spin phenomena because the electron spin polarization (\mathcal{P}) can be directly measured from the spectroscopic information—a shift in the Larmor resonance, known as Knight shift, is proportional to \mathcal{P} . Unfortunately, the sensitivity of an NMR experiment of a single 2-dimensional electron system (2DES) is very poor. The signal is proportional to the number of nuclei and their average spin polarization. Consequently, in order to measure an NMR signal from a 2DES, multiple quantum well samples and optical pumping techniques were used in previous works to overcome these difficulties. In chapter 5, we presented a method developed in this thesis where the electron spin polarization was measured in a *single* 2DES. It consisted of performing a resistance detected (RD)NMR experiment, i.e. monitoring the changes of the longitudinal resistance during RF-irradiation of the nuclear spins, and comparing the signal to a conventional NMR signal from the substrate nuclei. The differences in the signal frequencies rendered the Knight shift and as a result the electron spin polarization. In addition to the elec-

trical transport measurements, we applied this technique to study various aspects of the spin phenomena mentioned above. In the following, we summarize the main results of the thesis.

• **The spin phase transition at $\nu = 2/3$ in the low and high current regime**

The initial purpose of this work was to understand the origin of the anomalous resistance peak reported in the FQHE at filling factor $\nu = 2/3$ [5]. By driving a sufficiently large current through a 15 nm GaAs QW, Kronmüller *et al.* found that a large peak in the longitudinal resistance, named huge longitudinal resistance (HLR), developed within minutes at filling $\nu = 2/3$. The long saturation time of the peak provided an indication for the involvement of the nuclear system in the effect. In fact, this assertion was proved shortly after by the same authors after conducting RDNMR experiments [6]. However, many questions remained unanswered. For example, a four-fold splitting was observed in the RDNMR lines which could not be explained by any of the known electron-nuclear interactions thus raising speculation of a new type of interaction. Furthermore, even though it was suggested that the HLR could be linked to the unpolarized-polarized phase transition at $2/3$, this seemed unlikely because the HLR appeared at much higher magnetic field values than the ones observed for the transition by Eisenstein *et al* [55].

Properties of the transition: In the course of this thesis, in collaboration with the work by S. Kraus [7], we could establish a connection between the HLR and the spin phase transition at $2/3$. A main goal of the present work was to clarify differences and similarities which exist between the HLR and the transition by means of electrical transport and NMR experiments. Additionally, we were able to explain the four-fold splitting anomaly in the RDNMR lines. Our findings could be summarized as follows: The transition at $2/3$ between a spin unpolarized and a spin polarized state is characterized in transport by a peak in the longitudinal resistivity, ρ_{xx} , at temperatures below ≈ 600 mK. The size and characteristics of the peak are strongly dependent on the current density used in the experiments. If a small current density is used, the transition will become apparent by a small longitudinal resistance (SLR) peak which decreases in size with decreasing temperature. In fact it completely disappears at $T \leq 22$ mK. On the other hand, an increment in the current density results in the development of a large peak in ρ_{xx} known as the huge longitudinal resistance. We proved that this peak is not the result of non-linear effects but is solely caused by the hyperfine interaction between electron and nuclear spins. The HLR peak develops at the same position of the small current transition peak and therefore both effects are intrinsically related. But the question remained, why the transition, or equivalently the HLR, developed at much higher magnetic field values than the ones measured in previous experiments. The answer lies in the thickness of the QW structures which were used in our studies. Since the QWs are only 15 nm thin, finite corrections of the Coulomb

energy and the g -factor are not negligible. The transition depends on the interplay between the Coulomb and Zeeman energies and therefore their ratio, defined as η , and not the magnetic field alone determines the polarization of the favorable ground state. In such narrow QWs, the critical ratio where the transition occurs is shifted towards higher B -field values. The ground state polarization can be chosen by tuning this ratio which can be achieved either by tilting the sample with respect to the external B -field or varying the carrier density. This is mainly due to the $\sqrt{B_{\perp}}$ dependence of the Coulomb energy in comparison to the B_{tot} dependence of the Zeeman energy. It was thereby necessary to design a sample where the density could be varied in a range large enough for the $2/3$ ground state to transit from an unpolarized to a polarized phase. The samples were grown at the *Walter Schottky Institute* in Munich. In this work, we performed density-sweeps and tilted B -field experiments and observed how the ground state polarization changes from unpolarized to fully polarized. We conducted the experiments in the SLR and HLR regimes and noticed that they both appear at the same η_c value. Nevertheless, striking differences were also measured in both regimes. For example the HLR, besides being much larger in amplitude, is also much broader than the SLR peak. In fact, the HLR always extends from the position at the $2/3$ minimum in ρ_{xx} where it initiates up to the end of the minimum. Furthermore, a hysteresis, measured from B -field and gate voltage sweeps, is present at the transition. At temperatures higher than 70 mK, however, the hysteresis only prevails in the HLR regime. The time dependence of the equilibration time is also markedly different in both regimes. Whereas the SLR takes seconds to almost reach its saturation value, the HLR needs several minutes to do so.

Model of the transition: From these experiments, we proposed a model explaining the mechanism which leads to dissipation as indicated by the SLR and HLR peaks. In the small current regime, similar works carried out at the $2/3$ transition suggested that the transition could be explained in terms of 2D Ising ferromagnetism, where domain formation with different polarization (in the case of $2/3$, unpolarized and polarized) should occur [58]. For that purpose, the composite fermion model was used in which the transition at electron filling factor $2/3$ becomes a crossing of the spin-down state of the lowest CF-LL and the spin up state of the second CF-LL. The formation of domains can be caused by potential fluctuations in the 2DES, due to disorder, which would create a spatial variation of the density. Therefore, part of the sample could favorize an unpolarized state while others a fully polarized state. Around the same time, theoretical works suggested that resistance spikes in Ising quantum Hall ferromagnets could be caused by backscattering of electrons moving from one side of the sample to the other *along* domain walls [107]. Based on this idea, we proposed that in the HLR regime, which is induced by increasing the current, electrons scatter *between* domain walls. Since the domains have different spin polarization, electron spin flips must be accompanied by another

mechanism in order to conserve angular momentum. A possible candidate for such a mechanism could be electron-nuclear spin flip-flop process via the hyperfine interaction. An enhanced current-induced nuclear spin polarization would then build up at the domain boundaries and a local hyperfine field would act back on the electron spins changing their Zeeman energy¹. As a result, additional disorder will be created in the electronic system leading to a changing of the domain structure—probably more and larger domain walls—and thus increasing dissipation. The broadening of the HLR peak is likewise a result of a shifting of the peak to either higher or lower magnetic field values, depending on the sign of the hyperfine field B_N . The width of the peak delivers information on the value of B_N . The small current peak, on the other hand, is affected by the nuclei only at low enough temperatures for these to be sufficiently polarized. At the lowest temperatures of our experiments $T \approx 20$ mK, about 15% of the nuclei are thermally polarized. The hyperfine field created by these nuclei is homogeneously distributed across the sample and therefore merely shifts the spin phase transition. The shifting of the peak as a function of temperature has been presented in section 4.7. Furthermore, in resistance detected (RD)NMR measurements at $T = 250$ K, a signal has been obtained at high currents, but not at low currents.

Spectroscopic evidence of domain formation: By conducting NMR experiments, in addition to transport, we were able to study the spin phase transition in the low current and HLR regimes more thoroughly and prove some of the assumptions of our model. Also, one main objective was to reproduce and further investigate the four-fold splitting of the RDNMR lines observed in reference [6] by applying the NMR technique presented in section 5.2.1. We chose the sample with a front gate in order to tune the density to an adequate value for the transition to exist at the $2/3$ minimum. However, to our surprise, two lines rather than four were measured in our RDNMR experiments. The frequency of one of the lines coincided exactly with the substrate of the zero-shift line. The frequency difference of the lines indicated the Knight shift of the second resonance. We also determined the maximum Knight shift as a function of density by applying the same technique to a fully polarized state. The state at filling factor $\nu = 1/2$ at B -fields higher than 10 T was an appropriate candidate to obtain a $K_{s,\max}(\mathcal{P} = 1)$ vs density calibration curve. From this information, the electron spin polarization was determined via the equation $\mathcal{P} = K_s/K_{s,\max}$. By replotting the RDNMR spectra as a function of polarization, we could identify one resonance line as a change in the resistance due to nuclei interacting with unpolarized electrons and the second line as a line caused by nuclei interacting with polarized electrons. With these experiments, we were able to *spectroscopically prove the existence of*

¹Even though the spin-orbit interaction is an alternative mechanism which would allow electrons to flip their spins while conserving angular momentum, it is believed to be irrelevant in our system [116]. Recent experiments, however, indicate that spin-orbit interactions might suppress the electron-nuclear spin coupling if the QW potential asymmetry is increased [118]. In our system, the electron-nuclear interaction plays the dominant role.

$\mathcal{P} = 0$ and $\mathcal{P} = 1$ electron domains at the $\nu = 2/3$ transition in the high current regime. These domains seem to be static in the time scale of the measurements ($\approx 20 \mu\text{s}$). To our knowledge, the presence of domains at level crossings had not been previously measured by a local probe like NMR. Nevertheless, these measurements could not explain the discrepancy between the two-fold and the four-fold splitting observed in other samples. In this thesis, we recognized that the reason for the four lines is an additional interaction of the nuclei: Besides the hyperfine interaction with electrons, nuclei with a non-spherical charge distribution can also interact with an electric field gradient. Furthermore, if these nuclei are not located at sites of cubic symmetry, which is the case for stressed GaAs samples, a three-fold quadrupole splitting of each resonance line should occur. In our experiments, we showed that samples without stress show two resonance lines while samples with stress can show a multiple of lines. The number of lines depends on the Knight shift and on the quadrupole splitting, which in our samples, are of the same order of magnitude. The four-fold splitting is a consequence of the Knight shift and the quadrupole splitting being almost the same, causing an overlapping of the lines into four. RDNMR experiments at twice the Larmor frequency and at tilted B-fields confirmed this interpretation.

NMR studies of the SLR and HLR: The low current regime of the transition was also investigated by NMR at $T = 55 \text{ mK}$. Here, two distinct lines in the spectrum indicate the existence of $\mathcal{P} = 0$ and $\mathcal{P} = 1$ domains also in this regime. However, important differences were observed between the HLR and the low current peak. By measuring RDNMR spectra at various positions of the transition peaks, we noticed that whereas the HLR peak decreases in all spectra, the SLR peak decreases if RDNMR is performed on one side of the peak, but increases if it is done on the other side. This proves our assertion that the HLR is caused by an additional disorder of the electron system due to an inhomogeneous nuclear spin polarization thus destroying the peak with RF-irradiation. The SLR, on the other hand, is affected by a homogeneous thermal polarization and the RF-signal merely shifts the peak. Another interesting difference is the weighting of the two resonance lines. In the HLR, we showed that the RDNMR signal is stronger for the minority rather than the majority domains. At low currents, the weighting between the lines seem to remain constant for all RDNMR spectra. This could indicate that the HLR appears even if one domain type is more abundant than the other, while the SLR occurs only when both domain types are equally represented.

Time and temperature dependence: Some questions still remained unanswered concerning the small current and large current transition peaks. For example, the HLR is usually measured with an AC current. A DC current also induces the HLR peak, as showed in section 4.6.2, independent of the current direction. Nevertheless, the time dependence differs greatly between AC and DC current. The HLR peak seems to decay with time if a DC current is applied while

it remains constant with AC. This points to the presumption that the nuclear hyperfine field is being kept inhomogeneous by an AC current, but becomes homogeneous (or disappears at high temperatures), possibly due to spin diffusion, if DC is used. Preliminary surface acoustic wave experiments in the MHz regime, presented in appendix A, do not show the HLR anomaly. This behavior is still not well understood and is the material of future work.

Furthermore, it was necessary to clarify the issue regarding the mechanism leading to dissipation at the transition in more depth. Even though we showed a simple model describing the scattering processes present at low and at high currents, a more detailed, theoretical description should be addressed. We tried to confront this matter by measuring the low current transition resistance peak as a function of temperature (shown in section 4.7.1). The calculation of an activation energy, extracted from the measurements, revealed that a gap of about 320 mK remains at the transition. This situation contradicts the idea that a simple crossing of levels describes the transition. A gap could exist, for example, if spin-orbit interactions were non-negligible. However, if this were the case, a mixing of the different spin states would be expected thus contradicting our NMR experiments where domain formation was proven. Likewise, spin-orbit interaction would strongly affect the electron-nuclear spin interaction, since it would provide for an alternate path for electron flips; a situation which is not observed in our experiments. The gap could be probably explained by deviating from the single particle model and including exchange interaction. The position of the transition would no longer be exactly at the crossing, but rather slightly away from it where a gap is still present. Another issue which can be extracted from the measurements is that at and near the level crossing, the slope of the activation gap becomes steeper than the one expected for a single spin flip. Similar behavior has been previously reported in the IQHE for a pseudospin easy-axis ferromagnet at the crossing between two levels [119]. In that contribution, it was speculated that such a behavior may arise due to a collective topological excitation resembling a skyrmion inside a domain wall. In fact, it could be possible that such excitations moving across the sample dissipate energy and contribute to the resistance. One could imagine that in the low current regime only a few excitations exist leading to a small resistance and few flip-flop processes so that the thermal nuclear spin polarization dominates. On the other hand, a large current increases the number of excitations, thus leading to more spin-flips, and as a result higher nuclear spin polarization. The large resistance could be caused by both an increased number of excitations and an inhomogeneous hyperfine field. We also mentioned in that section, that the resistance peak *completely* vanishes at temperatures below $T \approx 22$ mK. This in accordance with the expectation from reference [107] that domain walls decrease in size with decreasing temperatures, until the domains cease to overlap thus suppressing backscattering (see also [79]). In the future, this issue could be further investigated by measuring samples with artificial inhomogeneities.

• The spin phase transitions at other filling factors

In addition to the experiments at filling factor $\nu = 2/3$, we also measured spin phase transitions occurring at $\nu = 3/5$ and $4/7$. From those measurements, several conclusions were drawn about spin transitions in general occurring in the LLL. At the other filling factors, a large resistance peak with long time constants also characterize the transition in transport at high currents. The critical parameter which determines the ground state polarization at all filling factors is the ratio between the Zeeman and Coulomb energies. However, a better description is given by the composite fermion (CF) model in which a transition occurs when the CF cyclotron energy equals the Zeeman energy. This has been demonstrated in section 4.2. Furthermore, domain formation has been observed in all transitions.

• Spin polarization of composite fermions

At $\nu = 1/2$, CFs experience a zero effective magnetic field and thereby form a CF Fermi sea. The external magnetic field, however, still acts on the spin of the electron ($E_Z \neq 0$), so that CF will be completely polarized if the Zeeman energy is larger than the CF Fermi energy. From previous experiments, this was expected to occur near $B = 10$ T [60, 62]. By means of our NMR technique, we could measure the Knight shift with respect to a substrate signal at various fields at constant filling $\nu = 1/2$. We observed that for magnetic fields above 10 T, the measured Knight shift, which varies linearly with density, falls on a straight line. Below 10 T, the Knight shift does not longer follow this behavior indicating a depolarization of the CFs at $1/2$. Apart from using this curve as a calibration for a maximum Knight shift, we were also able to extract the CF polarization mass from the results, which compared well with previous experiments.

Deviating from $\nu = 1/2$, CFs experience a finite effective magnetic field and CF LLs form. The fractional filling factors of electrons can be mapped to an integral filling factor of CFs. The CF polarization is then given by the difference between occupied spin up and spin down CF LL divided by the total number of levels. The expected polarization at fillings $2/3$, $3/5$ and $4/7$ could be proven by our experiments.

• Skyrmions and spin-reversed quasiparticle excitations

Skyrmions are low-lying energy excitations which are believed to occur in the vicinity of filling factor $\nu = 1$. They have a certain spatial extent and involve flipping several spins while accommodating only one unit of extra charge. Recently, an anomalous line shape in the RDNMR spectra [93] taken around filling factor $\nu = 1$ were interpreted as evidence for skyrmions. For that purpose, we performed experiments around $\nu = 1$, but also around $\nu = 1/3$, $\nu = 2/3$ and other filling factors where skyrmions are not expected to exist. The same anomalous line shape was also seen in some cases, which led us to believe that not skyrmions, but rather a coupling

between nuclei and spin-reversed quasiparticle excitations, which exist around all filling factors investigated, is responsible for such a line shape. It still remains unclear why such an anomalous line shape occurs for quasi-electrons and not for quasi-hole excitations.

• **Outlook**

Even though we have clarified many aspects of the $\nu = 2/3$ transition, some issues remain to be understood. For example, the mechanism leading to dissipation could be further investigated by creating artificial inhomogeneities in the sample while monitoring the behavior of the longitudinal resistance as a function of time, frequency and current. Up to now, it is still unclear why the resistance develops to such a high value. Furthermore, we could acquire a better understanding of the domain structure which forms at the transition by measuring with another local probe—in addition to NMR—such as a single electron transistor (SET). Surface acoustic waves could also deliver interesting information about phase transitions. Moreover, it would be of great benefit to go beyond the RDNMR/NMR technique developed in this work by performing a direct NMR experiment on a single 2DES.

In section 5.6 we proposed applying the RDNMR/NMR technique to study other spin phenomena (other than the transition at $2/3$) occurring in the QHE. For example, the ground states at filling factors $5/2$ and $7/2$ are believed to exist due to a pairing of CFs. The polarization of these states, which could be measured with our method, would provide an insight into the nature of the wavefunction. We also mentioned that it could be of interest to measure the electron spin polarization at the exciton condensate state of $\nu_T = 1$ which occurs in a bilayer system, as suggested in reference [142].

In conclusion, we would like to remark that the ability to grow very high mobility samples, combined with the opportunity to measure at lower temperatures has led to the continuous discovery of a wide range of rich physical phenomena occurring in the QHE. Studying the spin degree of freedom has delivered and will persist to render essential information about these phenomena.

Chapter 7

Zusammenfassung

Im Rahmen dieser Arbeit werden Spin-Phänomene untersucht, die in dem tiefsten Landau Niveau (LL) des Quanten-Hall-Effekts auftreten. Dazu werden Magnetotransport und Kernspinresonanz (NMR) Experimente an 2-dimensionalen Elektronensystemen (2DES) durchgeführt, die sich unter dem Einfluß eines senkrechten magnetischen Feldes (bis 18 T) und tiefen Temperaturen (20 mK) befinden. Unter diesen Bedingungen, besetzen die Elektronen eine ganzzahlige Anzahl von hoch entarteten Energieniveaus, die durch die Zyklotronenergie getrennt sind. Berücksichtigt man den Spin der Elektronen, so werden diese Niveaus aufgrund der Zeemanenergie weiter in zwei Niveaus aufgespalten. Wenn die Elektronen nur das tiefste LL besetzen, erwartet man, dass die Spins aller Elektronen gleich ausgerichtet sind, was zu einer vollständigen Spinpolarisation des 2DES führen würde. Demzufolge würde dann der Spinfreiheitsgrad keine wesentliche Rolle spielen. Man hat allerdings in dieser Überlegung die Wechselwirkung der Elektronen vernachlässigt. Dennoch weisen die Elektronen tatsächlich eine starke Korrelation wegen der Coulombenergie auf. Im Magnetotransport zeigen sich neue inkompressible QH Zustände bei bestimmten gebrochenzahligen Füllfaktoren [(s. Gl.(2.10)], die nur unter der Berücksichtigung der Elektron-Elektron Wechselwirkung erklärt werden können. Da die Elektronenpolarisation der Grund- und Anregungszustände im Bereich des gebrochenzahligen Quanten-Hall-Effekts (FQHE) vom Verhältnis zwischen Zeeman und Coulomb Energien abhängt, wird der Spin im tiefsten LL wieder zu einer wichtigen Größe. Das führt zu Phasenübergängen zwischen Zuständen verschiedener Polarisationen und zu andere Spin-Phänomenen wie Quasiteilchen-Anregungen mit verschiedener Spin-Orientierungen und topologischen Anregungen mit einer ausgedehnten Spin-Struktur, genannt Skyrmionen, die Polarisation von Composite Fermions (CFs) und die Kopplung zwischen Elektronen- und Kernspins.

Außer Magnetotransport Experimente sind NMR Methoden besonders geeignet zur Untersuchung des Spin-Freiheitsgrades. Damit erhält man nicht nur ein besseres Verständnis der Kopplung zwischen Kernen und Elektronen, sondern man kann auch die Elektronenspinpolari-

sation mittels einer Verschiebung der NMR Resonanzfrequenz (Knight Verschiebung) messen. Da das NMR Signal proportional zur Anzahl der Kerne im System und dessen durchschnittlicher Polarisation ist, kann man die Empfindlichkeit des Experiments durch die Verwendung von mehreren aufeinander gestapelten Quantumwells (QWs) und/oder durch optisches Pumpen erhöhen. Diese Techniken zeigen erhebliche Nachteile. In einem mehrlagigem System beispielsweise verursachen Inhomogenitäten in den verschiedenen Schichten nicht-identische Bedingungen für die QWs. Außerdem ist es nicht möglich die Dichte aller Schichten mittels eines Gates zu variieren, und durch optisches Pumpen wird das System aus dem Gleichgewicht gebracht. In Kapitel 5 wird eine im Rahmen dieser Arbeit entwickelte Methode gezeigt, um die Elektronenspinpolarisation eines 2DES messen zu können. Dazu ist es erforderlich ein widerstandsdetektiertes (RD)NMR-Experiment durchzuführen, bei dem die Änderung des spezifischen Längswiderstandes verfolgt wird, während auf das System mit einem Radiofrequenz-Signal (das mit der Resonanz- oder Larmorfrequenz der Kerne (ω_L) abgestimmt wurde) eingestrahlt wird. Das erhaltene Signal wird dann mit einem Referenzsignal der Substratkerne verglichen, um die durch die QW-Leitungselektronen verursachte Knight-Verschiebung zu ermitteln. In unseren Untersuchungen haben wir diese Methode verwendet, um diverse Aspekte von Spin-Phänomenen in den tiefsten LL zu studieren. Die wichtigsten Ergebnisse der Arbeit werden im Folgenden zusammengefaßt.

• **Spin-Phasenübergang bei $\nu = 2/3$: kleiner und großer Strombereich**

Im Bereich des FQHE entdeckten Kronmüller *et al.*, dass bei ausreichend hohen Stromdichten und sehr langsamen Magnetfeldraten ein großes Maximum im Längswiderstand bei $\nu = 2/3$ auftritt. Die ursprüngliche Motivation dieser Arbeit war, Klarheit über die physikalische Prozesse, die in dieser Anomalie involviert sind, zu schaffen. Es war bekannt, dass das Maximum, genannt “huge longitudinal resistance” oder HLR, mehrere Minuten brauchte um sich vollständig zu entfalten. Die langen Zeitkonstanten deuteten darauf hin, dass das Kernsystem eine wesentliche Bedeutung in dem HLR haben könnte. Diese Vermutung wurde auch bei Kronmüller *et al.* mittels RDNMR Experimenten bestätigt. Es wurde ein Modell präsentiert, bei dem der HLR als Phasenübergang zwischen dem spin-unpolarisierten ($\mathcal{P} = 0$) zu dem spinpolarisierten ($\mathcal{P} = 1$) Zustand bei $\nu = 2/3$ dargestellt wurde. Es wurde auch vorgeschlagen, dass am HLR sich Domänen unterschiedlicher Polarisation bilden könnten. Trotzdem blieben viele offene Fragen bezüglich des Ursprungs des HLR-Maximums. Zum Beispiel war es rätselhaft, warum der HLR bei Magnetfeldern von etwa 10 T existiert, obwohl der spin unpolarisierte Übergang bei viel niedrigerem Magnetfeld erwartet wurde. Außerdem wurde im Spektrum des RDNMRs eine vierfache Aufspaltung der Resonanzlinien gemessen, die nicht mit den konventionellen Elektron-Kern-Wechselwirkungen erklärt werden konnten, was zu der Vermutung einer neuen Art von Wechselwirkung führte.

Eigenschaften des Spinübergangs: Im Verlauf dieser Dissertation ist es gelungen die Verbindung zwischen dem Phasenübergang und dem HLR herauszufinden. Durch unsere Messungen konnten wir zahlreiche Ähnlichkeiten und Unterschiede dieser beiden Effekte feststellen. Dazu konnten wir die Ursache der anomalen vierfachen Aufspaltung des NMR Spektrums erklären. Diese Resultate werden im Folgenden beschrieben: Der Übergang von einem unpolarisierten zu einem polarisierten Zustand bei $\nu = 2/3$ wird durch einen endlichen Wert des spezifischen Längswiderstands (ρ_{xx}) in dem FQH-Minimum gekennzeichnet, der nur bei Temperaturen unter ≈ 600 mK erscheint. Die Größe und andere Eigenschaften des Widerstandsmaximums sind stark von der Stromdichte abhängig. Bei Verwendung einer kleinen Stromdichte beobachtet man nur ein kleines Maximum im Widerstand (SLR), das mit absteigender Temperatur auch abnimmt. Unter 22 mK ist das Widerstandsmaximum nicht mehr zu sehen. Erhöht man andererseits die Stromdichte und reduziert die Änderungsrate des Magnetfeldes, so tritt das große Maximum in dem Längswiderstand auf, bekannt als HLR. Anhand von Strom- und Zeitabhängigkeitsmessungen konnten wir beweisen, dass nichtlineare Effekte für das Auftreten des HLR-Maximum nicht verantwortlich sind. Da der HLR und der Spinübergang sich an der gleichen Stelle entwickeln, konnte man zeigen, dass diese Effekte tatsächlich zusammenhängen. Allerdings, konnte man noch nicht verstehen warum der Spinübergang bzw. das HLR-Maximum bei viel höheren Magnetfeldern als in früheren Untersuchungen des $2/3$ Übergangs stattfand. Entscheidend ist die Dicke (15 nm) der in unsere Arbeit verwendeten QWs. Durch die endliche Ausdehnung der Wellenfunktion im QW ist es erforderlich die magnetische Länge und den g -Faktor zu korrigieren, die wiederum die Coulomb- und Zeemanenergie verändern. Da die Grundzustandspolarisation vom Verhältnis zwischen Zeeman- und Coulombenergie $\eta = E_Z/E_C$ abhängt, wird der Übergang in schmalen QWs aufgrund dieser Korrekturen zu höheren Magnetfeldern verschoben. Die Polarisation des Grundzustands kann durch Variation des kritischen Parameters η gewählt werden. Dies geschieht entweder durch Messungen bei gekippten Magnetfeldern, bei dem eine zusätzliche parallele Komponente des Feldes existiert, oder durch die Änderung der Ladungsträgerdichte mit einem Gate ($E_Z \propto B_{\text{tot}}$ und $E_C \propto \sqrt{B_{\perp}}$). Für die zweite Methode wurde eine Probe am *Walter-Schottky-Institut* in München gewachsen, bei der die Dichte zwischen $2.03 \times 10^{11} \text{cm}^{-2}$ and $0.8 \times 10^{11} \text{cm}^{-2}$ variiert werden kann, nachdem ein 8.5 nm AuPd-Frontgate aufgedampft wurde. Die beide Polarisationszustände ($\mathcal{P} = 0$ und $\mathcal{P} = 1$) und der ganze Bereich des Übergangs können damit erreicht werden. In dieser Arbeit zeigen wir Experimente sowohl bei gekipptem B -feld als auch mit Dichteänderungen im Bereich des Phasenübergangs. Obwohl SLR und HLR am gleichen kritischen η_c existieren, können wir auch beachtliche Unterschiede feststellen. Außer dem Größenunterschied der Maxima wurde beispielweise auch beobachtet, dass der HLR viel breiter als der SLR ist. Die Breite ist eigentlich immer gegeben durch den Anfang des Widerstandsmaximums bis zum Ende des $2/3$ Minimums. Zudem ist das HLR-Maximum durch eine markante Hysterese geprägt (auch

bei $T = 350$ mK), während der SLR nur eine kleine Hysterese aufweist, die bei $T > 70$ mK verschwindet. Die Zeitabhängigkeit hat auch ein völlig anderes Verhalten in beiden Strombereichen. Das SLR-Maximum erreicht nur nach wenigen Sekunden das Gleichgewicht, das HLR aber braucht Minuten bis zu Stunden, um ins Gleichgewicht zu kommen.

Modell des Spin-Phasenübergangs: Mit Hilfe der oben genannten Messungen konnte ein Modell erarbeitet werden, das die Ursache der SLR- und HLR-Maxima erklärt. In der Literatur wird vorgeschlagen, den Spinübergang als eine Kreuzung von zwei energetisch gleichen CF-LL zu interpretieren [58]. Im CF-Modell, überkreuzt der tiefste CF-LL mit der Spin-Orientierung nach unten den zweiten CF-LL mit der Spin-Orientierung nach oben (s. Abbildung 4.1). An der Koinzidenz der zwei Niveaus kann das System als ein 2D-Ising Ferromagnet beschrieben werden, bei dem Domänen mit $\mathcal{P} = 0$ und $\mathcal{P} = 1$ existieren. Dies geschieht wegen Potenzialfluktuationen, die durch Unordnungen des 2DES zustande kommen. Die Dissipation im System würde bei kleinen Strömen wegen der Rückstreuung der Elektronen entlang der Domänenwände stattfinden. Andererseits könnten bei hohen Strömen die Elektronen die Domänenwände überwinden, wobei ein Elektron seine Spin-Orientierung ändern müsste. Dieser Prozess ist aber nur möglich, wenn ein anderer Mechanismus vorhanden ist, der es erlaubt den Drehimpuls zu erhalten. Die Spin-Bahn Kopplung wäre so ein Mechanismus. Allerdings könnte dann das Kernsystem keine wesentliche Rolle beim HLR spielen, was unseren Beobachtungen widersprechen würde. Deswegen ist es wahrscheinlicher, dass der Drehimpuls durch einen Flip-Flop Prozess der Elektronen und Kernspins erhalten bleibt. Eine erhöhte strombedingte Kernspinpolarisation könnte sich dann an den Domänengrenzen aufbauen. Das würde die Zeemanenergie der Elektronen lokal beeinflussen, was zu einer zusätzlichen Unordnung im System führen würde. Die Domänenstruktur wäre durch diese Extra-Unordnung zwangsläufig beeinflusst und mehr, oder größere, Domänenwände könnten sich entwickeln. Die Dissipation wäre dann erhöht und so könnte sich das HLR-Maximum entwickeln. Die Breite des Maximums kann man als eine Verschiebung des Übergangs zu niedrigeren oder zu höheren Magnetfeldern betrachten, die wegen der inhomogenen Hyperfeld (B_N) verursacht wird. Bei kleinen Strömen ist die Situation anders. Das Kernsystem würde dann nur eine Rolle spielen, wenn die thermische Kernpolarisation nicht vernachlässigbar klein ist, d.h. nur bei den tiefsten Temperaturen. Beispielsweise können wir ausrechnen, dass die thermische Kernpolarisation bei $T = 20$ mK etwa 15% beträgt, während bei $T = 250$ mK die thermische Polarisation unter 1% liegt. Aufgrund des durch die Polarisation erzeugten homogenen hyperfine Feldes, B_N , wird das Widerstandsmaximum lediglich verschoben, aber nicht erhöht. Die Größe des B_N Wertes, bzw. die Verschiebung des Maximums als Funktion der Temperatur wurde in Abschnitt 4.7 dargestellt. RDNMR Experimente haben diese Aussage bekräftigt, weil bei Temperaturen über 250 mK nur ein Signal im HLR- aber nicht im SLR-Bereich gemessen werden konnte.

Spektroskopischer Beweis der Domänenstruktur: Anhand von NMR Experimenten konnten wir den Spinübergang bei $\nu = 2/3$ genauer untersuchen und auf diese Art und Weise einige unserer Annahmen des Modells beweisen. Zudem haben wir auch die vierfache Aufspaltung der NMR-Linien am HLR reproduziert und mit Hilfe der in Abschnitt 5.2.1 beschriebenen Technik weiter studiert. Für diese Messungen war es vorteilhaft, die Probe mit dem Frontgate zu verwenden, um die Dichte über dem ganzen Bereich des Spinübergangs variieren zu können. Erstaunlicherweise konnten wir nur zwei Resonanzlinien im RDNMR beobachten und nicht vier, wie es in vorherigen Experimenten gemessen worden war. Mit Hilfe der Substratreferenzmessungen mit konventioneller NMR konnten wir feststellen, dass die Frequenz einer der Resonanzlinien des RDNMR-Spektrums mit der Null-Verschiebungs-Referenzlinie übereinstimmte. Die zweite Linie war wegen der Knight-Verschiebung um einige kHz von der ersten Linie verschoben. Anhand einer “Kalibrierungsmessung” eines vollpolarisierten Zustands, in diesem Fall $\nu = 1/2$ bei B -Felder höher als 10 T, konnten wir die erwartete maximale Knight-Verschiebung $K_{s,\max}(\mathcal{P} = 1)$ als Funktion der Dichte ermitteln. Die Elektronenspinpolarisation wurde dann nach der Gleichung $\mathcal{P} = K_s/K_{s,\max}$ bestimmt. Diese Information lieferte einen Beweis dafür, dass die zweite Resonanzlinie durch die Wechselwirkung der Kerne mit vollpolarisierten Elektronen verursacht wird. Diese Experimente haben *spektroskopisch bewiesen, dass tatsächlich eine Domänenstruktur am $\nu = 2/3$ Übergangsmaximum vorhanden ist, und dass diese Domänen statisch sein müssten, zumindest in der Zeitskala der Experimente ($\approx 20 \mu\text{s}$).* Unseres Wissens wurde vor diesen Messungen noch keine Domänenstruktur an Spin-Übergängen mittels einer lokalen Meßmethode wie NMR nachgewiesen. Es blieb aber noch zu klären, warum in vorherigen Experimenten vier Resonanzlinien beobachtet wurden. Weitere Untersuchungen ergaben, dass einige Proben, die sich unter Verspannung geringfügig verformten, eine zusätzliche Quadrupol-Aufspaltung zeigten. Dies geschieht aufgrund der Wechselwirkung zwischen Kernen ohne einer sphärischen Ladungsverteilung ($I > 3/2$) und einem elektrischen Feld Gradient. Durch die Verspannung ist die kubische Symmetrie von GaAs aufgehoben und jede NMR Resonanzlinien spaltet in drei Linien auf. Unsere Experimente haben gezeigt, dass Proben ohne Verspannung in zwei Linien aufspalten, während verspannte Proben mehrere Resonanzlinien aufweisen. Die Anzahl der Linien hängt hauptsächlich von der Größe der Knight-Verschiebung und der Quadrupol-Aufspaltung ab. In einigen unserer Proben sind beide Effekte gleich groß, so dass mehrere Linien überlappen und nur vier Resonanzen im Spektrum auftreten. Diese Interpretation wurde mit Hilfe von Doppelfrequenz und gekipptem B -Felder RDNMR-Experimente bestätigt.

NMR Untersuchungen an SLR- und HLR-Maxima: Das SLR-Übergangsmaximum wurde auch mit NMR untersucht. Allerdings waren diese Messungen nur bei Temperaturen tiefer als 100 mK möglich ($T = 55 \text{ mK}$ in unserem Fall). Zwei deutliche Linien im Spektrum zeigen,

dass auch in diesem Strombereich Domänen mit Polarisation $\mathcal{P} = 0$ und $\mathcal{P} = 1$ existieren. Jedoch wurden auch wichtige Unterschiede zwischen beiden Zuständen festgestellt. Die RD-NMR Messungen an verschiedenen Stellen des HLR-Maximums verursachten immer eine Absenkung des Widerstands. Andererseits haben die gleichen Messungen am SLR-Maximum eine Absenkung oder Erhöhung des Widerstandes hervorgerufen in Abhängigkeit davon, an welcher Stelle des Maximums das RDNMR Experiment durchgeführt wurde. Dies bekräftigte unsere Behauptung, dass das HLR wegen einer durch die Kerne verursachte zusätzliche Unordnung im Elektronensystem induziert wird, während das SLR-Maximum nur durch eine homogene thermische Kernspinpolarisation beeinflusst wird. Eine weitere Erkenntnis der Messungen war die unterschiedlichen Gewichtungen der $\mathcal{P} = 0$ und $\mathcal{P} = 1$ Resonanzlinien in beiden Strombereichen. Im HLR Fall ist die Amplitude der Resonanzlinie stärker, wenn die Kerne mit Elektronen in den Minoritätsdomänen und nicht in den Majoritätsdomänen eine Wechselwirkung aufzeigen. Andererseits bleibt am SLR die Gewichtung der beiden Resonanzlinien immer gleich. Man kann daraus schließen, dass das HLR existiert, auch wenn nur eine Domänenart überwiegt, aber das SLR kann nur existieren, wenn beide Domänenarten gleich vertreten sind.

Zeit- und Temperaturabhängigkeit: Einige Fragen bezüglich der SLR- und HLR-Maxima bleiben weiterhin noch ungeklärt: Verwendet man anstatt eines AC-Stroms einen DC-Strom, so tritt auch das HLR-Maximum unabhängig von der Stromrichtung auf. Dennoch unterscheidet sich das Zeitverhalten der beiden Ströme deutlich. Mit einem AC-Strom bleibt der Widerstand vom HLR auch nach längerer Zeit konstant, während mit einem DC-Strom der Widerstand ein Maximum erreicht, dann aber wieder bis zum ursprünglichen Wert wieder abfällt. Aufgrund dieser Tatsache liegt die Vermutung nahe, dass das inhomogene B -Feld durch den AC-Strom erhalten wird. Der DC-Strom andererseits erzeugt auch ein inhomogenes Feld, das aber nach einer gewissen Zeit, vielleicht wegen einer Spin-Diffusion, entweicht. Vorläufige Experimente mit akustischen Oberflächenwellen (SAW) im Megahertz Bereich zeigten keine HLR-Anomalie (siehe Anhang A). Dieses Verhalten ist noch nicht in ausreichendem Maß untersucht worden und sollte noch weiter studiert werden.

Weiterhin ist es noch erforderlich, den Dissipationsmechanismus am Spin-Übergang besser zu verstehen. Eine Erweiterung des Modells zum Streuungsprozess des Widerstandsmaximums wurde durch temperaturabhängige Messungen am SLR erarbeitet. Aus den Aktivierungsmessungen konnten wir eine Energielücke von ≈ 320 mK am Übergang ermitteln. Dennoch ist die Existenz von einer Energielücke mit der Vorstellung einer einfachen Kreuzung von zwei Niveaus nicht zu vereinbaren. Eine Lücke könnte wegen der Spin-Bahn-Wechselwirkung existieren. Das ist aber nicht sehr wahrscheinlich, weil dann eine Mischung verschiedener Spinzustände erwartet würde, was die Formation von Domänen verhindern könnte. Gleichzeitig wäre dann die Hyperfine-Kopplung zwischen Elektronen und Kernen unterdrückt, da die Elek-

tronen eine Alternative hätten, ihren Spin zu flippen. In unseren Experimenten haben wir sowohl eine Domänenstruktur als auch eine starke Hyperfine-Kopplung gemessen. Die Energielücke könnte beispielsweise auch erklärt werden, wenn wir aus dem Einteilchen-Modell abweichen und die Austauschenergie berücksichtigen würden. Der Übergang wäre dann nicht mehr am Kreuzungspunkt, sondern an der Stelle, wo noch eine Lücke vorhanden ist. Außerdem konnte man einen steilen Abfall der Aktivierungsenergie in unmittelbarer Nähe der Kreuzung beobachten. Ein solches Verhalten hat man in einem Pseudospin “easy-axis” Ferromagnet im ganzzahligen Quanten-Hall-Effekt auch gemessen [119], wobei spekuliert wurde, dass am Übergang kollektive topologische Anregungen—ähnlich wie ein Skyrmion im Innern einer Domänenwand—existieren können. Diese Anregungen könnten sich dann über die Probe bewegen und zurückstreuen. Die Folge wäre dann Energieverbrauch und ein resultierendes Widerstandsmaximum im Transport. Man könnte sich vorstellen, dass bei kleinen Strömen nur wenige Anregungen existieren und deswegen nur ein kleines Maximum und wenige flip-flop Prozesse auftreten. Auf der anderen Seite, gäbe es bei großem Strom mehrere dieser Anregungen und deshalb auch mehr flip-flop Prozesse. Der große Widerstand käme dann durch eine erhöhte Anzahl von Anregungen und aufgrund eines inhomogenen B -Feldes zustande. Wir zeigten auch, dass unter $T \approx 22$ mK das Widerstandsmaximum vollständig verschwindet. Das stimmt mit den Erwartungen überein, dass die Domänengröße mit absinkender Temperatur ebenfalls abnimmt. Bei ausreichend tiefen Temperaturen würden die Domänenwände nicht mehr überlappen und die Rückstreuung wäre dann unterbrochen [107]. Diese Situation sollte in der Zukunft mit Proben, in welchen künstliche Inhomogenitäten aufgebracht worden sind, untersucht werden.

• Spin-Phasenübergang bei anderen Füllfaktoren

Zusätzlich zu den Experimenten bei $\nu = 2/3$, haben wir auch Spinphasenübergänge bei $\nu = 3/5$ und $4/7$ untersucht, von denen man einige allgemeine Schlussfolgerungen ziehen konnte. Auch bei anderen Füllfaktoren führt die Verwendung eines großen Stroms zu einem anomal großen Widerstandsmaximum mit einer langen Zeitkonstante. Der kritische Parameter, der die Polarisation der Grundzustände bei allen Füllfaktoren bestimmt, ist das Verhältnis zwischen der Zeeman- und Coulombenergie. Dennoch konnten wir im Abschnitt 4.2 zeigen, dass eine genauere Beschreibung eines Phasenübergangs mit Hilfe des CF Modells erreicht werden kann. In diesem Modell findet ein Phasenübergang zwischen zwei Polarisationen statt, wenn die Zeemanenergie der CF-Zyklotronenergie entspricht. Außerdem konnten wir auch bei allen untersuchten Füllfaktoren eine Domänenstruktur am Übergang beobachten.

• Spin Polarisation von Composite Fermions

Die Spinpolarisation von gebrochenzahligen QHE-Zuständen sind anhand des Modells von CF klarer zu verstehen. Bei halb gefüllten tiefsten LL werden Elektronen mit zwei magnetischen Flussquanten verbunden, so dass die neu geformten Teilchen ein effektives B -feld (B_{eff}) unterschiedlich vom externen Magnetfeld (B_{ext}) spüren. Bei diesem Füllfaktor ($\nu = 1/2$) ist $B_{\text{eff}} = 0$ und die CFs bilden einen Fermi-See. Dennoch wirkt das externe B -Feld auf den Spin Freiheitsgrad des CFs. Deshalb kann die Polarisation vom CF-Fermi-See vollständig sein, wenn die Zeemanenergie kleiner als die CF Fermienergie ist. In der Literatur wurde eine vollständige CF Fermi-See Polarisation für Magnetfelder grösser als 10 T beobachtet [60, 62]. Mit der vorher beschriebenen NMR-Methode konnten wir die Knight-Verschiebung bezüglich des Substratreferenzsignals bei $\nu = 1/2$ als Funktion des B -Feldes bestimmen. Für $B > 10$ T konnten wir feststellen, dass das System völlig polarisiert ist. Unter 10 T beginnt das System sich zu depolarisieren. Diese Messungen dienten sowohl als “Kalibrierungskurve” zur Bestimmung der maximalen Knight-Verschiebung als auch zur Untersuchung der CF Spin Polarisation bei $\nu = 1/2$ und zum Vergleich mit anderen Experimenten.

Wenn man von $\nu = 1/2$ abweicht, ist das effektive B -Feld, das auf das CF wirkt nicht mehr gleich null. Es bilden sich CF-LLs und der FQHE von Elektronen wird zu den IQHE von CFs. Man kann dann die elektronische Füllfaktoren in CF-Füllfaktoren umrechnen. Die CF Spin Polarisation ist durch die Differenz von CF LLs mit Spin nach oben und Spin nach unten dividiert durch die Anzahl der besetzten Niveaus gegeben (siehe Gleichung 1.1). Die erwartete Polarisation von den Füllfaktoren $2/3$, $3/5$ und $4/7$ konnten mit unseren Experimenten nachgewiesen werden.

• Skyrmionen und Quasiteilchen Anregungen

Skyrmionen sind die niedrigste energetische Anregungen vom Ferromagnetischen Grundzustand $\nu = 1$. Aufgrund des Wechselspiels zwischen der Zeeman und die Austauschenergie ist eine ausgedehnte Spinstruktur-Anregung eher als ein einzelner Spin-Flip bevorzugt. Vor kurzem wurden in NMR Experimenten eine Anomalie in der Resonanzlinien der Spektren beobachtet [93]. Dieses Verhalten wurde als Andeutung für die Existenz von Skyrmionen in der Nähe von $\nu = 1$ interpretiert. Aus diesem Grund haben wir NMR Experimente um $\nu = 1$ aber auch um $\nu = 1/3$, $2/3$ und andere Füllfaktoren durchgeführt, wo normalerweise keine Skyrmionen vorhanden sein sollten. Die gleiche Anomalie wird bei allen untersuchten Füllfaktoren beobachtet. Daraus könnten wir schließen, dass wahrscheinlich nicht Skymionen sonder eher Quasiteilchen-Anregungen dieser ungewöhnliche NMR-Linienform verursachen. Es ist noch zu klären, warum diese Anomalie für Quasielektronen aber nicht für Quasilöcher existiert.

• Ausblick

In dieser Arbeit konnten wir viele Aspekte des Spinübergangs bei $\nu = 2/3$ aufklären. Trotzdem bleiben weiterhin viele offene Fragen: Der Streuungsmechanismus sollte anhand von künstlichen inhomogenen Proben als Funktion der Zeit, Frequenz und Strom weiter untersucht werden. Außerdem wäre es möglich die Domänenstruktur mittels einer lokalen Meßprobe, wie ein Einzelelektrontransistor (SET), zu untersuchen. Akustische Oberflächenwellen könnten auch wichtige Informationen bezüglich Phasenübergänge im allgemeinen liefern. Zusätzlich sollte man versuchen an einem einzelnen QW ein standard NMR Experiment durchzuführen.

Im Abschnitt 5.6 haben wir vorgeschlagen, die in dieser Arbeit entwickelten RDNMR/NMR Meßmethode an weitere QHE-Spinphänomene zu verwenden: Ein Beispiel dafür wäre die Untersuchung von den Grundzuständen bei den Füllfaktoren $5/2$ und $7/2$. Diese Zustände existieren aufgrund der Paarung von zwei CFs. Die Bestimmung der Elektronenspinpolarisation dieser Zustände würde wichtige Aufschlüsse über die Natur der Wellenfunktion geben. Zudem konnte man auch die Elektronenspinpolarisation der stark korrelierten $\nu_T = 1$ Exzitonischen-Zustand messen, wie es im Referenz [142] vorgeschlagen wurde.

Zum Schluß möchten wir erwähnen, dass das Wachstum von Proben mit sehr hohen Mobilitäten und die Fähigkeit bei extrem tiefen Temperaturen messen zu können, hat die stetige Entdeckung von faszinierenden Phänomenen im QHE ermöglicht. Die Untersuchung des Spinfreiheitsgrades liefert immer wieder wesentliche Informationen über die Natur dieser Phänomene.

Appendix A

Surface Acoustic Waves: High Frequency Regime

The experiments presented in this appendix were conducted in cooperation with C. Mellor and G. Dunford from the University of Nottingham. They consist of surface acoustic waves (SAW) performed at the $\nu = 2/3$ transition peak in the high current regime and are part of the frequency dependent measurements of section 4.6. In the following, we summarize the main aspects of SAWs applied to a GaAs crystal needed for the interpretation of our results. A more general description is given in reference [143].

Surface acoustic waves are modes of elastic energy which propagate along the surface of an elastic body. The amplitude of the wave decays exponentially into the bulk so that most of the energy density is contained within a depth of one wavelength λ_S . In a piezoelectric material, a mechanical deformation produces an electric field and inversely an applied electric field produces a mechanical deformation of the material. Hence, the propagation of a SAW in GaAs is accompanied by an electric field which is responsible for the interaction that exists between a 2DES and the SAW. The coupling of the wave to the mobile carriers of the material causes power to be transferred from the SAW to the 2DES. This leads to induced currents and ohmic losses which result in attenuation, Γ , and velocity changes, $\Delta v/v_0$, of the wave. Since the time it takes the perturbed electron system to relax back to equilibrium is dependent on the conductivity σ , the degree of attenuation and velocity shift will also depend on σ . These are given by the following equations:

$$\Gamma = k_S \frac{K_{\text{eff}}^2}{2} \frac{\sigma_{xx}/\sigma_M}{1 + (\sigma_{xx}/\sigma_M)^2} \quad (\text{A.1})$$

and

$$\frac{\Delta v}{v_0} = \frac{K_{\text{eff}}^2}{2} \frac{1}{1 + (\sigma_{xx}/\sigma_M)^2} \quad (\text{A.2})$$

Here, v_0 is the sound velocity in GaAs (≈ 2700 m/s), k_S is the wave vector of the SAW

given by $k_S = 2\pi/\lambda_S$, K_{eff} is the effective electromechanical coupling coefficient, σ_{xx} is the diagonal tensor component of the conductivity and σ_M is the conductivity at which the maximum interaction occurs. In the particular case of a (100) GaAs surface with a SAW propagating in the [011] direction, $K_{\text{eff}} = 6.4 \times 10^{-4}$ and $\sigma_M \approx 3.3 \times 10^{-7} \Omega^{-1}$ [50, 143]. Since the conductivity of a 2DES is of similar order of magnitude as the latter value, SAW presents an effective method to study the QHE. They can be regarded as intermediate experiments between quasistatic transport (DC and low frequency AC) and microwave radiation measurements. For example, SAW has been used in the FQHE in order to demonstrate the existence of a Fermi surface at $\nu = 1/2$ [50]. In this section, we apply SAW to the $\nu = 2/3$ transition in the high current regime in order to investigate the HLR anomaly¹.

A schematically picture of the sample layout used in the SAW experiments is shown in Fig. A.1. The Hall bar, processed on a sample from wafer 052098.4, is $2400 \mu\text{m}$ long and $150 \mu\text{m}$

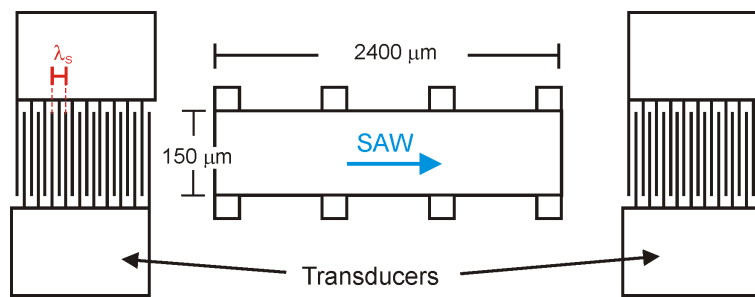


Figure A.1: Schematical picture of the Hall bar and interdigital transducers (IDT) used in the SAW experiments.

wide. A transmitting and a receiving interdigital transducer (IDT) are also shown. The SAW is sent from one of the transducers at a frequency given by $f = v_0/\lambda_S$, where the wavelength λ_S is determined by the distance between the fingers of the transducer. In our case, we used a frequency of 108 MHz, which corresponds to a wavelength of $\approx 25 \mu\text{m}$. A shift in the frequency of the wave, which in turn relates to the shift of the SAW velocity, is detected by the second transducer. A detailed description of the experimental setup including the homodyne system for SAW detection is presented in reference [144].

Here, we study the HLR by carrying out transport and SAW measurements simultaneously. In Fig. A.2(a), we plot the longitudinal resistivity ρ_{xx} vs magnetic field at a density of $n = 1.7 \times 10^{11} \text{cm}^{-2}$, a temperature of $T = 340 \text{mK}$ and a current of $I = 400 \text{nA}$. A large current value is used due to the $150 \mu\text{m}$ wide Hall bar. The expected HLR peak is observed in

¹The acoustoelectric-effect can also provide additional information of a 2DES. This consists of measuring the voltages and currents induced by the transfer of momentum from the SAW to the mobile carriers of the 2DES. In this work, however, we only study the velocity shift of the SAW.

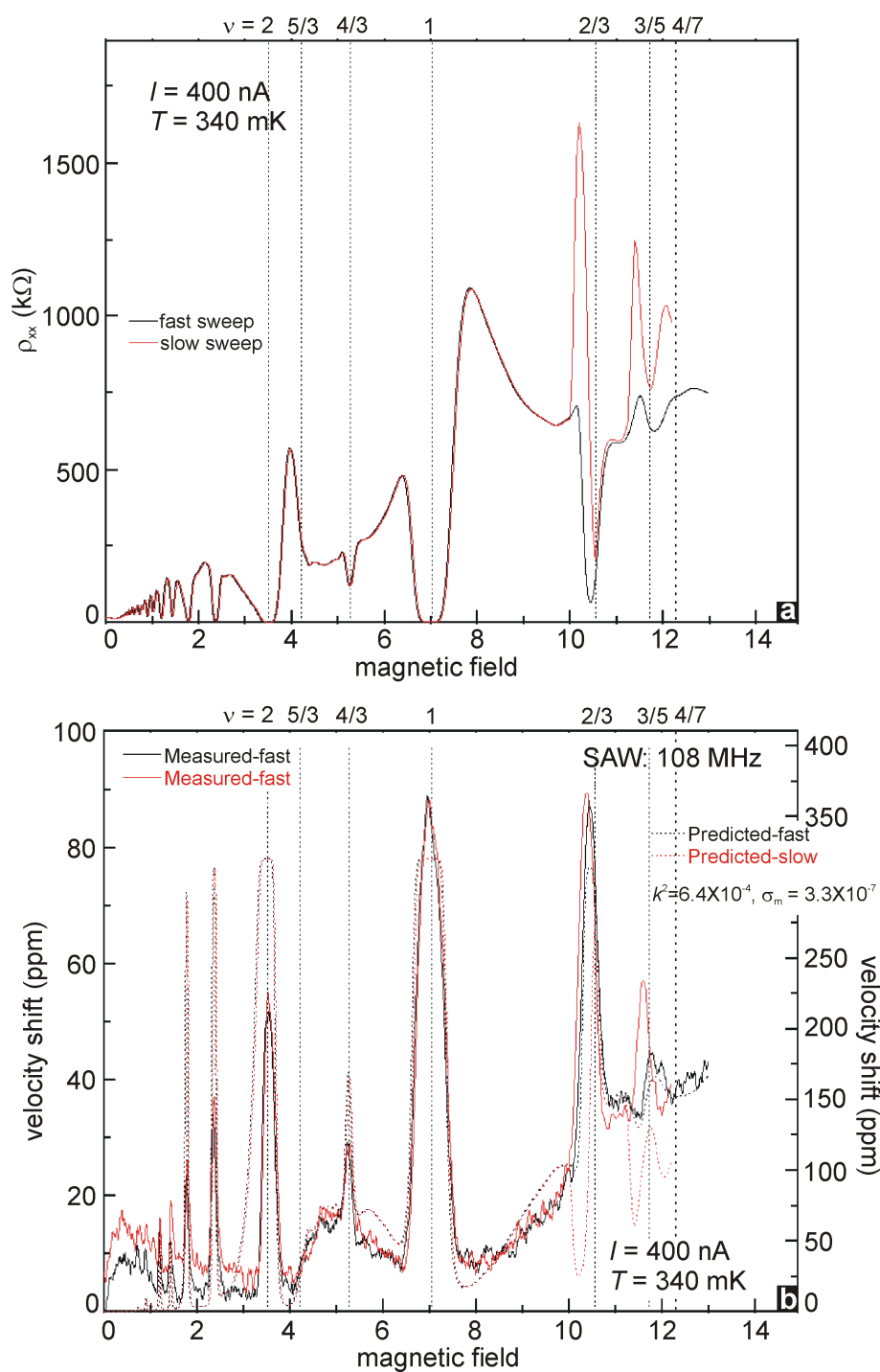


Figure A.2: (a) Transport measurement in the high current regime ($I = 400$ nA) for a fast (black curve) and a slow (red curve) sweep of the B -field. (B) Measurement of the SAW velocity shift at fast and slow B -field sweeps and the predicted values calculated by using equation A.2.

this transport experiment. A fast sweep of the B -field (black curve) does not show any anomalous behavior while the slow sweep shows a well developed HLR peak at both filling factors $\nu = 2/3$ and $\nu = 3/5$ ². The SAW measurements, on the other hand, do not reveal the HLR anomaly, even during a slow B -field sweep, as can be extracted from Fig. A.2(b). Here, we plot the velocity shift in ppm vs the magnetic field for a fast (black, solid curve) and a slow (red, solid curve) B -field sweeps. We can infer that a minimum in ρ_{xx} in transport is usually accompanied by a peak of the SAW velocity shift $\Delta v/v_0$ as can be seen at various filling factors ($\nu = 2, 4/3, 1, 2/3$ and others). The behavior of the shift can be calculated by using equation A.2, where σ_{xx} was extracted from the measured ρ_{xx} by using equation 2.5. The predicted curves are shown by the dotted lines in the same figure. We can see that the position of the predicted peaks are in good agreement with the position of the measured peaks except for the slow sweep curve at the field where the HLR appears in transport. A clear deviation from the predicted value is observed both at $2/3$ ($B \approx 10.3$ T) and at $3/5$ ($B \approx 11.5$ T). At these fillings, the predicted velocity shift of the SAW diminishes (red dotted curve), corresponding to the increase in ρ_{xx} in transport. In the measurements, however, we observe an increase of the shift as if no HLR anomaly were present. This surprising behavior might be caused by the following reasons: Firstly, as it was discussed throughout this thesis, it is likely that the scattering mechanism leading to the dissipation observed at the transition occurs due to reflections at the walls of domains with different spin polarization which cause backscattering. Since the size of the domain wall is most likely only a small fraction of the whole domain size, the carriers contributing to transport are also much less than the whole number of carriers. The domain wall carriers would then only minimally affect the shift in SAW velocity and as a result it could not be observed in the experiment. A second possibility could be that the size of the domains is bigger than the wavelength of the acoustic wave. In this case it would mean the domain size $\gg 25 \mu\text{m}$. Even though this would imply that only a few domain walls could exist in our sample, this situation cannot be ruled out. Thirdly, if the electrons which backscatter across the sample and contribute to transport are pinned or trapped at the domain walls, they would only be slightly affected by the SAW propagating along the sample. This would result in a small damping of the wave and therefore no shift in the velocity would be seen. These measurements might provide some insight into the nature of the domain structure which forms at the transition. However, they were only performed on one sample and therefore remain inconclusive. This topic will continue to be investigated by D. Dini in the future [145]. Furthermore, it should be supplemented by frequency dependent measurements over a wide range of frequencies.

²The B -field sweep rates are comparable to the ones stated in section 4.2

Appendix B

Structuring Procedure for Sample B (020502)

Mesa etching:

Due to the thick cap layer, we etched the sample by 420 nm using a so-called “deep-etching solution,” which consists of:

- Water: 400 ml
- H₂O₂: 8 ml
- H₂SO₄: 1 ml

This solution led to the following *etching rates*:

- GaAs: 100 nm/min
- AlGaAs: 150 nm/min

Contact etching:

Prior to the contact evaporation, it was necessary to first etch away 230 nm at the position of the contacts followed by immediate cleaning with HCl and semicoclean. This extra step was done to assure diffusion of enough contact material down to the QW due to the thick cap layer (250 nm).

Au/Ge/Ni contact evaporation:

The Au/Ge/Ni contacts were evaporated onto the Hall bar in the following order:

- Au: 321.6 nm, Rate: 0.3 – 0.35 nm/min
- Ge: 158.4 nm, Rate: 0.3 – 0.4 nm/min
- Ni: 80.0 – 90.0 nm, Rate: 0.2 nm/min

The saw-tooth shape contacts [see Fig. 3.1(c)] increase the area connecting the 2DES with the contacts and allows for an even distribution in both crystallographic directions ([011] and perpendicular to it). The contacts were alloyed at $T = 440^\circ\text{C}$.

Front gate and metallization:

- A thin 8.5 nm AuPd gate was evaporated at a rate of 0.1nm/s.
- 15.0 nm Ti and 150.0 nm Au were used for the metallization process needed to bond the samples to a chip carrier.

Bibliography

- [1] For a review of the Stern-Gerlach experiment see, J. J. Sakurai, *Modern Quantum Mechanics* (Addison-Wesley Publishing Company, Inc. , USA, 1995).
- [2] Nobel lecture: The method of molecular rays, From *Nobel Lectures. Physics 1942-1962* (Elsevier Publishing Company, Amsterdam, 1964).
- [3] S. Goudsmit and G. Uhlenbeck, *Nature* **117**, 264 (1926).
- [4] S. Kronmüller, Ph.D. thesis, Max-Planck-Institut für Festkörperforschung, Stuttgart, 1999.
- [5] S. Kronmüller, W. Dietsche, J. Weis, K. von Klitzing, W. Wegscheider and M. Bichler, *Phys. Rev. Lett.* **81**, 2526 (1998).
- [6] S. Kronmüller, W. Dietsche, K. von Klitzing, G. Denninger, W. Wegscheider and M. Bichler, *Phys. Rev. Lett.* **82**, 4070 (1999).
- [7] S. Kraus, Ph.D. thesis, Max-Planck-Institut für Festkörperforschung, Stuttgart, 2003.
- [8] For a review see, T. Chakraborty and P. Pietiläinen, *The Quantum Hall Effects: Integral and Fractional*, 2nd ed. (Springer-Verlag, Berlin, 1995).
- [9] M. A. Herman and H. Sitter, *Molecular beam epitaxy, Springer series in Material science 7*,(Springer, Berlin, 1996).
- [10] For a review see, T. Ando, A. Fowler and F. Stern, *Rev. Mod. Phys.* **54**, 437 (1982).
- [11] R. Dingle, H. Störmer and A. Gossard, *Appl. Phys. Lett.* **33**, 665 (1978).
- [12] R.R. Gerhardts to be published.
- [13] L. Pfeiffer and K. West, *Physica E* **20**, 57 (2003).
- [14] L. Landau, *JETP Lett.* **30**, 1058 (1956).
- [15] K. v. Klitzing, G. Dorda and M. Pepper, *Phys. Rev. Lett.* **45**, 494 (1980).

- [16] K. v. Klitzing, *Rev. Mod. Phys.* **58**, 519 (1986).
- [17] B. N. Taylor, *IEEE Trans. Instrum. Meas.* **38**, 164 (1989).
- [18] H. Bachmair, E. Göbel, G. Hein, J. Melcher., B. Schumacher, J. Schurr, L. Schweitzer and P. Warnecke, *Physica E* **20**, 14 (2003).
- [19] R. E. Prange, *Phys. Rev. B* **23**, 4802 (1981).
- [20] M. Janßen, O. Viehweger, U. Fastenrath, and J. Hajdu, *Introduction to the Theory of the Integer Quantum Hall Effect*, Hrsg. J. Hajdu (VCH, Weinheim Heidelberg, 1994).
- [21] *Perspectives on Quantum Hall Effects*, edited by S. Das Sarma and A. Pinczuk (Wiley, New York, 1996).
- [22] S.M. Girvin, in *Topological Aspects of Low Dimensional Systems*, Proceedings of the Les Houches Summer School of Theoretical Physics, Session LXIX, 1998, edited by A. Comtet, T. Jolicoeur, S. Ouvry, and F. David (Springer-Verlag and EDP Sciences, Berlin, 1999).
- [23] N. Freytag, Ph.D. Thesis, Université Grenoble 1, 2001.
- [24] B. Halperin, *Phys. Rev. B* **25**, 2185 (1982).
- [25] M. Büttiker, *Phys. Rev. B* **38**, 9375 (1988).
- [26] R.J. Haug and A.H. MacDonald and P. Streda and K. von Klitzing, *Phys. Rev. Lett.* **61**, 2797 (1988); S. Washburn, A.B. Fowler, H. Schmid, and D. Kern *Phys. Rev. Lett.* **61**, 2801 (1988).
- [27] G. Müller, D. Weiss, S. Koch, K. von Klitzing, H. Nickel, W. Schlapp, and R. Lösch, *Phys. Rev. B* **42**, 7633 (1990); G. Müller, D. Weiss, , A.V. Khaetskii, K. von Klitzing, S. Koch, H. Nickel, W. Schlapp, and R. Lösch, *Phys. Rev. B* **45**, 3932 (1992); G. Müller, Ph.D. Thesis, Max-Planck-Institute, Stuttgart, 1992.
- [28] B.J. van Wees, E.M.M. Willems, C.J.P.M. Harmans, C.W.J. Beenakker, H. van Houten, J.G. Williamson, C.T. Foxon, and J.J. Harris, *Phys. Rev. Lett.* **62**, 1181 (1989).
- [29] D. Chklovskii, B. Shklovskii and L. Glazman, *Phys. Rev. B* **46**, 4026 (1992).
- [30] A. Siddiki and R.R. Gerhardts, *Phys. Rev. B* **68**, 125315 (2003), and references therein.
- [31] E. Ahlswede, Ph.D. Thesis, Max-Planck-Institute, Stuttgart, 2002.

- [32] S. Ilani, J. Martina, E. Teitelbaum, J.H. Smet, D. Mahalu, V. Umansky and A. Yacoby, *Nature (London)* **427**, 328 (2004).
- [33] D. C. Tsui, H. L. Störmer and A. C. Gossard, *Phys. Rev. Lett.* **48**, 1559 (1982).
- [34] D. C. Tsui, *Rev. Mod. Phys.* **71**, 891 (1999).
- [35] H. L. Störmer, *Rev. Mod. Phys.* **71**, 875 (1999).
- [36] *Composite Fermions: A Unified View of the Quantum Hall Regime*, edited by O. Heinonen (World Scientific, Singapore, 1998).
- [37] R. Tao and D. Thouless, *Phys. Rev. B* **28**, 1142 (1983).
- [38] D. Lee, G. Baskaran and S. Kivelson, *Phys. Rev. Lett.* **59**, 2467 (1987).
- [39] G. Murthy and R. Shankar, *Rev. Mod. Phys.* **75**, 1101 (2003).
- [40] R. B. Laughlin, *Phys. Rev. Lett.* **50**, 1395 (1983).
- [41] R. B. Laughlin, *Rev. Mod. Phys.* **71**, 863 (1999).
- [42] B.I. Halperin, *Helv. Phys. Acta* **56**, 75 (1983).
- [43] B.I. Halperin, *Phys. Rev. Lett.* **52**, 1583 (1984).
- [44] R. de Picciotto, M. Reznikov, M. Heiblum, V. Umansky, G. Bunin and D. Mahalu, *Nature* **389**, 162 (1997).
- [45] V. Goldman and B. Su, *Science* **267**, 1010 (1995).
- [46] F. Haldane, *Phys. Rev. Lett.* **51**, 605 (1983).
- [47] R. Laughlin, *Surf. Sci.* **141**, 11 (1984).
- [48] J. Jain, *Phys. Rev. Lett.* **63**, 199 (1989).
- [49] J. Jain, *Science* **266**, 1199 (1990).
- [50] R. Willett, R. Ruel, K. West and L. Pfeiffer, *Phys. Rev. Lett.* **71**, 3846 (1993).
- [51] W. Pan, H. Störmer, D. Tsui, L. Pfeiffer, K. Baldwin and K. West, *Phys. Rev. Lett.* **90**, 016801 (2003).
- [52] J. Smet, *Nature* **422**, 391 (2003).

- [53] M. Lilly, K. Cooper, J. Eisenstein, L. Pfeiffer and K. West, Phys. Rev. Lett. **82**, 394 (1999).
- [54] J. Göres, Ph.D. thesis, Max-Planck-Institut für Festkörperforschung, Stuttgart, 2004.
- [55] J. Eisenstein, H. Stromer, L. Pfeiffer and K. West, Phys. Rev. B **41**, R7910 (1990).
- [56] W. Kang, J. Young, S. Hannahs, E. Palm, K. Campman and A. Gossard, Phys. Rev. B **56**, R12776 (1997).
- [57] J. Eom, H. Cho, W. Kang, K. Campman, A. Gossard, M. Bichler and W. Wegscheider, Science **289**, 2320 (1998).
- [58] J. Smet, R. Deutschmann, W. Wegscheider, G. Abstreiter and K. von Klitzing, Phys. Rev. Lett. **86**, 2412 (2001).
- [59] S. Kraus, O. Stern, J. Lok, W. Dietsche, K. von Klitzing, M. Bichler, D. Schuh and W. Wegscheider, Phys. Rev. Lett. **89**, 266801 (2002).
- [60] I. Kukushkin, K. von Klitzing and K. Eberl, Phys. Rev. Lett. **82**, 3665 (1999).
- [61] A. Dementyev, N. Kuzma, P. Khandelwal, S. Barrett, L. Pfeiffer and K. West, Phys. Rev. Lett. **83**, 5074 (1999).
- [62] N. Freytag, M. Horvatic, C. Berthier, M. Shayegan and L. Lévy, Phys. Rev. Lett. **89**, 246804 (2002).
- [63] E. Rezayi, Phys. Rev. B **43**, 5944 (1991).
- [64] S. Sondhi, A. Karlhede, S. Kivelson and E. Rezayi, Phys. Rev. B **47**, 16419 (1993).
- [65] H. Fertig, L. Brey, R. Côté and A. MacDonald, Phys. Rev. B **50**, 11018 (1994).
- [66] L. Brey, H. Fertig, R. Côté and A. MacDonald, Phys. Rev. Lett. **75**, 2562 (1995).
- [67] R. Côté, A. MacDonald, L. Brey, H. Fertig, S. Girvin and H. Stoof, Phys. Rev. Lett. **78**, 4825 (1997).
- [68] S. Barrett, G. Dabbagh, L. Pfeiffer, K. West and R. Tycko, Phys. Rev. Lett. **74**, 5112 (1995).
- [69] T. Chakraborty, Phys. Rev. B **34**, 2926 (1986).
- [70] For a review see, C.P. Slichter, *Principles of Magnetic Resonance* (Springer-Verlag, Berlin, 1990).

- [71] For a review see, A. Abragam, *Principles of Nuclear Magnetism* (Oxford Univ. Press, New York, 1961).
- [72] K. Hashimoto, K. Muraki, T. Saku and Y. Hirayama, *Phys. Rev. Lett.* **88**, 176601 (2002).
- [73] N. Freytag, Y. Tokunaga, M. Horvatic, C. Berthier, M. Shayegan and L. Lévy, *Phys. Rev. Lett.* **87**, 136801 (2001).
- [74] J. Eisenstein, H. Störmer, L. Pfeiffer and K. West, *Phys. Rev. Lett.* **62**, 1540 (1989).
- [75] R. Clark and P. Maksym, *Physics World* **2**, 39 (1989).
- [76] M. Dobers, K. von Klitzing and G. Weimann, *Phys. Rev. B* **38**, 5453 (1988).
- [77] U. R. G. Lommer, F. Malcher, *Phys. Rev. B* **32**, 6965 (1985).
- [78] F. Zhang and S. D. Sarma, *Phys. Rev. B* **33**, 2903 (1986).
- [79] L. Höppel, Ph.D. thesis, Max-Planck-Institut für Festkörperforschung, Stuttgart, 2004; private communications.
- [80] K. Park and J. Jain, *Phys. Rev. Lett.* **80**, 4237 (1998).
- [81] R. Du, A. Yeh, H. Störmer, D. Tsui, L. Pfeiffer and K. West, .
- [82] J. Lok, S. Kraus, O. Stern, W. Dietsche, K. von Klitzing, W. Wegscheider, M. Bichler and D. Schuh, *Physica E* **22**, 138 (2004).
- [83] K. Hashimoto, T. Saku and Y. Hirayama, *Phys. Rev. B* **69**, 153306 (2004).
- [84] I. Kukushkin, K. von Klitzing and K. Eberl, *Phys. Rev. B* **55**, 10607 (1997).
- [85] E. Mariani, N. Magnoli, F. Napoli, M. Sasseti and B. Kramer, *Phys. Rev. B* **66**, 241303(R) (2002).
- [86] I. Kukushkin, J. Smet, K. von Klitzing and W. Wegscheider, *Nature* **415**, 409 (2002).
- [87] T. H. R. Skyrme, *Proc. Royal Soc. (London)* **A262**, 233 (1961).
- [88] I. Kukushkin, K. von Klitzing and K. Eberl, *Phys. Rev. B* **60**, 2554 (1999).
- [89] D. Leadley, R. Nicholas, D. Maude, A. Utjuzh, J. Portal, J. Harris and C. Foxon, *Phys. Rev. Lett.* **79**, 4246 (1997).
- [90] M. Dobers, K. von Klitzing, J. Schneider, G. Weimann and K. Ploog, *Phys. Rev. Lett.* **61**, 1650 (1988).

- [91] K.R. Wald, L.P. Kouwenhoven, P.L. McEuen, N.C. van der Vaart, and C.T. Foxon, *Phys. Rev. Lett.* **73**, 1011 (1994); D.C. Dixon, K.R. Wald, and P.L. McEuen, *Phys. Rev. B* **56**, 4743 (1997).
- [92] T. Machida, S. Ichizuka, T. Yamazaki, S. Komiyama, K. Muraki and Y. Hirayama, *Phys. Rev. B* **65**, 233304 (2002).
- [93] W. Desrat, D. Maude, M. Potemski, J. Portal, Z. Wasilewski and G. Hill, *Phys. Rev. Lett.* **88**, 256807 (2002).
- [94] G. Denninger, *Hyperfine Interaction*(2002). http://www.physik.uni-stuttgart.de/ExPhys/2.Phys.Inst./official/g.denninger/GKMR2002/PDF/hyperfine_interaction.PDF.
- [95] A. Overhauser, *Phys. Rev.* **92**, 411 (1953).
- [96] S. Barrett, R. T. G., L. Pfeiffer and K. West, *Phys. Rev. Lett.* **72**, 1368 (1994).
- [97] W. Hofmann, G. Denninger and H. Pascher, *Phys. Rev. B* **48**, 17035 (1993).
- [98] J. Smet, R. Deutschmann, F. Ertl, W. Wegscheider, G. Abstreiter and K. von Klitzing, *Phys. Rev. Lett.* **92**, 086802 (2004).
- [99] V. Bayot, M.B. Santos, and M. Shayegan, *Phys. Rev. B.* **46**, 7240 (1992); V. Bayot, E. Grivei, S. Melinte, M.B. Santos, and M. Shayegan, *Phys. Rev. Lett.* **76**, 4584 (1996), S. Melinte, E. Grivei, V. Bayot, and M. Shayegan, *Phys. Rev. Lett.* **82**, 2764 (1999).
- [100] S.A.J. Wieggers, M. Specht, E.D. Bibow, Lévy, S. Melinte, E. Grivei, V. Bayot, M.Y. Simmons, D.A. Ritchie, M. Shayegan, A. Cavanna, B. Etienne, G. Martinez, P. Wyder, *Physica (Amsterdam)* **256B**, 16 (1998).
- [101] I. Meinel, T. Hengstmann, D. Grundler, D. Heitmann, W. Wegscheider and M. Bichler, *Phys. Rev. Lett.* **82**, 819 (1999).
- [102] M. Eickhoff and D. Suter, *J. Magn. Reson.* **166**, 69 (2004).
- [103] R. Tycko, G. Dabbagh, S. Barrett, L. Pfeiffer and K. West, *Science* **268**, 1460 (1995).
- [104] H.D.M. Davies, R.L. Brockbank, J.F. Ryan, and A.J. Tuberfield, *Physica (Amsterdam)* **256B**, 104 (1998); R.L. Brockbank, H.D.M. Davies, J.F. Ryan, M.A. Thomson, and A.J. Tuberfield, *Physica (Amsterdam)* **6E**, 56 (2000).
- [105] G. F. M. Eickhoff, B. Lenzman and D. Suter, *Phys. Rev. B* **65**, 125301 (2002).

- [106] For a review see, N.H. Balshaw, *Practical Cryogenics: An introduction to laboratory cryogenics*, (Published by Oxford Instruments Superconductivity Limited, England, 2001).
- [107] T. Jungwirth, A. MacDonald, L. Pfeiffer, K. West and R. Tycko, *Phys. Rev. Lett.* **87**, 216801 (2001).
- [108] S. Kronmüller, W. Dietsche, K. von Klitzing, W. Wegscheider and M. Bichler, *Physica B* **256**, 82 (1998).
- [109] S. Koch, R. Haug, K. v. Klitzing and M. Razeghi, *Phys. Rev. B* **47**, 4048 (1993).
- [110] U. Zeitler, H. Schumacher, A. Jansen and R. Haug, *Phys. Rev. Lett.* **86**, 866 (2001).
- [111] E. de Poortere, E. Tutuc, S. Papadakis and M. Shayegan, *Science* **290**, 1546 (2000).
- [112] J. Lok, M. Lynass, W. Dietsche, K. von Klitzing and M. Hauser, *Physica E* **22**, 94 (2004).
- [113] N. Kumada, D. Terasawa, Y. Shimoda, H. Azuhata, A. Sawada, Z. Ezawa, K. Muraki, T. Saku and Y. Hirayama, *Phys. Rev. Lett.* **89**, 116802 (2002).
- [114] T. Jungwirth, S. Shukla, L. Smrcka, M. Shayegan and A. MacDonald, *Phys. Rev. Lett.* **81**, 2328 (1998).
- [115] T. Jungwirth and A. MacDonald, *Phys. Rev. B* **63**, 035305 (2000).
- [116] U. R. G. Lommer, F. Malcher, *Phys. Rev. Lett* **60**, 728 (1988).
- [117] L. Engel, S. Hwang, T. Sajoto, D. Tsui and M. Shayegan, *Phys. Rev. B* **45**, 3418 (1992).
- [118] K. Hashimoto, K. Muraki, N. Kumada, T. Saku and Y. Hirayama cond-mat/0407729.
- [119] K. Muraki, T. Saku and Y. Hirayama, *Physica E* **12**, 8 (2002).
- [120] D. Maude, M. Potemski, J. Portal, M. Henini, L. Eaves and G. Hill, *Phys. Rev. Lett.* **77**, 4604 (1996).
- [121] D. Paget, G. Lampel, B. Sapoval and V. Safarov, *Phys. Rev. B* **15**, 5780 (1977).
- [122] J.P. Hornak, *The Basics of NMR* (1999). [<http://www.cis.rit.edu/htbooks/nmr/inside.htm>].
- [123] P. Khandelwal, N. Kuzma, S. Barrett, L. Pfeiffer and K. West, *Phys. Rev. Lett.* **81**, 673 (1998).
- [124] N. Kuzma, P. Khandelwal, S. Barrett, L. Pfeiffer and K. West, *Science* **281**, 686 (1998).

- [125] W. Desrat, D. Maude, M. Potemski, J. Portal, Z. Wasilewski and G. Hill, *Physica E* **12**, 149 (2002).
- [126] B. Halperin, P. Lee and N. Read, *Phys. Rev. B* **47**, 7312 (1993).
- [127] J. Sinova, A. MacDonald and S. Girvin, *Phys. Rev. B* **62**, 13579 (2000).
- [128] N. Freytag and L.P. Lévy to be published.
- [129] M. Schreiner, H. Pascher, G. Denninger, S. Studenikin, G. Weimann and R. Lösch, *Solid State Commun.* **102**, 715 (1997).
- [130] J. Smet, R. Deutschmann, F. Ertl, W. Wegscheider, G. Abstreiter and K. von Klitzing, *Nature* **415**, 281 (2002).
- [131] K. Moon, H. Mori, K. Yang, S. Girvin, A. MacDonald, L. Zheng, D. Yoshioka and S.-C. Zhang, *Phys. Rev. B* **51**, 5138 (1995).
- [132] A. Koulakov, M. Fogler and B. Shklovskii, *Phys. Rev. Lett.* **76**, 499 (1996).
- [133] R. Willet, J. Eisenstein, H. Störmer, D. Tsui, A. Gossard and J. English, *Phys. Rev. Lett.* **59**, 1776 (1987).
- [134] W. Pan, J.-S. Xia, V. Shvarts, D. Adams, H. Stormer, D. Tsui, L. Pfeiffer, K. Baldwin and K. West, *Phys. Rev. Lett.* **83**, 3530 (1999).
- [135] F. Haldane and E. Rezayi, *Phys. Rev. Lett.* **60**, 956 (1988).
- [136] J. Eisenstein, R. Willet, H. Störmer, D. Tsui, A. Gossard and J. English, *Phys. Rev. Lett.* **61**, 997 (1988).
- [137] R. Morf, *Phys. Rev. Lett.* **80**, 1505 (1998).
- [138] E. Rezayi and F. Haldane, *Phys. Rev. Lett.* **84**, 4685 (1998).
- [139] J. Eisenstein, K. Cooper, L. Pfeiffer and K. West, *Phys. Rev. Lett.* **88**, 076801 (2002).
- [140] J.P. Eisenstein and A.H. MacDonald, cond-mat/0404113 and references therein.
- [141] R. Wiersma, J. Lok, S. Kraus, W. Dietsche, K. von Klitzing, D. Schuh, M. Bichler, H.-P. Tranitz and W. Wegscheider, *Phys. Rev. Lett.* **93**, 266805 (2004).
- [142] I. B. Spielman, L.A. Tracy, J.P. Eisenstein, L.N. Pfeiffer and K.W. West, cond-mat/0410092.

- [143] A. Wixforth, J. Scriba, M. Wassermeier, J. Kotthaus, G. Weimann and W. Schlapp, *Phys. Rev. B* **40**, 7874 (1989).
- [144] I. Kennedy, Ph.D. thesis, University of Nottingham, England, 1998.
- [145] D. Dini, Ph.D. thesis, Max-Planck-Institut für Festkörperforschung, Stuttgart, to be published.

Acknowledgments

In the following, I would like to thank the people who contributed to the completion of this work.

- Klaus von Klitzing möchte ich danken für die Aufnahme in seine Gruppe, für das Interesse an meiner Arbeit, die Übernahme des Hauptberichtes und für die Fähigkeit seine Begeisterung zu übermitteln.
- Werner Dietsche für das Interessante Projekt, die gute Betreuung und die enge Zusammenarbeit während die ganze Zeit meiner Promotion.
- G. Denninger für die Übernahme des Mitberichtes.
- Nicolas Freytag möchte ich besonders danken für die gute Zusammenarbeit, die viele Diskussionen und Anregungen, das Korrekturlesen dieses Manuskripts und vor allem für die gute Zeiten in Grenoble, merci beaucoup Nicola.
- Das Team der Dietsche Gruppe, insbesondere Stefan Kraus, Sjoerd Lok, Mark Lynass, Dimitri Dini und Rodney Wiersma für viele Diskussionen, Anregungen und vor allem gute Zeiten.
- Jurgen Smet für die Möglichkeit im Mischungskryostat zu messen und die wissenschaftliche Diskussionen.
- Aurélien Fay for his help with many measurements during his “maitrise” work in our group and the good times.
- Werner Rauscher für seine Unterstützung und Hilfsbereitschaft in vielen technischen Probleme sowie spannende Fussballdiskussionen.
- Monika Riek für die Einführung im Reinraum und die Präparation der Proben.
- Jürgen Weis für die Meßzeiten im Mischkryostat.
- W. Wegscheider und D. Schuh für die Herstellen hochbeweglicher Proben, die dieser Arbeit ermöglicht haben.

- C. Berthier, M. Horvatic and P. van der Linden for the opportunity to use the NMR facilities at the Grenoble High Magnetic Field Laboratory.
- Koji Muraki for enlightening discussions during his stay in our group.
- Ulli Waizmann möchte ich speziell für Ihre Unterstützung aber vor allem Ihre sehr wichtige Freundschaft während allen diesen Jahren danken.
- Jörn Göres (MMM) für viele wissenschaftliche und nicht-wissenschaftliche Diskussionen, für das Korrekturlesen der Arbeit und weil wir einfach super gute Freunde geworden sind.
- Afif Siddiki and Martin Geisler for many interesting discussions and for the great friendship which developed over the years.
- An allen andere Mitglieder und ehemalige Mitglieder der Gruppe, wie Thomas Reindl, Jan Hüls, Michael Pohlt, Armin Welker,... und alle andere die ich hier nicht erwähnt habe für die tolle Atmosphäre.
- Bernd Weidner, mi amigo que conozco por mayor tiempo en Alemania, für viele Interessante Gespräche.
- Nikki Webb for her support, love and patience during my thesis.
- A mi familia (Gleb, Patita, Edgar, Pato y Pau) por todo lo que han hecho por mi.

Lebenslauf

Name: Omar I. Stern Gonzalez
Geburtsdatum: 07.08.1971
Geburtsort: Monterrey, Mexiko

1987-1990 Gymnasium am Instituto Tecnologico y de Estudios Superiores de Monterrey, Mexiko.

1990-1994 Studium der technischen Physik am Worcester Polytechnic Institute, Massachusetts, USA.

1992-1993 Austauschstipendiat an der ETH, Zürich, Schweiz.

1994-1995 Praktikum bei Mannesmann Rexroth.

1996 Praktikum bei dem Bayerischen Zentrum für Angewandte Energieforschung.

1997-1999 Diplomstudiengang Physik an der Universität Würzburg.

1999 Diplomarbeit am Lehrstuhl für Technischen Physik: Magnetolumineszenz an Quantenpunkten.

11/99 Diplom in Physik

seit 05/2000 Anfertigen der vorliegenden Dissertation am Max-Planck-Institut für Festkörperforschung bei Prof. K. von Klitzing.